Performance Trade-Offs of Fine Attitude Control Actuators for Small Earth Observation Satellites in Low Earth Orbit

J.R. van der Ploeg

Delft University of Technology

TU Delft

Performance Trade-Offs of Fine Attitude Control Actuators for Small Earth Observation Satellites in Low Earth Orbit

by

J.R. van der Ploeg

at the Delft University of Technology.

Student number:	4372107
Master:	MSc Aerospace Engineering
Programme:	Space Flight
Profile:	Space Engineering
Issue:	Final report
Date of submission:	January 4, 2026
Thesis supervisor:	Dr. Ir. J. Bouwmeester

TU Delft

Abstract

The selection of a Fine Attitude Control Actuator (FACA) is a systems engineering decision for small satellites in Low Earth Orbit (LEO), directly impacting mission success by affecting pointing accuracy, stability, and image quality. This thesis addresses the lack of a standardised rationale for selecting one actuator over another, and a quantitative selection methodology, by developing a model-based framework to determine the most suitable FACA for nadir-pointing small satellites (20–300 kg) performing sub-meter spatial-resolution Earth observation.

A 4-DOF modular simulation is developed to model orbital dynamics, dominant disturbance torques present at altitudes of 200 to 500 km (atmospheric, gravity-gradient, residual-dipole, and solar-radiation-pressure), and closed-loop PID attitude control. This tool enabled quantitative trade-off analysis between Momentum Wheel (MW) and Reaction Wheel (RW) assemblies, evaluating their pointing accuracy and precision under identical mass and volume constraints.

The results demonstrate that for the defined mission scope, an RW assembly is the most suitable actuator, consistently achieving superior pointing performance. Under perfect sensing conditions, RW systems can achieve sub-meter precision, outperforming MW systems by an order of magnitude for the same mass allocation. While MW systems exhibited lower susceptibility to sensor noise, their best-case precision remained around 2 meters, at the expense of significantly higher pointing-accuracy error (approximately 200 m). The primary trade-off is quantified as the required torque authority, which depends on orbital altitude and satellite cross-section, versus the total mass of the actuator assembly.

The main contribution of this work is a generalised and validated framework for quantitatively predicting closed-loop attitude performance from high-level mission parameters, providing a practical tool for rapid preliminary actuator sizing and selection during early-phase mission design studies.

Keywords: *Attitude Determination and Control System (ADCS), Fine Pointing, Fine Attitude Control Actuator, Reaction Wheels, Momentum Bias, Momentum Wheels, PID attitude control, Disturbance Torques, Small Satellites, Low Earth Orbit (LEO), Trade-off Analysis.*

Preface

This master's thesis, titled *Performance Trade-Offs of Fine Attitude Control Actuators for Small Earth Observation Satellites in Low Earth Orbit*, concludes the Master of Science programme in Space Engineering as part of the Aerospace Engineering faculty at Delft University of Technology. The research presented herein was conducted in partial fulfilment of the requirements for the degree of Master of Science.

The work was carried out at the Space Engineering faculty under the supervision of Dr. Ir. Jasper Bouwmeester. The project spanned from June 2023 to December 2025.

This academic journey coincided with a period of grief due to personal loss, demanding immense fortitude. Yet, it concluded with the immense joy of welcoming my son, Theo. This contrast shaped my perspective, making the completion of this work a milestone I am deeply proud of.

In that daylight, I want to express my sincere gratitude to my supervisor for his guidance, insightful feedback, and support throughout this research endeavour. His expertise and willingness to discuss the project's conceptual challenges were greatly appreciated.

I also extend my thanks to my family, friends, and colleagues for their encouragement and understanding during this intensive period.

Johannes Rijpke van der Ploeg
Leiden, January 2026

Contents

List of Tables

List of Figures

Nomenclature

Acronyms

ADCS Attitude Determination and Control System

CMGs Control Moment Gyroscopes

COM Center of Mass

DCMs Direction Cosine Matrices

ECEF Earth-Centered Earth Fixed

ECI Earth-centered inertial

EUV Extreme Ultraviolet

FACA Fine Attitude Control Actuator

FOV Field of View

GOCE Gravity field and steady-state Ocean Circulation Explorer

GSD Ground Sampling Distance

LEO Low Earth Orbit

LVLH Local Vertical Local Horizontal

MARG Magnetic, Angular Rate, and Gravity

MWs Momentum Wheels

NED North-East-Down

NIR Near-Infrared

NOAA National Oceanic and Atmospheric Administration

ODE Ordinary Differential Equation

PFM Proto-Flight Model

PQR Angular rates

PSF Point Spread Function

RAAN Right Ascension of the Ascending Node

RD Residual Dipole

RDT Residual Dipole Torque

RF Radio-Frequency

RWs Reaction Wheels

S/C Spacecraft

SQP Sequential Quadratic Programming

SRP Solar Radiation Pressure

std Standard deviation

TIR Thermal Infrared

TPMC Test-Particle Monte Carlo

Greek

α	Angle of attack, absorption coefficient, contact angle	[rad]
β	Incidence angle	[rad]
δ	Gimbal angular velocity	[rad/s]
ϵ	Emissivity	
η	Efficiency	
γ	Specific heat ratio, optical coefficient of diffuse reflectivity	
λ	Wavelength	[nm]
μ	Gravitational parameter, molecular weight	$[m^3/s^2]$, [amu]
ν	Frequency	
Ω	Right Ascension of the Ascending Node (RAAN)	[deg]
ω	Argument of the periapsis, rotational velocity	[deg], [rad/s]
ω_w	Wheel speed	[rad/s]
ϕ	Roll angle	[rad]
ψ	Yaw angle	[rad]
ρ	Density	$[kg/m^3]$
σ	Stefan-Boltzmann constant, standard deviation	$[W/m^2K^4]$
τ	Torque	[Nm]
θ	True anomaly, Angle of incidence, Pitch angle	[deg], [rad]
υ	True anomaly	[rad]

Subscripts and Superscripts

0	Initial value
a	Absorption
adt	Aerodynamic Torque
b	Body-fixed frame
bb	Blackbody
c	Cross-coupling, cage
cg	Center of gravity
D	Diagonal
d	Diffuse, diameter
Earth	Earth
eff	Effective
fw	Flywheel
ggt	Gravity Gradient Torque

H	Horizontal
i	Initial, inner, i-th wheel
max	Maximum
min	Minimum
MW	Momentum wheel
o	Outer
perfect	Perfect sensing
RD	Residual Dipole
RW	Reaction Wheel
s	Specular
safe	Safe value
SRP	Solar Radiation Pressure
tot	Total
tp	Thermal pressure
V	Vertical
w	Wheel

Variables

A	Area	$[m^2]$
Ap	Geomagnetic Ap index	
CD	Drag coefficient	
CF	Force Coefficient	
D	Aperture diameter, Pitch circle diameter	[m]
d	Pixel size, Diameter of roller elements	[m]
Doffset	Steiner Term	$[kg \cdot m^2]$
E	Energy	[J]
e	Eccentricity	
es	Unit vector pointing from the spacecraft to the Sun	
ev	Unit vector directed towards the velocity vector	
F	Force	[N]
f	Focal length	[m]
F10	Solar radio flux at ten centimeters	
FB	Direction Cosine Matrix, body frame	
Frad	Radial force	[N]
H	Angular Momentum	$[kg \cdot m^2/s]$

h	Altitude, height	[m]
h'	Geocentric Altitude	[m]
Htotal	Total angular momentum	$[kg \cdot m^2/s]$
I	Moment of Inertia	$[kg \cdot m^2]$
Ibb	Black-body radiation	$[W/m^2]$
Iinitial	Initial	$[W/m^2]$
J2	Second zonal harmonic coefficient	
K	Gain	
kf	Fraction coefficient	
kn	Knudsen number	
L	Characteristic length	[m]
Lb	Satellite body length	[m]
M	Mean anomaly	
m	Mass	[kg]
Ma	Applied Moment	[Nm]
N	Number of reflections, Number of rolling elements	
n	Mean motion	
P	Pressure	[Pa]
Q	Quality factor, Heat Flux	[W]
q	Quaternion	
R	Geocentric distance	[m]
r	Radial distance	[m]
RCP	Center of Pressure	
RD	Dipole strength	$[Am^2]$
REarth	Earth's radius	[m]
Rinitial	Initial radius	[m]
Ro	Geocentric radius, Outer Radius	[m]
S	Surface area	$[m^2]$
SR	Spatial Resolution	[m]
T	Temperature, Period	[K], [s]
t	Time, Thickness	[s], [m]
tw	Wall thickness	[m]
V	Velocity	[m/s]
Vm	Macroscopic velocity	[m/s]
Vt	Molecular thermal velocity	[m/s]
W	Power, Width	[W], [m]
X	Ground resolution element	[m]
z	Zenith angle	

1 Introduction

This chapter establishes the motivation for this research project, providing background information in section 1.1 on the challenges of selecting a fine attitude control actuator (FACA) for small satellites in Low Earth orbit (LEO). The complexities arising from significant aerodynamic disturbances and the lack of a standardised selection process are highlighted. The research objectives are then defined in section 1.2, along with specific research questions that guide the investigation in section 1.3. A brief overview of the methodology is given in section 1.4. Finally, in section 1.5, an overview of the thesis structure is presented, outlining the organisation of the subsequent chapters.

1.1 Background information

The design and operation of small satellites in Low Earth Orbit (LEO) have gained traction due to their potential to provide valuable services to humanity [41], thanks to the performance benefits of flying at lower altitudes, such as improved resolution and lower launch mass [19]. These small satellites serve a diverse range of purposes, including Earth observation, scientific research, communication, and technology demonstration. To succeed, they all share a common need: precise and stable orientation in space [30]. Achieving this precise attitude control is vital for mission success, as it influences a satellite's ability to capture data, communicate effectively, and maintain operational efficiency. Designing a proper Attitude Determination and Control System (ADCS) encompasses a detailed study on the combination of algorithms and sensors together with actuator-based control [29], especially when pointing accuracies with sub-arcsec to milli-arcsec levels are desired [10].

Although actuators on flying satellites are well documented, the trade-offs among them and the satellite design space are often not published. Thus, the rationale is not always traceable, allowing for speculation. It is therefore important to examine options and identify factors that affect actuator selection.

Selecting suitable actuators for a LEO satellite is a complex and time-consuming process. It is not immediately clear which actuator best serves the mission, given the numerous influencing factors [12]. At altitudes of 230-650 km, aerodynamic disturbances add complexity, causing unwanted torque that control torques generated by the actuators must compensate for.

In this research, control torque and angular-momentum counter-disturbances are studied using Fine Attitude Control Actuators (FACAs). However, any rotational mechanism generates micro-vibrations that worsen jitter performance and require power [108]. This often necessitates a systems engineering approach, and the rationale for selecting a specific actuator may be limited and in need of improvement.

Choosing FACAs directly affects a satellite's ability to orient and stabilise itself [93], thereby influencing attitude stability, pointing accuracy, and image quality due to unwanted micro-vibrations. Common FACAs include Reaction Wheels, Momentum Bias Wheels, and Control Moment Gyroscopes (CMGs), each with distinct advantages and disadvantages. Exploring selection criteria and the performance of FACAs is particularly interesting for small satellites (20–300 kg). For nanosatellites (less than 10 kg, up to $10 \times 10 \times 11.35$ cm), the FACA choice is driven by the design space; larger satellites (300+ kg) are less constrained and thus less interesting to examine.

1.2 Research objectives

This thesis aims to provide a comprehensive understanding of the decision-making surrounding the choice of fine attitude control actuators for small satellites of $20 - 300\ kg$ in Low Earth Orbit (LEO) at altitudes of $200 - 650\ km$, where aerodynamic forces can have a significant effect on the orbital and attitude dynamics [19]. It aims to enhance and streamline the decision-making process for selecting actuators, bridging the gap between the system's engineering approaches and academic research on a particular design. The objective of this thesis is twofold:

- Identifying the key trade-off arguments for choosing fine attitude control actuators to achieve stability performance (pointing accuracy, pointing precision). To accomplish this, the balance between orbital selection (altitude and inclination) and spacecraft size is investigated under certain design constraints.

- To identify the factors driving the pointing and stability performance of these actuators and explore potential solutions for their improvement. To achieve this, the dominant design aspects that influence the performance of fine attitude control actuators are discussed, too.

Ultimately, the knowledge gained from this research may enable a more informed choice when selecting a fine attitude control actuator in a premature state.

1.3 Main and sub-research questions

In this section, two main research questions are presented, each accompanied by four sub-questions. A motivation for their relevance is provided for each sub-question.

A. What are the key performance trade-offs for selecting a fine attitude control actuator for a nadir-pointing small satellite in Low Earth Orbit?

The selection of fine attitude control actuators is a critical decision in the design and operation of small satellites in Low Earth Orbit. Attitude control is essential for satellite stability, proper orientation, and effective mission execution [11]. However, selecting the appropriate type of fine attitude control actuator entails trade-offs, as each has distinct advantages and disadvantages. The rationale for this research question is the need to understand these trade-offs. Comparing FACAs based on the equivalent mass and design-space budgets of the underlying components will provide insights into the performance differences they impose. Assessing nadir-pointing performance ensures that the satellite is aligned with the local-vertical-local-horizontal (LVLH) reference frame, thereby automatically capturing the forward- and zenith-pointing performance as well. Moreover, nadir-pointing requires an operational profile dominated by fine stabilisation rather than agile manoeuvring, allowing the trade-off analysis to focus on precision-based performance metrics. In addition, this constraint enables comparison of the measured attitude with the LVLH reference frame, thereby simplifying modelling and simulation. By exploring trade-off arguments, this research aims to improve the selection of FACAs given a pointing accuracy and precision of small satellites. To address the first primary research question in more detail, the following sub-research questions have been formulated:

(A.1) What are the mission trade-off arguments to select a fine attitude control actuator?
Different missions have varying objectives and constraints. Specific mission objectives may affect the selection of suitable attitude-control actuators. Understanding how these factors influence actuator selection ensures that the chosen FACA aligns with the mission's goals.

(A.2) What are the minimum satellite bus dimensions needed to house a diffraction-limited imager for sub-meter resolution to limit the trade-space?
This sub-question addresses a systems engineering challenge in a high-resolution Earth observation mission: the trade-off between desired performance and practical feasibility. The drive for sub-meter resolution necessitates a feasible combination of imager aperture size, orbital altitude, and detector technology, thereby determining the minimum satellite bus dimensions. Hence, it transforms a mission goal into a viable minimum physical design per scenario.

(A.3) What are the quantitative models for the dominant external disturbance torques acting on a satellite in LEO, and how can a modular simulation be developed and verified to generate these torques?
The selection and sizing of attitude control actuators are systems engineering decisions that are fundamentally constrained by the external disturbance environment. An accurate quantification of these disturbance torques is therefore a prerequisite for all subsequent design choices. A modular simulation enables a performance evaluation across the mission envelope and various satellite configurations.

(A.4) For representative small satellite designs, how do these disturbance torques vary with key orbital parameters (altitude, inclination, RAAN) and satellite geometry and attitude?
For a representative satellite configuration, a parametric analysis can evaluate torque variations as functions of orbital parameters, satellite geometry, and attitude. Establishing these relationships helps define worst-case scenarios and determine the operational boundaries that drive actuator sizing.

B. For a sub-meter spatial-resolution nadir-pointing Earth observation mission, which fine attitude control actuator is the most suitable candidate when evaluated against pointing error?

This research question examines the factors influencing the pointing and stability performance of the fine attitude control actuators selected for a typical LEO Earth observation mission. Factors affecting stability should be considered to determine whether and how to improve performance further. To create a fair performance trade-off, the following sub-questions are posed:

(B.1) How can a parametric model be developed to determine the size and mass of the FACAs as a function of the maximum required counter-torque derived from the worst-case disturbance analysis?
To transition from a theoretical torque requirement to a practical hardware selection, a quantitative model is essential. This sub-question establishes a direct relationship between the disturbance torque and the actuator mass, a factor that drives satellite feasibility.

(B.2) How can the trade-space of various orbits and designs be reduced to a manageable set of key driving parameters?
The number of variables influencing actuator performance could be a lot. This analysis identifies parameter variability, thereby reducing the trade space to a manageable set. This enables efficient, focused simulation and analysis while avoiding unnecessary computational effort.

(B.3) How does the performance of each actuator type compare when evaluated in a closed-loop simulation against pointing accuracy and precision for a disturbance-rejection scenario?
This sub-question validates actuator performance in a closed-loop simulation by assessing pointing error under realistic disturbance conditions. This provides empirical evidence for the trade-off analysis.

(B.4) How can the quantitative results from the simulations be synthesised into a robust, generalizable selection methodology to recommend the optimal actuator for the stated mission?
The ultimate goal is a defensible and generalizable design decision for the stated mission. This sub-question synthesises the performance data into an overview. This ensures the final recommendation is transparent and adaptable to similar mission profiles.

1.4 Methodology

The methodology for this research aims to address the research objectives by facilitating the selection of suitable fine-control actuators for small LEO satellites to achieve stable nadir pointing. The systematic approach involves the following steps, which are interlinked to the sub-research questions (A.1-B.4):

1. **Identification of candidate satellites and actuators (A.1-A.3, B.1):** The first step is to identify the range of satellites and orbits, and fine attitude control actuators suitable for sub-meter spatial resolution imaging, while keeping the size and mass of the satellite minimal. It is established using textbook methods and a literature review. FACA sizing is performed using an optimising design methodology.

    - Define the Trade-Space: Based on a literature review of small EO satellites, a representative baseline satellite will be defined (mass, dimensions, geometry properties). Key parameters to vary will include imager sizing, orbital altitude, inclination, and satellite geometry (squared versus elongated).
    - Quantify Disturbance Torques: The simulations will run at multiple points in the trade space to identify the worst-case disturbance torque magnitudes and profiles.
    - Develop automatic FACA sizing: Data sheets from an actuator manufacturer will be analysed to compare and verify the developed FACA sizing methodology (as a function of maximum torque, angular momentum capacity, and design space).

2. **A modular 4-DOF hybrid simulation (A.3):** The satellite must be propagated through a Keplerian orbit to be able to analyse the attitude stability performance (pointing accuracy and precision). MATLAB is used to program and run simulations.
   - Orbital Dynamics: Numerical propagation in a circular Keplerian orbit, whereby the orbital position is solely orbit parameter and time-dependent, and is therefore considered 1-DOF. The attitude must be determined more accurately by solving the 3-DOF Euler equations, accounting for the dominant disturbances.
   - Disturbance Torque Models: realistic environmental models for the dominant torques will be implemented as a function of orbital position and attitude.
   - Actuator Models: Low-fidelity models for momentum and reaction wheels will be developed to capture their operational envelopes.
   - Controller: A PID controller will be implemented for closed-loop attitude control.
3. **Case study verification (A.2, A.3, B.1):** The fidelity of each model is evaluated by comparing the intermediate output results to existing case studies documented in research papers as a benchmark. This will provide practical insights into how the generated overview can support the final decision-making.
4. **Tradespace exploration (A.4, B.2-B.4):** The theoretical pointing and stability performance will have to be estimated quantitatively for numerous satellites in various orbits that reflect real-world design possibilities. These estimations rely on the simulation framework developed and verified in steps 1-3. Again, MATLAB is employed to set up, run, and extract the (final) results.
   - Closed-Loop Performance Evaluation: For the identified scenarios, the performance of MW- and RW-controlled satellites will be evaluated in closed-loop simulations. Key metrics include pointing accuracy and precision.
   - Trade-Space Analysis: A Trade-Space analysis addressing (sensor noise versus perfect sensing {2}, MW- versus RW-controlled {2}, trade-space {128}: $2 \times 2 \times 128 = 512$) simulations that account for variations in satellite geometry, inertia, orbital and disturbance parameters will be conducted to evaluate the preferred actuator selection.

1.5 Report structure

This report comprises five parts, ranging from foundations and problem setup to analysis, results, and conclusions, and is presented in Figure 1.

Figure 1: Report flowchart

The structure is detailed below:

I **Foundation & Problem Setup**:
This part establishes the groundwork for the research. *Chapter 1* introduces the background, objectis, and methodology. *Chapter 2* provides definitions and outlines the scope, anatomises Fine Attitude Control Actuators (FACAs), and details the key concepts of Earth observation parameters and satellite design considerations that underpin the research.

II **Core Theory & Modelling**:
This is the theoretical backbone of the research. *Chapter 3* derives the orbital dynamics, reference frames, and equations of motion governing satellite attitude. *Chapter 4* reviews the external disturbance torques acting on a satellite in LEO. *Chapter 5* then details the implementation and verification of the environmental models for atmospheric drag, gravity-gradient, magnetic, and solar-radiation-pressure torques.

III **Satellite Design & Control**:
This addresses the application of the developed models. *Chapter 6* defines a representative satellite configuration and details the methodology for sizing the MW and RW assemblies based on the derived disturbance torques. It also introduces the attitude PID control laws used to command these actuators.

IV **Analysis & Results**: This presents the simulation work of this thesis from which the conclusions are drawn. *Chapter 7* explains how the Tradespace exploration is set up, including how samples are generated and filtered. *Chapter 8* describes the data-processing methods used to obtain performance metrics from the simulation results. Finally, *Chapter 9* presents and discusses the simulation results, comparing actuator performance with both perfect and imperfect sensing.

V **Final Conclusions**: This part synthesises the research findings. *Chapter 10* summarises the main findings, reflects on the scientific contributions and limitations, and provides recommendations for both industry and future academic research.

Finally, the appendix contains the complete sets of simulation input data and actuator design parameters that support the analysis within the main body of this report.

2 Scope and definitions

To provide an understanding of the involvement of fine attitude control actuators in satellite imaging, this chapter outlines the key areas explored. First, the momentum actuators for controlling the satellite's orientation, which are referred to as Fine Attitude Control Actuators (FACAs), are presented in 2.1. Next, the foundational definitions of Earth's shape and altitude are given in section 2.2. From there, the assumed satellite size and shape are discussed in 2.3, the wavelengths of interest in 2.4, the resulting ground sampling distance in 2.5, and the definitions of sway and swath width are outlined in 2.6.

Specifically, this chapter answers the following research questions:

(A.1) *What are the mission trade-off arguments to select a fine attitude control actuator?*
This question is answered in section 2.1 by evaluating the mission's objectives against the functionality of the FACA.

(A.2) *What are the minimum satellite bus dimensions needed to house a diffraction-limited imager for sub-meter resolution to limit the trade-space?*
This question is answered in sections 2.2-2.6 by defining the scope of the study. In particular, these sections limit the scope to **momentum exchange fine attitude control actuators** onboard **small mini satellites of** 20 **to** 300 kg. For smaller S/C, volumetric constraints drive the choice of FACAs; larger satellites can accommodate any actuator more easily. Secondly, to further reduce the scope, only **optical Earth observation satellites** flying at **altitudes between 200 and 600 kilometres** are considered. At these altitudes, disturbances vary with time due to space weather phenomena, which must be accounted for. In the study, the imager is intended to point in the **NADIR direction** as depicted in Figure 2.

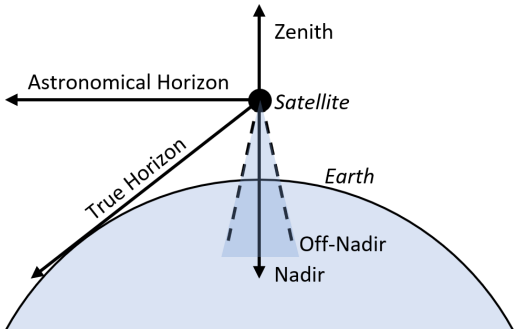

Figure 2: The NADIR is the direction pointing directly below the satellite, orthogonal to the Earth's surface. Off-NADIR is defined as the angle between the sensing direction and the vertical (NADIR) direction.

2.1 Fine Attitude Control Actuators

This study focuses on the subsystem **Actuators** within the Attitude Determination and Control System (ADCS), as discussed in section 2.1.1. Multiple actuators work together to control the satellite's orbit and attitude. Actuators that actively control attitude along one or more axes are of particular interest for Earth observation missions, as they play a significant role in the pointing and stability performance of the satellite's imager. Moreover, the type of actuation must be continuous and smooth. Therefore, this study is concerned with *momentum actuators* and will be referred to as **Fine Attitude Control Actuators** (or FACAs).

Momentum wheels (MWs), Reaction wheels (RWs), and control moment gyroscopes (CMGs) are actuators used for fine attitude control and satellite stabilisation. Each of these systems operates on different principles and offers advantages. The working principles and advantages are elicited in section 2.1.2 for MWs (momentum bias), in 2.1.3 for RWs (momentum exchange), and in 2.1.4 for CMGs (momentum directing).

The broad choice between FACAs, 'MWs', 'RWs', and 'CMGs' is explored in section 2.1.5 and depends on mission requirements, satellite size, and available power. It compares FACAs for two higher-level objectives: stability and agility. To limit the scope of this research, missions that require stability are selected, thereby limiting the research to **MWs and RWs**.

2.1.1 Attitude Determination And Control System

An Attitude Determination And Control System (ADCS) typically consists of multiple subsystems as indicated in Figure 3: sensors, actuators, controller and interface.

- **Sensors**: The ADCS Sensors system comprises absolute sensors for continuous monitoring of the satellite's attitude relative to an external frame of reference, as well as relative sensors to track changes in attitude relative to the previous state, like an Inertial Measurement Unit. The sensors are out of the scope of this research. The sensed error can be implemented as described in section 6.3.1.
- **Actuators**: The primary function of the actuators is to orient the satellite to the desired attitude by performing rotations around at least one of three axes: Yaw, Pitch, and Roll. The actuators are strategically positioned to exert control over the corresponding axes.
- **Controller and interface**: The ADCS Controller uses data retrieved from the sensors to determine the current attitude of the satellite. The algorithm embedded in the controller calculates the target attitude and subsequently computes the necessary rotations required for each axis. The ADCS Interface is the hardware component responsible for transmitting signals received from the sensors to the controller. Additionally, it manages the distribution of power to the actuators.

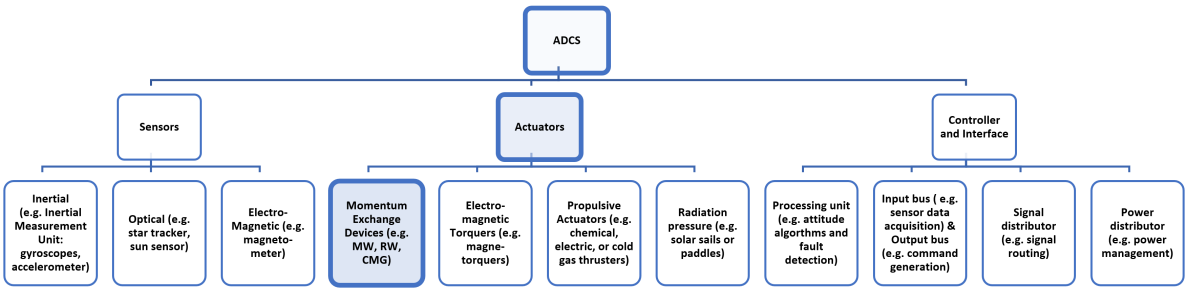

Figure 3: ADCS subsystems - Fine Attitude Control Actuators are working through momentum exchange and are highlighted under ADCS/Actuators/Momentum Exchange

2.1.2 Momentum Wheel

Momentum wheels are a primary type of angular momentum exchange device used for satellite attitude control [82]. They consist of a spinning flywheel whose angular speed is adjusted to control satellite attitude. Momentum bias wheels are specifically designed to maintain a constant angular momentum, providing inherent stability along one or more axes [8]. The *bias* refers to a constant, non-zero angular momentum that helps stabilise the satellite with minimal control inputs. This inherent stability rejects disturbances and maintains the desired orientation. External torques are counteracted by transferring angular momentum from the wheel to the satellite, maintaining a stable reference orientation. This bias can then be augmented with other attitude control devices.

Advantages:

- Momentum wheels exhibit a straightforward design.
- These devices enable continuous attitude stabilisation along the axis with imposed momentum bias.

Limitations:

- Momentum wheels are susceptible to saturation, necessitating the implementation of momentum management strategies.

- Momentum dumping, often using thrusters or magnetorquers, is necessary to remove accumulated momentum [60].

Topology
Momentum wheels possess a topology similar to that of reaction wheels. Their primary components include a flywheel assembly (rotor), a motor (comprising stator, coils, and magnets), bearings, control electronics such as position sensors, and mounting brackets. Two representative examples are illustrated in Figure 4.

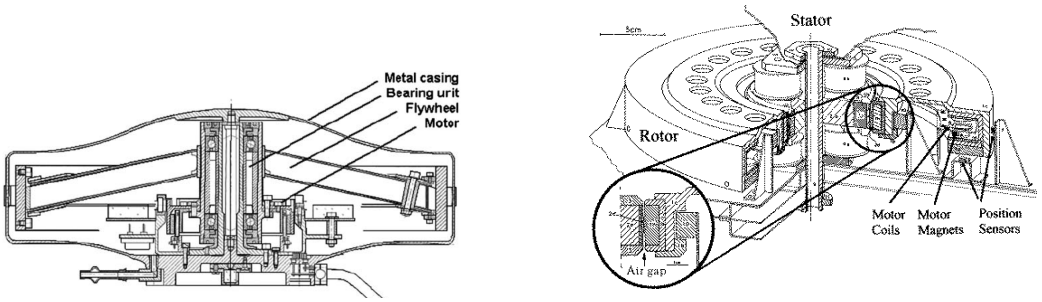

(a) Conventional momentum wheel assembly: a flywheel driven by an electric motor. Source: [82]

(b) Drawing of the magnetic-bearing momentum wheel. Source [83]

Figure 4: Typical momentum wheels with (a) mechanical bearings and (b) magnetic bearings

Modelling
The dynamic behaviour of a momentum bias wheel is modelled using the principle of angular momentum conservation, which yields the following equation of motion:

$$\frac{dH_{wheel}}{dt} = \tau_{ext} \tag{1}$$

In this context, τ_{ext} denotes the total external torque acting on the momentum wheel.

$$H_{wheel} = I_{wheel} \cdot \omega_{wheel} \tag{2}$$

H_{wheel} represents the angular momentum stored in the flywheel, I_{wheel} is the moment of inertia of the rotor, and ω_{wheel} is the angular velocity of the rotor.
A change in the wheel speed, denoted as $\Delta\omega_{\text{wheel}}$, generates a reaction torque τ_{reaction} that is applied to the satellite:

$$\tau_{\text{reaction}} = -I_{\text{wheel}} \cdot \Delta\omega_{\text{wheel}} \tag{3}$$

2.1.3 Reaction Wheel

Reaction wheels (RWs) are devices used for precise satellite attitude control [87]. By controlling the rotational speed of one or more wheels, the satellite can generate torques in orthogonal directions, allowing for attitude adjustments [31]. Due to the accumulation of disturbance torques, the reaction wheels will saturate after a certain period, and the momentum must be unloaded from the reaction wheels to use them again for attitude control [42]. RWs are therefore often accompanied by actuators that can unload the momentum [1], such as magnetorquers.

Advantage:

- Attitude control in multiple axes.
- Can be used for stability and agile applications.

Limitations:

- Over time, reaction wheels can accumulate momentum and reach their operational limits. This phenomenon is known as wheel saturation.

- Because of cross-coupling due to gyroscopic stiffness, the control algorithm requires feed-up and feedback.
- When reverting rotational direction, zero-crossing causes additional complexity.

Topology
The key components and topology of reaction wheels are listed below and are depicted in Figure 5.

1. **Flywheel** - The flywheel (rotor) is made of material like aluminium, steel, or bronze. The wheel is precisely balanced to minimise vibrations.
2. **Motor and Bearings** - The flywheel is driven by an electric motor (stator). Precision bearings are used to minimise friction.
3. **Encoder and Encoder Mount** - Control electronics are used to regulate the motor's speed and direction. These electronics receive commands from the satellite's control system to adjust the wheel's rotational speed, generating the desired torque for attitude control.
4. **Mounting bracket** - Reaction wheels are mounted inside the satellite with their rotational axes oriented in specific directions.
5. **Sensor Feedback** - Reaction wheels are equipped with sensors to provide feedback to the control electronics to achieve the desired rate of rotation.
6. **Power Supply** - Reaction wheels are powered by the satellite's electrical system. They require a stable power supply to maintain the desired wheel speeds and generate the necessary torque.

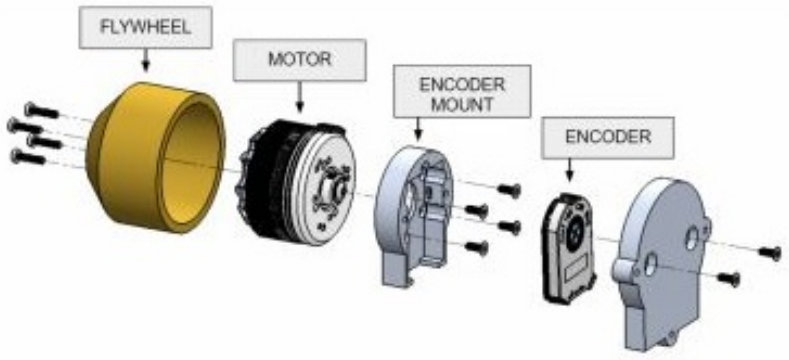

Figure 5: A typical layout of a reaction wheel. Source [88]

Reaction wheels (RWs) are generally assembled to enable control over the satellite's roll, pitch, and yaw axes. When three wheels are employed, each is oriented along a specific axis to facilitate attitude adjustments. To enhance reliability, a fourth reaction wheel may be added for redundancy, allowing the satellite to maintain control even if one wheel fails. These wheels come in various sizes and configurations. For example, NASA's Kepler satellite used three reaction wheels, two of which are shown in Figure 6a. In smaller satellites such as CubeSats, it is common to group three or four reaction wheels together, as depicted in Figure 6b.

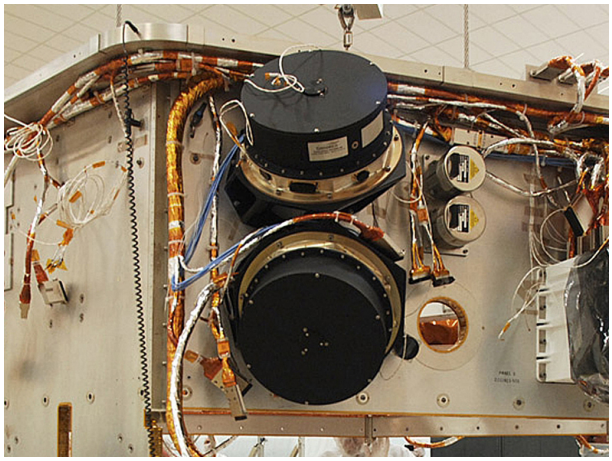

(a) Reaction wheel assembly on Kepler satellite. Source: [36]

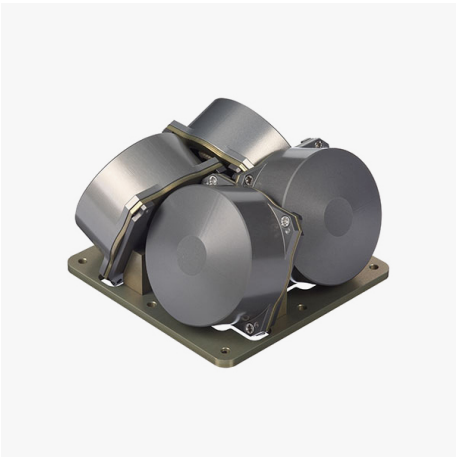

(b) Cubesat RWs Control System Satbus 4RWO. Source: [20]

Figure 6: Reaction wheel pairs examples

Modelling
The dynamic modelling of reaction wheels follows the same principles as control moment gyroscopes (CMGs) without their gimbals, utilising the equations of rotational motion. The governing equations are obtained by replacing the subscript 'gyro' with 'reactionwheel' in Equations 4-6.

2.1.4 Control Moment Gyroscope

Control Moment Gyros (CMGs) are attitude control actuators that generate torque by changing the orientation of a spinning rotor, see Figure 8. CMGs offer higher torque capabilities compared to reaction wheels, making them suitable for agile satellites requiring rapid re-orientation [106]. CMGs consist of a spinning rotor suspended in a gimbal assembly. When the satellite needs to change its orientation, it adjusts the orientation of the CMG gimbals. This causes a change in the direction of the gyroscopic torque, which results in a change in the satellite's attitude.

Advantages:

- CMGs provide very high torque for attitude control and can rapidly adjust satellite orientation.
- Suitable for agile applications.

Limitations:

- CMGs employ gimbals and various motors. This adds to the complexity and can be expensive to develop.

Topology
The structure of a CMG typically consists of several key components as depicted in Figure 7.
Below, the corresponding items are described:

1. **Gyroscope Rotor** - At the core of a CMG is the gyroscope rotor, which is a spinning wheel or disk. The rotor is mounted on a set of gimbals, allowing it to move in multiple axes.
2. **Gimbal Assembly** - The gimbal assembly is a mechanical structure that holds the gyroscope rotor and allows it to pivot or tilt in different directions. It usually consists of two or three gimbals, each oriented perpendicular to the others. These gimbals are often referred to as pitch, yaw, and roll axes.
3. **Motor and Bearings** - To spin the gyroscope rotor, a high-speed motor is used. The rotor is mounted on precision bearings to minimise friction.
4. **Torque Motors** - CMGs are equipped with torque motors that can tilt the gimbals and thus change the orientation of the spinning rotor. By adjusting the speed and direction of these motors, the CMG generates torque in a specific direction.

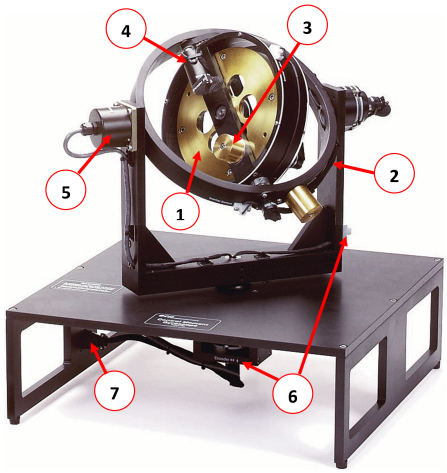

Figure 7: Example Control Moment Gyroscope. Source [57]

5. **Sensor and Control Electronics** - Sensors provide feedback on the desired orientation. Control electronics process this feedback and compute the necessary adjustments to control the CMG's operation.

6. **Power and Communication Interfaces** - CMGs are powered by the satellite's electrical system and are controlled through onboard computer systems.

Modelling

The equations of motion for CMGs involve the principles of angular momentum and torque. CMGs are used to generate torques to control the orientation of a satellite by adjusting the orientation of the spinning rotor. A CMG can be modelled as a plant, as shown in Figure 8.

Configuration	Simple Rigid Body	Reaction Wheel	Gyroscopic Torquer	Reaction / Gyroscopic positioner (Special case)	Reaction / Gyroscopic positioner (General Case)
Equations of Motion	$J\ddot{\theta} = T$	$J_2\dot{\omega}_2 = -T$ $\omega_1 = \omega_{1o} + \int_0^t T(\tau)/J_1\, d\tau$	*For small θ_2 and symetric mass properties:* $\dot{\omega}_3 = (\Omega\omega_2 J_1^2 + (T_1 + (J_1^2 + 2(J_2^2 - J_1^2 - J_2^2))\omega_2\omega_3)\theta_2)/J_{eq}$ *where J_i^j is the jth diagonal element of $\boldsymbol{J}_i$ and* $J_{eq} = J_1^1 + J_4^3 + J_3^3 + J_2^3$ *For $\Omega >> \omega_3$,* $\dot{\omega}_3 \cong \Omega\,\omega_2 J_1^2/J_{eq}$	$\dot{\omega}_1 = \frac{J_2^2 + J_3^2 + J_4^2}{J_4^1 (J_2^2 + J_3^2)} T_1$ $\dot{\omega}_2 = \frac{J_4^2 \Omega\, \omega_4}{J_3^1 + J_4^1} + \frac{1}{J_3^1 + J_4^1} T_2$ $\dot{\omega}_3 = -\frac{1}{J_2^2 + J_3^2} T_1$ $\dot{\omega}_4 = \frac{J_4^2 \Omega\, \omega_4}{J_4^1 + J_1^3 + J_2^3 + J_3^3}$	$\dot{\boldsymbol{\omega}} = \left[f(\theta_k, \omega_i, J_i^j)\right]\boldsymbol{\omega} + \left[g(\theta_k, J_i^j)\right]\boldsymbol{T}$ *where: $i = 1,2,3,4$ $j = 1,2,3$ $k = 2,3$* *Other notation as given at left*
	Brakes are applied on all axes except rotor to minimize system order	Brakes applied at second and fourth axes - see reverse page	Brake applied at third axis	*Applicable to small motions in θ_2 & θ_3, arbitrarily large motions in θ_1 and θ_4, $\omega_1 \approx \Omega$ (nom. value)*	Explicit expressions provided in system documentation

Figure 8: A Variety of Simple and Advanced Plant Configurations. Source [57]

The primary principle behind CMG operation is the conservation of angular momentum. The total angular momentum of a closed system remains constant unless acted upon by an external torque. Mathematically, this can be expressed as:

$$H_{total} = H_{gyro} + H_{satellite} = \text{constant} \tag{4}$$

Where H_{total} is the total angular momentum of the satellite system, H_{gyro} is the angular momentum of the CMG rotor, and $H_{satellite}$ is the angular momentum of the satellite (including the CMG). The change

in angular momentum of the CMG rotor is related to the torque applied to it, according to Equation 5.

$$\Delta H_{gyro} = \int_{t1}^{t2} \tau_{CMG} dt \tag{5}$$

In which ΔH_{gyro} is the change in angular momentum of the CMG rotor and τ_{CMG} is the torque generated by the CMG. The torque is proportional to the rate of change of its rotor's angular momentum. This is expressed in Equation 6.

$$\tau_{CMG} = I_{gyro} \cdot \dot{\omega}_{gyro} \tag{6}$$

Where I_{gyro} is the moment of inertia of the CMG rotor, and $\dot{\omega}_{gyro}$ is the rate of change of angular velocity of the CMG rotor.

2.1.5 Rudimentary trade-off

This section presents a preliminary comparison of momentum wheels (MWs), reaction wheels (RWs), and control moment gyroscopes (CMGs) with respect to two primary mission requirements: stable pointing and agility. Due to the complexity of a CMG, this research focuses on MWs and RWs for stable pointing to maintain a defined scope.

Stable applications
For missions that require long-term attitude stability and minimal disturbance rather than rapid manoeuvring, MWs and RWs are preferred. MWs provide inherent single-axis stability by generating a constant angular momentum, which acts as gyroscopic stiffness and resists external torques that could alter the satellite's orientation. Increased momentum enhances resistance to disturbances, making MWs suitable for missions such as Earth observation or communication satellites that require fixed pointing. RWs can provide multi-axis control, but are less efficient for bias stability due to higher power consumption at the same size. Instead, RWs are primarily used to counteract disturbance torques through momentum exchange.

CMGs are not considered for stable applications because they are fundamentally more complex than RWs or MWs. I.e., it contains a (high-speed) rotor mounted on one or more gimbals. This introduces additional moving parts (gimbals, bearings, motors, sensors), increasing mechanical complexity and the number of potential failure points. Also, it requires more sophisticated algorithms to manage singularities; avoiding or manoeuvring through these singularities adds unnecessary complexity to the attitude control system for a nadir-pointing mission. Moreover, the gimbals are inherently less stiff than suspending RWs or MWs, potentially increasing micro-vibrations that degrade image quality.

In Earth observation missions, both pointing accuracy and imaging performance are critical. Determining the optimal fine attitude control actuator (FACA) depends on specific operational and mission constraints. Often, a combination of FACAs and other systems, such as magnetorquers, is employed to achieve the required attitude control and stability. The trade-off between MWs and RWs is quantitatively assessed through simulations, which are discussed in detail in Chapter 9.

Further research could examine the possibility of developing hybrid control strategies that integrate the advantages of both MWs and RWs. For example, an MW can provide baseline stability, while RWs can be used for infrequent, minor corrections to counteract accumulated disturbances or perform small attitude adjustments. Advanced control algorithms are required to coordinate these actuators efficiently, minimising power consumption and maximising system performance.

Agile applications
For satellites that require rapid re-orientation, RWs and CMGs are suitable actuator options. RW assemblies and multi-gimbal CMGs can provide full three-axis control. In contrast, the single-axis control and inherent stability of MWs limit their effectiveness in agile manoeuvres, so they are not considered for these applications.

Votel and Sinclair published a paper titled *Comparison of control moment gyros and reaction wheels for small earth-observing satellites* [106]. They compared the performance of RWs to that of CMGs for agile Earth observation applications. Hereby, a slew rate (the speed at which a satellite can change its pointing

direction) of 3.0 deg/s and slew acceleration of 1.5 deg/s^2 were the agility requirements to point and repoint to the area of interest.

Some key trade-off findings were:

1. CMGs excel at providing significantly higher torque than RWs for a given momentum capacity, while RWs can be considered to increase the acceleration in the short run better.
2. CMGs can produce significantly more torque at a fraction of the power required by RWs, but RWs are more power-efficient for lower performance demand.
3. For a small satellite with a low moment of inertia, RWs can perform better in comparison to CMGs. This is only when the CMG does not use its torque generation potential.
4. RWs outperform CMGs in terms of angular momentum capacity per unit volume and mass.
5. CMGs are more complex than RWs, both mechanically and algorithmically (due to singularity issues).
6. Earth-observing satellites with a mass exceeding 30 kg should prioritise CMGs, as their torque efficiency enables them to meet demanding acceleration requirements while minimising power consumption.

The underlying principles of these actuators are illustrated in Figure 9. In this figure, the resultant torque vector is denoted by T, the flywheel momentum vector by h, and for the CMG, the gimbal angular velocity by $\dot{\delta}$. A reaction wheel generates torque by accelerating or decelerating the flywheel. In contrast, a CMG produces torque by reorienting the flywheel, which changes the direction of the angular acceleration vector. This reorientation, achieved by actuating the gimbal, is more efficient and allows a small gimbal motor to generate significant torque.

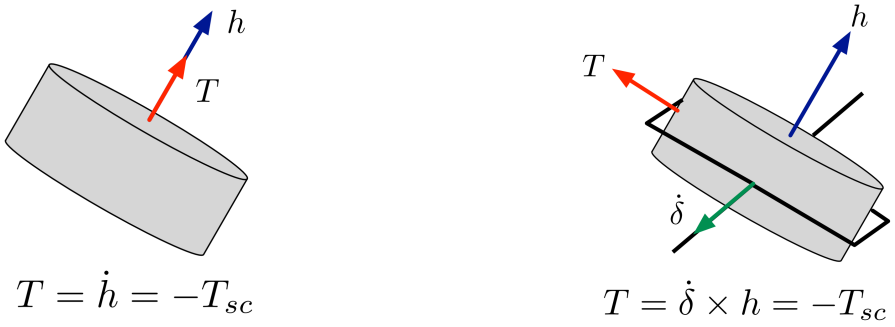

(a) Reaction wheel.

(b) Control moment gyroscope.

Figure 9: Torque diagrams with governing equations for (a) reaction wheels and (b) single-gimbal control moment gyroscope. Source: [106]

Selection procedure:
The first step is to choose (a,b,c) the overall purpose of the FACA: Stabilise, (re-)orient, and fast manoeuvring. Below, the mission objectives are stated, and the FACA of choice is presented too:

a. Stabilise, (re-)orient, and fast manoeuvring (CMG): by leveraging high torque, multi-axis CMGs can perform fast manoeuvres.

b. Stabilise and (re-)orient (RW, CMG): when the purpose is to actively control multiple axes, a set of RWs or multi-axis CMGs can fulfil the job. Typically, RWs can store more angular momentum and are mechanically simpler, requiring simpler control algorithms. CMGs are the most potent and power-efficient option for equal torque output. Both have their disadvantages; RWs can saturate more easily, while CMGs can encounter gimbal lock.

c. Stabilise (MW, RW): When stabilising the satellite in a fixed orientation with respect to Earth or the Earth's surface, both MW- and RW-, and CMG-controlled satellites can fulfil this task, though through different operating principles. If the sole purpose is to stabilise the satellite, a CMG is too complex and is therefore deemed unnecessary for further assessment.

In this thesis, stabilisation is the main objective. Therefore, the second step is to determine the disturbance torques as functions of time and orbital position to size either the MWs or RWs. For that, the interaction between the environment and the satellite must be modelled.

The third step is to check for available design space in the satellite volume budget. For equal mass, the sizing of the MW or RWs must be within the available design volume. If a design volume is available and is solely constrained by the satellite bus outer dimensions, both satellite types can be simulated.

The fourth step is to simulate and compare pointing performance, then select the best-performing one.

2.2 Earth's shape and altitude definition

In this study, altitude is defined to ensure that the spatial location (XYZ) remains independent of Earth's shape. Specifically, altitude is defined as the geocentric distance from the Earth's surface. This approach assumes a spherical Earth for orbit definition.

When a more accurate representation of Earth's ellipsoidal shape and topographic variations is required (e.g., for sharp imaging), the geocentric altitude, geocentric radius, and geodetic altitude must be used. Thus, although for imaging the closest distance between the satellite and Earth's surface is the fundamental distance (the geodetic altitude), this distance is not considered in this study. For completeness, these definitions are included though.

Geocentric distance
The geocentric distance R represents the straight-line distance from any specific point of interest to the Earth's centre and is calculated using Equation 7. This measure extends beyond points lying on the reference surface, unlike the geocentric radius, R_0.

$$R = \sqrt{X^2 + Y^2 + Z^2} \tag{7}$$

This definition, which does not account for the precise shape of Earth's ellipsoid, is used to define both the altitude h and Earth's radius R_{Earth} as shown in Equation 8.

$$R = R_{Earth} + h \tag{8}$$

In Figure 28, an indication of disturbance torques are presented. From the figure, it is observed that the Atmospheric disturbance is reduced to about the same level as the solar radiation torque at an altitude $h = 600\ km$. At lower altitudes, the density increases rapidly (see Figure 31 in section 4.1), causing the Atmospheric torque to exceed the gravity gradient torque by about two orders of magnitude at $h = 200\ km$. When disturbances are too significant, the satellite must counter orbital decay; otherwise, its lifetime is shortened considerably. For that reason, orbital altitudes of a range of $200 < h < 600\ km$ are chosen as appropriate to investigate.

Geocentric altitude
The geocentric altitude h' is defined as the difference between the geocentric distance R and the geocentric radius R_0 and is given by Equation 9. It represents the height of a point above the reference ellipsoid along a line passing through the Earth's centre.

$$h' = R - R_0 \tag{9}$$

Geocentric radius
The geocentric radius is the distance from the Earth's centre to a point on its reference ellipsoid, an idealised mathematical model of the Earth's shape [62]. This reference ellipsoid closely approximates the Earth's actual shape, accounting for its equatorial bulge and polar flattening. Consequently, the geocentric radius is slightly larger at the equator (due to the semi-major axis) compared to the poles (due to the semi-minor axis).

Geodetic altitude
The geodetic altitude, on the other hand, is measured as the distance between a point on or above the Earth's surface and the closest point on the geoid. Thus, it also accounts for the Earth's actual physical

shape, including topographic features such as mountains and valleys. The geoid is a model of the global mean sea level, influenced by the Earth's gravity and rotation.

2.3 Satellite sizes and shape

The satellite shape of interest is illustrated in Figure 10. The satellite must carry a large-diameter imager to capture images at the highest possible ground resolution. Since it needs to be powered, solar arrays must be installed. To prevent asymmetric disturbances, the satellite will be built symmetrically. Hence, two solar arrays are present. The exact location of the satellite's hardware will be varied mathematically by shifting the centre of gravity location, rather than being designed.

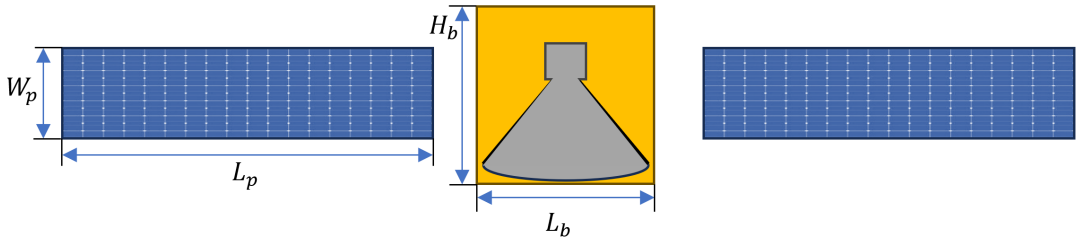

Figure 10: Schematic representation of a satellite. Lay-out: solar array (left), S/C bus (middle), solar array (right).

Satellite shape
Although many satellite shape configurations are thinkable, for this study the satellite consists of three components: the satellite bus, which houses the FACAs and the imager payload, and two solar arrays. The measurements used in later analysis are documented in Appendix A.1.

Satellite dimensions
In Figure 10, various measurements are depicted: the solar arrays (blue rectangles) have a Length $\times$ Width $\times$ Thickness of $L_p \times W_p \times t_p$, and the satellite's bus (yellow square in the middle) measures $L_p \times H_b \times W_b$. The measurements are taken in meters. The physical quantities for those measurements depend on the size of the satellite's imager needed (grey object inside the S/C bus) and how well the satellite can cope with the disturbances present.

In section 2.5.2 it is concluded that a native spatial resolution of 0.55 meter is achievable with an aperture size of $0.42m$ using equations 14 and 15 with wavelengths appropriate to generate panchromatic images ($0.47 \leq \lambda \leq 0.83$) at an altitude of 400 km. This indicates the dimensions needed to achieve the objective of sub-meter spatial resolution.

Depending on the mission requirements, such as mission duration, the satellite could fly at lower or higher altitudes, which impacts its pointing stability and precision. This, in turn, would affect the size of the FACA needed to keep the satellite operable at the desired performance.

2.4 Wavelengths

Exploring optical remote sensing involves delving into the electromagnetic spectrum. Two types of Earth observation imagery are classified: passive and active. Passive sensing refers to detecting electromagnetic emissions from the Earth's surface and atmosphere, see section 2.4.1. These emissions include thermal radiation from vegetation in the infrared spectrum and sunlight reflected off the Earth's surface in the visible spectrum. Active sensing consists of a transmitter that emits a specific electromagnetic signal and a sensor that detects the interaction of this signal with the Earth's surface. In this work, **passive sensing** is included, and active sensing is excluded. Within passive sensing, various spectral imaging options are available. This research considers **panchromatic imaging** because it allows for sub-meter spatial resolution and is discussed in section 2.4.2.

2.4.1 Atmospheric window

When considering the atmospheric window, presented in Figure 11, passive imagery systems can observe Earth's surface in the visible spectrum (0.39 to 0.70 µm), portions of the infrared spectrum (0.70 to 14 µm), and the radio wave range (1 cm to 11 m).

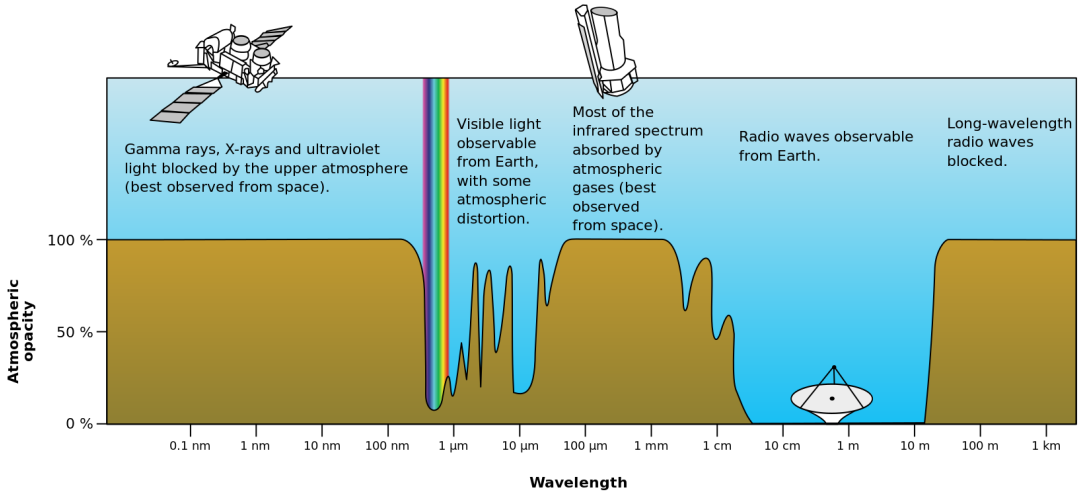

Figure 11: The atmospheric window/atmospheric electromagnetic transparency or opacity: a specific range of electromagnetic waves that can pass through the Earth's atmosphere. These ranges are determined by the composition of gases in the atmosphere [24].

For this research, radio waves are excluded, thereby reducing the optical remote sensing scope to wavelengths λ ranging from the visible spectrum at 380 nanometers to the near-infrared (NIR) and extending to the thermal infrared (TIR) at 14 microns. However, the detectable limits are defined by the sensitivity spectrum of silicon, which ranges from 380 to 1100 nm [27]:

$$380nm \leq \lambda \leq 11000nm \tag{10}$$

In this range, various imagers are possible: Panchromatic, Multi-spectral, Pan-sharpened, and Hyperspectral [66]: Panchromatic images comprise a wide range of wavelengths, typically covering wavelengths between 0.47 and 0.83 µm, allowing for sub-meter resolutions. Multispectral images can be composed of several narrow bands centred around different wavelengths (e.g., blue, green, and red wavelengths to compose the natural colours). Measurements can also be taken outside the visible bands (e.g., infrared, ultraviolet, microwave), allowing for the detection of features such as vegetation, soil moisture content, and fires. Pan-sharpened processes merge the panchromatic images with those taken with multi-spectral imagers, allowing for improved spectral and spatial resolution images, and are done numerically. Hyperspectral imagers take the concept of multispectral imagers to a more refined level. They aim to capture a nearly continuous spectrum for each pixel, allowing for the identification and quantification of surface materials, inferring biological and chemical processes.

2.4.2 Panchromatic imaging

To reduce the range further and achieve a meaningful trade-off between FACAs, panchromatic wavelengths are considered. With data collected from panchromatic imagers, multispectral images can be sharpened significantly. An example is depicted in Figure 12. The benefits of pansharpening become very clear when zooming in, for example, on a part of the roundabout.

$$0.47\mu m \leq \lambda \leq 0.83\mu m \tag{11}$$

Figure 12: Multispectral image (left) vs. pan-sharpened image (right). The red boxes are areas highlighted in Figure 13. Source: [97]

In Figure 13, the multispectral image, one can distinguish the road from the trees and the buildings. A trained algorithm might be able to identify more objects. However, when examining the pan-sharpened image, in addition to the already identifiable objects, individual cars can be recognised, and the distance between them can be measured, among other things.

Figure 13: Zoomed-in image taken from Figure 12. Multispectral image (left) vs. pan-sharpened image (right).

2.5 Ground Sampling Distance

Ground Sampling Distance (GSD) is a key parameter in earth observation missions, particularly in remote sensing and satellite imaging, see 2.5.1. GSD quantifies the minimum ground feature size that can be resolved in an image acquired by a satellite or satellite sensor. The value of GSD is determined by the native spatial resolution, as detailed in section 2.5.2. The dimensions of individual detector pixels must be selected to ensure that relevant features are captured, as discussed in section 2.5.3.

There is an inverse relationship between GSD and spatial resolution: lower GSD values correspond to finer detail and higher resolution, whereas higher GSD values correspond to lower spatial resolution. Techniques such as interpolation and resampling, including learning-based, frequency-based, and probabilistic-based methods, can enhance the apparent GSD during data processing. However, these methods do not improve the native spatial resolution of the images [114]. Consequently, native spatial resolution serves as the primary driver for the feasible designs in this research. The range of current GSDs is examined in section 2.5.4.

2.5.1 Imager system

In optical systems that use a detector array with dimensions $N_x \times N_y$, each pixel functions as the fundamental sensing element, as illustrated in Figure 14. The size of each pixel determines the resolution element in the image. The optical system, situated below the detector, comprises lenses and apertures that focus incoming light onto the detector array. The F-number $F/\#$ affects both the light-gathering capability and the depth of field, which in turn influence image quality. The field of view (FOV) defines the observable area, while the instantaneous field of view (IFOV) specifies the size of a single pixel as projected onto the ground. Ground sampling distance (GSD) represents the area on the ground corresponding to one pixel and is typically expressed in meters per pixel $[m/pixel]$.

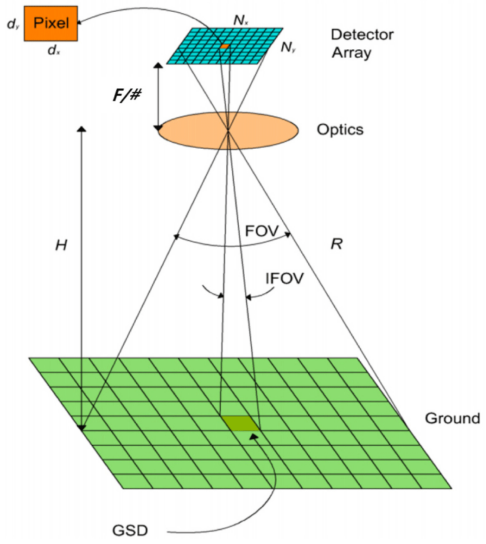

Figure 14: Outline Ground Sample Distance. Source: [40]

2.5.2 Native spatial resolution

Although spatial resolution by itself does not define the performance of the imager's sensor [100], it gives a good indication of how small a discernible object can be. The spatial resolution of an optical system is determined by its point spread function (PSF). The PSF characterises the system's response to a point source of light and directly influences the ability to resolve fine details. A two-dimensional PSF is presented in Figure 15, and can be looked at as the cross-sectional view of a three-dimensional PSF. The green line represents the light intensity resulting from radial interference (constructive and destructive). The majority of the incoming light is bounded by the focused area of the 'airy disc', where the first maxima occurs. The intensity becomes smaller for the subsequent outbound rings.

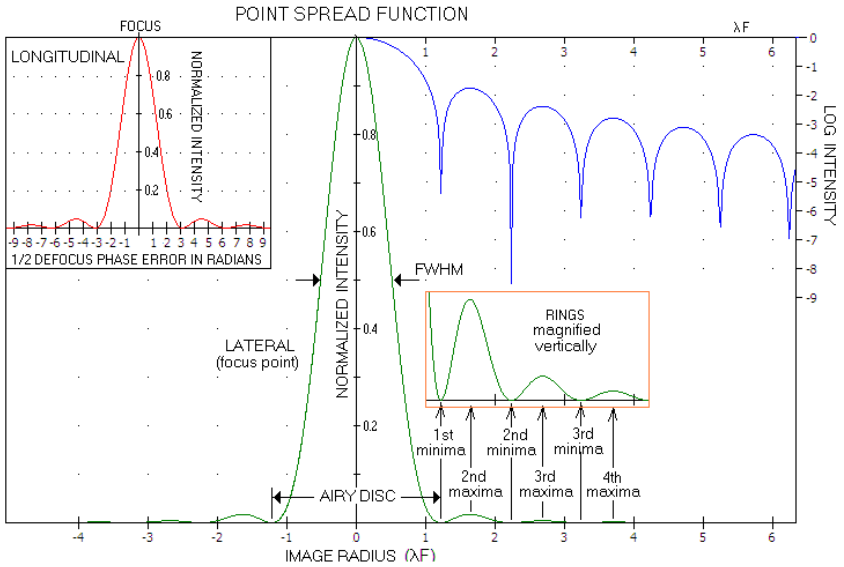

Figure 15: Point Spread Function of a clear aberration-free aperture. Source: [98]

The approximate diameter of this diffraction-limited spot, D_{spot}, can be expressed by Equation 12. The value of 2.44 corresponds to the airy disc width as depicted with 'AIRY DISC' in Figure 15.

$$D_{spot} = 2.44 \cdot \lambda \cdot \frac{f}{D} \tag{12}$$

In which λ is the wavelength of light, f is the focal length of the optical system, and D is the diameter of the aperture. The angle between the maximum and the first minimum of the airy pattern, θ, is known as the diffraction limit, as given by Equation 13.

$$\sin\theta = 1.22\frac{\lambda}{D} \tag{13}$$

The resolution of the imager is fundamentally determined by the detector characteristics, aberrations introduced by the optics, and jitter of the sensor line of sight [34]. When aberrations are disregarded, the maximum resolution of a sensor is determined by the diffraction it causes in the incoming radiation. The angle between two point sources of equal intensity that the optical system can resolve is known as the diffraction limit. At this limit, the angular resolution θ_r is described by the Rayleigh criterion in Equation 14. This situation occurs when two airy discs are spaced half an airy disc apart and defines the minimum resolvable detail in an optical system. Equation 14 presents the Rayleigh criterion for an optical system with a circular aperture, which is considered for this research. It shows that the larger the diameter of the aperture D (e.g., the lens or mirror in the optical system), the smaller the resolvable angular resolution θ_r $[rad]$ becomes.

$$\theta_r \approx \tan(\theta_r) \equiv \frac{d'}{2f} = \frac{X'}{2h} = 1.22\frac{\lambda}{D} \tag{14}$$

Herein, d' is the width of the airy disc, f is the focal length, X' is the ground resolution element, and h is the altitude, as illustrated in Figure 16. The (native) spatial resolution SR at NADIR is proportional to the flying height h and the tangent of θ_r, as is described by Equation 15.

$$SR = h \cdot \tan\theta_r = h \cdot \tan\left(1.22\frac{\lambda}{D}\right) \tag{15}$$

2.5.3 Detector pixel sizing

To determine the pixel size of the detector, only perfect optics are considered. Additionally, the signal-to-noise ratio required to extract relevant information from the detectors is outside the scope of this research. This research is only concerned with the physical implementation of a detector array onboard the NADIR pointing satellite. The parameters involved are: the quality factor, magnification, pixel size

and number of reflections.

With the information described in section 2.5.2, the spatial resolution on the ground, or ground resolution element X', at NADIR can be determined for a satellite at altitude h by rearranging Equation 14 into Equation 16.

$$X' = 2.44\frac{\lambda}{D} \cdot h \tag{16}$$

It is schematically presented in Figure 16. It illustrates the relationship between key parameters influencing the resolution of an optical imaging system in remote sensing. The PSF is shown on the left side of the detector array. The width of the airy disc is depicted by d'. The optics are represented by a single (limiting) aperture and lens with focal length f. Finally, the ground resolution element X' is shown on the right.

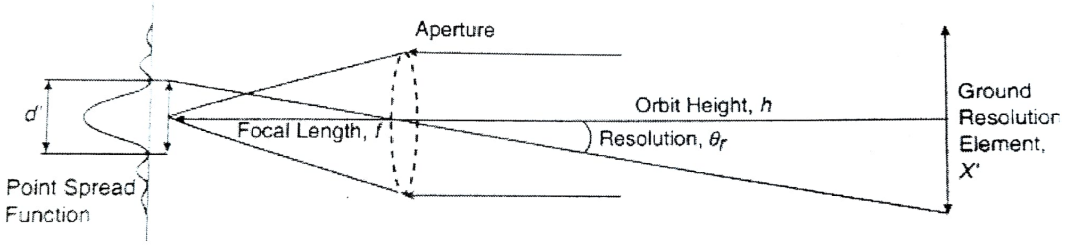

Figure 16: Point Spread Function for an imaging system with diffraction. Source: [110]

Quality factor
The Quality Factor (Q) is defined as the ratio between pixel size d and the diameter of the airy disc d' per Equation 17.

$$Q \equiv \frac{d}{d'} = \frac{X}{X'} \tag{17}$$

The value of Q typically ranges from 0.5 to 2 [110]. For this research, $Q = 1/1.3 \approx 0.77$, as then the pixels are 30% smaller than the airy disc, meaning that the optical system is limited by diffraction in optics.

Magnification
The term magnification refers to the factor by which an object or image is enlarged or reduced in an optical system, and is given by Equation 18.

$$\text{magnification} = \frac{d}{X} = \frac{d'}{X'} = \frac{f}{h} \tag{18}$$

Herein, the first term, $\frac{d}{X}$, represents the ratio of the image or projection size d on the sensor to the ground pixel size X. The second term, $\frac{d'}{X'}$, is the ratio of the airy disc projection d' to the ground resolution X' (ground feature size), and, lastly, the third term, $\frac{f}{h}$ is the ratio of the focal length of the optical system f to the altitude h.

Pixel size
The pixel size d is expressed by combining equations 14 with 17 and 18, and is given by Equation 19.

$$d = \frac{d'X}{X'} = d'Q = \frac{2.44\lambda f}{D}Q \tag{19}$$

An example calculation for a satellite of size $0.42 \times 0.42 \times 0.42\ m^3$, whereby the aperture $D = 0.42$ and smallest panchromatic wavelength $\lambda = 0.47\ \mu m$ is presented in Equation 20. It is shown that the pixel size is linearly proportional to the focal length.

$$d = \frac{2.44\lambda f}{D}Q = \frac{2.44 \cdot 0.47 \cdot 10^{-6} \cdot f}{0.42} \cdot 0.77 = 8.6 \cdot 10^{-7} f \tag{20}$$

Detector arrays used for GSD in the range of meters to sub-meter typically have a frame size of 1280×720 up to 3840×2160 pixels [35]. Employing a detector of size 1 to 2.5 cm result in pixel sizes in the range of $2.5 - 35$ μm, which is a realistic assumed value considering that arrays with pixel sizes of 4.6 and 5.7 μm are reported in an article titled *The essential contribution of CMOS imaging technologies to Earth Observation applications* [46] in 2021. To fall within such a range, a large focal length must be achieved (larger than the size of the satellite). These focal lengths can be achieved using mirrors. When mirrors are used, light is reflected and focused onto the surface across the reflection angle. For the example in Equation 20, f must be in the range of $2.9 - 40.7$ meters, which is equivalent to 7 to 97 number of reflections to make the pixel sizes fall in the typical range.

Number of reflections
Figure 17 illustrates the decay of illumination as a function of the number of reflections (bounces) for different mirror reflectivities. Each curve represents the fraction of initial illumination remaining after successive bounces, with reflectivity values R ranging from $R = 0.8$ to $R = 0.99$. The plot demonstrates that higher reflectivity surfaces retain a larger proportion of the incident light over multiple bounces, exhibiting a more gradual decrease by a factor of $1/N$. Conversely, lower reflectivity surfaces result in diminished signal strength after only a few reflections. This indicates that when multiple bounces are necessary to achieve a large focal length f in a small form factor, the reflectivity of the mirror coating becomes important.

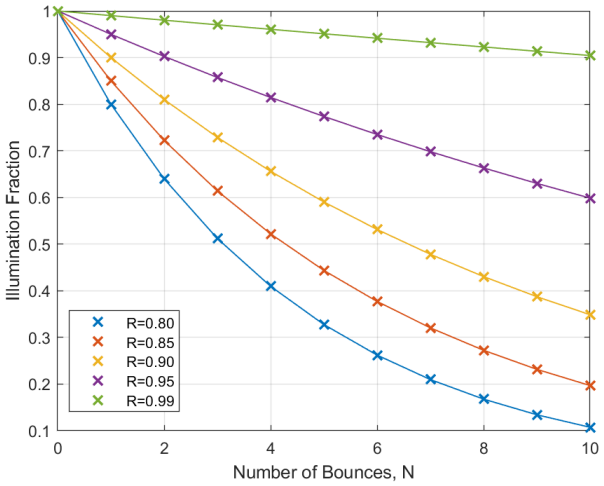

Figure 17: Illumination decay with number of bounces for different reflectivities

The figure emphasises that, for a given number of bounces, the cumulative loss becomes significant for lower-reflectivity coatings. In contrast, near-perfect reflectors maintain illumination levels at nearly unity even after multiple reflections. Surface coatings (silver) with 95% reflectivity ($R = 0.95$) for wavelengths above $\lambda = 0.47 \mu m$ is possible [84]. Since this research only considers aberration-free mirrors, 10 reflections would still leave 60% of the light available for detection. When coatings with $R = 0.9$ are considered, only five reflections yield similar illumination results. To prevent overly optimistic simulations, seven reflections are permitted.

2.5.4 Native spatial resolution for current satellites

The following typical satellite sizes (on the order of magnitude) are considered. To capture the full range of ADCS requirements, both (soon to be) flying satellite/imagers combinations are considered, as well as stand-alone (theoretical) diffraction-limited telescopes flying at a similar altitude that could be conceptually feasible:

1. **12U, $20kg$, scheduled launch:** The smallest size satellite considered is the Twin Anthropogenic Greenhouse Gas Observers (TANGO) mission that consists of two 12U CubeSats that are scheduled to launch in 2024. The size of these satellites is representative of their class [70]. In the particular case of TANGO, the imagers have a field of view (FoV) of 30×30 square kilometres with a spatial resolution of 300×300 square meters at an altitude of $500km$ [13], and will operate in the visible

spectral range, of $405nm - 490nm$. The imagers are built on the existing instrument heritage of the TROPOspheric Monitoring Instrument (TROPOMI) instrument [102], which was carried on the Sentinel-5 Precursor mission. Thus, the onboard imager is considered state-of-the-art and therefore relevant to defining the lower boundary of the scope. The TANGO-Nitro instrument requirements are listed in Table 1.

Table 1: TANGO-Nitro instrument requirements relevant to the optical design. Source: [13]

Parameter	**Unit**	**Value**
Altitude	km	500
Swath	km	30
ACT GSD at NADIR	km	0.3
ALT GSD at NADIR	km	0.3
Minimum wavelength	nm	405
Maximum wavelength	nm	490
Spectral resolution	nm	0.6
Spectral oversampling	-	2.3
Science sample etendue	mm2sr	3.5E-4
Instrument volume	U	8

2. **12U, $20kg$, conceptually feasible:** The volumetric shape of a 12U satellite is typically configured $30 \times 20 \times 20$ cubic centimetres. Considering a diffraction-limited telescope, a maximum physical aperture size (D) of $30cm$ is thinkable without having to resort to foldable structures. The smallest resolvable angular resolution (θ) at wavelengths (λ) of $400nm$ would be $1.63 \cdot 10^{-6} rad$ or $0.335 arcsec$. This translates to a theoretical spatial resolution of $0.4 - 0.8m$ at an altitude of $250 - 500km$ respectively at NADIR.

   When comparing the claimed optical performance of the TANGO satellites to the theoretically achievable, the performance differs by two orders of magnitude, namely hundreds of meters versus meters (or even sub-meter) in spatial resolution. Still, it is theoretically possible and will be used as a lower-bound case study to pose the most stringent requirements for the ADCS.

3. **Small mini satellite, $< 300kg$, Planned to be launched:** Part of the results of the ESA's InCubed program, H. Law *et all.* published a survey on cutting-edge imaging sensors that reduce instrument size and cost, enabling sub-50cm imaging for small satellites [44] at a flying altitude of $500km$. It details a sub-50cm instrument Proto-Flight Model (PFM) and its advantages, and shows how the trend in ground sampling distance (GSD) versus satellite mass is breached. In Figure 18, the SSTL-Mini Precision satellite that houses the PFM is highlighted at a mass of $280kg$ with a GSD of $0.3m$, enabled by equipping half-pixel offset sensors. The native spatial resolution, however, is $0.6m$ with an aperture size of $0.42m$.

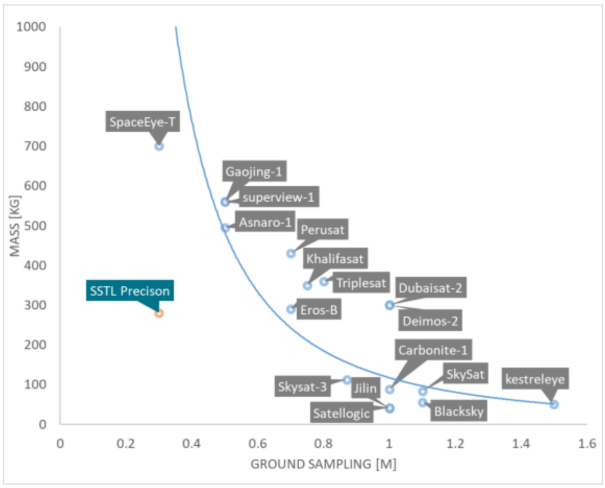

Figure 18: Ground sampling against mass. Source: [44]

4. **Small mini satellite, $< 300kg$, conceptually feasible:** Based on a $340kg$ Coronagraph satellite, as part of the Proba-3 Platforms [95], that has a volume of $1.1 \times 1.8 \times 1.7$ cubic metres, a diffraction limited telescope with an aperture of $1.0m$ would be possible. By Equation 14, the native spatial resolution could be as low as $0.24m$ at wavelengths of $\lambda = 400nm$ at an altitude of 500km, which is a factor of three better than similar-sized (flying) satellites.

To define stability requirements that affect the choice of fine attitude control actuator, it is concluded that a **native spatial resolution range at NADIR** should be:

$$SR \leq 1.0m \tag{21}$$

Herein, the lower bound is defined by a 300 kg small mini satellite and the upper bound by the 20 kg 12U satellite. For the extreme scenarios, a lower bound of 0.24 m and 0.8 m should be considered for the 300 kg and 20 kg satellites, respectively. Note that for satellites smaller than $100kg$ the GSD is approximately 1.0 m as is seen in Figure 18.

2.6 Sway and Swath width

In Earth observation missions, the terms *sway* and *swath width* describe aspects of a satellite's observation or imaging capabilities. An illustration of the definitions is given in Figure 19. The Pointing Coverage of the AVNIR-2 instrument (REF) was 88 degrees or ±44 degrees of sway. The swath width at NADIR for the particular mission was $70km$.

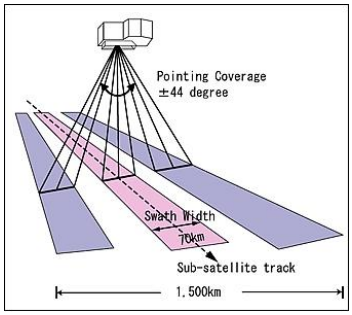

Figure 19: Illustration of Swath Width definition (AVNIR-2 observation capabilities). Source [7]

2.6.1 Sway

Sway refers to the side-to-side or horizontal movement of a satellite or satellite while it is in orbit. It is a form of attitude or orbit control that allows the satellite to shift its position within a specific range.

Sway control can be used to adjust the satellite's viewing angle or to compensate for variations in its orbit. This movement can be used to optimise the satellite's imaging or observation capabilities. Sway control is significant in Earth observation missions where the satellite needs to capture images or data over a specific area of interest. By controlling sway, the satellite can position its sensors or instruments more accurately to capture the desired information.

To make a valid comparison between FACAs, **controlled sway is not considered**. In more detail, this research aims to compare the performance of reaction wheels with that of momentum bias wheels. When momentum bias is built using a momentum bias wheel, it naturally prohibits achieving comparable performance in sway to that of a set of RWs (the trade-off between stability versus agility, see section 2.1.5).

2.6.2 Swath Width

Swath width, also known as ground swath width or swath coverage, is the width of the area on Earth's surface that a remote sensing instrument or sensor on a satellite can image or observe. Swath width is a key parameter in Earth observation, as it determines the coverage area of each image or observation. A wider swath width means that the satellite can capture a larger area with each pass over the Earth. In Earth observation missions, a larger swath width can be advantageous for various purposes, such as mapping, disaster monitoring, and environmental studies. It allows for quicker coverage of large regions and can be essential for time-sensitive applications such as disaster response at the expense of resolution.

While a wider swath enables rapid coverage, a smaller swath width also offers advantages, particularly when combined with higher spatial resolution (see section 2.5.2). Smaller swaths permit the use of sensors with larger focal lengths and more precise optics, since the system does not need to cover extensive surface areas. This leads to a finer GSD, facilitating detailed analysis of small features. Additionally, a smaller swath results in a narrower field of view (FOV), as illustrated in Figure 14. The swath width can be approximated as the product of the number of pixels (N_p) in one dimension and the native spatial resolution SR (GSD per pixel) in that dimension. For detectors referred to in section 2.5.3 with an $SR \approx 1$ meter, the swat width would be about 3.000 to 4.000 meters or $3 - 4$ km.

3 Orbital dynamics

This chapter establishes the orbital dynamics framework for satellite attitude determination and control, enabling modelling of the satellite's interactions with its environment in subsequent chapters and ultimately allowing for FACA performance comparisons. It therefore builds the mathematical framework in support of the research question:

(B.3) *How does the performance of each actuator type compare when evaluated in a closed-loop simulation against pointing accuracy and precision for a disturbance-rejection scenario?*
To be able to model and create the simulation (models), a mathematical framework must be developed first. More specifically, the reference frames for defining satellite position and orientation are presented in 3.1. Next, the coordinate transformations between these frames are then detailed in 3.2, followed by equations of motion 3.3, and an overview of disturbance torques 3.4. Next, the attitude propagation is addressed in 3.5 and the initial conditions for the angular velocity and angular momentum are set in 3.6. Finally, section 3.7 presents the orbital model, its adopted assumptions, and the mathematical formulation, followed by the verification of the orbit-propagation method used in later analyses.

3.1 Reference frames

The reference frames are: Earth-Centred Inertial 3.1.1, Earth-Centred Earth-Fixed 3.1.2, North-East-Down 3.1.3, Local Vertical Local Horizontal 3.1.4, and the body-fixed reference frame 3.1.5. These frames provide a basis for describing the position, velocity, and orientation of a satellite, both relative to the Earth and relative to itself. The ECI frame is chosen as the default reference frame for the simulations in this study. All intermediate steps are first related to the ECI frame.

3.1.1 Earth-centred inertial reference frame (ECI)

The Earth-centred inertial (ECI) coordinate system is a fundamental, right-handed, orthogonal, Cartesian spatial inertial reference frame, denoted as F_I. The term 'inertial' signifies that this frame is non-accelerating and non-rotating relative to the fixed stars. It is not fixed to the rotating Earth, making it suitable for representing the positions and velocities of objects in space relative to the Earth's centre of mass over extended periods. The coordinates X_I, Y_I, and Z_I are measured from the planet's centre of mass, with the axes fixed relative to the stars rather than the Earth's surface, as illustrated in Figure 25.

The Z_I-axis is precisely aligned north along the Earth's mean spin-axis, extending through the geographic poles. While the Earth's actual spin axis experiences slight variations due to nutation and precession, the Z_I-axis represents the average orientation of the Earth's spin axis. The X_I-axis lies within the Earth's equatorial plane and points towards the vernal equinox, which is the location where the ecliptic (the plane of Earth's orbit around the Sun) intersects the equator. The vernal equinox serves as a fixed reference point in space. The Y_I-axis completes the right-handed coordinate system, ensuring that the frame is orthogonal and well-defined.

3.1.2 Earth-Centred Earth Fixed reference frame (ECEF)

The Earth-centred Earth Fixed (ECEF) reference frame, F_C, also called the geocentric coordinate system, is a Cartesian spatial reference framework that rotates with the Earth. Unlike the ECI frame, the ECEF frame is fixed to the Earth's surface. The coordinates X, Y, and Z are measured from the planet's centre of mass, as shown in Figure 20.

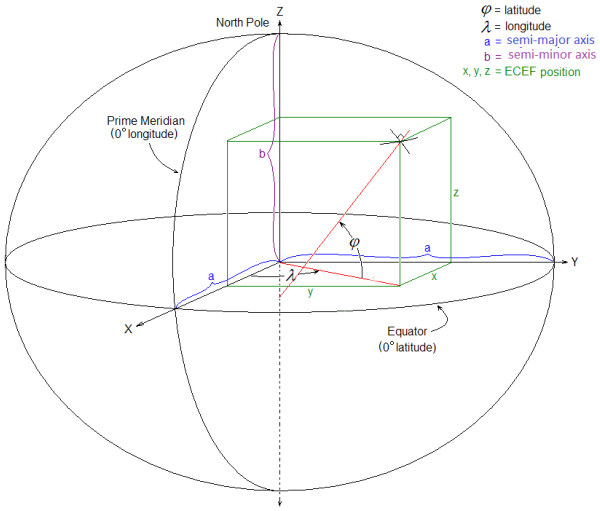

Figure 20: The ECEF coordinates (XYZ) are shown in relation to the latitude and longitude. Source: [18]

Typically, the X-axis of the ECEF frame extends from the Earth's centre of mass through the point where the Prime Meridian (0° longitude) intersects the Equator (0° latitude). The Y-axis is orthogonal to the X-axis and lies within the equatorial plane, pointing towards 90° East longitude. The Z-axis aligns with the Earth's rotational axis, pointing towards the North Pole.

For this study, however, the ECEF reference is spawned at the location of the ECI reference frame. It rotates along the positive Z axis by the rotational speed of the Earth Ω_{Earth} from the start of the simulation. Earth's rotation rate is given by Equation 22 [62].

$$\Omega_{Earth} = \frac{15.04106717866910\,\texttt{[deg/h]}}{3600\,\texttt{[s/h]}} \cdot \frac{\pi\,\texttt{[rad]}}{180\,\texttt{[deg]}} = 7292115 \cdot 10^{-11}\,\texttt{[rad/s]} \tag{22}$$

3.1.3 North-East-Down reference frame (NED)

The North-East-Down (NED) reference frame, denoted as F_N, is a non-inertial local coordinate system. This means that it is not an inertial frame, as it is subject to accelerations due to the Earth's rotation. The NED frame is a Cartesian coordinate system defined relative to a specific point on the Earth's surface. The orientation of the NED frame is defined as follows, as seen in Figure 21. This frame is used for describing the Earth's magnetic field, as described in section 4.6.2. Since the NED frame is locally level, it simplifies the calculations for the torques arising from interaction with Earth's magnetic field.

- North (N): The positive X-axis points towards the geographic North Pole, aligning with the local meridian.
- East (E): The positive Y-axis points towards the geographic East, perpendicular to the North axis and tangent to the local parallel of latitude.
- Down (D): The positive Z-axis points directly downward, towards the centre of the Earth, along the local vertical.

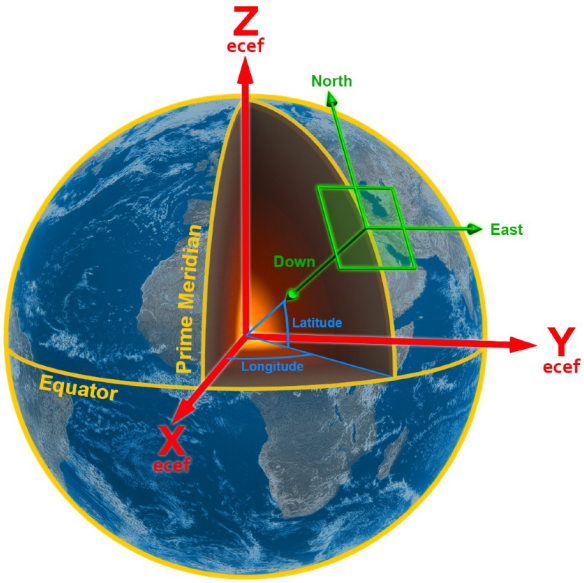

Figure 21: A graphical representation of the NED reference frame at a position on the Earth. The (XYZ) denote the ECEF reference frame. Source: [2]

3.1.4 Local Vertical Local Horizontal reference frame (LVLH)

The Local Vertical Local Horizontal (LVLH) reference frame, also known as the Orbital Frame or the Radial-Tangential-Normal frame, is a coordinate system used to describe the motion and orientation of a satellite in orbit around the Earth. It is a dynamic coordinate system, as its orientation changes continuously as the satellite orbits. The LVLH frame is centred on the satellite and is defined as follows:

- X-axis (Radial): Points from the Earth's centre of mass directly towards the satellite. This direction is referred to as the radial or the local vertical direction.
- Y-axis (Along-Track): Lies in the orbital plane and is perpendicular to the X-axis. It points in the direction of the satellite's instantaneous velocity vector, indicating the satellite's motion along its orbit. This is the along-track or tangential direction.
- Z-axis (Orbit Normal): Is perpendicular to both the X and Y axes, completing the right-handed coordinate system. It points in the direction of the orbit's angular momentum vector, which is normal to the orbital plane. This is the orbit normal direction.

The LVLH frame is used for attitude control because it provides a natural frame of reference for describing the satellite's orientation relative to the Earth. For this study, the attitude control system is designed to maintain orientation with the LVLH frame, such that the imager points towards NADIR. The LVLH reference frame is illustrated in Figure 22.

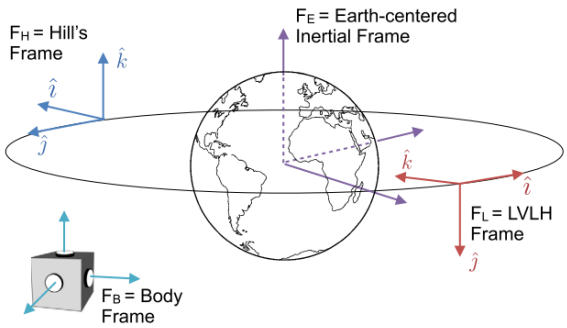

Figure 22: A graphical representation of the LVLH reference frame w.r.t. the Earth. The ijk denote the unit axis. Source: [109]

3.1.5 Body-fixed reference frame (BFRF)

The body-fixed reference frame, F_b, is a Cartesian spatial reference frame that is rigidly attached to the satellite. It is used to represent the positions, orientations, and motions of components and systems relative to the satellite itself. The coordinates XYZ are measured from the centre of mass, denoted as cg, with the axes X_B, Y_B, Z_B fixed relative to the physical structure and orientation, as shown as $\vec{i}, \vec{j}, \vec{k}$ in Figure 23. The origin of this frame is located at the satellite's centre of gravity. The axes are aligned with the principal axes of the satellite's inertia.

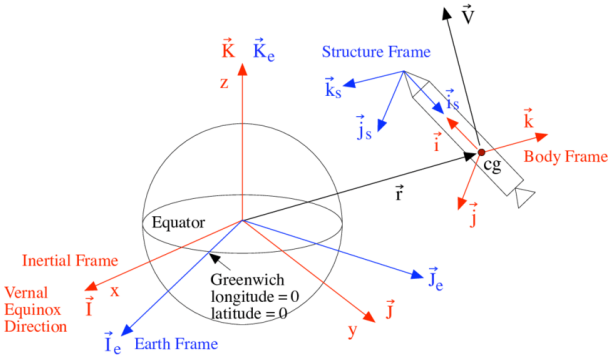

Figure 23: Illustration of the Earth-centred inertial reference frame with I, J, K, the Earth-fixed reference frame with Ie, Je, Ke, the structure reference frame with is, js, ks, and the body-axis reference frame with i, j, k. Source: [21]

The body axis reference frame is used to determine and describe the disturbance torques acting on the satellite and for implementing attitude control strategies. It allows analysing how external forces and torques affect the satellite's orientation, and to design control systems that maintain the desired attitude. Furthermore, the satellite's inertia tensor is also expressed in the body frame.

3.2 Transformation between reference frames

This section describes the transformation matrices, which are direction cosine matrices (DCMs), used in this research: DCM Earth-centred inertial (ECI) 3.2.1, from ECI to Earth-centred Earth-fixed F_C 3.2.2, from ECI to North-East-Down (NED) T_{NI} 3.2.3, from Orbital to ECI T_{IO} 3.2.4, from Local Vertical Local Horizontal (LVLH) to ECI F_L 3.2.5, and from Body-fixed (BFRF) to ECI F_B 3.2.6.

The three column vectors (v_1, v_2, v_3) in each DCM are orthogonal to each other. This means that the matrixes $([v1, v2, v3])$ are orthonormal, which causes the inverse of the matrix to be the transpose of the matrix $T_{12}^{-1} = T_{12}^T$, and that the multiplication of the matrix by its inverse or transpose gives the identity matrix $(T_{12} \cdot T_{12}^{-1} = T_{12} \cdot T_{12}^T I)$.

Taking the inverse of the matrix changes the rotation direction from forward transformation to backwards transformation. Combining this property with the DCMs provided allows for expressing all knowns in the same coordinate system.

All transformation matrices can be expressed using Euler angles. These matrices are based on three individual rotation matrices, $R_x(\phi)$, $R_y(\theta)$, and $R_z(\psi)$, and are defined in Equation 23. The rotation order must be consistent throughout the study, as a changed order can yield different outcomes. For this study, the XYZ direction is chosen such that $X_1 = T_{12}X_2$ with $T_{12} = R_x(\phi)R_y(\theta)R_z(\psi)$.

$$R_x(\phi) = \begin{bmatrix} 1 & 0 & 0 \\ 0 & \cos(\phi) & \sin(\phi) \\ 0 & -\sin(\phi) & \cos(\phi) \end{bmatrix} R_y(\theta) = \begin{bmatrix} \cos(\theta) & 0 & -\sin(\theta) \\ 0 & 1 & 0 \\ \sin(\theta) & 0 & \cos(\theta) \end{bmatrix} R_z(\psi) = \begin{bmatrix} \cos(\psi) & \sin(\psi) & 0 \\ -\sin(\psi) & \cos(\psi) & 0 \\ 0 & 0 & 1 \end{bmatrix} \quad (23)$$

3.2.1 Direction cosine matrix for the ECI frame

Since the Earth-centred inertial reference frame (see section 3.1.1) is the leading reference frame in the simulation, it is defined by the identity matrix F_I and is presented in Equation 24.

$$F_I \equiv \left[[X_{ECI}], [Y_{ECI}], [Z_{ECI}]\right] = \left[\begin{bmatrix}1\\0\\0\end{bmatrix}\begin{bmatrix}0\\1\\0\end{bmatrix}\begin{bmatrix}0\\0\\1\end{bmatrix}\right] = \begin{bmatrix}1,0,0\\0,1,0\\0,0,1\end{bmatrix} \tag{24}$$

3.2.2 Transformation from ECI to ECEF

The transformation from Earth-Centred Inertial frame, F_I (refer to 3.1.1), to the Earth-Centred Earth-Fixed frame, F_C (discussed in 3.1.2), is given by Equation 25. This transformation is used to plot the ground path traced by the satellite as the Earth rotates.

$$F_C = T_{CI}(\Omega_t, t)F_I = R_z(\Omega \cdot t) = \begin{bmatrix}\cos(\Omega \cdot t) & \sin(\Omega \cdot t) & 0\\ -\sin(\Omega \cdot t) & \cos(\Omega \cdot t) & 0\\ 0 & 0 & 1\end{bmatrix} \tag{25}$$

where T_{CI} is the transformation matrix, Ω_t is the Earth's angular velocity, and t is the time elapsed.

3.2.3 Transformation from ECI to NED

The transformation from the Earth-Centred Inertial frame (see 3.1.1) to the North-East-Down (NED) frame (reviewed in 3.1.3) is computed using the transformation matrix T_{NI}. This transforms a vector from the ECI frame to the NED frame.

$$T_{NI} = R_x(\pi/2)R_y(-\Phi_{lat})R_z(\lambda_{lon}) = \begin{bmatrix}-\sin(\Phi_{lat})\cos(\lambda_{lon}) & -\sin(\Phi_{lat})\sin(\lambda_{lon}) & \cos(\Phi_{lat})\\ -\sin(\lambda_{lon}) & \cos(\lambda_{lon}) & 0\\ -\cos(\Phi_{lat})\cos(\lambda_{lon}) & -\cos(\Phi_{lat})\sin(\lambda_{lon}) & -\sin(\Phi_{lat})\end{bmatrix} \tag{26}$$

This transformation matrix T_{NI} is constructed using the latitude Φ_{lat} and longitude λ_{lon} calculated from the ECI position vector `r_eci`.

The longitude measures angular position east or west of the X_{ECI} axis. It is calculated using the `atan2` MATLAB function [99]. The longitude is expressed in Equation 27.

$$\lambda_{lon} = \text{atan2}(y_{ECI}, x_{ECI}) \tag{27}$$

The latitude Φ_{lat} is the angular position measured from the equator. It measures the angles north or south of the equator, with the equator being at zero degrees. The latitude is expressed in Equation 28.

$$\Phi_{lat} = \text{atan2}\left(z_{ECI}, \sqrt{(y_{ECI}^2 + x_{ECI}^2)}\right) \tag{28}$$

3.2.4 Transformation from orbital reference frame to ECI

The orbital reference frame is a spherical coordinate reference frame, which is illustrated in Figure 24. Describing the orbital position and velocity in the ECI reference frame (see 3.1.1), r_{ECI} and V_{ECI}, requires three sequential rotations: rotation around the Z-axis by the argument of periapsis ω, rotation around the X-axis by the inclination i, and rotation around the Z-axis by the right ascension of the ascending node (RAAN) Ω. The order is described by Equation 29.

$$\begin{aligned} T_{IO} &= R_z(\Omega)R_x(i)R_z(\omega) \\ &= \begin{bmatrix}\cos(\Omega)\cos(\omega) - \sin(\Omega)\cos(i)\sin(\omega) & -\cos(\Omega)\sin(\omega) - \sin(\Omega)\cos(i)\cos(\omega) & \sin(\Omega)\sin(i)\\ \sin(\Omega)\cos(\omega) + \cos(\Omega)\cos(i)\sin(\omega) & -\sin(\Omega)\sin(\omega) + \cos(\Omega)\cos(i)\cos(\omega) & \cos(\Omega)\sin(i)\\ \sin(i)\sin(\omega) & \sin(i)\cos(\omega) & \cos(i)\end{bmatrix} \end{aligned} \tag{29}$$

The position vector in the ECI frame r_{ECI} is calculated by Equation 30.

$$r_{ECI} = T_{IO} \cdot P_{\text{initial}} = R_z(\Omega)R_x(i)R_z(\omega) \cdot \begin{bmatrix} \frac{p\cos(\nu)}{1+e\cos(\nu)} \\ \frac{p\sin(\nu)}{1+e\cos(\nu)} \\ 0 \end{bmatrix} \tag{30}$$

The velocity vector in the ECI frame V_{ECI} is calculated by Equation 31

$$V_{ECI} = T_{IO} \cdot V_{\text{initial}} = R_z(\Omega)R_x(i)R_z(\omega) \cdot \sqrt{\frac{\mu}{p}} \begin{bmatrix} -\sin(\nu) \\ e+\cos(\nu) \\ 0 \end{bmatrix} \tag{31}$$

Herein, P_{initial} is the initial position in the orbital plane, V_{initial} is the initial velocity in the orbital plane, $\mu = 398600.435436 \times 10^9$ $[m^3/s^2]$ is the Earth's gravitational constant, p is the semi-latus rectum, given by $p = a(1-e^2)$, where a is the semi-major axis and e is the eccentricity, and ν is the true anomaly.

3.2.5 Transformation from LVLH frame to ECI

The transformation from the Local Vertical Local Horizontal frame (presented in 3.1.2) to the Earth-Centred Inertial frame (refer to 3.1.1) is determined by the orbital position r_{ECI} and velocity V_{ECI} of the satellite. The DCM that transforms a vector from the LVLH frame to the ECI frame is determined. The X-axis of the LVLH frame is aligned with the velocity vector in the ECI frame and normalised, see Equation 32.

$$X_{LVLH} = \frac{V_{ECI}}{\|V_{ECI}\|} \tag{32}$$

The Z-axis of the LVLH frame points towards the Earth (NADIR direction) and is calculated by normalising and inverting the position vector in the ECI frame r_{ECI}, and is given by Equation 33

$$Z_{LVLH} = -\frac{r_{ECI}}{\|r_{ECI}\|} \tag{33}$$

The Y-axis of the LVLH frame completes the right-handed coordinate system and is calculated as the cross product of $\hat{Z}_{body}$ and $\hat{X}_{body}$, and then normalised:

$$Y_{LVLH} = \frac{Z_{LVLH} \times X_{LVLH}}{\|Z_{LVLH} \times X_{LVLH}\|} \tag{34}$$

The DCM from the LVLH frame to the ECI frame is composed of those vectors according to Equation 35.

$$F_L = \left[[X_{LVLH}], [Y_{LVLH}], [Z_{LVLH}]\right] \tag{35}$$

3.2.6 Transformation from BFRF to ECI

The orientation of the body-fixed reference frame F_B (discussed in 3.1.5) with respect to the ECI frame F_I (see 3.1.1) is given by the direction cosine matrix (DCM) F_B. This DCM can be obtained from a set of Euler angles, ϕ, θ, and ψ, representing rotations around the X, Y, and Z axes, respectively, and is given in Equation 36.

$$\begin{bmatrix} X_{ECI} \\ Y_{ECI} \\ Z_{ECI} \end{bmatrix} = F_B \begin{bmatrix} X_B \\ Y_B \\ Z_B \end{bmatrix} = R_x(\phi)R_y(\theta)R_z(\psi) \begin{bmatrix} X_B \\ Y_B \\ Z_B \end{bmatrix} \tag{36}$$

Herein, the attitude in the ECI frame, $\text{attitude}_{\text{ECI}}$, is expressed in Euler angles (ϕ, θ, and ψ), and are a summation of the satellite attitude when spawned, $\text{attitude}_{\text{init}}(t_0)$, plus the change in attitude $\Delta\text{attitude}(t)$, see Equation 37. The rotation matrices used are derived from Equation 23.

$$\text{attitude}_{\text{ECI}}(t) = \text{attitude}_{\text{init}}(t_0) + \Delta\text{attitude}(t) \tag{37}$$

The change in attitude over time is due to the roll, pitch, and yaw rates (ω or PQR) as the satellite propagates through the orbit.

3.3 Equations of motion

In the presence of disturbances, the satellite will experience linear and angular accelerations according to Newton's second law of motion. The linear accelerations are negligible for the mission's outcome, as their effects are considered insignificant for analysing angular disturbances. The angular accelerations, however, cannot be neglected as they impact the satellite's attitude.

Any torque acting on the satellite causes a change in the attitude, and is described by Euler's equation for rigid bodies [113] through Equation 38. This equation of motion describes the satellite's attitude dynamics in time:

$$I \cdot \dot{\omega} + \omega \times (I \cdot \omega) = \sum \tau \tag{38}$$

Herein, I is the moment of inertia of the satellite, $\dot{\omega}$ is the rate of change of angular velocity of the satellite, ω is the angular velocity of the satellite, $(I \cdot \omega)$ is the total angular momentum of the satellite (upon spawning, see 3.6.1) and $\sum \tau$ represents the sum of the disturbance torques plus the counter torque generated by the FACAs onboard the satellite. Expanded, in scalar form, it can be presented as Equation 39.

$$\begin{aligned} I_{xx}\frac{d\omega_x}{dt} &= \tau_x - (I_{zz} - I_{yy})\omega_y\omega_z \\ I_{yy}\frac{d\omega_y}{dt} &= \tau_y - (I_{xx} - I_{zz})\omega_z\omega_x \\ I_{zz}\frac{d\omega_z}{dt} &= \tau_z - (I_{yy} - I_{xx})\omega_x\omega_y \end{aligned} \tag{39}$$

It should be noted that the greater the magnitude of the satellite's inertia I is, the larger the resistance against angular acceleration. Also, the larger the angular momentum about an axis, the greater the gyroscopic stiffness. Both contribute positively to countering disturbances.

3.4 Disturbance torque

The equations of motion discussed in section 3.3 require the disturbance torques to be modelled as an input, causing them to play a role in the dynamics of a satellite. Two groups of disturbance torques are differentiated: external disturbances and internal disturbances.

External torque
Depending on their nature, cyclic or secular, their effect may be larger or smaller for the pointing precision and accuracy, as well as contributing to jitter. Cyclic torque refers to a periodic or oscillatory torque that is applied to a satellite. It arises from external factors such as gravitational perturbations, magnetic field variations, or other cyclic disturbances. Secular torque refers to a long-term or gradual torque that acts on a satellite. It is often associated with non-cyclic, secular changes in external forces, such as atmospheric drag, radiation pressure, or mass distribution asymmetries in the satellite. Secular torque causes a slow and continuous change in the satellite's attitude over an extended period. Unlike cyclic torque, which induces periodic motion, secular torque contributes to a persistent drift or trend in the satellite's orientation.

Compensation for cyclic torques requires (rapid) spool up and spool down of the FACAs used. Their net effect over a period is approximately zero. It is not precisely zero due to the coupling effect between the axes, as shown in Equation 39, which causes the effective disturbance to change (slightly) due to continuously changing orientation. The stored angular momentum is designed to be large enough that the cyclic motion remains within the pointing specification with active control during an orbit, if possible.

Secular torques are more difficult to compensate for by solely employing FACAs, because they accumulate over time. This means that the FACA used will saturate over time. For that reason, periodic torquing or 'offloading' for this accumulation must be done during (a fraction) of the orbit(s). This offloading is not modelled in this research. The FACAs employed will be initialised in a steady state and simulated for a defined number of orbits.

Chapter 4 elicits nine external disturbances. Out of these, atmospheric, gravity gradient, magnetic field and solar radiation pressure are taken into consideration for their significance, and are presented in chapter 5.

Internal torque
A distinction is made between desired and undesired internal torques. Desired internal torques are present to control the satellite's attitude or its equipment positively. Undesired internal torque can be listed as disturbances, such as vibrations stemming from actuators or instruments, or imperfect control. This thesis considers only the effect of employing FACAs on the satellite's attitude in terms of vibration sources, and is presented in chapter **??**.

3.5 Attitude propagation

The satellite's attitude (orientation) is represented by a quaternion ($q = [w, x, y, z]$). Quaternions are used to prevent gimbal lock during the propagation. The following steps outline the quaternion-based attitude propagation.

First, the derivative of the quaternion $\dot{q}$ is computed using the `quatmultiply` function in MATLAB [54]. The derivative is expanded in Equation 40.

$$\dot{q} = 0.5 \cdot \texttt{quatmultiply}(q, \omega_{quat}) = 0.5 \cdot \begin{bmatrix} (0 \cdot w - \omega_x \cdot x - \omega_y \cdot y - \omega_z \cdot z) \\ (0 \cdot x + \omega_x \cdot w - \omega_y \cdot z + \omega_z \cdot y) \\ (0 \cdot y + \omega_x \cdot z + \omega_y \cdot w - \omega_z \cdot x) \\ (0 \cdot z - \omega_x \cdot y + \omega_y \cdot x + \omega_z \cdot w) \end{bmatrix} \tag{40}$$

Where q is the current quaternion, and $\omega_{quat} = [0, \omega] = [0, \omega_x, \omega_y, \omega_z]$, whereby ω is the angular velocity vector expressed in the body frame.

Next, the quaternion is updated using Euler integration, as shown in Equation 41.

$$q_{t+\Delta t} = q_t + \dot{q}_t \Delta t \tag{41}$$

where $q_{t+\Delta t}$ is the quaternion at time $t + \Delta t$, q_t is the quaternion at time t, $\dot{q}_t$ is the quaternion derivative at time t, and Δt is the time step. Since Euler integration is a first-order numerical method that approximates the solution to the differential equation, a sufficiently small time step Δt must be selected.

Lastly, to prevent numerical drift of the quaternion, the quaternion is normalised after each integration step, according to Equation 42.

$$q = \frac{q}{\|q\|} \tag{42}$$

where $\|q\|$ is the Euclidean norm ($\|q\| = \sqrt{w^2, x^2, y^2, z^2}$) of the quaternion q.

3.6 Initial conditions

Euler's equation, Equation 38 in section 3.3, describes the angular motion given as a set of variables. Upon spawning, the following components must be known:

1. Inertia tensor for the entire satellite (including the FACAs). For convenience, it is assumed that the FACAs's inertia tensor is part of the larger total inertia tensor I_{total}. The latter is determined by equations 113 till 115 presented in 6.1.4.
2. The angular velocity expressed in the body-fixed reference frame. This is given by Equation 47 in 3.6.1.
3. For the undisturbed scenario, the angular momentum is constant, and is determined via Equation 48 in 3.6.2.
4. The initial torque τ is assumed zero. This is to start the simulation from a steady state condition, whereby the angular momentum vector is aligned with the orbital normal.

3.6.1 Initial angular velocity

The instantaneous angular rate of the satellite within its orbital trajectory is dependent on the position and velocity of the Keplerian orbit. The angular rate in the body-fixed reference frame (BFRF) is determined by transforming the orbital angular velocity vector from the Earth-Centred Inertial (ECI) frame to the satellite's body frame.

First, the angular momentum vector in the ECI frame H_{ECI} is computed by taking the cross product of the satellite's position vector, r_{eci}, and the velocity vector, V_{eci}, both expressed in the ECI frame, and is given by Equation 43.

$$H_{ECI} = r_{eci} \times V_{eci} \tag{43}$$

By normalising the angular momentum vector, the orbital normal unit vector $\hat{n}$ is found in Equation 44.

$$\hat{n} = \frac{H_{ECI}}{||H_{ECI}||} \tag{44}$$

In which the magnitude of the angular momentum vector, $||H_{ECI}||$, represents the specific angular momentum of the orbit. To account for the varying orbital rate due to the elliptical nature of the orbit, the instantaneous angular rate ω_{orbit} is calculated in Equation 45.

$$\omega_{orbit} = \frac{||H_{ECI}||}{||r_{eci}||^2} \tag{45}$$

The angular velocity vector in the ECI frame, ω_{ECI}, is then defined as the product of the instantaneous angular rate and the orbital normal vector by Equation 46

$$\omega_{ECI} = \omega_{orbit} \cdot \hat{n} \tag{46}$$

Finally, the angular velocity vector is transformed from the ECI frame to the BFRF via premultiplying with the transpose of F_B (the transformation matrix from the BFRF to the ECI frame, see 3.2.6), and is given by Equation 47.

$$\omega_{B_{\text{init}}} = F_B^T \cdot \omega_{ECI} \tag{47}$$

The resulting $\omega_{B_{\text{init}}}$ vector represents the initial angular rates in the BFRF (PQR). This vector serves as the basis for the attitude propagation simulations discussed in sections 3.5.

3.6.2 Initial angular momentum

For the angular momentum vector decomposed along the body reference frame axes (see 3.1.5), the angular momentum H_B is expressed in Equation 48.

$$H_B = I_{xx}\omega_x + I_{yy}\omega_y + I_{zz}\omega_z \tag{48}$$

When spawning the NADIR pointing satellite aligned with the orbital plane, the initial angular velocity about the X_B axis (roll ϕ), ω_x, is zero; this is also the case for the Z_B axis (yaw ψ), $\omega_y = 0$. At this instance, the satellite only has an angular momentum about the Y_B axis (pitch θ), $H_Y = I_{yy}\omega_y$, whereby $\omega_y = \omega_{orbit}$ (given by Equation 45). That means that the initial angular momentum $H_{B_{\text{init}}}$ can be expressed as $H_{B_{\text{init}}} = [0; H_Y; 0]$. This choice of initial conditions prevents cross-products in the equations of motion, Equation 38, at the initial time because the components of the angular velocity vector that are multiplied together in the cross-terms are zero (the terms like $(I_{yy} - I_{zz})\omega_y\omega_z$ are zero). This creates a decoupled starting point for analysing the satellite's stability and response to disturbances. Similarly, aligning the FACAs with the body axis also prevents those nonlinearities from occurring.

3.7 Orbital Model

This section provides an overview of the orbital model used to simulate the satellite's position and orbital velocity. It outlines Keplerian propagation, coordinate-system transformations, and the underlying mathematical framework. Moreover, it describes the verification process used to ensure the accuracy and

reliability of the orbital model.

Typically, orbital positions, velocities, and orientations are modelled using Newton's second law of motion for both translational and rotational motion. This requires simultaneous integration to determine the satellite's orbital velocity and position, as well as its angular rates and orientation. Since these parameters are all related, one would solve such a system of differential equations using solvers like `ODE45` or `ODE113`. Such solvers are relatively expensive to evaluate compared with simple Euler integration, but are designed to allow variable time steps. Also, to isolate the impact of reaction wheels versus momentum wheels on image performance, the orbital model assumes that disturbances do not affect the satellite's translational motion. This allows for the decoupling of translational and rotational dynamics. As a secondary effect, this reduces computational costs. Therefore, the translational motion is determined by axes transformations and Keplerian propagation, whereas the rotational dynamics are captured using the `ODE45` solver.

3.7.1 Assumptions

The following assumptions apply to the orbital model:

1. The Earth is modelled as a perfect sphere with a gravitational parameter GM. This allows latitude to be defined as a function of geocentric rather than geodetic latitude.
2. Only the Earth's gravitational force is considered (two-body problem), resulting in a pure Keplerian orbit.
3. Perturbations are not included for modelling the orbital position and velocity. This means that the orbital path is fixed with respect to the inertial reference frame. This means that the orbital position and velocity depend solely on time.
4. In reality, Earth's rotation vector is subject to changes in orientation and magnitude due to lunisolar gravitational torques and geodynamical processes, causing polar motion [86]. The effects are negligible when considering a single orbit. Thus, in the simulation, it is assumed that the rotation vector is aligned with the axis from the South Pole to the North Pole.

3.7.2 Modelling

The orbital model defines the satellite's position and velocity throughout the Keplerian orbit around Earth. It is built upon the initial parameters defined within the `initialParameters()` function. This function specifies the satellite's initial Keplerian orbital elements [39], orientation, and angular rates.

Parameter Definition
The initial orbital configuration is defined through the `initialParameters()` function. This function specifies the shape and orientation of a Keplerian orbit using various parameters: Semimajor axis (`orbitalElements.semimajoraxis`, a), Eccentricity (`orbitalElements.eccentricity`, e), Inclination (`orbitalElements.inclination`, i), Right ascension of the ascending node (`orbitalElements.raan`, Ω), Argument of periapsis (`orbitalElements.argumentofperiapsis`, ω), and the True anomaly (`orbitalElements.trueanomaly`, ν). A visual depiction of such an orbit is presented in Figure 24.

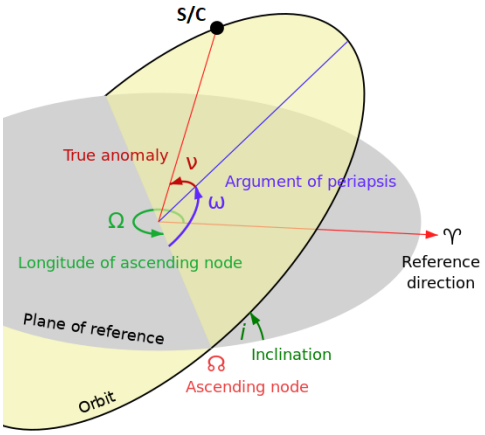

Figure 24: Keplerian orbit elements. The satellite (S/C) follows the orbital path in the direction of the ascending node. The current position of the S/C is a function of the parameters shown. Source: [90]

The interpretation of a Keplerian orbit around a rotating Earth requires defining various axis systems. For starters, the orbit is defined in Spherical coordinates around any inertial reference frame. For convenience, this is translated into Cartesian coordinates defined in the Earth-Centred-Inertial (ECI) reference frame.

Next, Earth rotates with a rotational rate about its rotation axis, which, for simplicity's sake, coincides with the poles. This causes the position relative to the ground to change over time. For that reason, the Earth-Centred-Earth-Fixed (ECEF) reference frame is defined. This frame rotates along with the Earth, causing the apparent path traced by the S/C to diverge away from the initial orbital path. To amplify this effect, the path traced for five polar orbits is presented in Figure 25. In the figure, the S/C is spawned to the left of South America, where the X_{ECEF} axis coincides with the red dashed line. The satellite is then propagated along the Keplerian path in the direction of the North pole. As can be seen, the path does not return to the spawning point but revolves around the poles with a continuous offset, which is a direct consequence of the Earth's rotational rate. The instantaneous location at each point in time will later be used to determine the disturbances acting on the S/C, which, in turn, will cause angular accelerations.

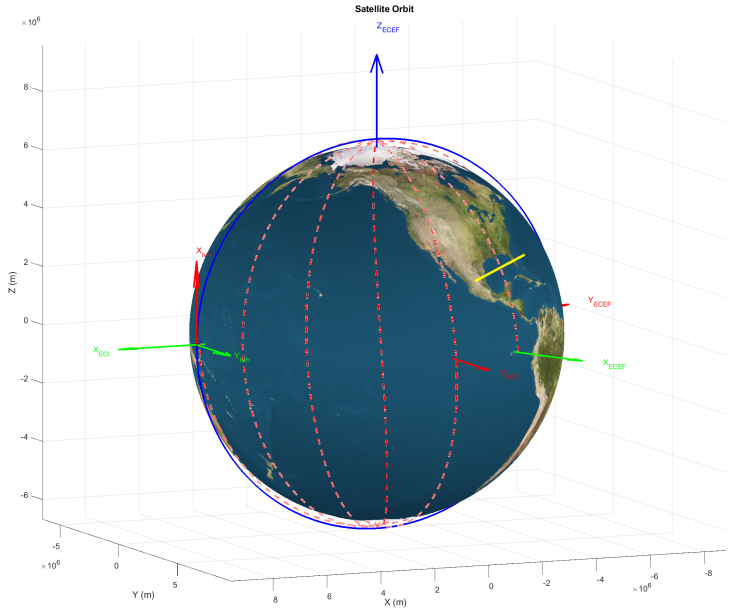

Figure 25: Five polar orbits. The satellite (S/C) follows the orbital path in the direction of the ascending node.

The model can assume any Keplerian orbit given the parameters previously described. A visual representation is given in Figure 26, wherein the inclination angle i (see Figure 24) is varied from (a) 0 degrees, via (b) 45, to (c) 90 degrees. This allows for selecting orbits of choice. Now, the performance of reaction wheels and momentum bias wheel can be compared in a series of orbits rather than a fixed one.

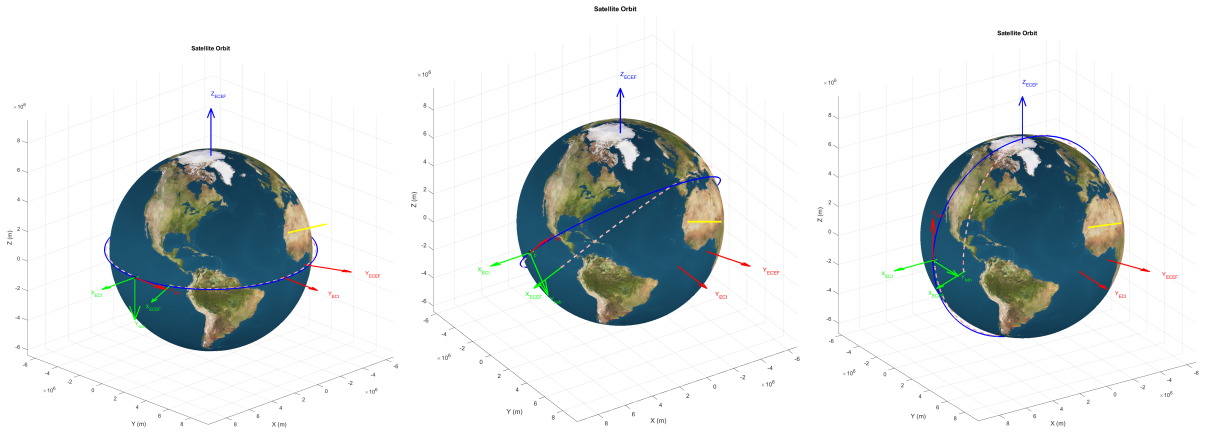

(a) S/C equatorial orbit (b) S/C 45 degrees inclination (c) S/C polar orbit

Figure 26: Illustration of orbits for (a) $i = 0$, (b) $i = 45$, and (c) $i = 90$ degrees. The blue circular line depicts the instantaneous projected orbit for a non-rotating Earth, the dashed red line represents the satellite's path traced due to the rotating Earth, and the arrows indicate the axis systems in use. Subscripts 'ECI', 'ECEF', 'LVLH' and 'b' denote the axis systems.

3.7.3 Verification

The verification process ensures that the calculated orbital position and velocity are realistic and usable by comparing the results from the orbital model against expected values.

The `keplerianToCartesian` function calculates the position and velocity vectors in the ECI frame based on the updated orbital elements at each time step. The position and velocity are updated through the simulation loop, using the following equations:

Mean motion calculation:

$$n = \sqrt{\frac{GM}{a^3}} \tag{49}$$

Update the mean anomaly:

$$M = \mod\left(M_0 + n \cdot t, 2\pi\right) \tag{50}$$

Calculate the Eccentric Anomaly E, using an iterative solver. Calculate the true anomaly from E:

$$\nu = 2 \cdot \tan\left(\frac{\left(\sqrt{1+e} \cdot \sin\left(\frac{E}{2}\right)\right.}{\sqrt{1-e} \cdot \cos\left(\frac{E}{2}\right)}\right) \tag{51}$$

Wherein, n is the mean motion, GM is the Earth's gravitational parameter, a is the semimajor axis, M is the mean anomaly, M_0 is the initial mean anomaly, E is the eccentric anomaly, e is the eccentricity, and ν is the true anomaly.

For the orbits shown in Figure 26, the orbital position and velocities are calculated and presented in Figure 27. It should be noted that the orbital position and velocities are expressed in the ECI reference frame. In Figure 27a, the solid green line depicts the Y-position. As expected, as the orbit is initiated to move in the Eastern direction, the Y-position follows a sinusoidal curve (sin), and the X-position has a 90-degree offset (cos). Similarly, for $i = 45$ degrees, the Z- and Y-coordinates are overlaying while the X-position remains unaltered, see Figure 27b. Finally, for the polar orbit in Figure 27c, the figure is identical to Figure 27a with the exception that the Z- and Y-axes have swapped position (for $i = 0$, the orbit takes place in the XY-plane, and for $i = 90$, in the XZ-plane).

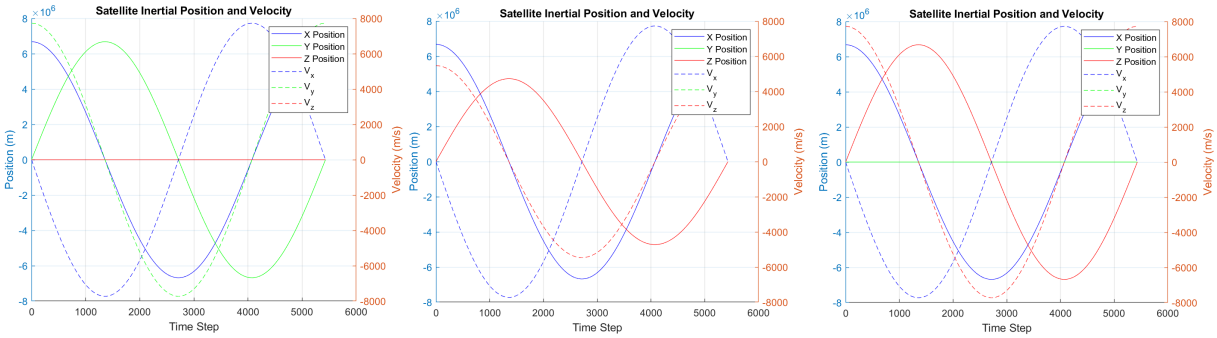

(a) S/C equatorial orbit (b) S/C 45 degrees inclination (c) S/C polar orbit

Figure 27: Illustration of orbital positions and velocities for (a) $i = 0$, (b) $i = 45$, and (c) $i = 90$ degrees.

To verify the quantities, the initial velocities are compared to the manual calculation for orbital speed displayed in Equation 52.

$$V^2 = GM\left(\frac{2}{r} - \frac{1}{a}\right) \tag{52}$$

Wherein V is the orbital velocity of the satellite, G the gravitational constant ($6.67430 \times 10^{-11} \mathrm{m}^3/\mathrm{kg}\cdot\mathrm{s}^2$), M is the mass of Earth (5.972×10^{24} kg), and r is the distance between the centre of Earth and the satellite (radius of the orbit). In the case of simulated circular orbits, the semi-major axis a is equal to the radius of the orbit $r = R_{Earth} + h$. Herein, $h = 300\ km$ is the flying height for the selected orbits. The orbital composed velocity $V = \sqrt{V_x^2 + V_y^2 + V_z^2}$ should be $V = 7725\ m/s$ according to Equation 53.

$$V = \sqrt{\frac{GM}{R_{Earth} + h}} = \sqrt{\frac{3.986004418 \cdot 10^{14}}{6378136 + 300 \cdot 10^3}} = 7725\ [\mathrm{m/s}] \tag{53}$$

From the data extracted to create Figure 27, the velocities indeed amount to $V_{i=0} = \sqrt{0^2 + 7725^2 + 0^2} = 7725\ m/s$, which is in line with reported low Earth orbital speeds of about 7.8 $[km/s]$ reported by the European Space agency [23].

Similarly, at an altitude of 300 $[km]$ the orbital period is expected to be approximately 90 minutes, or 5400 $[s]$. The orbital model shows that it will take 5431 seconds. Thus, with that, the orbital model is verified.

4 External disturbances

This chapter presents an overview of the external disturbances examined, focusing on their absolute values and variations over an orbit.

(A.3) *What are the quantitative models for the dominant external disturbance torques acting on a satellite in LEO, and how can a modular simulation be developed and verified to generate these torques?* This chapter assesses the significance of common external disturbances in terms of magnitude and variations across orbits. The dominant disturbances will be incorporated in the environmental model presented in chapter 5.

Ramnath [78] presented the relative influence of the external torques in a figure, copied here in Figure 28. At an altitude of 200 to 300 km, the dominant disturbance is the atmospheric (or Atmospheric) torque. Then, gravity gradient torque is the second dominant, followed by geomagnetic torque. Fourthly, solar pressure torque could play a substantial role. Micro-meteorite impacts are assumed to be negligible because the torque is orders of magnitude smaller.

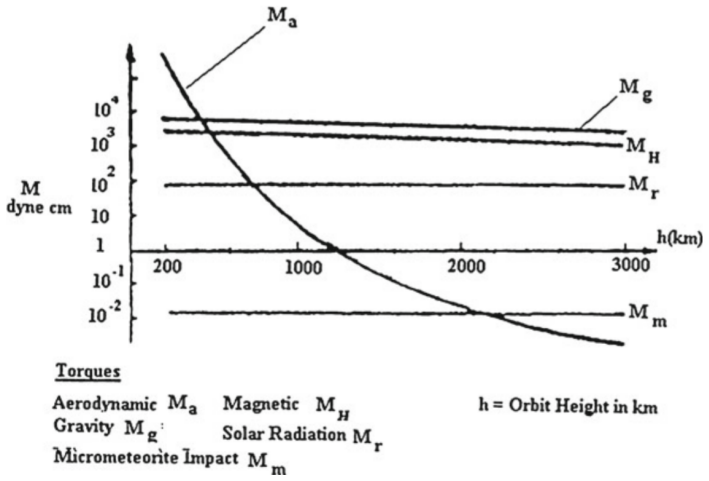

Figure 28: Environmental torques on an Earth satellite. Source: [78]

To explore the external disturbances in greater detail, nine disturbances are examined: Atmospheric drag 4.1, Albedo Pressure 4.2, Gravity gradient 4.3, Outgassing 4.4, Planetary Radiation Pressure 4.5, Residual Dipole 4.6, Radio Frequency 4.7, Solar Radiation Pressure 4.8, and Thermal Pressure 4.9.

Table 2 summarises those external disturbance sources (each subsection corresponds to the enumeration in the table under column one '*Type*'), their characteristics, and the rationale for including or neglecting each in the disturbance model. Next, their significance in this research (i.e. to include or exclude the disturbance for simulation) is investigated in their corresponding subsections. The table indicates the type of disturbance, its source and characteristic, and whether the disturbance is considered relevant for simulation. The table highlights four disturbances that are relevant to simulate: **Atmospheric drag, gravity gradient, residual dipole, and solar radiation pressure**. This finding is consistent with the dominant environmental torques acting on satellites orbiting the Earth described by Ramnath [78]. These four disturbances are implemented in the Environmental model in MATLAB, see chapter 5.

Table 2: External Disturbances

Type	Source	Characteristic	Included and rational
1. Atmospheric drag 4.1	Planetary atmosphere	Altitude and position relative to the Sun influence drag and lift on the satellite. This is due to the variations in atmospheric density and composition.	**Yes. Atmospheric disturbance torque is a significant factor. The dynamic pressure can exceed $80\mu Pa$, which is 16 times larger than the solar radiation pressure.**
2. Albedo Pressure 4.2	Sun reflection from the Earth.	The solar flux for Earth averages 0.29 [92]. Albedo varies with the satellite's latitude, longitude, season, and the specific surface properties. The force direction is determined by the relative angle of the Sun.	No, the albedo pressure is only about 7.3% compared to the Solar radiation pressure. The variations across an orbit are about 15%, which in absolute terms is very small.
3. Gravity gradient 4.3	Inertia and distance from the planet	If the satellite includes off-diagonal inertia terms, it generates a body-fixed torque for a planet-pointing satellite. Diagonal terms result in a gravity-gradient modal frequency. Gravity-gradient-stabilised satellite utilises a specific momentum distribution to maintain stable oscillation. In the dynamical model, gravity gradient functions as a pure stiffness term and cannot provide damping, which must come from another source.	**Yes. Earth's J2 affects the satellite's orientation, influencing the pointing stability.**
4. Outgassing 4.4	Moisture embedded in the structure	Outgassing, the emission of gases from materials due to heating [71], can introduce forces and torques on a satellite [56].	No. Typically, outgassing is only a concern at early stages of a satellite's life.
5. Planetary Radiation Pressure 4.5	The temperature of the planet	The black-body radiation of the planet, which amounts to roughly 255 W for Earth, exerts radiation pressure at infrared wavelengths. The optical properties at infrared wavelengths must be considered when planetary radiation is included.	No, the intensity of planetary radiation is much lower than that of Solar Radiation Pressure because Earth's emitted radiation is in the infrared spectrum, and is reduced due to atmospheric absorption. In LEO, the radiation from Earth to the satellite is roughly 16% of the Sun's.
6. Residual Dipole 4.6	Residual dipole on the satellite	This torque arises from the interaction between an external magnetic field and internal dipoles created by current loops. Magnetic torquers that employ a torque rod inherently have some residual dipole. Systems containing magnetic materials can also retain a residual dipole.	**Yes. Slight misalignment between the centre of mass and the magnetic centre causes the residual dipole to have a cyclical effect.**
7. Radio Frequency 4.7	Transmit antennas	Radiation pressure can be calculated by dividing the transmittance wattage by the speed of light. Satellites equipped with large offset transmitting antennas can exert considerable accumulating torques on the satellite.	No. For small-sized satellites, the RF torque is a factor of 50 smaller compared to the SRP.
8. Solar Radiation Pressure 4.8	Solar radiation	The Sun exerts forces on satellite. If a satellite is asymmetric, the offset between its centre of mass and centre of pressure can result in a torque. The solar flux at Earth's orbit is $1368W$ and varies inversely with the square of the distance from the Sun.	**Yes. The solar radiation pressure can reach about $5\mu Pa$, which is substantial given the projected area of the satellite.**
9. Thermal Pressure 4.9	Radiators	Heat radiates diffusely from all radiators, generating a force proportional to the heat flux. The satellite's temperature is not uniform, and heat-generating components may possess radiators.	No. The satellite of interest is chosen to irradiate homogeneously and omni-directionally. Thus, the thermal pressure is zero.

4.1 Atmospheric drag

The atmosphere is present during LEO flight. Therefore, atmospheric drag plays a significant role when modelling disturbances. The atmospheric torque $\mathbf{T}_A$ can be computed with Equation 54. Its implementation for the environmental model in MATLAB is presented in section 5.1.

$$\mathbf{T}_A = (\mathbf{r}_{cp} - \mathbf{r}_{cg}) \times \mathbf{e}_V \cdot C_D \frac{1}{2}\rho V^2 S \tag{54}$$

in which $\frac{1}{2}\rho V^2$ is the dynamic pressure exerted on the satellite, S is the frontal surface area, $\mathbf{e}_V$ the unit vector which is directed towards the velocity vector, $\mathbf{r}_{cp}$ is the centre of pressure vector in the body reference frame, and $\mathbf{r}_{cg}$ is the centre of gravity vector in body coordinates. For CubeSats, the centre of pressure typically coincides with the centre of symmetry.

According to Space Academy [91], above an altitude of 180 km, relying on a mean reference model for air density is inadequate. At these higher altitudes, ambient space weather conditions are highly variable over time, particularly due to solar Extreme Ultraviolet (EUV) radiation (covering wavelengths of 10-120 nm) and geomagnetic activity, which significantly influence atmospheric conditions.
The proposed model uses the solar radio flux at ten centimetres (F_{10}) as a proxy for solar EUV output, and the geomagnetic A_p index [22] to gauge geomagnetic activity. This model is well-suited for studying orbital decay and predicting satellite lifetimes in altitudes ranging from 180 to 500 km. The following equations can determine the atmospheric density in this altitude range:

$$\begin{aligned} T &= 900 + 2.5(F_{10} - 70) + 1.5A_p \\ \mu &= 27 - 0.012(h - 200) \\ H &= \frac{T}{\mu} \\ \rho &= 6 \cdot 10^{-10} \exp\left(-\frac{(h - 175)}{H}\right) \end{aligned} \tag{55}$$

Herein, the pseudo parameters T, μ, and H do not necessarily agree with the actual temperature in Kelvin, molecular weight, and scale height at the altitude of interest. The density ρ, however, can be regarded as the model output, see Figure 29.

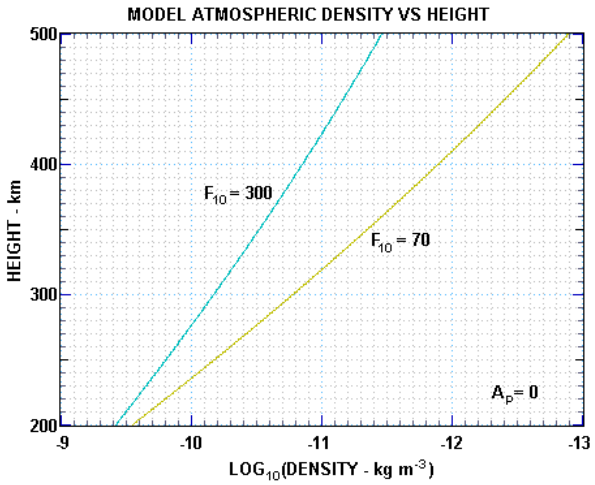

Figure 29: Values of the density model between 200 and 500 km in height for the case of minimal ($F_{10} = 70$) and maximal ($F_{10} = 300$) solar extreme ultraviolet and soft X-ray output. Source: Space Academy [91]

4.1.1 Total density calculation

To accurately simulate drag forces, the density can be calculated using the MATLAB implementation of the NRLMSISE-00 model [52], which provides a mathematical representation of the 2001 United States Naval Research Laboratory Mass Spectrometer and Incoherent Scatter Radar Exosphere [77]. NRLMSISE-00 is an empirical, global reference atmospheric model of the Earth from ground to space. It models the temperatures and densities of the atmosphere's components. A primary use of this model is to aid predictions of satellite orbital decay due to atmospheric drag [76].

The total mass density is derived from the combined contributions of various atmospheric constituents, including helium (He), oxygen (O), nitrogen (N2), oxygen (O2), argon (Ar), hydrogen (H), and nitrogen (N). This density is variable and depends on altitude, reflecting local fluctuations influenced by longitude, latitude, and temporal factors.

Scivision [85] built animations that showcase those fluctuations. A snapshot in time is presented in Figure 30.

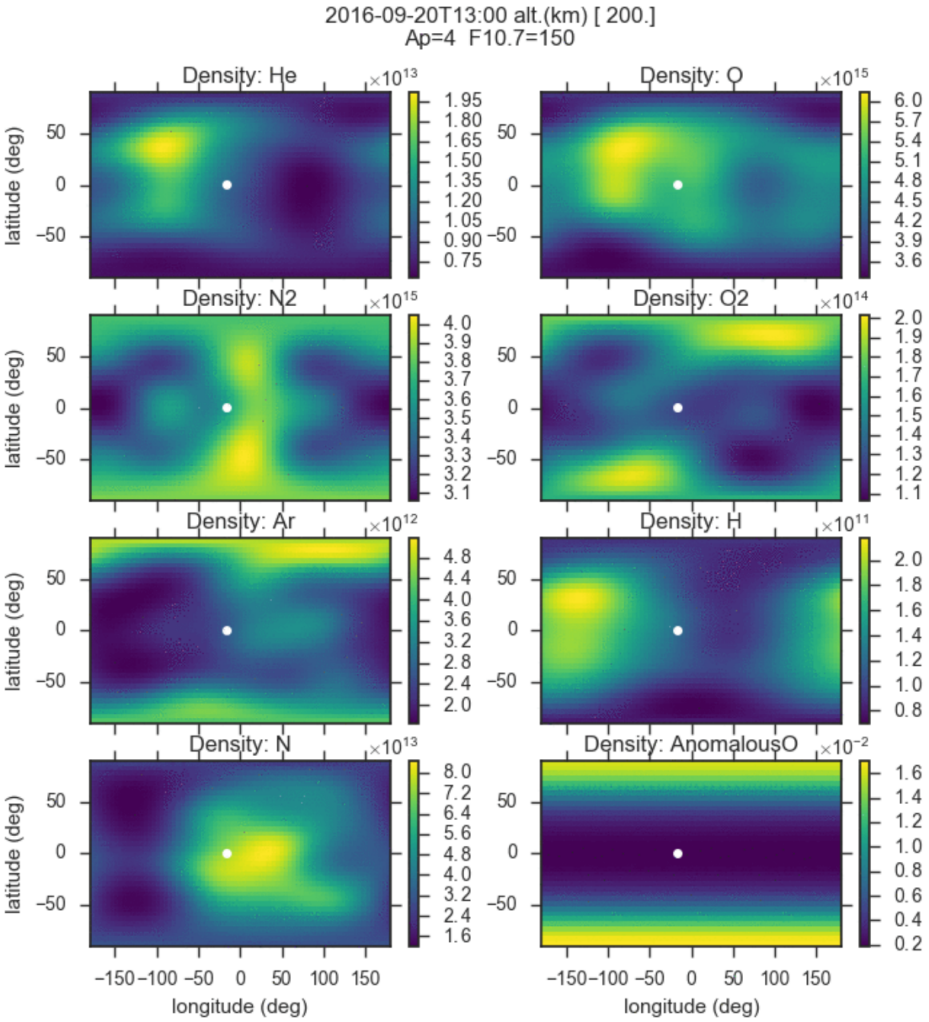

Figure 30: A slice at 200km on a world-wide grid for various atmospheric constituents, including helium (He), oxygen (O), nitrogen (N2), oxygen (O2), argon (Ar), hydrogen (H), nitrogen (N), and anomalous Oxygen (O). The yellow ball represents the sun's footprint on Earth. Source: Scivision [85].

The relation between total mass density ρ and altitude, from sea level to 1000 km, is illustrated in Figure 31a. The red box in this figure highlights the altitude range of interest, which is further detailed in Figure 31b. The graphs depict the total mass density at 0,0 longitude and latitude on January 1, 2010.

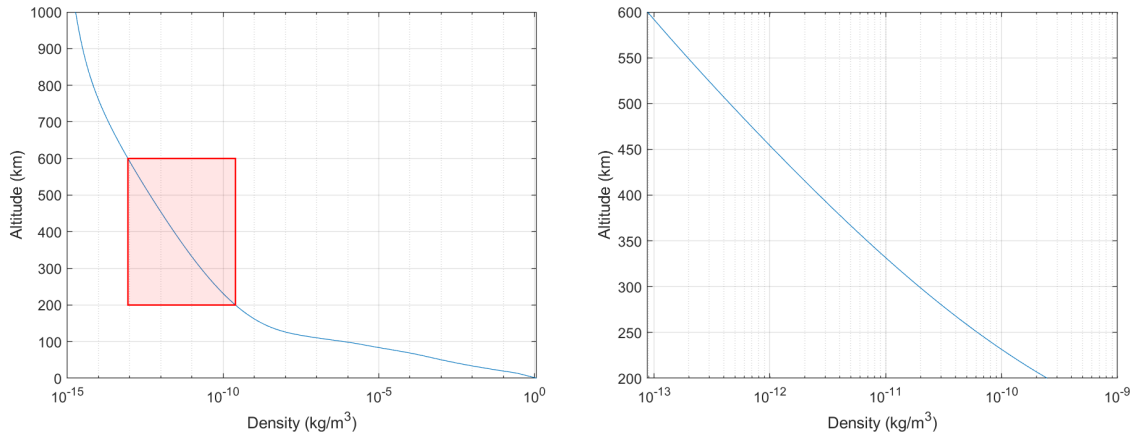

(a) Density vs Altitude from 0 km to 1000 km (b) Density vs Altitude from 200 km to 600 km

Figure 31: Atmospheric density versus altitude at (a) 0-1000 km and (b) low-Earth orbit regime of 200-600 km.

It should be noted that because of variations in density with altitude and across longitudes and latitudes, Atmospheric drag is not constant throughout an orbit. To signify the magnitude of variation, half a Polar orbit is chosen. Figure 32a shows that the most significant differences occur at the South Pole, and increase with altitude. To explore how the variability changes with altitude, Figure 32b depicts three extremes. First, the density at the North Pole (Latitude = 90 degrees) is compared to that at the equator (Latitude = 0 degrees); the maximum difference occurs at approximately 500 km, where the atmosphere is about 16% thinner. Secondly, as the orbital altitude increases, the change in atmospheric density between the South Pole (latitude = -90 degrees) and the equator becomes more pronounced, increasing monotonically with altitude and reaching more than double the density observed at 500 km, and over 150% at 600 km. When comparing the density differences between the North and South Pole, differences of close to 200% are observed at 600 km altitude. In short, the `atmosnrlmsise00` function shall determine the total density at the point of interest during the simulation to account for those effects.

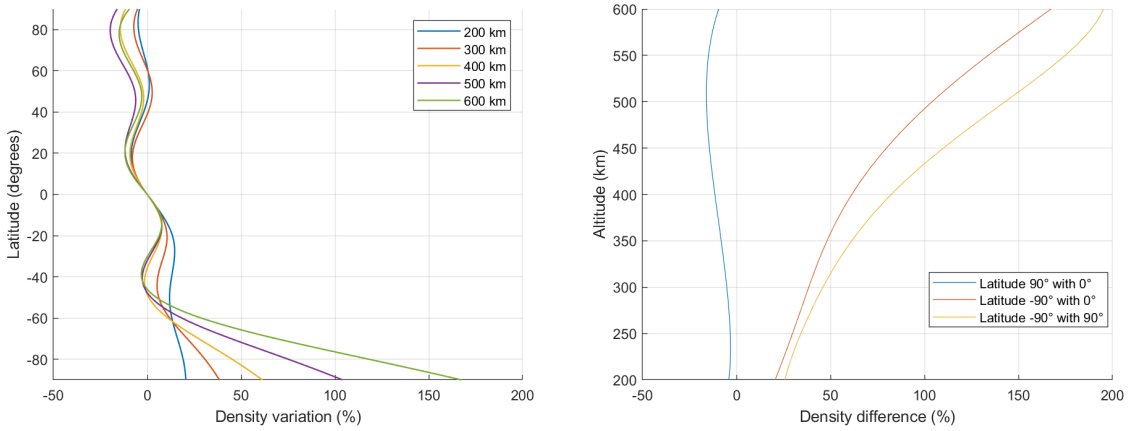

(a) Density vs Latitude for Different Altitudes. (b) Density difference vs Latitude at 400km

Figure 32: Atmospheric Density variations (a) with Latitude for various altitudes and (b). -90 Degrees latitude depicts the South Pole, and +90 degrees the North Pole. The reference value is set at the equator (latitude = 0 degrees).

4.1.2 Dynamic pressure estimation

The dynamic pressure q must be determined to estimate the Atmospheric drag for a satellite flying a circular orbit at an altitude of, for example, 400 km. The orbital velocity varies with altitude and orbit type according to:

$$V^2 = GM\left(\frac{2}{r} - \frac{1}{a}\right) \tag{56}$$

Where V is the orbital velocity of the satellite, G is the gravitational constant $6.67430 \cdot 10^{-11}\text{m}^3\text{s}^2/\text{kg}$, M is the mass of Earth $5.972 \cdot 10^{24}kg$, r is the distance between the centre of Earth and the satellite (or radius of the orbit), and a is the semi-major axis. Inserting all values into Equation 56, and substituting the result into the dynamic pressure equation gives Equation 57.

$$q = \frac{1}{2}\rho \cdot V^2 = \frac{1}{2} \cdot 2.66 \cdot 10^{-12} \cdot 7672.5^2 = 7.82 \cdot 10^{-5}\text{Pa} = 78.2\mu\text{Pa} \tag{57}$$

It should be noted that at the South Pole, the atmosphere would be 61% thicker, and thus the dynamic pressure would become $126.2\mu Pa$; similarly, at the North Pole, 11.5% thinner, thus becoming $69.2\mu Pa$.

4.1.3 C_D estimation

In addition to the dynamic pressure, the drag coefficient times the projected area ($C_D \cdot S$) must also be considered. At altitudes between $120km$ and $400km$, the drag coefficient of a cube is in the range $[2.2-2.4]$ according to [**majid2018Atmospheric**], and changes with angle of attack α. The drag coefficient in hypersonic flow is complex to calculate accurately. However, simplistic estimations for a flat plate exist (see Figure 33) when flying in LEO, and only vary with the incidence angle β, see Figure 33a, or in Atmospheric terms angle of attack α [1]:

$$C_{D_{\text{plate}}} = 2\sin\alpha \tag{58}$$

In the paper [32], various simulations were run. From these simulations, it is shown that a more accurate estimate is about 0.1 larger than Equation 58 suggests. The corrected version that can be used in this thesis is Equation 59.

$$C_{D_{\text{plate}}} = 2\sin\alpha + 0.1 \tag{59}$$

The satellite's bus is box-like, and the two solar panels are flat plates; the effective drag coefficient can be estimated using Equation 60.

$$(C_D \cdot S)_{|_{\text{total}}} = \sum C_{D_i} \cdot S_i = C_{D_{\text{bus}}} \cdot S_{\text{bus}} + C_{D_{\text{s-panel}}} \cdot S_{\text{s-panel}} + ... \tag{60}$$

In terms of Atmospheric drag, the highest drag occurs when the solar panels face 90 degrees to the satellite's velocity vector, and will produce a C_{D_p} of 2.1, and similarly, when $\alpha = 0$, $C_D = 0.1$. A more accurate model, Equation 61, was proposed by J. Storch in an aerospace report titled *Atmospheric Disturbances on satellite in Free-Molecular Flow* [**storch2002Atmospheric**], but requires the determination of accommodation coefficients representing the momentum exchange that occur between the molecules and arresting surfaces, and the ratio of macroscopic velocity V_m to the most probable molecular thermal velocity V_t, which in turn depend on the Knudsen number $Kn = \lambda/L$ where λ is the average mean free path of the molecules and L is the characteristic length of the satellite and the surface temperature T. As Equation 59 captures the overall trend, attains a minimum and a maximum at identical angles and provides a similar output value, this model is chosen for its simplicity. A comparison of the models is found in Figure 45 in *Verification* in 5.1.

$$C_D = 2\left[\sigma_t + \sigma_n \frac{V_w}{V}\sin\beta + (2 - \sigma_n - \sigma_t)\sin^2\beta\right]\sin\beta \tag{61}$$

[1] "*The quantity $S = \frac{v_m}{v_t}$ is the molecular speed ratio, which represents the ratio of the gas macroscopic velocity (v_m) to the most probable molecular thermal velocity (v_t). The molecular speed ratio S characterises the extent to which the flow behaves like a collimated beam of molecules. Particularly, when $S > 5$, the flow is called a hyperthermal flow and is a common situation in the LEO region. In this case, the limiting value of the drag coefficient of the flat plate is* Equation 58". Source: [32]

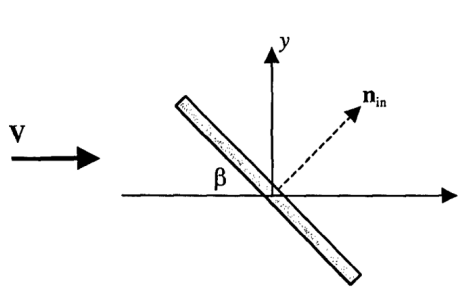

(a) Flat plate placed in free-stream velocity V at an incidence angle β. The lift generated is directed perpendicular to V, and the drag is directed with V.

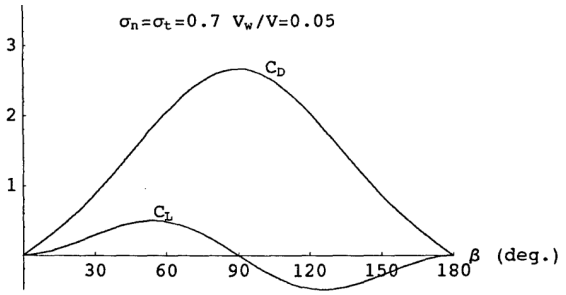

(b) Flat plate C_L and C_D as a function of incidence angle β with accommodation coefficients $\sigma_n = \sigma_t = 0.7$.

Figure 33: The lift C_L and drag C_D coefficients for a flat plate in free molecular flow at hypersonic speeds. Source: [**storch2002Atmospheric**]

To estimate the drag coefficient of the satellite's bus, it is considered to be fixed in space w.r.t. the velocity vector, as the ADCS controlled satellite points at NADIR, thus $C_D \approx 2.2$, see Figure 34 [2].

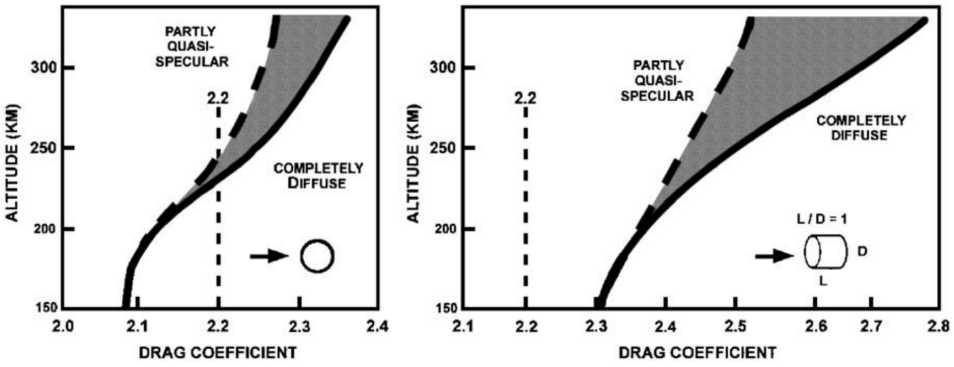

Figure 34: Uncertainties in the drag coefficient caused by quasi-specular reemission. The solid curves represent drag coefficients calculated using Sentman's model, which assumes completely diffuse re-emission. The dashed curves represent Moe's estimated upper bound on the effect of a quasi-specular component of re-emission on the drag coefficient. Source: [58]

The drag force will be modified by changing the projected area relative to the satellite's attitude. For a more comprehensive CD model of the satellite bus, which will be assumed to be shaped like a cube, please refer to C. Reynerson's article titled *Atmospheric Disturbance Force and Torque Estimation for satellite and Simple Shapes Using Finite Plate Elements – Part I: Drag Coefficient* [**author2011Atmospheric**]. Here, the flat-panel model is extended into the third dimension to form a cubical satellite bus. His findings are used for verification, though, in Figure 45 in section 5.1.

4.1.4 Atmospheric centre estimation

The centre of pressure r_{cp} represents the point at which the total Atmospheric force can be applied to produce an equivalent torque on the satellite. For satellites in orbit, free molecular flow must be considered to quantify the cp_{aero}. The approach takes three steps:

1. **Discretising the satellite surface**: Dividing the surface into small elements and calculating the force on each element based on atmospheric density, velocity, and surface accommodation

[2] *"Drag coefficient, CD: It has been a common practice to assume a constant CD equal to 2.2 for low earth orbit flying satellites. Due to the lack of precision of existing atmospheric density models, any modelling effort to refine the drag coefficient was normally considered of little advantage, since it does not compensate for the imprecise density model. Nowadays, it is widely accepted that the drag coefficient is not constant and can vary significantly depending on the satellite's shape and the atmospheric temperature and composition at the flying altitude. Note that atmospheric density models obtained from satellite observations directly incorporate any error on the drag coefficient as density biases"* - [59].

coefficients. The latter quantifies the efficiency with which gas molecules exchange energy and momentum with a surface during collisions [72]. The surface-accommodation coefficients are a function of the incidence angle and type of molecule. There are four primary computational methods for analysing the Atmospherics of a satellite in free molecular flow [59]:

(a) Panel method: A body may be composed of many discrete panels, each of which can be modelled as a flat plate with one side exposed to the flow.

(b) Ray-Tracing Panel Method: improves upon the panel method because it considers the shielding of satellite surfaces from the incident free stream flow by upstream components of the body;

(c) Test-Particle Monte-Carlo: TPMC can be used to model the effects of multiple reflections and different flow conditions;

(d) Direct Simulation Monte-Carlo: The DSMC method directly simulates molecules. Each simulated molecule represents 10^{12}–10^{20} real molecules. Unlike in TPMC, the simulated molecules can collide with one another.

2. **Calculating total force and torque**: Summing the forces and torques from all surface elements about the satellite's centre of mass (CoM).

3. **Solving for** r_{cp}: Determining the position vector r_{cp} from the centre of mass to the centre of pressure using Equation 62:

$$r_{cp} = \frac{\vec{F}_{total} \times \vec{\tau}_{total}}{|\vec{F}_{total}|^2} \tag{62}$$

where $\vec{F}_{total}$ is the total force vector and $\vec{\tau}_{total}$ is the total torque vector.

Given that the goal of the FACAs is to stabilise the S/C for NADIR pointing, the angle of attack, α, and the side-slip angle, β, are assumed to vary little throughout the orbits. For that reason, the shift in centre of pressure, which can be significant for large variations in incidence angles, is assumed to be minimal. The mean value of the centre-of-pressure shift can be modelled as an offset percentage of the satellite bus size relative to the S/C centre of mass. The offset between the centre of mass and the centre of pressure is set to be between 1% and 5% of the satellite bus dimensions. This will make the Atmospheric torque more or less effective, as it ultimately scales the torque values in Equation 54.

4.2 Albedo Pressure

Albedo pressure is the radiation pressure exerted on a satellite by sunlight reflected from Earth. When a satellite is in Earth orbit, it is subjected to radiation pressure. Albedo pressure is a component of radiation pressure and can affect a satellite's dynamics. Unlike radiation pressure from the Sun, which is treated as a point source, albedo pressure from Earth requires the Earth to be modelled as a non-point source, as reflectivity varies across its surface. The Albedo pressure is difficult to simulate because the torque disturbance depends on several factors, including the satellite's surface area, its orientation relative to the Earth and the Earth's reflectivity. The latter is challenging to model, as the consequences of reflected sunlight from Earth hitting the S/C, including effects such as hemisphere differences, atmospheric and surface contributions, seasonal changes, spectral differences, and location in the reflected fluxes, must be taken into account. Since regional changes are the most significant factor, the annually averaged reflected fluxes are presented in Figure 35. As indicated, the most significant averaged flux differences are between the Polar Southern Hemisphere (Polar SH, 60-90 degrees South) and the tropics (Tropics, 30 degrees North-South), amounting to 14.5 W/m^2. In absolute values, the average global total flux is 99.7 W/m^2 or about 7.3% of the Sun's flux. Since the variations across the orbit are much smaller than the Atmospheric variations, and the absolute value is considered small enough, the Albedo pressure will not be modelled to compare the performance of FACAs.

Averaging Scale	Total		Atmosphere		Surface	
	Flux	σ(x)	Flux	σ(x)	Flux	σ(x)
Global	99.7	0.23	86.9	0.29	12.9	0.10
Tropics (30°N–30°S)	94.3	0.32	82.27	0.37	12.1	0.09
Midlatitude NH(30°–60°N)	103.8	0.52	91.5	0.53	12.3	0.15
Midlatitude SH(30°–60°S)	104.1	0.56	98.9	0.65	5.26	0.10
Polar NH (60°–90°N)	97.0	0.87	78.7	0.87	19.1	0.47
Polar SH (60°–90°N)	118.8	0.68	84.4	1.26	35.5	0.97

Figure 35: Annually Averaged Reflected Fluxes Over the Regions Indicated. The top-of-atmosphere reflected flux (W /m2) and the contributions to this flux by scattering from the atmosphere and reflection from the surface are given. The standard deviation of the deseasonalized flux is also given. Source: [92]

4.3 Gravity gradient

Next to the atmospheric torque caused by Atmospheric drag, the gravity-gradient torque is the most important. Gravity gradient torque is a disturbance experienced by a satellite orbiting a planet, such as Earth. It arises from variations in the gravitational force along the satellite's length. Essentially, three aspects play a significant role: the distance from the S/C to the gravitational field 4.3.1, Earth's gravitational perturbations 4.3.2, and the inertia tensor due to mass distribution onboard the satellite 4.3.3. Its implementation for the environmental model in MATLAB is presented in section 5.2.

4.3.1 The distance to the gravitational field

The magnitude of the position vector of the satellite to the Earth's centre $R = |\mathbf{R}|$ can be expressed in terms of the orbital elements according to:

$$R = \frac{a(1-e^2)}{1+\cos(f)} \tag{63}$$

In which a is the semi-major axis, e is the eccentricity, and f is the true anomaly.
The orbital angular velocity is expressed as:

$$\omega_{orbit} = \sqrt{\frac{\mu}{a^3}} \tag{64}$$

where $\mu = 3.986004418(8) \cdot 10^{14}\ m^3 s^{-2}$ is the Earth gravity constant.

The gravitational force scales with $1/R^2$. The further the mass is positioned from the centre of mass of the Earth, the less the gravitational pull is. That phenomenon causes a stronger pull on the Earth-pointing side of the satellite than the space-pointing side. This difference in gravitational force is responsible for the so-called gravity gradient torque $\mathbf{T}_{ggt}$, and is expressed in vector form in body-fixed coordinates:

$$\mathbf{T}_{ggt} = \left[3\omega_{orbit}\frac{(1+e\cos(f))}{(1-e^2)^3}\right]\left(\frac{\mathbf{R}^b}{R}\times\right) I_3 \left(\frac{\mathbf{R}^b}{R}\right) \tag{65}$$

Note that $\mathbf{R}^b$ is the position vector of the satellite to the Earth's centre in body-fixed coordinates. And in case of a circular orbit for which the eccentricity $e = 0$, and substituting for ω_{orbit}, the expression reduces to:

$$\mathbf{T}_{ggt} = \frac{3\mu}{R^5}\mathbf{R} \times I_3\mathbf{R} \tag{66}$$

From this equation, it follows that the closer the orbit is to Earth, the larger the gravity-gradient torque becomes. Thus, in LEO, the $\mathbf{T}_{ggt}$ must be considered.

4.3.2 Earth's gravitational perturbations

The more misshapen the celestial body, and the less uniform its mass distribution, the more involved the calculation of the gravitational moment (and force) It exerts. For an oblate body, like the Earth, a second-order estimate that only includes the J_2 term can be computed using zonal harmonics of degree 2 [80] according to Equation 67 and is also described by [16] in Equation 68. Since the J_2 term ($\approx 1.08262668e-3$) is $O(2)$ larger in its effect than the rest of the gravity perturbing forces, it is good enough for the environmental model described in section 5.2. In other words, the higher-order terms are neglected as they become smaller and smaller: the J3-term, for example, is at least two orders of magnitude smaller than the J2-term [80].

$$\begin{aligned} T_{gg} = 3\mu \frac{\bar{u_r} \times I\bar{u_r}}{|r|^3} + \frac{\mu J_2 R_p^2}{2|r|^5} [30\bar{u_r}\bar{u_n}\left(\bar{u_n} \times I\bar{u_r} + \bar{u_r} \times I\bar{u_n}\right) \\ + (15 - 105(\bar{u_r}\bar{u_n})^2)\bar{u_r} \times I\bar{u_r} - 6\bar{u_n} \times I\bar{u_n}] \end{aligned} \tag{67}$$

Herein, T_{gg} is the total gravity gradient torque, μ the Earth's gravitational parameter ($\mu \approx 3.986 \cdot 10^{14} m^3/s^2$), J_2 the second zonal harmonic coefficient, accounting for the Earth's equatorial bulge due to its non-uniform shape, R_p the mean radius of the Earth ($R_p \approx 6,371 \times 10^6 m$), $|r|$ the distance from the centre of the Earth to the satellite, and $\bar{u_r}$ and $\bar{u_n}$ unit vectors that represents the vector pointing from the satellite centre of mass to the centre of the planet and along the rotation axis of the Earth respectively.

$$\begin{aligned} T_{gg} = \left(\frac{3\mu}{\rho^5}\right)(r \times (I \cdot r)) + \mu J_2 \left(-\frac{3}{\rho^5}(z \times (I \cdot z))\right. \\ + \frac{15(r \cdot z)}{\rho^7}(z \times (I \cdot r) + r \times (I \cdot z)) \\ \left. + \frac{15}{2}\left(\frac{1}{\rho^7} - \frac{7(r \cdot z)^2}{\rho^9}\right)(r \times (I \cdot r))\right) \end{aligned} \tag{68}$$

4.3.3 Inertia tensor due to mass distribution onboard the satellite

In section 6.1.3, the satellite (static) inertia tensor is computed according to Equation 115. It should be noted that because the inertia tensor I might contain off-diagonal terms, due to asymmetries, instabilities in attitude motion may occur due to cross-products being present. Also, since most satellites are not point-symmetric, the diagonal terms (e.g. I_{xx}, I_{yy}, I_{zz}) have unequal values. This means that the satellite tends to have a preferred spin direction: a major-axis spinner occurs when $I_{yy} > I_{xx} > I_{zz}$, for minor-axis $I_{xx} > I_{zz} > I_{yy}$, and an intermediate-axis spinner for other inequalities. For both the major-and minor-axis spinners, the satellite spin is stable. For an intermediate-axis spinner, the motion is unstable [69].

4.4 Outgassing

Polymeric composites are often used as the material of choice for satellite design due to their high specific strength and stiffness. These composites are prone to outgassing in the harsh space environment, releasing gaseous species [71].

Miller and Weeks [56] presented a model based on the kinetic theory of gases to characterise the thrust acceleration resulting from satellite outgassing, see Equation 69:

$$F_{outgassing} = \sqrt{\frac{3RT}{M}}\sqrt{\frac{8}{3\pi}}\frac{dm}{dt} \tag{69}$$

Where R is the gas constant, T is the absolute temperature, M is the molecular weight, and $\frac{dm}{dt}$ is the change in mass over time. Their analysis demonstrates that the random expansion of vented gas molecules, even at relatively low temperatures, generates a non-negligible thrust force that can perturb the satellite's trajectory, similar to the operation of rockets, with a specific impulse I_{sp} in a gravitational field with acceleration g_0, see Equation 70:

$$F_{rocket} = g_0 I_{sp}\frac{dm}{dt} \tag{70}$$

This force, although less efficient than rocket propulsion, is significant enough to introduce errors in initial orbit determination and warrants consideration, particularly in the early stages of a mission when volatile elements are still evaporating. These effects can be considered irrelevant once most of the outgassing has occurred and the detumbling sequence has finished, leaving the satellite in a steady-state condition.

4.5 Planetary Radiation Pressure

Planetary radiation pressure (PRP) is the pressure exerted by a planet's thermal emissions, primarily from Earth for satellites in LEO. To determine the value of the PRP, the Stefan-Boltzmann law, expressed in Equation 71, can be used to determine the total emissive power I of the Earth in W/m^2, assuming that on average it can be treated as a blackbody (indicated with subscript bb).

$$I_{bb} = \sigma T^4 \tag{71}$$

where σ is the Stefan-Boltzmann constant ($5.67 \cdot 10^{-8} W/m^2K^4$), the effective temperature of the Earth T is around 255 K. Inserting these values into Equation 71, and substituting in Equation 79 yield:

$$P = \frac{I_{bb}}{c} = \frac{\sigma T^4}{c} \quad \rightarrow \quad P = \frac{5.67 \cdot 10^{-8} \cdot 255^4}{c} = \frac{239.7}{299792458} = 8.03 \cdot 10^{-7}\text{Pa} \approx 0.8\mu\text{Pa} \tag{72}$$

This estimate indicates that Earth's radiation pressure is approximately 18% of the Sun's. Its effects are noticeable when interested in accurately predicting the orbit and the satellite's attitude, but can be neglected when comparing the performance of FACAs.

4.6 Residual Dipole

As the S/C orbits Earth, it moves through a varying magnetic field (due to the field's spatial gradients and the satellite's changing orientation). This interaction causes a torque that tries to align the satellite's dipole, as described in section 4.6.1, with the local magnetic field, as discussed in section 4.6.2, perturbing its attitude. This attitude perturbation works periodically and is described in section **??** in terms of precession and nutation. Its implementation for the environmental model in MATLAB is presented in section 5.3.

The direction and magnitude of the torque change as the satellite's position and orientation vary relative to the magnetic field. It should be noted that this interaction also enables the utilisation of the Earth's magnetic field to control the satellite's attitude, for example, by running an electric current through an onboard coil to create torque intentionally (the working principle of magnetorquers).

The residual dipole arises from a slight misalignment between the satellite's centre of mass and its magnetic centre. Magnetic imbalances or onboard electronics often cause this misalignment. The misalignment should be determined through computer-aided design modelling or by physical measurements. It is also possible that the satellite's magnetic moment is unintentionally induced by any current-carrying devices on board. This can be due to the payload or to eddy currents in the metal structure. In this case, the magnetic dipole moment is not constant.

4.6.1 Residual dipole moment

This residual dipole torque T_{RD} is a function of the residual dipole's strength $\mathbf{m}$, the intensity of the external magnetic field $\mathbf{B}$ (in LEO about $22 - 65\ \mu T$ [14]), and the angle between these two vectors as presented in Equation 73. It's magnitude is $T = mB\sin(\theta)$, where θ is the angle between $\mathbf{m}$ and $\mathbf{B}$.

$$\mathbf{T_{RD}} = \mathbf{m} \times \mathbf{B} \tag{73}$$

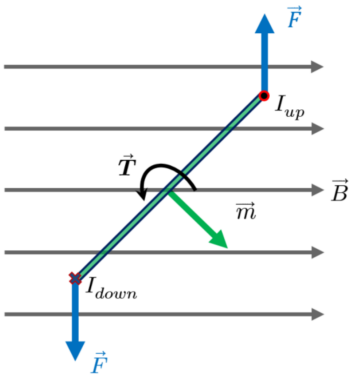

Figure 36: Illustration of the magnetic torque on a current loop. Source: [43]

For a fixed residual dipole **m**, the torque oscillates as the angle θ between **m** and **B** changes. This results in a periodic disturbance that repeats each orbit, with no net accumulation of angular momentum over one orbit if the satellite's attitude remains relatively stable and the magnetic field is symmetric over the orbit. If the ADCS does not counteract the torque, or if the dipole moment changes (e.g., due to varying electrical currents), the torque can cause a gradual drift in attitude over multiple orbits. This drift is cumulative because the torque may consistently bias the satellite's orientation in a particular direction, depending on the orbit and the magnetic field. For example, in polar orbits, where the magnetic field varies significantly, the torque may cause a non-reversing attitude error if left uncorrected.

For small-sized satellites, the residual dipole moment m is assumed to be in the range of $0 - 0.2\ [A \cdot m^2]$ because magnetic shielding is considered not to be present. This will be used for the implementation of Equation 73 in section 5.3. To justify its implementation, a reference is computed using Equation 74: the maximum magnitude of the residual dipole torque is calculated at 400 km.

$$|T_{RD_{\max}}| = mB\sin(\theta) = 0.2 \cdot 65 \cdot \sin(\pi/2) = 13\mu Nm \tag{74}$$

Such a magnitude is comparable to the solar radiation pressure torque and is therefore relevant to consider in the simulation.

4.6.2 Earth's magnetic field

The geomagnetic field can be modelled as a dipole in the form of Equation 75 presented by [78].

$$\mathbf{B} = \frac{\mu_B}{R^5}\left[R^2\mathbf{e}_B - 3(\mathbf{e}_B \cdot \mathbf{R})\mathbf{R}\right] \tag{75}$$

where $\mu_B = 8.1 \cdot 10^{25}\ gauss - cm^3$ is the magnetic moment when the magnetic field of the Earth, R is the magnitude of the position vector of the satellite to the Earth's centre and can be found with Equation 63, $\mathbf{e}_B$ is a unit vector directed towards the geomagnetic dipole axis (inclined 11.5 degrees from the geophysical polar axis), and **R** is the satellite position vector. Although neither the geomagnetic field nor the satellite magnetic moment can be determined precisely in general, one can model both as dipoles, and this approach will likely be sufficiently accurate [94]. The geomagnetic torque in body-fixed coordinates can be expressed as:

$$\mathbf{T}_{gm} = [\mathbf{V}_{mm}\times]\, C_{ib}\frac{\mu_B}{R^5}\left[R^2\mathbf{e}_B^i - 3(\mathbf{e}_B^i \cdot \mathbf{R}^i)\mathbf{R}^i\right] \tag{76}$$

Where C_{ib} is expressed as a function of three periodic matrices with period T_w by Floquet theory [15], and the $'i'$ denotes perigee coordinated. For further investigation of the geomagnetic torque refer to equation 3.4.16 in [94] by Y. Tao and R. Ramnath.

4.7 Radio Frequency

The operational principle of radio-frequency (RF) torque is that any electromagnetic transmission will produce a force and a torque, and is given by Equation 77.

$$T_{RF} = -\frac{p}{c} r \times u \tag{77}$$

Herein, p is the transmitted power, c is the speed of light, r is the vector to the antenna axis of maximum radiated power from the satellite centre-of-mass, and u is in the direction opposite to that.

For a smaller satellite, the RF torques can be considered negligible, as given by the following example: Assume that a 50 kg satellite can downlink with a power of about 20 Watts for 10 minutes [3]. For a smaller-sized satellite, the mean density is typically higher than for larger ones. Considering a mean density of 400 kg/m^3, such S/C could be sized about $0.125m^3$ or $50 \times 50 \times 50$ cm^3. Assuming the antenna is positioned outboard of the S/C, Equation 78 shows that the RF torque could be as large as $0.1\mu Nm$.

$$T_{RF} = -\frac{20}{299792458} \begin{bmatrix} 0.5 \\ 0.5 \\ 1 \end{bmatrix} \times \begin{bmatrix} 0.5 \\ 0.5 \\ -1 \end{bmatrix} = \begin{bmatrix} 0.0667 \\ -0.0667 \\ 0 \end{bmatrix} \mu Nm \quad \rightarrow \quad ||T_{RF}|| = 0.094 \approx 0.1\mu Nm \tag{78}$$

In comparison, the estimated solar radiation pressure torque for a similarly sized satellite, assuming a centre of pressure offset of 5% from the centre of mass, is about 4.5 μNm. This indicates a relative magnitude of nearly a factor of 50, rendering the RF torque negligible. When considering larger high-power (communication) satellites, radio-frequency (RF) torques can become relevant, mainly if they transmit power continuously, leading to torque accumulation.

4.8 Solar Radiation Pressure

Solar Radiation Pressure (SRP) is caused by the momentum transfer of photons from the Sun. The intensity of solar radiation decreases with distance from the Sun; however, at LEO, radiation pressure is significant because the satellite is at 1 AU from the Sun and receives a substantial amount of light. Solar radiation pressure varies with the satellite's orientation and reflective properties; see section 4.8.1. To determine an estimate of the SRP, Equation 79 can be used, wherein P is the radiation pressure (Pa), I is the solar irradiance, which at 1 AU is about 1368 W/m^2, and c is the speed of light in a vacuum ($3 \cdot 10^8$ m/s).

$$P = \frac{I}{c} \quad \rightarrow \quad P = \frac{1368}{299792458} = 4.56 \cdot 10^{-6}\text{Pa} \approx 5\mu\text{Pa} \tag{79}$$

The magnitude of the disturbance torque generated by SRP is dependent on the moment arm. To determine the moment arm, the distance between the centre of mass and the centre of pressure, the centre of pressure location must be determined, and is discussed in 4.8.2. A reference value estimation is made to determine the relevance of the SRP torque in section 4.8.3. Its implementation for the environmental model in MATLAB is presented in section 5.4.

4.8.1 Reflectivity properties

The disturbance torque caused by SRP depends on the reflectivity of the satellite's surfaces. When incident radiation hits the satellite, (part of) the radiation is absorbed, reflected specularly, and/or reflected diffusely, see Figure 37.

[3] "*A small satellite with 50 kg, however, can generate only as small as a power of 100 W as total. A high-data-rate communication system could allocate approximately 20 W for a 10-minute communication pass. This is a power constraint for a high-data-rate communication system for small satellites.*" - [81]

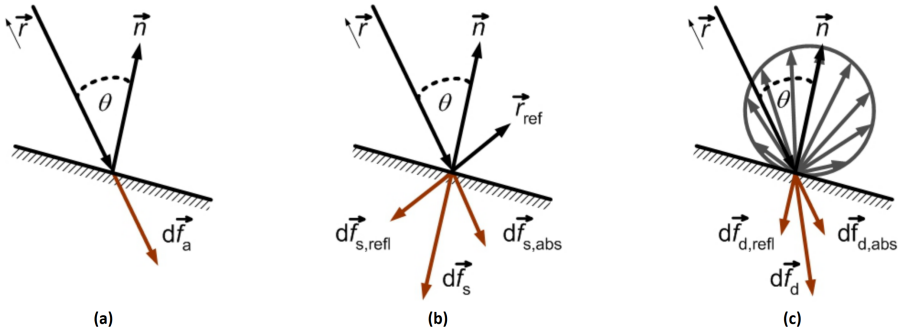

Figure 37: Recoil force components for (a) absorption, (b) specular reflection and (c) diffuse reflection. Source: Rivers *et al.* [79]

The solar pressure caused by absorption P_{absorb} that acts normal to the Sun is given by the momentum flux of light P $[N/m^2]$, which is equal to the power flux density Ψ $[W/m^2]$ over the speed of light c $[m/s]$. Assuming that only the Sun's irradiance gives rise to the power flux density ($\Psi = I$), then P_{absorb} is expressed as:

$$P_{absorb} = \frac{\Psi}{c} = \frac{I}{c} = P \tag{80}$$

The power flux density of solar radiation incident upon a horizontal surface at the top of the Earth's atmosphere at zero zenith angle is 1368 W/m^2 [26]. The fraction of radiation that is fully absorbed causes a force df_a according to Equation 81 following (a) in Figure 37:

$$df_a = -\gamma_a \cos(\theta) \mathbf{e}_S \frac{I}{c} dA \tag{81}$$

In which γ_a is the absorption coefficient, θ the angle of incidence, and $\mathbf{e}_S$ is the unit vector pointing from the satellite to the Sun.

The second contribution is due to specular reflection as depicted in (b) in Figure 37. That solar pressure P_{spec} acting on a surface normal to the sun is expressed as:

$$P_{spec} = \frac{2\Psi}{c} = 2P \tag{82}$$

This poses a radiation force which is due to the part of the radiation that is reflected specularly df_s according to:

$$df_s = -2\gamma_s \cos^2(\theta) \mathbf{e}_n \frac{I}{c} dA \tag{83}$$

Herein, γ_s is the optical coefficient of specular reflectivity, and $\mathbf{e}_n$ is the normal unit vector of the small surface area dA.

Lastly, the radiation force due to the radiation that is reflected diffusely is dependent on the distribution of the radiation over all directions. It is depicted in (c) in Figure 37. It is found by integration over all angles. When applying Lambert's cosine law [73], the diffuse portion of the radiation force is presented by:

$$df_d = -\gamma_d \cos(\theta) \left(\mathbf{e}_S + \frac{2}{3} \mathbf{e}_n \right) \frac{I}{c} dA \tag{84}$$

Where γ_d is the optical coefficient of diffuse reflectivity.

When assuming that the satellite has zero radiation emittance and that the Sun is the only light source, the SRP force can be determined. The sum of the radiation coefficients equals one ($\gamma_a + \gamma_s + \gamma_d = 1$). Now, the resulting total solar radiation pressure force is solely dependent on the orientation of the receiving surface and its optical properties. The sum of three components ($df_{srp} = df_a + df_s + df_d$) give the force per area. Hence, grouping equations 81, 83, 84 and expressing the reflectivity condition as $\gamma_a + \gamma_d = (1 - \gamma_s)$ gives Equation 85.

$$df_{srp} = -\frac{I}{c} \left[(1 - \gamma_s) \mathbf{e}_S + 2(\gamma_s \cos(\theta) + \frac{1}{3} \gamma_d) \mathbf{e}_n \right] \cos(\theta) dA \tag{85}$$

In this equation, the term $-\frac{I}{c}$ represents the negative pressure P exerted by all radiation. This equation encapsulates the interactions between the solar radiation and the satellite's surfaces. Summing over all lighted surfaces gives the total solar radiation pressure force F_{srp}:

$$F_{srp} = \sum_{i=1}^{n} df_{srp} \tag{86}$$

Now, the resulting torque due to solar radiation pressure T_{srp} is found by multiplying the force by the moment arm per Equation 87.

$$\mathbf{T}_{srp} = (\mathbf{r}_{cp} - \mathbf{r}_{cg}) \times \mathbf{F}_{srp} \tag{87}$$

4.8.2 Centre of pressure

When the reflecting properties of a surface element are assumed to be homogeneous, the centre of pressure, *cp*, coincides with the geometric centre of that surface element [101]. However, the combined solar radiation pressure acting on a satellite's various surfaces determines its centre of pressure. Non-uniform illumination conditions can lead to unequal forces on these surfaces, resulting in a shift in the overall *cp* location.
Solar radiation pressure is relevant because the solar panels are at a large offset from the centre of mass, compared to the satellite's bus. That means that slight changes in illumination conditions have a relatively large impact on $\mathbf{r}_{cp}$, thereby impacting the T_{srp}. At the same time, precise determination of the centre of pressure location requires detailed CAD modelling and on-orbit estimation [47]. For this analysis, a cp-offset in the range of $5 - 10\%$ of the satellite's centre of mass is expected, because of the asymmetry arising from changing illumination conditions.

4.8.3 Reference value estimate

For the reference satellite of 50 kg S/C, sized $50 \times 50 \times 50\ cm^3$ flying in a polar orbit at 400km altitude with a 5% offset in centre of pressure from the centre of mass, with deployable solar arrays, the maximum torque is approximately 4.472 μNm. This estimate is the result of taking a coefficient of absorptivity $\gamma_a = 0.37$, a specular reflection $\gamma_s = 0.53$, and a diffuse reflection $\gamma_d = 0.1$, and substituting in Equation 85. The resultant torque is computed by Equation 87.

4.9 Thermal Pressure

Thermal pressure, or thermal radiation pressure, from radiators on small satellites is caused by the radiation of infrared energy as the satellite dissipates excess heat. This can generate pressure on the radiating surfaces onboard the satellite, similar to planetary radiation pressure, but instead of reflections, due to irradiation from a heat source with absolute temperature T_{rad} and its emissivity e (where $e = 1$ for an ideal radiator). When the radiative surfaces are placed or loaded asymmetrically, a torque about the centre of mass is generated, see section 4.9.1. An estimation of the satellite's heat flux is given in section 4.9.2.

4.9.1 Thermal radiation pressure torque

An estimate of the radiation pressure $P_{tr} = F/A\ [N/m^2]$ can be determined through the following. First, the thermal irradiance I_r must be determined using Equation 88.

$$I_r = \sigma e T^4 \tag{88}$$

The thermal irradiance $[W/m^2]$ can be converted to radiation power $\dot{Q}\ [W]$ by multiplying both sides with the radiation area A:

$$\dot{Q} = \sigma e A T^4 \tag{89}$$

The emitted thermal radiation is distributed directionally, as shown in Figure 38. The heat distribution is proportional to the angle ϕ from the normal. This is known as Lambertian radiation. To account for the emittance close to the normal being larger than that off-axis, a scaling factor C_F is used and is named the force coefficient.

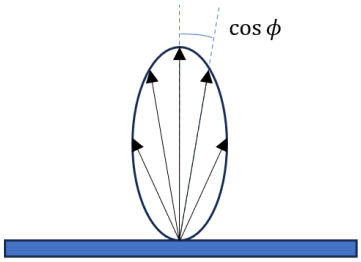

Figure 38: Diffuse emission of a Lambertian surface

To derive the force coefficient C_F, the integral of the angular distribution of force contributions is compared with that of a simpler isotropic distribution in Equation 90, following Lambert's cosine law:

$$C_F = \frac{\int_0^{2\pi}\int_0^{\frac{\pi}{2}} \cos^2\phi \sin\phi \, d\phi \, d\theta}{\int_0^{2\pi}\int_0^{\frac{\pi}{2}} \cos\phi \sin\phi \, d\phi \, d\theta} = \frac{\int_0^{\frac{\pi}{2}} \cos^2\phi \sin\phi \, d\phi}{\int_0^{\frac{\pi}{2}} \cos\phi \sin\phi \, d\phi} = \frac{\int_0^{\frac{\pi}{2}} \cos^2\phi \sin\phi \, d\phi}{(\frac{1}{4})} = \frac{(\frac{1}{3})}{(\frac{1}{4})} = \frac{4}{3} \tag{90}$$

This value indicates that the effective radiative force, influenced by the directional distribution of the emitted radiation, is approximately 4/3 greater than what would be assumed from an isotropic perspective.
The thermal radiation force F_{TR} can be determined with Equation 91.

$$F_{TR} = C_F \cdot \frac{\dot{Q}}{c} = \frac{4}{3} \cdot \frac{\dot{Q}}{c} \tag{91}$$

The radiation pressure is determined by dividing the radiation force F by the radiation area A.

$$P_{tr} = \frac{F_{TR}}{A} = \frac{4}{3} \cdot \frac{\dot{Q}}{A \cdot c} \tag{92}$$

Similar to the solar radiation pressure, the thermal pressure torque $\mathbf{T}_{tr}$ can be calculated according to Equation 93 in which $\mathbf{F}_{tr} = F_{TR} \cdot \mathbf{e}_{rad}$.

$$\mathbf{T}_{tr} = (\mathbf{r}_{cp} - \mathbf{r}_{cg}) \times \mathbf{F}_{tr} = F_{TR} \cdot (\mathbf{r}_{cp} - \mathbf{r}_{cg}) \times \mathbf{e}_{rad} \tag{93}$$

If the normal vector $\mathbf{e}_{rad}$, which is located at the centre of pressure of the radiator, crosses through the centre of mass of the satellite, the resultant torque $\mathbf{T}_{tr}$ generated reduces to zero. If that is the case, the thermal pressure torque can be neglected. For an asymmetric design, the satellite heat flux must be considered.

4.9.2 Estimation of satellite's heat flux

The thermal performance of the satellite can be estimated by setting up a heat equilibrium in a steady state. The first step is to select a closed control volume and apply conservation of energy (first law of thermodynamics ($\Delta U = Q - W$): the change in internal energy ΔU $[J]$ is equal to the heat Q $[J]$ minus the work done W $[J]$. The latter is zero for the satellite because no work is done. Thus, the stored heat Q_{stored} $[J]$ can be determined with the energy balance in Equation 94.

$$Q_{stored} = mC_p \frac{dT}{dt} = Q_{in} - Q_{out} + Q_{generated} \tag{94}$$

The stored heat takes the form of heating or cooling a mass over time. It includes thermal mass m $[kg]$, the specific heat capacity C_p $[J/kgK]$, and the time rate of change in temperature dT/dt. The heat in Q_{in} entering the control volume (denoted with subscript $_{CV}$) can take the form of conduction, radiation (see Equation 89), and convection. Conduction ($= \kappa A \Delta T/l$) consists of the thermal conductivity of the material κ, the cross-sectional area of the object A, the temperature difference from one side to the other ΔT, and the distance over which the heat is transferred l. Note that convection is left out because the satellite's heat transfer through a gas is negligible (the atmosphere is very thin at flying altitudes, see Figure 31a). The thermal equilibrium in steady state (whereby $dT/dt = 0$) is shown in Equation 95.

$$mC_p\frac{dT}{dt} = \frac{\kappa A}{l}\left(T_{ext} - T_{CV}\right) - \sigma Ae\left(T_{CV}^4 - T_{space}^4\right) + Q_{generated} = 0 \tag{95}$$

When applying Equation 95 to the control volume depicted in Figure 39, an estimation of the heat balance $Q_{in} = Q_{out}$ can be made, see Equation 96.

$$A_{P_{solar}}Q_{solar}\alpha_{rad} + A_{P_{Earth}}Q_{albedo}\alpha_{rad} + A_{P_{Earth}}Q_{Earth}\alpha_{rad} + Q_{gen} = \sigma A_{rad}e(T_{rad}^4 - T_{space}^4) \tag{96}$$

Herein, the following assumptions are applied:

- The satellite is in steady-state thermal equilibrium.
- $A_{P_{solar}}$ is the projected area normal to the Sun pointing vector.
- $A_{P_{Earth}}$ is the projected area normal to the Earth pointing vector.
- The Sun radiates uniformly such that the Solar irradiance $Q_{solar} = 1368$ W is uniform.
- The Earth's blackbody radiation temperature does not vary throughout the orbit and amounts to 255 K, thus radiating $Q_{Earth} = 239\ W/m^2$ into space [4].
- The average global total albedo flux is 99.7 W/m^2 (see Figure 35), and is assumed constant across the orbit for the thermal analyses.
- The solar panels are in thermal equilibrium, meaning they are thermally isolated from the satellite's bus.
- The satellite's bus receives the electrical power needed to power the electronics within the bus.
- The spectral properties for a white paint used in satellite, according to '*table 4.2 White & Color Coatings*' in [**kauder2005satellite**], at a wide range of operating temperatures $(60 - 300K)$ have a wide range in absorptivity and hemispherical emittance. For this analysis, values of $\alpha = 0.3$ and $\varepsilon = 0.9$ are used, respectively.

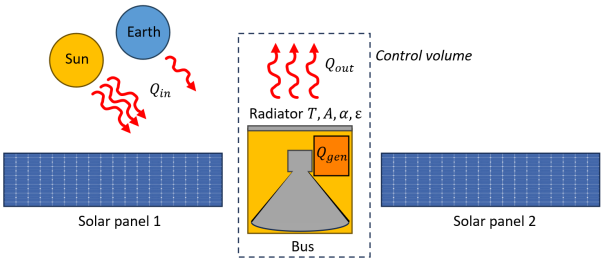

Figure 39: Satellite thermal equilibrium of the control volume considered.

The generated heat Q_{gen} ultimately stems from the conversion of electrical power to heat, which is, in turn, collected from the satellite's electrical systems and conducted to the radiating surfaces. Thus, a satellite that runs on solar energy has at most the capacity to dispense as much energy in heat as it receives power throughout an orbit. Of course, if energy can be stored, it can be released later, resulting in a larger Q_{gen}. However, by assuming a steady state, this possibility is ignored.
With state-of-the-art solar panels, solar panel efficiency of about $\eta_{sp} = 39\%$ is possible with four or more junction technologies [103]. This means that the maximum heat $Q_{gen_{max}}$ [W] occurs when the solar panels' normal are perpendicular to the Sun's pointing vector. Otherwise, the value must be multiplied by $\cos\theta$, whereby θ is the angle between the Sun pointing vector and the solar panel normal.

$$Q_{gen} = \eta_{sp}Q_{solar}\cos(\theta)\cdot A_{solar} = 533.5\cos(\theta)\cdot W_pL_p \tag{97}$$

The required power can range from 10 to 400 watts and is dependent on the satellite design. Since the satellite points at NADIR, $A_{P_{Earth}} \approx A_{rad}$.

$$Q_{gen_{max}} = 533.5 \cdot A_{solar} \quad \left(Q_{gen_{max}} \epsilon \{10, 11, ..., 400\} \text{Watts}\right) \tag{98}$$

Recalling Equation 96 and substituting the given values gives:

$$A_{P_{solar}} \cdot 1368 \cdot 0.3 + A_{rad} \cdot 99.7 \cdot 0.3 + A_{rad} \cdot 239 \cdot 0.3 + 533.5 \cdot A_{solar} = A_{rad} Q_{rad} \tag{99}$$

Thus, for one cubic meter cubic-shaped satellite, the maximum heat flux $Q_{rad_{max}}$ occurs when all electronics convert all received solar radiation into heat, at a Sun incidence angle of $45 - 45 - 45$ degrees resulting in $A_{P_{solar}} = \sqrt{3} A_{rad}$; the minimum $Q_{rad_{min}}$ when the satellite is in idle, and eclipsed:

$$Q_{rad_{max}} = 410.4\sqrt{3} + 29.9 + 71.7 + 400 = 912 \,\text{Watt} \quad Q_{rad_{min}} = 29.9 + 71.7 = 101.6 \,\text{Watt} \tag{100}$$

Next, the satellite dispenses heat in all directions, with some heat spots present, unless radiators are used. Now, thermal pressure only poses a problem when irradiated non-uniformly; it's noticeable only as a net effect. For that, the torque experience due to thermal pressure is calculated using Equation 101.

$$T_{tp} = A \cdot r_{cp} \times P \tag{101}$$

To reduce the complexity, the satellite of interest is chosen to irradiate homogeneously and omnidirectionally, meaning that the net effect of the thermal pressure is zero.

5 Environmental model

This chapter answers the research question:

(A.3) *What are the quantitative models for the dominant external disturbance torques acting on a satellite in LEO, and how can a modular simulation be developed and verified to generate these torques?* The satellite is subjected to various disturbances, as specified in chapter 4. The four dominant external disturbances have been identified: Atmospheric, gravity gradient, residual dipole, and solar radiation pressure, and were discussed in sections 4.1,4.3, 4.6, and 4.8 respectively. The subsequent sections (5.1-5.4) detail the implementation of the governing equations in MATLAB functions to achieve modularity.

The numerical values for attachment points for the disturbances discussed in the subsequent sections are elicited in appendix A.2.

5.1 Atmospheric torque implementation

The Atmospheric disturbance torque (ADT), see Equation 54, is calculated using the `calculateAtmosphericTorque` function. This function takes the current date, altitude, latitude, longitude, satellite velocity vector (`v_eci`), angle of attack (`alpha`), and a transformation matrix (`FB`) as inputs. The resulting torque vector $\vec{\tau_A}$ is returned as the output and is expressed in the body reference frame.

The assumptions made to model the ADT are listed in section 5.1.1. Next, the modelling (section 5.1.2) describes how the relevant equations are implemented. The verification of the ADT is carried out in section 5.1.3.

5.1.1 Assumptions

The following assumptions are made to compute the ADT:

1. The centre of pressure is constant and defined in the `config()` function.
2. The atmospheric density is calculated using a standard model `atmosnrlmsise00` [52], which may have limitations in accuracy, especially during periods of high solar activity.
3. The drag coefficients are based on simplified models (see C_D *estimation* in 4.1) and may not fully capture the complex aerodynamic interactions.

5.1.2 Modelling

First, the Atmospheric Density ρ is calculated using the `atmosnrlmsise00` function from the Aerospace Toolbox. This function models the Earth's atmosphere and provides density estimates based on location, time, and solar activity, as is illustrated in Figures 30, 31, and 32.

Secondly, the projected surface area relative to the free stream velocity (`v_eci`) is determined (for visualisation, see Figure 46): the satellite's geometry is defined in the `config()` function, providing surface normals (`normals`) and areas (`areas`) for the bus and solar panels, see Figure 40a.

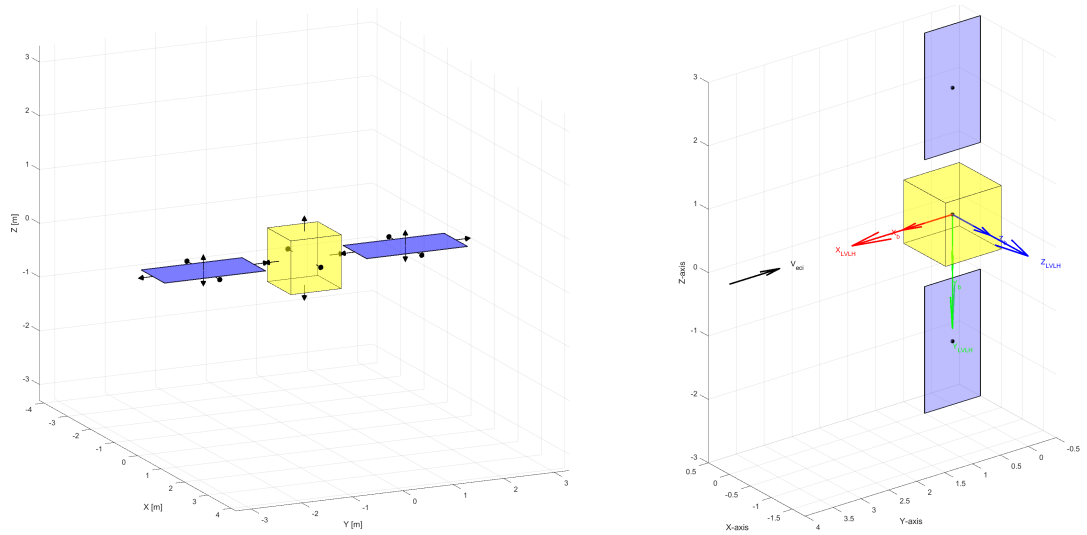

(a) Satellite normals and geometry

(b) Satellite geometry relative to V_{eci}

Figure 40: Visualisation of (a) the normals to the satellite's geometry and (b) the satellite geometry relative to the incoming velocity vector.

The projected area (`S`) is computed by summing the projected areas of the faces that are exposed to the incoming flow (i.e., the dot product of the surface normal and the velocity vector is positive). Suppose the satellite can rotate its solar panels relative to the satellite's bus. Then the angle of attack α_p is altered due to the rotation of the solar panels' normals using a rotation matrix (`R_y`) over angle (`alpha`). This allows for accounting for changes in the projected area as the satellite's solar panels rotate to keep better alignment with the Sun, if desired. By default, the solar panel rotation is set to zero degrees. Now, the solar panel incidence angle, or angle of attack, is $\alpha_p = \alpha_b + \alpha$, whereby α_b is the angle of incidence due to the satellite's attitude and α is the angle of rotation of the solar panels, as illustrated in Figure 41.

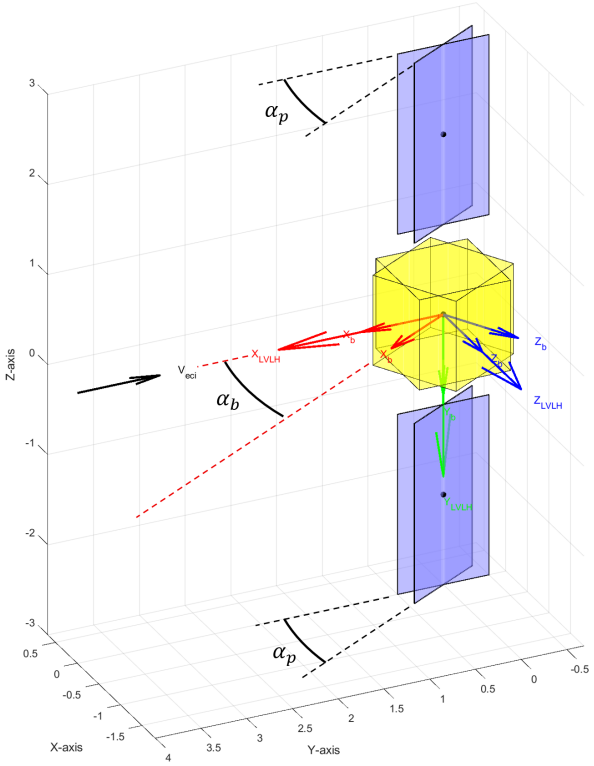

Figure 41: The incidence angles of the satellite's bus α_s and solar panels α_p

Thirdly, the function defines drag coefficients for the bus (C_{D_b}) and the panels (C_{D_p}), using a simplified model, Equation 59, where the solar panel drag coefficient depends on the angle of attack, see C_D *estimation* in section 4.1. The overall drag coefficient (C_D) is then computed as a weighted average of the individual coefficients, based on the projected areas (for the satellite's bus S_b, and the solar panels S_{p1} and S_{p2}) as per Equation 102:

$$C_D = \frac{C_{D_b} S_b + C_{D_p}(S_{p1} + S_{p2})}{S} \tag{102}$$

Fourthly, the magnitude of the Atmospheric force (F_A) is calculated using the standard drag equation $F_A = C_D \frac{1}{2} \rho V^2 S$, where V is the magnitude of the satellite's velocity. The direction of the force is opposite to the velocity vector ($e_{V_{dir}}$).

Finally, the Atmospheric torque T_A is calculated as the cross product between the vector from the centre of gravity (r_{cg}) to the Atmospheric centre of pressure (r_{cp}) which are both defined in `config()`, and the force vector (F_A), according to Equation 103.

$$T_A = (\vec{r_{cg}} - \vec{r_{cp}}) \times \vec{F_A} \tag{103}$$

An example of the centre of pressure location placement is illustrated in Figure 42.

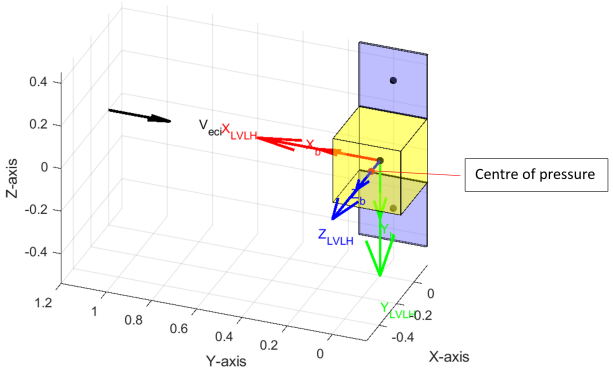

Figure 42: Atmospheric centre of pressure location r_{cp} indicated by the red dot. Here, r_{cp} is scaled by a factor of 10 for visualisation.

For coverage of the entire Earth at an altitude of 300 km, the simulation should run for at least 16 polar orbits ($\frac{\text{seconds per day}}{\text{orbital period}} = \frac{24h \cdot 60m \cdot 60s[s]}{5431[s]} = 15.9$). As discussed in section 4.1, due to the variations in atmospheric density, the torque component fluctuates with time. For the small satellite presented in Figure 42, the body axis torques attain the values shown in Figure 43. It should be noted that the noise in the X-axis is due to machine error in the axis transformation (from ECI to body). The Z-axis does not have this issue because, in this simulation, the centre of pressure coincides with the Z-axis, rendering the torque zero. Finally, the torque about the Y-axis oscillates and is negative because the torque vector rotates counterclockwise, determined by the right-hand rule.

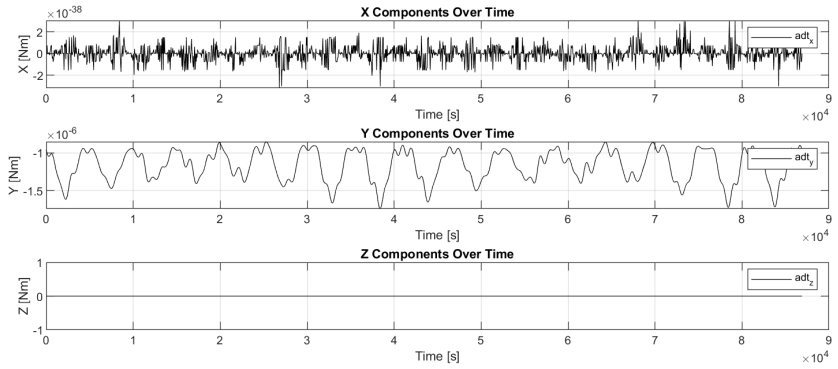

Figure 43: Atmospheric torque decomposition in the body axes reference frame: Y-axis torque is the only torque present due to no change in orientation relative to the V_{eci} vector.

When the satellite is allowed to change its orientation freely with only Atmospheric torques present, its attitude is unstable as determined by Equation 39. Because of this changing orientation, the satellite now also develops torques about the X-axis, see Figure 44. The rapid increase in the oscillation frequency showcases the attitude instability.

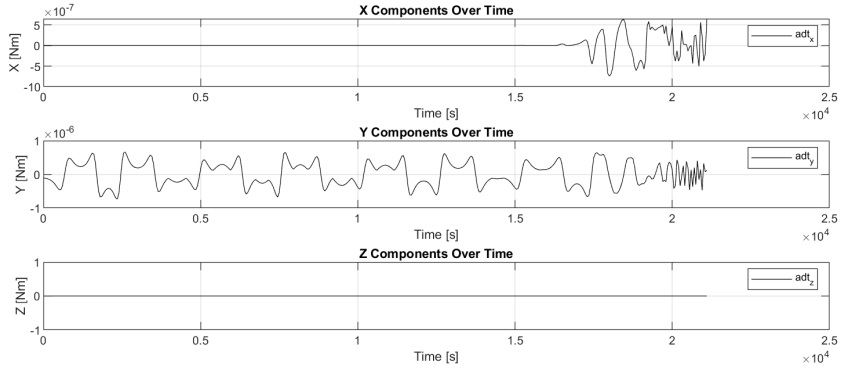

Figure 44: Atmospheric torque decomposition in the body axes reference frame: torques present in the X- and Y-axis. The centre of pressure coincides with the Z-axis, rendering the Z-component zero.

5.1.3 Verification

As stated before, the Atmospheric drag calculation relies on correctly determining the density ρ, the drag coefficient C_D, and the satellite's projected areas. The Atmospheric torque T_A, however, is a resultant of the drag force times the moment arm, as presented in equations 54 and 103.

Density
The density ρ is directly taken from past measurements. These measurements are implementable and relevant because they accurately depict a realistic variability throughout an orbit.

Drag coefficient
The total drag coefficient is the weighted summation of two elements: the $C_{D_b} = 2.2$ for the bus, which is a value commonly used for simulation satellite drag [59], and the solar panel drag coefficient C_{D_p}. As stated in C_D *estimation* in 4.1, the simple model ($C_{D_p} = 2\sin\alpha + 0.1$) is chosen for its simplicity. This model attains a maximum value of 2.1 at 90 degrees. This is an underprediction at high incidence angles whereby the more sophisticated model predicts values in the range of $2.3 - 3.0$ depending on the accommodation coefficients $\sigma_n = \sigma_t = [0.5 - 0.9]$, see Figure 45. Also, at angles below 45 degrees, the simple model over-predicts the drag coefficient. Nonetheless, since both σ_t and σ_n are difficult to determine as they depend on surface roughness and temperature, the simple model was chosen over Equation 61. Moreover, this study is not concerned with determining the exact values, but rather producing the correct trend and magnitude of the torques in play. Therefore, even though it is tempting, the simple model is not expanded into a fitting function that captures a 'better' trend.

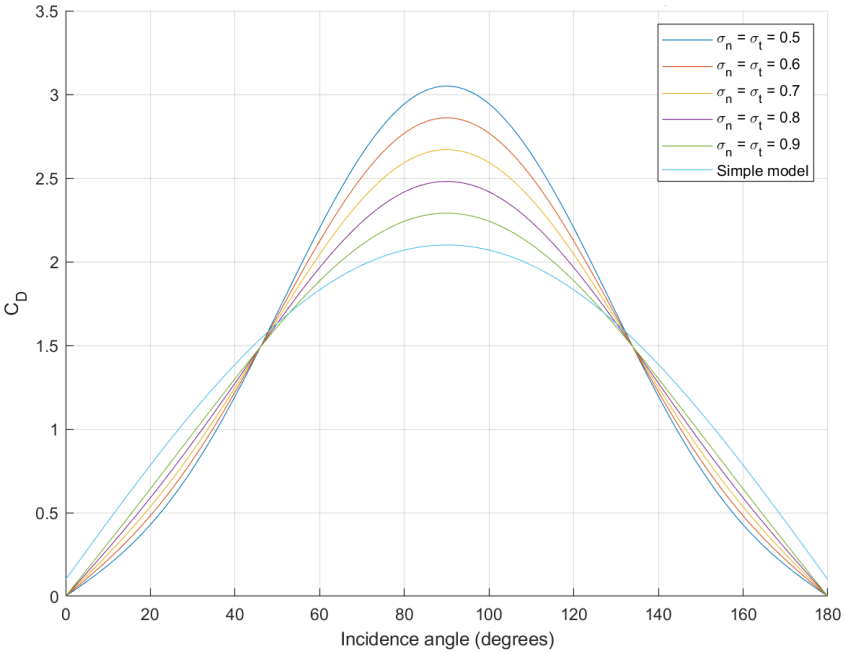

Figure 45: Drag Coefficient CD model comparison: mean free path model with different σ_n and σ_t versus simple model

Projected area

To verify the projected area calculation, various orientations (roll, pitch, and yaw angles) of the satellite relative to the incoming velocity vector V_{eci} are tested and manually checked. For convenience, the projected areas for verification are presented in Figure 46. The associated values are given in Table 3.

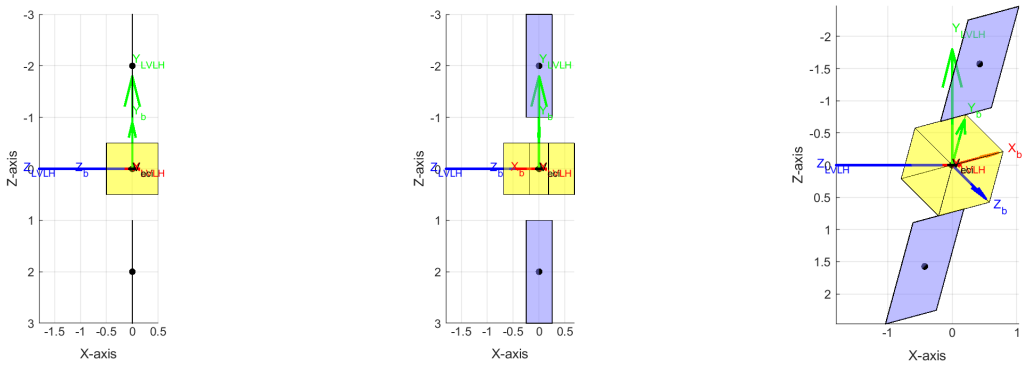

(a) $\alpha = 0$ degrees (b) $\alpha = 30$ degrees (c) Diagonally aligned

Figure 46: Projected area determination for various orientations.

The satellite is configured such that the satellite bus has dimensions $1 \times 1 \times 1$ m^3 and the solar panels $2 \times 1 \times 0.01$ m^3. As a reference, Figure 46a) illustrates the frontal area as seen from the V_{eci} vector, with the frontal areas $1 \times 1 = 1$ m^2 and $2 \times 0.01 = 0.02$ m^2, respectively. When the satellite pitches by 30 degrees (over the Y_B axis), it arrives at the orientation illustrated in Figure 46b. Now, for each component, two faces are exposed to the free stream velocity vector. For the satellite bus the projected surface area S becomes $1 \times \sin 30 + 1 \times \cos 30 = 0.5 + 0.866 = 1.366$ m^2, and for each solar panel, $S_p = 2 \times \sin 30 + 0.02 \times \cos 30 = 1 + 0.0173 = 1.0173$ m^2. Similarly, for Figure 46c whereby three faces are identically in sight, the bus area is maximised and becomes $\sqrt{1^2 + 1^2 + 1^2} = \sqrt{3} = 1.73$ m^2, etcetera. This shows that the projected area is calculated correctly. Note that the scaling quantity for the drag force of the entire satellite is $C_D \cdot S$. The larger that term becomes, the larger the drag force F_A.

Parameter	Value (a) (Figure 46a)	Value (b) (Figure 46b)	Value (c) (Figure 46c)	Unit
roll	0	0	225	[deg]
pitch	0	30	325	[deg]
yaw	0	0	225	[deg]
α	0	-30	35	[deg]
S_b	1	1.366	1.732	$[m^2]$
S_{p1}	0.02	1.0173	1.1645	$[m^2]$
S_{p2}	0.02	1.0173	1.1645	$[m^2]$
S	1.04	3.4007	4.0611	$[m^2]$
C_D	2.119	1.542	1.654	[-]
C_{D_b}	2.2	2.2	2.2	[-]
C_{D_p}	0.1	1.1	1.247	[-]
F_A	0.00128	0.00304	0.00389	[N]

Table 3: Drag coefficient and Projected surface area verification. The resultant Atmospheric drag force F_A is parallel to the free stream velocity V_{eci} but opposite in direction. For this data, a flying altitude of 300 km was selected with a density $\rho = 1.9401 \cdot 10^{-11}\ kg/m^3$.

Comparison with existing satellite

Using this method, and selecting a 1% offset for the centre of pressure relative to the satellite's bus dimensions, the resultant torque is in the range of $4 \cdot 10^{-8} - 6 \cdot 10^{-5}\ Nm$ for CubeSat-sized ($0.1 \times 0.1 \times 0.1$ m^3) till medium-sized satellites ($1 \times 1 \times 1\ m^3$), respectively. For verification, the following comparisons are made:

- GOCE satellite, size $5.3m \times 2.3m$, approximate Atmospheric disturbance torque in the order of $2.5 \cdot 10^{-4}\ Nm$ [105]. An impression of the satellite is presented in Figure 47a. Since the satellite does not have a rectangular cross-section, a rough estimation is made for the MATLAB model in Figure 47b of $5.3m \times 2.0m$, which is 30 cm smaller to account for the mismatch in shape (rectangular versus almost circular) to prevent over-prediction too much. Using the simple approximations, the calculated value is $2.9 \cdot 10^{-4}\ Nm$, which is in the same ballpark and deemed workable.

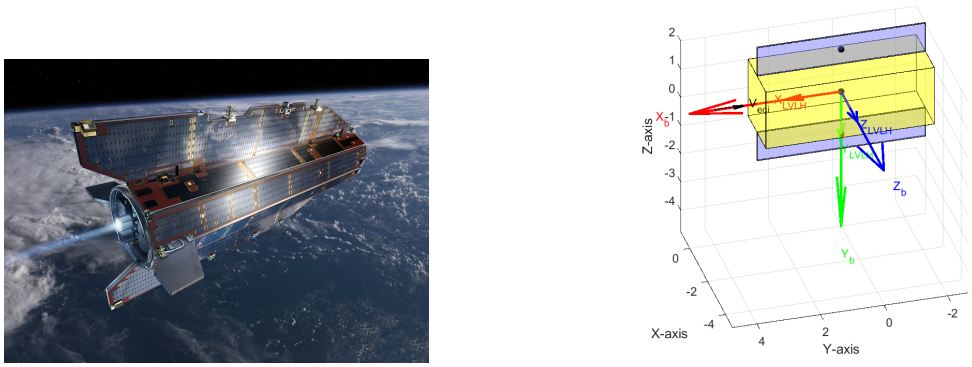

(a) (b)

Figure 47: Visualisation of (a) GOCE satellite artist impression (source: [105]) and (b) GOCE satellite MATLAB representation.

- K. N. Athreyas *et al.* presented a paper called *System Design for Small Satellites in Very Low Earth Orbit* [6]. Herein, they present three satellite configurations which will be launched into a 300 km circular orbit. The minimum projected area for the ram face is used to determine the drag force. The first one, a $0.3 \times 0.1 \times 0.1\ m^3$ sized satellite is presented in Figure 48a. Its MATLAB implementation is presented alongside in Figure 48b. According to the paper, the Atmospheric drag is $2.55 \cdot 10^{-5}\ N$, and the Atmospheric torque with a 1 cm centre of pressure arm is $3.32 \cdot 10^{-7}$ Nm (the paper takes a +30% margin on the lever arm ($L = \frac{T}{F} = \frac{3.32 \cdot 10^{-7}[Nm]}{2.55 \cdot 10^{-5}[N]} = 0.013[m]$)). The satellite's orbit is modelled for July 2000, as presented in the paper. The MATLAB model

calculates $1.95 \cdot 10^{-5}$ N and $1.95 \cdot 10^{-7}$ Nm for a zero degree incidence angle, respectively. Although the MATLAB model is a factor of 1.3 off in drag force, it is deemed good enough. In the article, the conversion from force to torque is inconsistent. Namely, and not the reported 0.01 m. After adjusting the torque value for the moment arm correction, the MATLAB model still underestimates the Atmospheric torque by 30%.

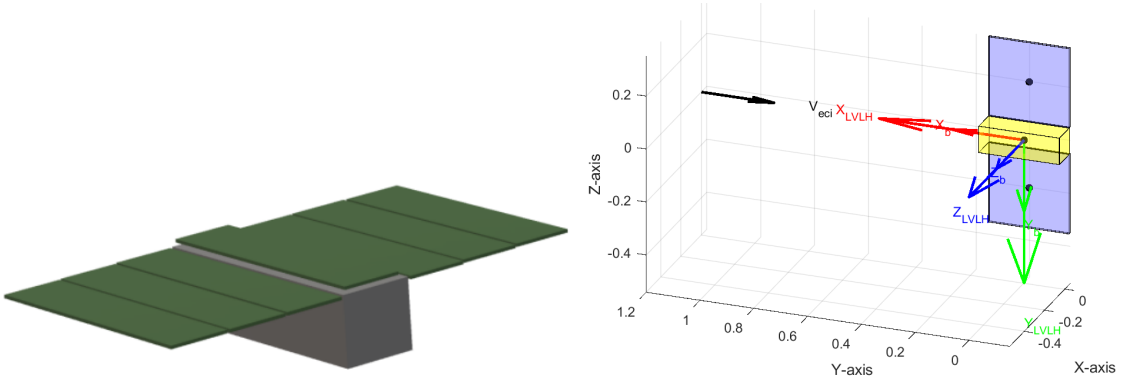

(a) Nano satellite configuration. Source: [6]

(b) Nano satellite MATLAB representation

Figure 48: Visualisation of (a) the nano satellite geometry and (b) the MATLAB implementation

- Their second satellite configuration is shaped similarly, but is a cube of size $0.3 \times 0.3 \times 0.3$ m^3. Its reported Atmospheric force and torque are $2.14 \cdot 10^{-4}$ N and $8.36 \cdot 10^{-6}$ Nm. Comparably, the MATLAB model gives $1.74 \cdot 10^{-4}$ N and $1.74 \cdot 10^{-6}$ Nm. This would mean that the calculated Atmospheric torque is almost a factor of five lower. This suggests that the MATLAB model is underestimating the Atmospheric torque significantly. However, since the conversion from force to torque in the article is inconsistent, a correction of 3.9 for the moment arm must be executed, as the moment arm is $L = \dfrac{T}{F} = \dfrac{8.36 \cdot 10^{-6}}{2.14 \cdot 10^{-4}} = 0.039$ instead of the stated 0.01. When correcting for this conversion, the MATLAB model predicts the Atmospheric torque about 23% lower.
- Lastly, their third satellite, the $0.8 \times 0.5 \times 0.5$ m^3 variant with reported Atmospheric force and torque of $6.09 \cdot 10^{-4}$ N and $61 \cdot 10^{-6}$ Nm. The MATLAB model gives $4.83 \cdot 10^{-4}$ N and $4.83 \cdot 10^{-6}$ Nm. Again, this suggests that the MATLAB model is more than an order of magnitude incorrect. However, when correcting for their conversion, in this case $L = 0.1[m]$, the underestimation is in line with the previous two configurations at a value of 26%.

From these comparisons, it is concluded that the `calculateAtmosphericTorque` function provides realistic Atmospheric disturbance torques that can be used for simulations. It should be noted, however, that when modelling multiple scenarios, an uncertainty must be taken into consideration. This uncertainty can be approximated as ±30% of the calculated torque values, accounting for variations in shape deviations and surface properties in the satellite configuration. This can be done by modifying the r_{cp} location in the `config()` function.

5.2 Gravity gradient torque implementation

The gravity gradient torque (GGT) function `calculateGravityGradientTorque` is an implementation of Equation 68 presented in section 4.3. It takes the position vector r_{eci}, the inertia tensor I_b, and the direction cosine matrix F_B as an input. The resulting torque T_{gg} is expressed in the body reference frame and returned as the output in Nm.

The assumptions made to model the GGT are listed in section 5.2.1. Next, the modelling (section 5.2.2) describes how the relevant equations are implemented. The verification of the GGT is carried out in section 5.2.3.

5.2.1 Assumptions

The following assumptions were made for the GGT torque calculation:

1. The Earth is modelled as an oblate spheroid, incorporating the J_2 zonal harmonic coefficient to account for its equatorial bulge.
2. The gravitational potential is dominated by the central body (Earth), and higher-order harmonics beyond J_2 are neglected.
3. The inertia tensor I_b is considered constant and expressed in the body frame.

5.2.2 Modelling

To model Equation 68, it is important to express the position vector and the inertia tensor in the coordinate frame of interest. Since the inertia tensor I_b is already expressed in the body reference frame, it is easiest to translate the position vector r_{eci} into the body reference frame too, through premultiplying with the direction cosine matrix F_B according to Equation 104.

$$r_b = F_B \cdot r_{eci} \tag{104}$$

To be able to test various effects, Equation 68 is calculated in two parts: first, the classical gravity gradient torque T_1 given by Equation 105. The magnitude of r is depicted with $\rho = |r_b| = |r_{eci}|$.

$$T_1 = \frac{3\mu}{\rho^5} \left(r \times (I \cdot r)\right)_{|_B} \tag{105}$$

and, second, the correction term T_2 to model the effect of Earth's oblateness as given by Equation 106.

$$\begin{aligned} T_2 =& \mu J_2 \left(-\frac{3}{\rho^5} \left(z \times (I \cdot z)\right) + \frac{15(r \cdot z)}{\rho^7} \left(z \times (I \cdot r) + r \times (I \cdot z)\right) \right. \\ &\left. + \frac{15}{2} \left(\frac{1}{\rho^7} - \frac{7(r \cdot z)^2}{\rho^9} \right) \left(r \times (I \cdot r)\right) \right)_{|_B} \end{aligned} \tag{106}$$

Here, J_2 is the first zonal harmonic coefficient, and z is the unit vector along the Earth's rotation axis (the $[0; 0; 1]$ direction in ECI reference frame). The complete gravity gradient torque in the satellite body reference frame is the sum of the two parts:

$$T_{gg} = T_1 + T_2 \tag{107}$$

5.2.3 Verification

To verify the gravity gradient model, the classical gravity gradient torque T_1 (Equation 105) is expanded into Equation 108.

$$T_1 = \begin{bmatrix} T_{1_x} \\ T_{1_y} \\ T_{1_z} \end{bmatrix} = \frac{3\mu}{\rho^5} \begin{bmatrix} (yI_{zx} - zI_{yx})x + (yI_{zy} - zI_{yy})y + (yI_{zz} - zI_{yz})z \\ (zI_{xx} - xI_{zx})x + (zI_{xy} - xI_{zy})y + (zI_{xz} - xI_{zz})z \\ (xI_{yx} - yI_{xx})x + (xI_{yy} - yI_{xy})y + (xI_{yz} - yI_{xz})z \end{bmatrix} \tag{108}$$

When the mass distributions align with the principal axis, the inertia tensor expressed in the body reference frame, I_b, becomes a diagonal matrix. Thus, the cross-terms become zero, which reduces Equation 108 to Equation 109.

$$T_1 = \begin{bmatrix} T_{1_x} \\ T_{1_y} \\ T_{1_z} \end{bmatrix} = \frac{3\mu}{\rho^5} \begin{bmatrix} yz(I_{zz} - I_{yy}) \\ xz(I_{xx} - I_{zz}) \\ xy(I_{yy} - I_{xx}) \end{bmatrix} \tag{109}$$

Symmetric mass distribution

From this, it becomes evident that when the satellite is spherically symmetric ($I_{xx} = I_{yy} = I_{zz}$), the resultant body torques must be zero. This is indeed the case, and is presented in Figure 49.

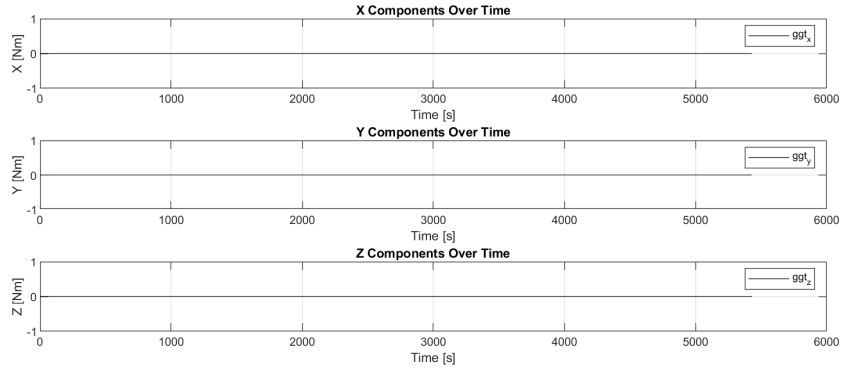

Figure 49: Gravity gradient torque for a spherically symmetric satellite (a sphere or a perfect cube) for one circular orbit presented in the body axes reference frame.

If the satellite is (artificially) forced to remain strictly aligned with the LVLH axis system ($X_B = X_{LVLH}$, etc.), meaning that one of the principal axes is parallel to the vector spanning radially outward from the centre of the Earth, the resultant gravity gradient torque would be zero too. This is because all the products ($yz = xz = xy$) would be zero, and leads to a similar depiction of the body torques as presented in Figure 49.

Non-aligned axis symmetric satellite
In the case of a non-aligned ($X_B \neq X_{LVLH}$, etc.) axis symmetric ($I_{xx} = I_{yy} \neq I_{zz}$) satellite, then, according to Equation 109, T_{1_x} and T_{1_y} must behave sinusoidally, whereby T_{1_x} lags 90 degrees behind (or $1/4 \cdot T_{orbit} = 1358\ [s]$), and T_{1_z} must be zero because of the axis symmetry.

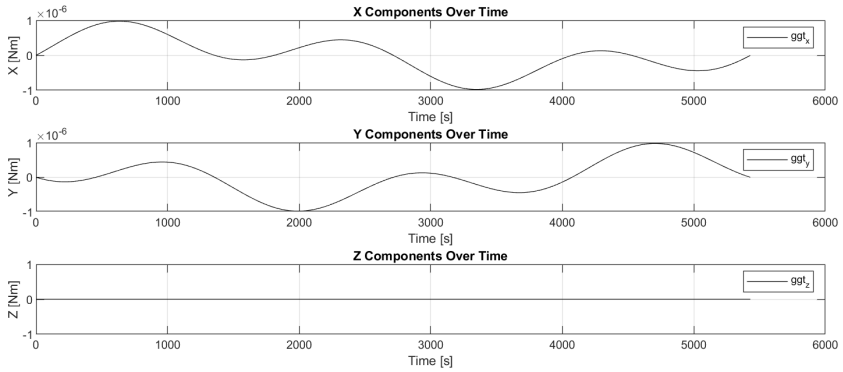

Figure 50: Gravity gradient torque for an axis-symmetric satellite (e.g. a solid cylinder whereby $I_{xx} = I_{yy} \neq I_{zz}$) for one circular orbit presented in the body axes reference frame. For this example, the cylinder is oriented 30 degrees in positive pitch direction (about the Y_B-axis).

When executing the same test cases, but for the T_2 components (Equation 106), one finds similar results. With that, the function is mathematically verified for working in the correct direction for these cases. The computed torque matches analytical expectations for both the main gravity gradient T_1 and the J_2 contributions through T_2. Therefore, the added sum presented in Equation 107 must also be correct.

Comparison with existing satellite
To verify the correct trend in magnitude and direction, the findings for the AilanSat-1 [33] gravity gradient disturbance are taken as a test case scenario. The exact orbit that AlainSat-1 flies in is not determined, unfortunately. To approximate the orbit, two orbital parameters are selected to be modified: the inclination and the Right Ascension of the Ascending Node Ω (RAAN) and are schematically shown in Figure 51.

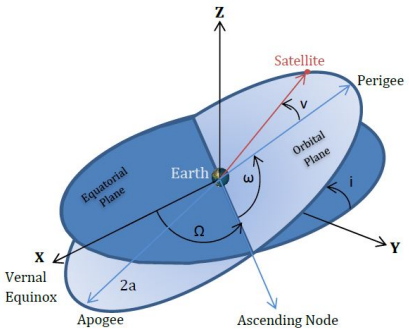

Figure 51: Right Ascension of the Ascending Node Ω (RAAN) and the inclination i. Furthermore, the reference 'starting point' that coincides with Earth's surface is the Vernal Equinox. Source: [65]

The orbital trajectory is approximated by an orbit with an inclination of ($i = 97.6°$) and a Right Ascension of the Ascending Node ($\Omega = -118°$) for this specific orbit. The results obtained from the MATLAB model (illustrated in Figure 63b) are compared to the findings published for AlainSat-1, and are presented in Figure 52. Even though the T_x and T_y components are out of phase for the Matlab model compared to the AlainSat-1 scenario, the magnitude and trend are similar. T_x oscillates between approximately $1.3 \cdot 10^{-8}[Nm]$ and $-2.5 \cdot 10^{-8}[Nm]$ for the Alainsat, and between $1.5 \cdot 10^{-8}[Nm]$ and $-2.4 \cdot 10^{-8}[Nm]$ for the Matlab model, capturing the correct motion. Similar observations within equal tolerances can be made for T_y and T_z.

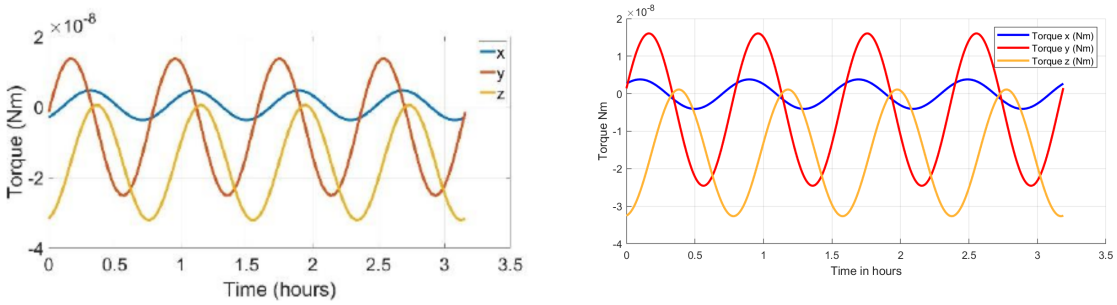

(a) AlainSat-1 [33]

(b) Matlab implementation

Figure 52: Gravity Gradient torques: (a) AilanSat-1 in the ECI frame and (b) Matlab implementation of Equation 105 translated to the ECI frame.

Overall, the function is found to be accurate enough for the range of configurations relevant to this study. The intermediate results confirm consistency and usability. Furthermore, the tests performed varied the satellite position, orientation, and inertia tensor parameters to ensure the output behaved as physically expected, such as producing zero torque for spherically symmetric inertia tensors. Therefore, it is concluded that the `calculateGravityGradientTorque` function is working properly.

5.3 Residual Dipole Torque Implementation

The residual dipole torque (RDT) is computed using the `calculateResidualDipoleTorque` function. This function considers the Earth's magnetic field and the satellite's magnetic dipole moment to calculate the resulting torque, as is described by Equation 73 in section 4.6. The residual dipole torque T_{RD} is expressed in the body axis system.

The assumptions made to model the RDT are listed in section 5.3.1. Next, the modelling (section 5.3.2) describes how the relevant equations are implemented. The verification of the RDT is carried out in section 5.3.3.

5.3.1 Assumptions

The following assumptions were made for the RDT torque calculation:

1. The Earth's magnetic field is modelled using the International Geomagnetic Reference Field model, inputs includes the position and time.
2. The satellite's residual magnetic dipole is constant throughout the orbit.
3. Both the magnitude and the direction of the residual magnetic dipole vector are considered arbitrary, since the particular design choices are not considered.

5.3.2 Modelling

Instead of simulating the Earth's magnetic field, the World Magnetic Model [63] is employed. It provides a comprehensive model of the Earth's magnetic field **B**. The model is updated every five years to reflect Earth's magnetic field changes. It uses the *.COF* files provided by the National Oceanic Atmospheric Administration (NOAA) [96]. The reference frame used is north-east-down (NED). To determine the field strength for years between 1900 and 2025, the `igrfmagm` function [17] can be employed.

Both magnetic declination and inclination are inputs to the `igrfmagm` function. As seen in Figure 53, the Magnetic declination D is the angle between the magnetic meridian and the geographical north at a particular location on the Earth's surface. The angle can change over time due to polar wandering. Magnetic inclination I is the angle at which the geomagnetic field is tilted to the Earth's surface. Magnetic inclination varies from 90 degrees, perpendicular to the surface, at the magnetic poles to 0 degrees, parallel to the surface, at the magnetic equator.

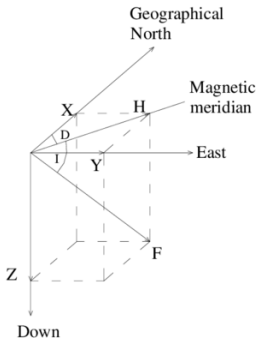

Figure 53: Magnetic-field components: Total Intensity (F), Horizontal Intensity (H), Vertical Intensity (Z), North-South Intensity (X), East-West Intensity (Y), Inclination (I), Declination (D). Source: [37]

First, the function converts the current date into a decimal year using the `decyear` function [48]. This is necessary for time-based magnetic field modelling, which is required to use the `igrfmagm` function.

Secondly, the Earth's magnetic field strength at the satellite's position is computed using the IGRF model. The satellite's altitude is calculated from its position vector, subtracting the Earth's average radius (6378 km). The magnetic field components are given in the North-East-Down (NED) reference frame (see 3.1.3) and returned in nanoteslas.

Thirdly, the magnetic field is converted from nanoteslas to Teslas and transformed to the Inertial Coordinate Frame (ECI) using the current position vector. The transformation matrix T_{NI} (see 3.2.3) is applied for conversion from NED to ECI.

Next, the magnetic field in the ICE frame is transformed to the Body-fixed Reference Frame using the direction cosine matrix `FB` given in 3.2.6. This transformation aligns the magnetic field with the satellite's orientation.

Finally, the residual dipole torque is calculated as the cross product of the satellite's dipole vector in the body frame with the transformed magnetic field vector (which is also in the body frame). The resulting torque vector is expressed in newton-meters.

5.3.3 Verification

AlainSat-1's residual dipole moment is reported to be of magnitude $|RD| = 0.008\ Am^2$ [33]. Considering that Figure 54a shows all components (T_x, T_y, T_z) to be oscillating two periods per orbit, it is deduced that the results are presented in the ECI reference frame. Moreover, all components are approximately equal, meaning that the residual dipole vector is directed equally in each axis $(x = y = z)$. Since the total residual magnitude is the norm of the components, the component strength (in x, y, z) can be determined by Equation 110.

$$\begin{aligned} |RD| &= \sqrt{x^2 + y^2 + z^2} \quad \text{with} \quad x = y = z \quad \rightarrow \quad |RD| = \sqrt{3x^2} \\ &\rightarrow x = \sqrt{\frac{|RD|^2}{3}} = \sqrt{\frac{(0.008)^2}{3}} \approx 0.0046 \\ &\Rightarrow RD = [0.0046, 0.0046, 0.0046]^T \end{aligned} \tag{110}$$

Evaluating the results generated by the MATLAB implementation presented in 54b in Figure 54 by comparing it to AlainSat's results in 54a, it is seen that the MATLAB model finds approximately a residual dipole strength that is twice as large. Furthermore, the shape of the oscillations is not perfectly sinusoidal, which is the case for AlainSat. The MATLAB implementation relies on the magnetic field strength measured as part of the `igrfmagm` function that uses International Geomagnetic Reference Field. It seems, therefore, that the results presented in 54a are solely reliant on an approximation $T_{RD} = RD \times B$ whereby the Earth's magnetic field B is approximated incorrectly.

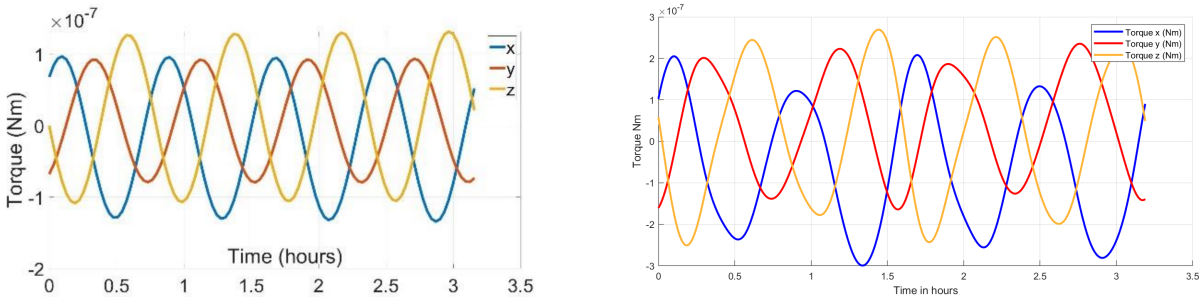

(a) AlainSat-1 [33]

(b) Matlab implementation

Figure 54: Residual dipole torques for two orbits (with $i = 97.6$ and $\Omega = -118$): (a) AilanSat-1 in the ECI frame and (b) Matlab implementation of Equation 73 translated to the ECI frame.

To evaluate the consistency of the function, two residual dipole vectors are considered: (a) $RD = [0.008, 0, 0]^T$ and (b) $RD = [0, 0, 0.008]^T$. The resultant body torques expressed in the body reference frame are presented in Figure 55. When the residual dipole vector is aligned with the magnetic field, the resultant torque must be zero (two parallel axes), as is the case for both 55a and 55b.

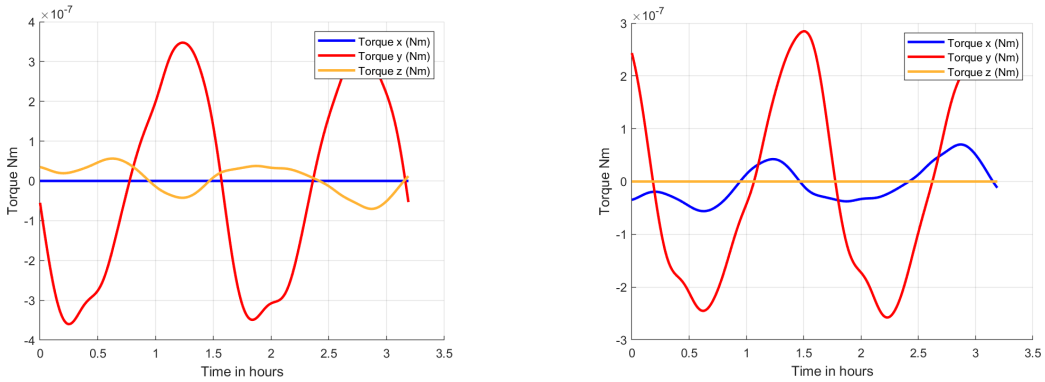

(a) $RD = [0.008, 0, 0]^T$ (b) $RD = [0, 0, 0.008]^T$

Figure 55: Residual dipole torques in the body reference frame for two orbits (with $i = 97.6$ and $\Omega = -118$) for two residual dipole vectors (a) RD_x (b) RD_z

To cross-check proper implementation of the `igrfmagm` function, the geomagnetic field is also modelled as a simple dipole in the form of Equation 75 as presented by Ramnath [78]. The results of using the simple model are compared to the results obtained from implementing the `igrfmagm` function in Figure 56. Both results show a good nominal behaviour: the cyclic nature is captured for the torque component that oscillates about the mean value of zero, and for the accumulating component (the mean value is unequal to zero), the simple model captures the mean as an offset, whereas the `igrfmagm` implementation demonstrates fluctuations too.

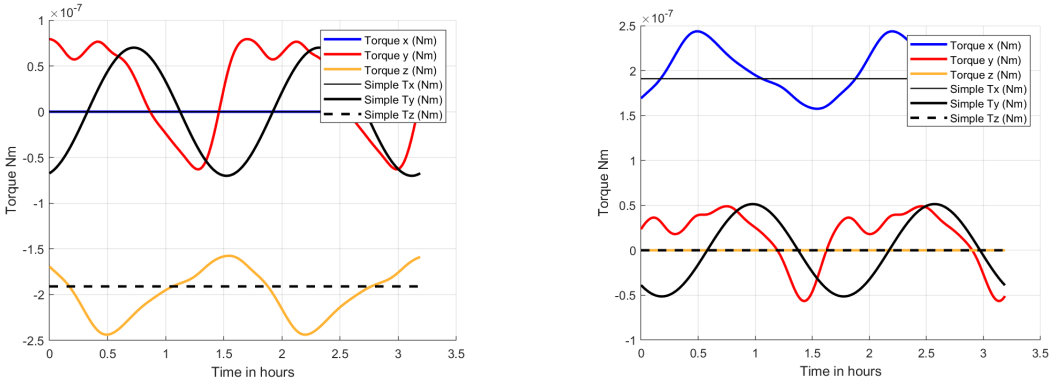

(a) $RD = [0.008, 0, 0]^T$ (b) $RD = [0, 0, 0.008]^T$

Figure 56: Residual dipole torques in the body reference frame for two orbits (with $i = 0$ and $\Omega = 0$) for two residual dipole vectors (a) RD_x (b) RD_z. The Earth's magnetic field is modelled by the `igrfmagm` function (coloured) and a simple dipole by Equation 75 (black).

Since the more accurate magnetic field model is available through the `igrfmagm` function, and the implementation shows consistent outputs with the simpler implementation, the `calculateResidualDipoleTorque` function will rely on the `igrfmagm` function. The magnitude of the residual dipole torque is fully dependent on the residual dipole moment. In theory, a satellite can be designed such that the residual dipole moment is zero. However, as stated in section 4.6, a residual dipole moment vector with magnitudes ranging between 0 and 0.2 $[Am^2]$ will be selected. The orientation of this vector will be in an arbitrary direction. With this scaling factor, the correct working of the `calculateResidualDipoleTorque` function is verified.

5.4 Solar radiation pressure torque implementation

This section details the implementation of the solar radiation pressure (SRP) torque calculation within the `calculateSolarRadiationPressureTorque` function. The function computes the torque exerted on a satellite due to the momentum transfer of photons from the Sun, considering the satellite's geometry,

optical properties, and orientation relative to the Sun.

The assumptions made to model the SRP are listed in section 5.4.1. Next, the modelling (section 5.4.2) describes how the relevant equations are implemented. The verification of the SRP is carried out in section 5.4.3.

5.4.1 Assumptions

The following assumptions were made for the SRP torque calculation:

1. Flat Plate Approximation: The satellite's surfaces are approximated as flat plates with uniform optical properties.
2. Constant Solar Irradiance: Solar irradiance is assumed constant at 1368 W/m^2 at 1 AU. Variations due to solar activity are neglected.
3. Single Light Source: The Sun is the sole source of radiation; Earth's albedo and infrared radiation are not considered.
4. Zero Emittance: The satellite is assumed to have zero thermal radiation emittance.
5. Perfectly Diffuse Reflection: Diffuse reflection follows Lambert's cosine law.
6. Shadowing: The `checkEclipse` function determines whether the satellite is in Earth's shadow, completely blocking solar radiation.

5.4.2 Modelling

The SRP torque calculation is based on Equation 85 and Equation 87 presented in section 4.8.

First, the illumination condition must be determined, as the satellite can be eclipsed ('hiding' from the Sun behind the Earth). The function `checkEclipse` is designed to determine if the Earth eclipses a satellite. It takes the following position vectors as inputs: the satellite r_{SAT}, the Earth r_{Earth}, and the Sun r_{Sun}. The function `calculate_r_celes` computes the position vectors of the Sun r_{Sun} and Earth r_{Earth} based on a given starting date, using the planetary coefficients loaded from `DE430Coeff.mat` data as interpreted by Jet Propulsion Laboratory [25]. With those inputs, the following relative vectors are found:

- The satellite position vector is defined from the Earth (subscript $_E$) to the satellite (for clarity denoted with a subscript $_e$): $r_{SAT} = r_{Ee} = r_{eci}$.
- The Sun's position (subscript $_S$) vector relative to Earth (from Sun to Earth): $r_{SE} = r_{Earth} - r_{Sun}$.
- The position vector from the Sun to the satellite: $r_{Se} = r_{Ee} - r_{SE}$.

Eclipsed
The eclipse condition is calculated using Equation 111. Herein, the radius of the Earth is denoted by R_E and the orbital distance measured from the centre of the Earth $|r_{eci}|$. If the value of `eclipse` is greater than zero, the function sets `isEclipsed` to `true`, indicating that the satellite is eclipsed by the Earth. Otherwise, `isEclipsed` is set to `false`.

$$\texttt{eclipse} = \tan^{-1}\left(\frac{R_E}{|r_{eci}|}\right) - \cos^{-1}\left(\frac{\texttt{r\_Ee} \cdot \texttt{r\_SE}}{\|\texttt{r\_Ee}\|\|\texttt{r\_SE}\|}\right) \tag{111}$$

The working of the `checkEclipse` function is schematically illustrated in Figure 57. For Earth orbits that are not sun-synchronous, a satellite will, at some point, be eclipsed by the Earth. The transition occurs in seconds, causing abrupt changes in solar radiation pressure loading. When eclipsed, the solar radiation pressure torque is considered zero ($T_{SRP} = [0, 0, 0]^T$).

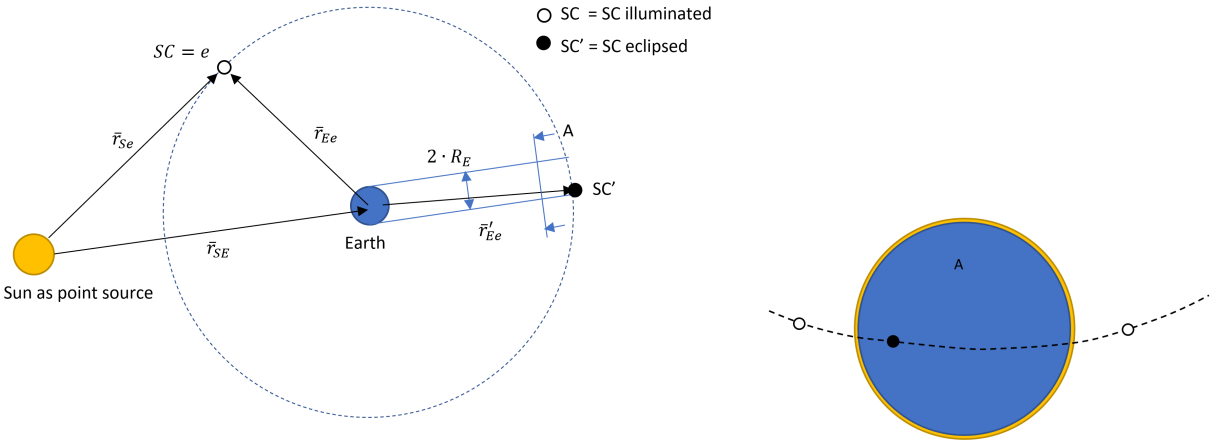

(a) Eclipse vectors.

(b) View A: S/C enters and exists eclipse.

Figure 57: Eclipse model explained: (a) presents the vectors relevant for determining whether the S/C is eclipsed and (b) demonstrates that for a non-sun-synchronous orbit, the S/C will be eclipsed for part of the orbit.

Illuminated

Secondly, when the satellite is not eclipsed, the solar radiation pressure must be calculated. The code iterates through each surface, calculates the cosine of the incidence angle ($\cos(\theta)$) by Equation 112 wherein $e_S = \dfrac{-r_{Se}}{|r_{Se}|}$.

$$e_S \cdot n_i = |e_S||n_i| \cos(\theta) \quad \rightarrow \quad \cos\theta = e_S \cdot n_i \tag{112}$$

The code only considers surfaces facing the Sun ($\cos(\theta) > 0$). The contributions of absorption, specular reflection, and diffuse reflection are calculated and summed to the total force vector. For simplicity's sake, the reflectivity coefficients $\gamma_a, \gamma_s, \gamma_d$ are assumed constant and identical for each surface.

5.4.3 Verification

For verification purposes, several scenarios are selected: the satellite is in a Sun-synchronous orbit such that no eclipse occurs, the satellite is in an equatorial orbit, whereby the satellite is illuminated most of the orbit, except for when it is eclipsed, for various centre of pressure positions. The orbital variation is selected to verify the proper working of the `checkEclipse` function, and the change in the centre of pressure axis variations is selected to verify the torque direction in the body reference frame.

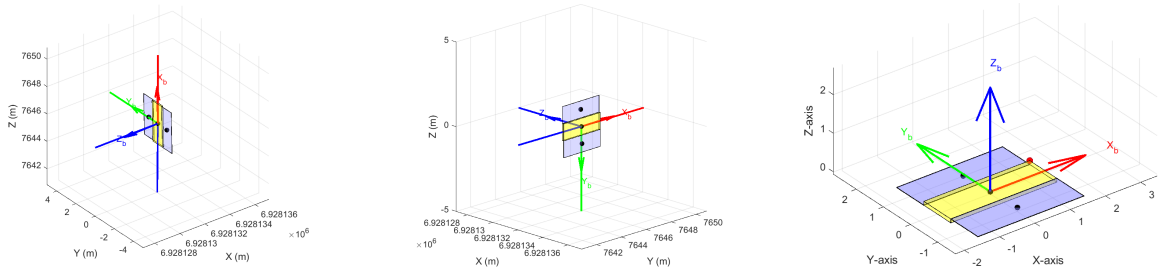

(a) Orbital path direction for the sun-synchronous orbit. Red indicates the direction of flight and is aligned with the X_B axis.

(b) Orbital path direction for the equatorial orbit. Red indicates the direction of flight and is aligned with the X_B axis.

(c) Centre of pressure location $(5/100 \cdot [Hb, Lb, Db])$. The C_p location is scaled by a factor of 10 for visibility.

Figure 58: Satellite of size $X_B, Y_B, Z_B = [3, 1, 0.1]$ m to emphasize the differences in solar radiation pressure torque for each axis.

The solar radiation pressure torque for a perfect Sun-synchronous orbit can most easily be described in the body axis. Since the Sun is positioned perpendicular to the $XZ_{|B}$ plane, the satellite experiences a torque about only two axes. In the case where the centre of pressure is located at 5% offset (relative to the bus dimensions) from the centre of mass, as is illustrated in Figure 58c, the torque about the X_B axis is positive, $T_x > 0$, and is what is expected with a positive moment arm and a positive force component in the respective axis (perpendicular to the torque axis). The torque about the Z_B axis is negative, $T_z < 0$, because the C_P is located in the positive X_B direction and the force is directed in the negative Y_B direction, which translates into an opposing force component times a positive distance and gives a negative torque.

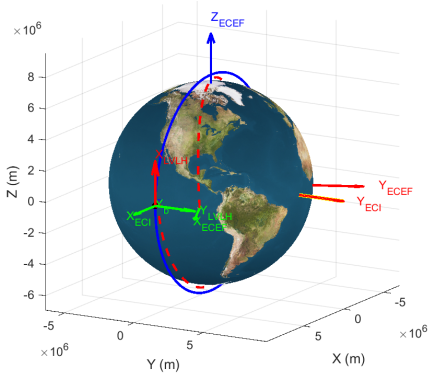

(a) Orbital path for the sun-synchronous orbit.

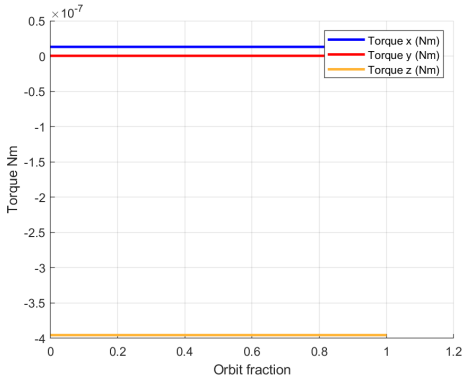

(b) The solar radiation pressure torque. The satellite is constantly illuminated.

Figure 59: Sun-synchronous orbit whereby the Sun is located on the positive Y_{ECI} axis: (a) orbital path, and (b) the solar radiation pressure torque.

The solar radiation pressure torque for a perfect equatorial orbit, where the Sun is positioned in the orbital plane (see Figure 60), is more difficult to understand. Whereby, for the prefect sun-synchronous case (the Sun is positioned perpendicular to the orbital plane, see Figure 59), the solar radiation pressure causes a constant accumulative torque; in the equatorial orbit, it causes cyclic and accumulative torques. Also, due to the satellite being eclipsed during part of the orbit, a discontinuity arises.

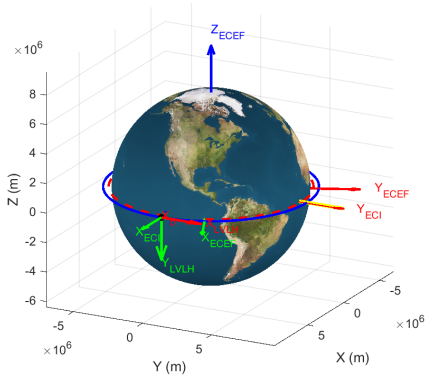

(a) Orbital path for the equatorial orbit.

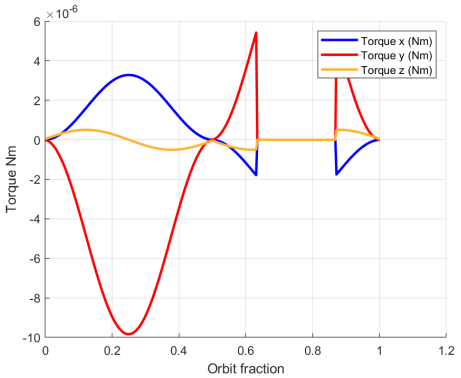

(b) The solar radiation pressure torque. The satellite is partially illuminated and partially eclipsed.

Figure 60: Equatorial orbit whereby the Sun is located on the positive Y_{ECI} axis: (a) orbital path, and (b) the solar radiation pressure torque.

When examining both Figure 58 and Figure 60, it can be seen that for the torque about the Y-axis, it should start at (negative) zero (small face is illuminated) and progressively become more negative as the larger surfaces are exposed to the Sun. Then, after a quarter-orbit, the magnitude should decrease gradually until the half-orbit crossing, at which point the smaller face is again exposed. Shortly after, the sign should flip as the satellite's opposite side is illuminated. Next, at about 0.65 T_{orbit}, the satellite

is eclipsed, rendering the torques zero until it exits the eclipse. Finally, the $\cos\theta$ becomes smaller as the satellite propagates through the orbit. A similar trace can be made for both the X- and Z-axis, thereby concluding that the function estimates the eclipsed state, magnitude, and sign of the SRP torque as the satellite orbits Earth.

5.5 An overview of the dominant disturbances

The magnitude of each disturbance torque depends on the environment, the satellite's geometry, and its orientation. This overview also considers the pressure centres as indirect parameters, as discussed in chapter 4. Precise determination of the centres of pressure requires detailed analysis; therefore, this study assumes that their locations are constant and known. To account for design variability, chapter **??** includes a range of centre-of-pressure values. Variations within the orbit from orientation changes are excluded from this section.

1. **Environment**: Space weather governs the physical interactions experienced by the satellite during orbital propagation. For example, the magnetic field strength and atmospheric density are higher at lower altitudes; incoming radiation exerts radiation pressure, with intensity dependent on illumination conditions. Solar activity and changes in Earth's magnetic field also influence atmospheric composition.

2. **satellite geometry**: The shape and structure of the satellite determine its interactions with the environment. Atmospheric, magnetic, gravity gradient, and radiative interactions depend on the satellite's size and shape.

3. **satellite surface properties**: For both Atmospheric and radiation disturbances, the magnitude and direction are determined by the surface characteristics. Absorption, diffuse reflection, and specular reflection each produce distinct effects, influencing the normal and tangential components of momentum exchange and thereby altering the strength and direction of the forces experienced, thereby shifting the centre of pressure.

4. **Orientation**: Orientation determines the effectiveness of environmental interactions, both in strength and directionality—alignment or misalignment with the centre of mass results in high, low, or zero torques exerted onto the satellite.

5. **Centres of pressure locations**: If the force vector passes through the centre of mass, the net disturbance torque is zero. Otherwise, torque is generated at ninety degrees off-axis because of the moment arm.

To indicate the variability of the (dominant) disturbances, two figures are presented in which the relative magnitude of the gravity-gradient torque (ggt), solar-radiation pressure torque (srt), residual dipole torque (rdt), and atmospheric disturbance torque (adt) are plotted per axis in the body-fixed reference frame for a typical orbit. The first, Figure 61, shows a satellite at an altitude of 200 km that has its body axes aligned with the local-vertical-local-horizontal axes system.

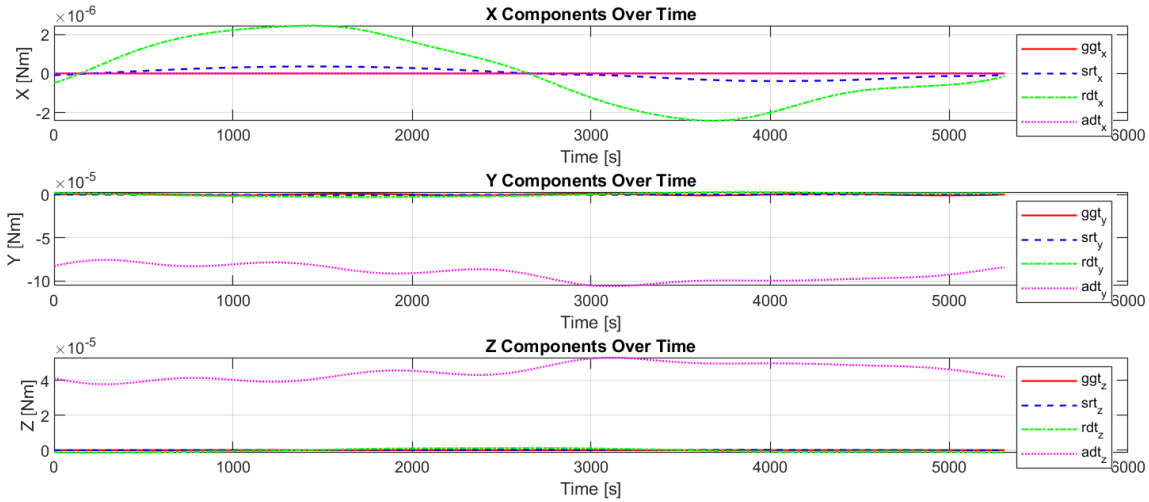

Figure 61: Disturbance torques for a LVLH-aligned example satellite at 200 km altitude.

Secondly, Figure 62 illustrates that when this satellite were to be employed at/designed for higher altitudes, such as 400 km, the dominant torque could change from Atmospheric to residual dipole torque. One can imagine that if the residual dipole were smaller about the Y-axis, the gravity-gradient torque could become dominant.

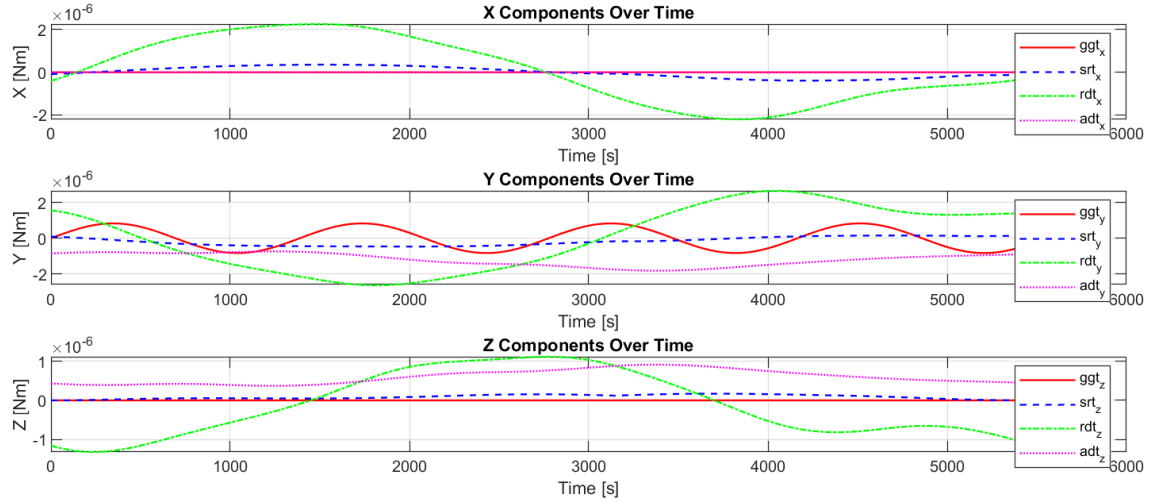

Figure 62: Disturbance torques for a LVLH-aligned example satellite at 400 km altitude.

It should be noted that, for this example, the disturbances at 200 km are in the order of 10^{-5} $[Nm]$, and at 400 km they are reduced to about 10^{-6} $[Nm]$. Based on this observation, it is concluded that FACAs should be designed for the specific satellite (geometry) with its orbital parameters (altitude and inclination).

6 Satellite Design and Control

This chapter presents the satellite design and control framework used throughout this thesis to answer the research question,

(B.1) *How can a parametric model be developed to determine the size and mass of the FACAs as a function of the maximum required counter-torque derived from the worst-case disturbance analysis?*
Section 6.2 addresses the design and sizing of reaction and momentum wheels, their covering assumptions, inertia calculations, design space, torque and momentum requirements, wheel-sizing optimisation, and verification results.

and to aid in answering the following research question:

(B.3) *How does the performance of each actuator type compare when evaluated in a closed-loop simulation against pointing accuracy and precision for a disturbance-rejection scenario?*
Section 6.1 describes the satellite's physical configuration, geometric representation, and the procedures applied to compute and validate the body inertia tensor. A description of actuator torque and control is given in section 6.3. Illustrative examples of employing FACAs are provided to contextualise the disturbance-rejection scenario within the presented framework. These examples involve an MW in Section 6.4 and an RW in Section 6.5, respectively.

Together, these sections establish the models, parameters, and verification steps that underpin the attitude-control simulations and design decisions presented in subsequent chapters.

6.1 Satellite configuration

This section details the setup of the satellite model used for the attitude dynamics simulation. It outlines the key assumptions, component definitions, and coordinate system conventions. Furthermore, it describes the verification process employed to ensure the accuracy and reliability of the developed model, including a comparison of the model's inertia characteristics with those of existing satellites.

6.1.1 Assumptions

The following assumptions were made for the satellite model:

1. The satellite components are assumed to be rigid bodies.
2. The mass is assumed to be homogeneously distributed within each component.
3. Hinge dynamics between the panels and the bus are not considered.
4. The satellite's body frame is defined as a right-handed Cartesian coordinate system with the origin located at the geometric centre of the satellite's bus. At spawning, the X-axis points along the orbital flight direction, the Z-axis points along the NADIR direction, and the Y-axis points orthogonally to the xz-plane, thereby completing the coordinate system.

6.1.2 Modelling

The satellite model comprises three primary components: the central bus and two deployable solar panels. Each component is modelled as a rectangular prism with defined mass, dimensions, and location within the satellite's body frame (see 3.1.5).

Component definition
The configuration of the satellite is defined through the `config()` function. This function specifies the following parameters for each component:

- **Masses**: The mass of each component is a critical parameter affecting the overall inertia properties of the satellite. The masses of the bus, panel 1, and panel 2 are denoted as masses.bus, masses.panel1, and masses.panel2, respectively. The total mass (masses.total) is calculated as the sum of the individual component masses.

- **Coordinates**: The coordinates define the position of each component's centre of mass within the satellite's body frame. The origin of the body frame is located at the geometric centre of the bus. The coordinates of the bus, panel 1, and panel 2 are defined as coordinates.bus, coordinates.panel1, and coordinates.panel2, respectively.
- **Dimensions**: The dimensions define the height, width, and depth of each component (corresponding to the xyz-axis, respectively). These parameters are used in calculating the inertia tensor of the satellite. The dimensions of the bus, panel 1, and panel 2 are defined as dimensions.bus, dimensions.panel1, and dimensions.panel2, respectively.

6.1.3 Geometry Model verification

The verification process aimed to ensure the accuracy of the satellite model in terms of its geometry and inertial properties. This is achieved through visual inspection, calculation verification, and comparison with existing satellite data.

Visual Inspection
The `plotSatellite()` function (see Appendix A) provides a 3D visualisation of the satellite model. This visualisation is used to inspect the following:

- Correct placement of satellite components based on the specified coordinates.
- Accurate representation of component dimensions.
- Proper orientation of the satellite in the body frame.

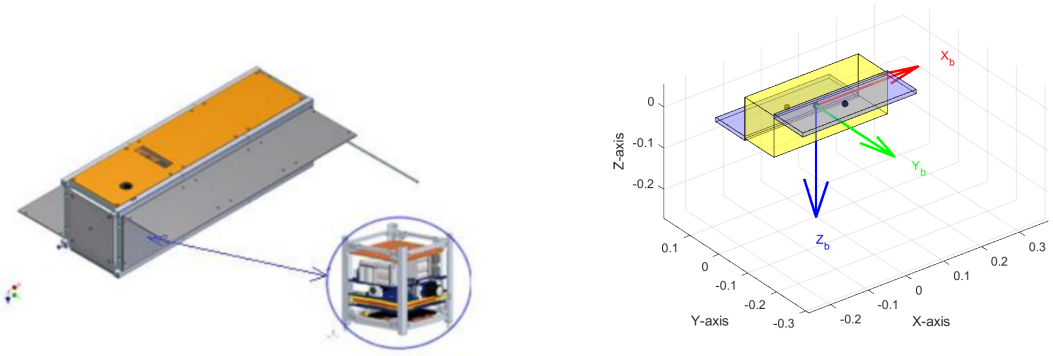

(a) AlainSat-1 satellite configuration. Source [33]

(b) Verification satellite model

Figure 63: Visual comparison between (a) the AlainSat-1 satellite configuration and (b) Matlab model presenting the Satellite's bus in yellow [0.3 m,0.1 m,0.1 m] with two solar arrays attached in blue. Both present the body axis system X_b, Y_b, Z_b using the red, green, and blue arrows, respectively.

6.1.4 Inertia Tensor Calculation Verification

The `calculate_system_inertia()` function calculates the total inertia tensor of the satellite system, based on the geometric inputs presented in section 6.1.2. The function inputs a structure containing the mass of each component, a structure defining the location of each component's centre of mass within the satellite's body frame, and a 3-element vector representing the (x,y,z) coordinates of the centre of mass of the whole satellite. This function sums the individual inertia tensors of the satellite's components (the bus and solar panels), accounting for their spatial arrangement using Steiner's theorem.

The inertia matrix of each component is calculated using the `calculateInertiaMatrix()` function, which implements the inertia tensor of a rectangular prism [9], see Equation 113.

$$I_{cm} = \frac{1}{12} m \begin{bmatrix} h^2 + d^2 & 0 & 0 \\ 0 & w^2 + d^2 & 0 \\ 0 & 0 & w^2 + h^2 \end{bmatrix} \tag{113}$$

Wherein, I_{cm} is the inertia tensor $[kg\ m^2]$ of a rectangular prism with mass m, width w, height h, and depth d, about its centre of mass.

It then applies Steiner's theorem (parallel axis theorem [112]) to transform the inertia tensors of the solar panels from their respective centres of mass to the satellite's centre of mass. The function `computeSteinerTerm()` is used to compute the translation terms that arise due to the offset between each component's centre of mass and the overall centre of mass, and is referred to as Steiner's term D. It is presented in Equation 114.

$$D_{offset} = m \begin{bmatrix} d_y^2 + d_z^2 & -d_x d_y & -d_x d_z \\ -d_y d_x & d_x^2 + d_z^2 & -d_y d_z \\ -d_z d_x & -d_z d_y & d_x^2 + d_y^2 \end{bmatrix} \tag{114}$$

Herein, D_{offset} is the Steiner term tensor $[kg\ m^2]$, m is the mass of the component $[kg]$, and d_x, d_y, and d_z are the components of the offset vector $[m]$.

The Steiner term is then added to the component's inertia tensor (calculated about its centre of mass, r_{cm}) to obtain the inertia tensor about the system's centre of mass, see Equation 115.

$$I_{total} = \sum I_i = \sum (I_{cm_i} + D_{offset_i}) \tag{115}$$

Using equations 113 till 115 allows for the inertia tensor calculation procedure verification. A numerical comparison between the inertia tensor of (a) the AlainSat-1 and (b) the MATLAB comparison model for verification is presented in Equation 116. For that, the selected mass of the satellite bus is `masses.bus = 3.39` [kg] and the masses of the solar panels `masses.panel1 = masses.panel2 = 0.095` [kg].

$$I_{AlainSat-1} = \begin{bmatrix} 0.0083 & 0 & 0 \\ 0 & 0.0303 & 0 \\ 0 & 0 & 0.032 \end{bmatrix} \qquad I_{\text{total}} = \begin{bmatrix} 0.0083 & -0.0001 & 0 \\ -0.0001 & 0.0303 & 0.001 \\ 0 & 0.001 & 0.032 \end{bmatrix}$$

(a) AlainSat-1 inertia tensor. Source [33] (b) Resulting inertia tensor from Matlab (116)

It should be noted that the off-diagonal terms in the Matlab model are one to two orders smaller than the diagonal term, and can therefore be neglected. When considering that the error between the inertia tensor is considered of an order smaller than the diagonal terms, thereby verifying the Matlab `calculate_system_inertia()` function. Alternatively, the satellite's mass distribution can be oriented so that its principal axis aligns with the mass distribution presented. If that is the case, the inertia tensor I_{total} would become a diagonal matrix like $I_{AlainSat-1}$ in Equation 116.

6.2 FACA sizing

The FACA sizing is automated to be applied to many satellite designs. To do that, some assumptions are made, see 6.2.1. Secondly, the shape of the flywheel of the reaction wheels and momentum wheel is determined in 6.2.2. It is implemented as the `size_FW` function. This function accounts for the design constraints specified in 6.2.3, various operational parameters in 6.2.4, and material properties to ultimately determine the dimensions and mass properties of the flywheels. It then determines suitable dimensions for the reaction wheels and the momentum wheel using the specified input parameters. The function uses a simple optimiser specified in 6.2.5 to ensure that the flywheel dimensions meet angular-momentum requirements while adhering to physical constraints. The intermediate results are verified by comparing them to a vendor's reaction wheel offering, and are presented in 6.2.6. Next, an equivalent momentum wheel is generated in 6.2.7. Finally, the outputs and inertia tensor for both the RWs and the MWs used are shown in 6.2.8. When an engineer is interested in a typical mass budget, 6.2.9 presents a good starting point. The results of the sizing procedure are documented in appendix A.3.

6.2.1 Assumptions

1. The flywheels are made of bronze with density $\rho = 8700\ km/m^3$.

2. To ensure manufacturability, the sizing will be executed in 0.1 mm increments.
3. The reaction wheels are ton-shaped (Figure 64), because a typical configuration houses the stator within the 'ton' as illustrated in Figure 5 and requires both radial and thrust bearings.
4. In contrast to the reaction wheel, the momentum wheel flywheel is ring-shaped (Figure 65). Because the radius is (much) larger by comparison, the inside does not have to be (fully) occupied by a dense stator. Thus, such a ring-shaped flywheel could be suspended like the outer ring of a bearing, thereby omitting the need for a 'top'. To ensure a feasible design, a minimum thickness of 5 mm is selected.
5. A safety factor of 2 is selected as a realistic angular momentum accumulation parameter.

6.2.2 Mass moment of inertia

This section outlines the procedure for sizing both reaction wheels and a momentum wheel for a satellite attitude control system. The flywheel used in both the reaction wheels and momentum bias wheel will have a hollow cylindrical design to maximise the mass moment of inertia about its central axis (longitudinal axis) for minimal mass.

The reaction wheel has a ton-shaped structure, similar to the reaction wheel presented in Figure 5. To size it, the design is schematically presented in Figure 64. The cross-section highlights key dimensions: outer radius R_o, inner radius R_i, height h, and wall thickness t_w. The frontal view reveals a circular shape with cutouts to reduce weight while maintaining structural integrity and moment of inertia.

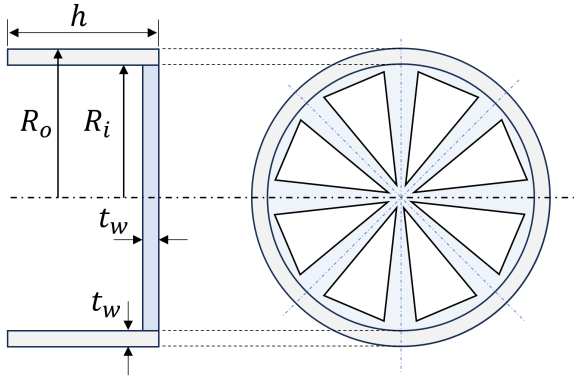

Figure 64: Schematic representation of the generic reaction wheel flywheel dimensions: cross-sectional view (left) and frontal view (right).

The flanges (grey horizontal elements) are the primary contributors to the moment of inertia, and are determined by Equation 117. The derivation of this mass moment of inertia of a hollow cylinder can be found via *Moment of Inertia: Hollow Cylinder* [64].

$$I_{fw} = \frac{1}{2} m_{fw} (R_i^2 + R_o^2) \tag{117}$$

In which m is the rotational mass. The rotational mass is calculated by multiplying the material density ρ (8700 $[kg/m^3]$ for bronze, 7850 $[kg/m^3]$ for steel, and 2700 $[kg/m^3]$ for aluminium) with the volume V $[m^3]$. The volume is computed by multiplying the cross-sectional area $A = \pi R^2$ $[m^2]$ with the height of the flanges h. Combining gives Equation 118.

$$m_{fw} = \rho V = \rho A t = \rho h \pi (R_o^2 - R_i^2) \tag{118}$$

The top (blue circular piece with cutouts) is presented with triangular cutouts. In reality, these cutouts are shaped such that stress concentrations are minimised. Because of the uniformly distributed cutouts present, the top is assumed to have a mass that is half that of the solid of the same shape (50% of the material is removed, thus the infill fraction $k_f = \frac{1}{2}$). Its contribution is determined by Equation 119.

$$I_{top} = k_f m_{top} R_i^2 = \frac{1}{2} t_w \pi R_i^2 \rho R_i^2 = \frac{1}{2} t_w \pi R_i^4 \rho \tag{119}$$

Combining equations 117, 118, and 119 and substituting the mass of the top $m_{top} =$ gives Equation 120.

$$I_{fw_{RW}} = \frac{1}{2}\rho h\pi(R_o^2 - R_i^2)(R_i^2 + R_o^2) + \frac{1}{2}(t_w \pi R_i^2 \rho)R_i^2 = \frac{1}{2}\rho\pi\left[h(R_o^2 - R_i^2)(R_i^2 + R_o^2) + t_w R_i^4\right] \quad (120)$$

A schematic depiction of a momentum bias wheel's flywheel is shown in Figure 65. The mass moment of inertia I_{MW} ($= I_{xx}$ in Figure 65) is determined by Equation 117. It should be noted that this is a simple mathematical model that represents a more complex design, as shown in Figure 4. The flywheel's shape depends on the entire actuator system assembly.

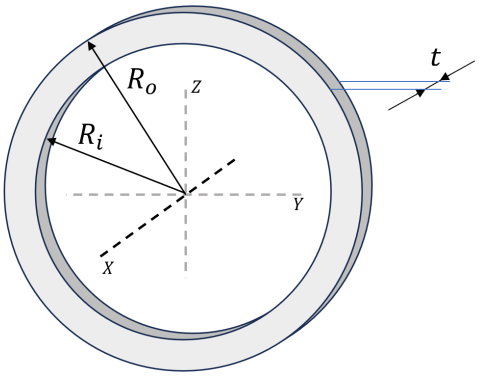

Figure 65: Schematic representation of flywheel dimensions. X denotes the axis of rotation.

6.2.3 Design space

The function takes the following input parameters to determine the allowable size of the flywheels: Satellite body dimension in the x,y,z-directions, H_b, L_b, D_b $[m]$, a scaling coefficient fraction_used so determine the 'a' dimension available for the wheels in term of satellite's length in Y_B direction, the density of the flywheel material rho_fw $[kg/m^3]$, a scaling coefficient k_ri_ro that relates the inner radius to outer radius of the flywheel $[-]$, the maximum angular velocity of the flywheel $omega\_fw\_max\_rpm$ $[RPM]$, a safety factor for the flywheel design SF_fw $[-]$, the average torque vector T_avg $[Nm]$, the time series data of the torque $torque\_history$ $[Nm]$, and the orbital period T_orbit $[s]$.

Based on the satellite dimensions (Hb, Lb, Db) and the `fraction_used` parameter, the function defines the maximum allowable dimensions (R_o, t) for the flywheels. A schematic representation of the design space $(a \times b \times c)$ is presented in Figure 66. The design space for the FACAs' flywheel, schematically illustrated by a yellow box-shaped volume, must not interfere with the incoming light rays, which are schematically represented by the grey cone-shaped volume. The 'tightest' space is defined by a square enclosing the circular aperture. To fit an MW in the Y_B direction, a maximum thickness of the MW $t_{\max}$ is set as 15% of the width (L_b) of the satellite's bus; thus `fraction_used` $= 0.15$ in Equation 123.

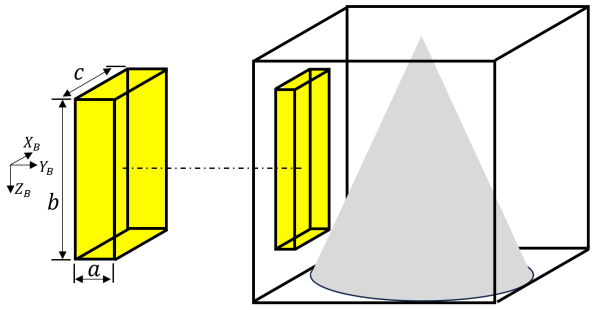

Figure 66: Schematic representation of flywheel design space within the satellite's bus. The maximum allowable volume is $V = a \times b \times c$, whereby the satellite bus dimensions constrain a, b, c

The maximum radius of the momentum wheel $R_{MW_{\max}}$ and reaction wheels $R_{RW_{\max}}$, along with the maximum thickness $t_{\max}$, are determined based on these constraints, and are presented in equations 121,

123, and 122, respectively. This ensures that the wheels fit within the allocated space inside the satellite. The value 2.1 is chosen so that the FACA housing fits within the design space as well ($D_{\text{assembly}} = 2(R_{\max} + 0.05R)$). This accounts for a 5% larger radius than that utilised by the flywheel alone.

$$R_{MW_{\max}} = \frac{\min(H_b, D_b)}{2.1} \tag{121}$$

Although the design space is schematically depicted as a single volume in Figure 66, the set of reaction wheels can be distributed throughout the satellite. The maximum radius of the reaction wheel $R_{RW_{\max}}$ is dictated by equating the surface area $(b \cdot c)$ occupied by the set of reaction wheels to that of the momentum wheel, according to Equation 122.

$$R_{RW_{\max}} = \frac{1}{2}\sqrt{\frac{(R_{MW_{\max}} \cdot 2)^2}{3}} \quad \rightarrow \quad R_{RW_{\max}} \approx 0.57 \cdot R_{MW_{\max}} \tag{122}$$

$$t_{\max} = L_b \cdot \text{fraction\_used} \quad (= a) \tag{123}$$

6.2.4 Angular momentum and torque requirements

The required angular momentum capacity is based on the average torque T_{avg} and the operational time between desaturation events $t_{\text{op}} = 2 \cdot T_{\text{orbit}}$, which is derived from the orbital period T_{orbit}. A safety factor SF_{fw} of 1.15 is applied to determine the safe angular momentum capacity H_{safe}, as shown in Equation 124. This safety factor accounts for unaccounted variations, such as the omitted disturbance torques, enhanced performance during de-tumbling and other (re-)orientation objectives.

$$H_{safe} = SF_{fw} \cdot \|T_{avg}\| \cdot t_{\text{op}} \tag{124}$$

The maximum torque T_{max} from the *torque_history* time series is also determined and scaled by the safety factor to obtain max_torque_safe.

$$max\_torque\_safe = SF_{fw} \cdot T_{max} \tag{125}$$

6.2.5 Reaction wheel sizing optimisation

The iterative optimisation process ensures that the wheels meet the necessary angular momentum requirements while remaining within the defined design space. The outer radius R_o and height $t = h$ of the reaction wheels are the design variables. The goal is to find dimensions that achieve the required moment of inertia I_{target}, which is calculated from the angular momentum that includes the safety factor H_{safe} $[Nms]$ and the maximum angular velocity $[rad/s]$ by Equation 126.

$$I_{target} = \frac{H_{safe}}{omega\_fw\_max\_rpm \cdot \frac{2\pi}{60}} \tag{126}$$

The optimisation loop adjusts R_o and t within defined bounds ($R_{o_{\min}}$, $R_{o_{\max}}$, $t_{\min}$, and $t_{\max}$) until the calculated moment of inertia $I_{calculated}$ is within a 5% tolerance of the target inertia I_{wheel}. The function uses Equation 117 and Equation 118 to calculate the inertia and mass for a hollow cylinder. Once the dimensions of the reaction wheel's flywheel are determined, they are rounded to manufacturable sizes (assumed to be accurate to 0.1 mm). Their mass m is calculated, and the moment of inertia tensor is assembled as presented in Equation 129.

6.2.6 Verification reaction wheels

Astrofein [5] is a vendor that sells various reaction wheels. Four of their reaction wheels are listed in Table 4: RW 25, RW 35, RW 100, and RW 150. Their design parameters are copied in as a reference and to verify the realism of the sizing algorithm used in this work.

Table 4: Astrofein Reaction Wheel Specifications [5]

Parameter	**unit**	**RW 25**	**RW 35**	**RW 100**	**RW 150**
Angular momentum	Nms	0.03	0.1	0.4	1.0
Nominal rotation speed	RPM	5000	5000	6000	6000
Nominal Torque	Nm	0.002	0.005	0.02	0.03
Moment of inertia	kgm^2	-	1.9e-4	6.52e-4	1.592e-3
Supply voltage	V	5	18-34	18-34	18-34
Motor constant Kt	Nm/A	-	-	-	-
Power Consumption (Nominal)	W	1.5	4.0	5.0	5.0
Power Consumption (Max)	W	2.8	9	20	42
Mass	kg	0.2	0.5	0.8	1.3
Dimension	mm^3	50 x 50 x 25.5	102 x 102 x 58	100 x 100 x 60	150 x 150 x 60

To validate the MATLAB model, Astrofein's published specifications for angular momentum, maximum outer radius, nominal rotation speed, and power consumption are used as inputs. Table 5 summarises the model's predicted performance characteristics for these reaction wheels.

Table 5: MATLAB model Reaction Wheel Specifications. Inputs are depicted with 'I' and outputs with 'O'

I or O — Parameter	**unit**	**RW 25 remake**	**RW 35 remake**	**RW 100 remake**	**RW 150 remake**
I — Angular momentum	Nms	0.03	0.1	0.4	1.0
I — Nominal rotation speed	RPM	5000	5000	6000	6000
I — Nominal Torque	Nm	0.002	0.005	0.02	0.03
O — Moment of inertia	kgm^2	0.547e-4	1.956e-4	6.063e-4	1.592e-3
I — Supply voltage	V	5	18	18	18
O — Motor constant Kt	Nm/A	0.006667	0.0225	0.0072	0.0072
I — Power Consumption (Nominal)	W	1.5	4.0	5.0	5.0
I — Power Consumption (Max)	W	-	-	-	-
O — Mass flywheel (excluding electronics)	kg	0.115	0.242	0.458	0.809
O — Dimensions (excluding electronics)	mm^3	50 x 50 x 24.9	66 x 66 x 28.8	86.4 x 86.4 x 28.8	101.8 x 101.8 x 38.4

When examining the results and comparing them to the vendor's specifications, some key differences are worth noting:

- RW 25: The MATLAB model predicts a moment of inertia of $0.5457 \cdot 10^{-4}\ kgm^2$, while the vendor does not provide this value for comparison. The model suggests dimensions of $50 \times 50 \times 24.9\ mm^3$ and a flywheel mass of 0.115 kg, which is 58% of the vendor's assembly mass of 0.2 kg.
- RW 35: The MATLAB model predicts a moment of inertia of $1.956 \cdot 10^{-4}\ kgm^2$, which is 2.9% more than the vendor's. The model estimates dimensions of $66 \times 66 \times 28.8\ mm^3$ with a mass of 0.242 kg, which is 48% of the vendor's assembly mass of 0.5 kg.
- RW 100: The MATLAB model predicts a moment of inertia of $6.063 \cdot 10^{-4}\ kgm^2$, which is within rounding error of the vendor's. The model dimensions are $86.4 \times 86.4 \times 28.8\ mm^3$ with a mass of 0.458 kg, which is 57% of the vendor's assembly mass of 0.8 kg.
- RW 150: The model dimensions are $101.8 \times 101.8 \times 38.4\ mm^3$ with a mass of 0.809 kg, which is 62% of the vendor's assembly mass of 1.3 kg.

Given that the Matlab model produces outputs within Astrofein's reaction wheel limits, they are deemed feasible. It should be noted that the flywheel size leaves roughly $70 - 90\%$ headroom; on average, the flywheel's mass accounts for 56% of the assembly mass. Thus, a headroom of $\frac{100}{56} - 100 \approx 80\%$ of the flywheel's mass can be added for the electronics to approximate the listed masses (i.e. RW25, $0.115 \cdot 1.8 \approx 0.2\ kg$, etc.). Moreover, as the reaction wheel assembly size increases, the discrepancy between the MATLAB estimate and the vendor-listed dimensions increases. Given that the sizes are well within the Vendor's specifications, it may be that different materials were selected.

6.2.7 Momentum wheel sizing

The dimensions of the momentum wheel are derived by equating the total mass of the reaction wheel assembly (three flywheels plus motors, i.e. three rotor-stator combinations) to that of a momentum wheel assembly (i.e. a single rotor-stator combination). Note that the maximum volume is derived from the design space stated in 6.2.3; it therefore does not matter how much the volume the material or outer dimensions occupy as long as it is within the constraints. Additionally, equating volumes would be an unfair comparison because, despite similar anatomy, the MW assembly's sizing and spacing differ from those of the RW.

From the RW comparisons made in 6.2.5, the computed RW flywheel mass is about 56% less than the reaction wheel assembly mass; the electronics and housing are assumed to use this mass. The 56% value is computed as the average of the differences across the RW25, RW35, RW100, and RW150 models. Henceforth, the total mass of the RW assembly is given by Equation 127.

$$m_{RW_{\text{assembly}}} = 3 \cdot \frac{m_{RW}}{0.56} \approx 5.4 \cdot m_{RW_{\text{fw}}} \tag{127}$$

The momentum wheel flywheel assembly is assumed to have a similar assembly mass because momentum wheels do not require heavier motors, as the torque requirements are deemed equal to those of the RWs. Thus, an optimistic mass of the momentum wheel flywheel can be computed by the right-hand side of Equation 128.

$$3 \cdot m_{RW_{\text{fw}}} < m_{MW_{fw}} < \left(1 - \frac{0.56}{3}\right) \cdot m_{RW_{\text{assembly}}} \approx 4.4 \cdot m_{RW_{\text{fw}}} \tag{128}$$

Given that the momentum wheel (MW) assembly is physically larger than the reaction wheel (RW) assembly, an equal flywheel-to-assembly mass ratio is considered plausible. This assumption would result in an MW flywheel mass of $m_{MW} = 3 \cdot m_{RW}$, as indicated by the left-hand side of Equation 128. However, this estimate is overly conservative because a momentum wheel is less densely packed than a reaction wheel. In fact, an MW assembly can have a hollow centre that is essentially empty, whereas an RW does not. Therefore, the MW flywheel mass is set at the midpoint, $m_{MW_{fw}} = 3.7 \cdot m_{RW_{\text{fw}}}$.

To summarise, the assembly mass of the RWs or MW is about 5.4 times the mass of a single reaction wheel flywheel ($m_{\text{assembly}} \approx 5.4 \cdot m_{RW}$); the reaction wheel flywheels take about 56% of this value and the momentum wheel flywheel about 69% (or total flywheel mass to total assembly ratio of 11:20 vs 14:20).

Based on these parameters, the MW flywheel is sized by first maximizing the outer radius, which most significantly affects the moment of inertia (see Equation 117). The wall thickness in the radial direction and the momentum wheel thickness (or height) are fixed at a minimum value of 5 mm. The outer radius is then incrementally increased by 0.1 mm until either the maximum mass ($m_{MW_{fw}} = 3.7 \cdot m_{RW_{\text{fw}}}$) or the maximum outer radius, defined as the smaller of dimensions b and c in Figure 66, is reached.

With the outer radius established, the thickness (or height) is incrementally increased by 0.1 mm until either the mass or the thickness (dimension a in Figure 66) reaches its maximum allowable value. At this stage, both the outer radius and the thickness (or height) are determined.

Finally, the inner radius is determined by incrementally decreasing its size by 0.1 mm, thereby increasing the wall thickness in the radial direction ($t_w = R_o - R_i$), until either the inner radius reaches $R_i = 0.1$ mm or the flywheel mass attains its design value of $m_{MW_{fw}} = 3.7 \cdot m_{RW_{\text{fw}}}$.

As an indication, by employing this optimisation, the following equivalent MW sizes are found for the RW25, RW35, RW100, and RW150 equivalent MWs given the constraints (a) $R_{o_{\max}} = 2.5 \cdot R_{RW}$ and (b) $t_{\max} = t_{RW_{\max}}$, and are called 'MW25','MW35','MW100', and 'MW150'. These are listed in Table 6.

Table 6: Design Parameters for MW Series Momentum Bias Wheels

Parameter	unit	MW25	MW35	MW100	MW150
Outer Radius	mm	62.5	127.5	125.0	187.5
Inner Radius	mm	57.5	122.5	120.0	182.5
Thickness	mm	25.4	25.6	49.0	57.6
Mass	kg	0.415	0.873	1.637	2.911
Volume Assembly	m^3	0.000312	0.001307	0.002405	0.006362
Flywheel Inertia	$kg{\cdot}m^2$	0.001498	0.013642	0.024583	0.099645
Relative Inertia (MW/RW)	-	27.4	69.7	40.5	62.6
Assembly Size	mm^3	125×125×25.4	255×255×25.6	250×250×49	375×375×57.6

The relative mass moment of inertia for a momentum wheel (MW) with an outer radius not exceeding $2.5 \cdot R_{o_{RW}}$ is approximately 50. Consequently, a flywheel of this size, rotating at the same angular velocity, possesses a mass moment of inertia about 50 times greater than that of the reaction wheel (RW) counterpart. If the design space allows, the MW radius may be further increased until the minimum allowable thickness or height of 5 mm is reached. In the limiting case where the design space imposes no dimensional constraints, the mass moment of inertia can become more than 1000 times greater, as shown in Table 7.

Table 7: Comparison of Reaction Wheel and Momentum Bias Wheel rotating at 5000 RPM

Parameter	unit	Reaction Wheel	Momentum Bias Wheel
Angular Momentum	Nms	0.05	56.3
Outer Radius	mm	28.0	430.9
Inner Radius	mm	25.2	425.9
Thickness	mm	28.0	5.0
Mass	kg	0.163	0.585
Volume Assembly	m^3	0.000228	0.002917
Inertia	$kg{\cdot}m^2$	9.63e-05	0.107431
Assembly Size	mm^3	28.0×28.0×28.0	861.8×861.8×5.0

This analysis indicates that maximising the effectiveness of an MW depends on optimising its size within the design space's feasible boundaries. A relative performance metric is therefore dictated by the design space allocated. To conclude, for subsequent analysis, the maximum design space yields the highest relative performance for an MW and provides a fair comparison.

6.2.8 Simulation output variables

Finally, the inertia matrices used for the simulation are assembled in Equation 129.

$$I_{MW} = \begin{bmatrix} 0 & 0 & 0 \\ 0 & I_{fw} & 0 \\ 0 & 0 & 0 \end{bmatrix} \qquad I_{RW} = \begin{bmatrix} I_{fw_{RW}} & 0 & 0 \\ 0 & I_{fw_{RW}} & 0 \\ 0 & 0 & I_{fw_{RW}} \end{bmatrix} \tag{129}$$

To facilitate a comparative analysis of satellite designs equipped with either an MW or an RW, the following parameters are stored:

- `RW_ri`: Inner radius of the reaction wheel [m].
- `RW_ro`: Outer radius of the reaction wheel [m].
- `RW_thickness_wheel`: Thickness of the reaction wheel [m].
- `RW_m_wheel`: Mass of the reaction wheel [kg].
- `RW_I_tensor`: Inertia tensor of the reaction wheel [kg m^2].
- `max_torque_safe`: Safe maximum torque [Nm].
- `MW_ri`: Inner radius of the momentum wheel [m].

- `MW_ro`: Outer radius of the momentum wheel [m].
- `MW_thickness_wheel`: Thickness of the momentum wheel [m].
- `MW_m_wheel`: Mass of the momentum wheel [kg].
- `MW_I_tensor`: Inertia tensor of the momentum wheel [kg m^2].

6.2.9 Mass budget FACA assembly

As an indication of the RW/MW assembly mass relative to the satellite mass, the percentage of $\frac{m_{fw_{\text{assembly}}}}{m_{total}}$ is presented in Figure 67. The exact values of the data are documented in appendix A.3.

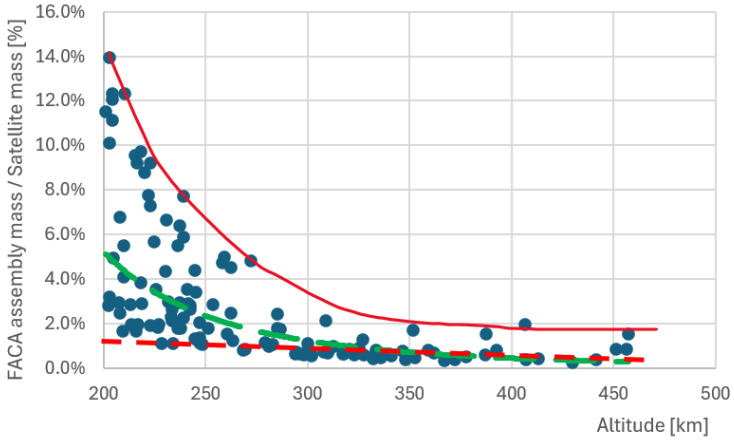

Figure 67: The percentage that the FACA assembly mass occupies relative to the total satellite mass versus altitude. The upper trend is depicted with a solid line (dark red), a power trendline is shown in the long-dashed line (green), and the lower linear trend is presented with a short-dashed line in red.

Generally speaking, the higher the orbit, the smaller the mass budget required for the ADCS. However, at each altitude, a spread in the mass budget is visible as numerous options exist. For example, at an altitude of approximately $200 - 210$ km, the mass of an FACA assembly can account for as little as 1.7% or as much as 14% of the total satellite mass. At these altitudes, this variation largely depends on the satellite's projected frontal area, as atmospheric disturbance torques scale with the square of the projected frontal area; thus, long, slender satellites have less frontal surface area than square ones, thereby requiring more miniature actuators.

At higher altitudes, i.e. 400 km, the residual dipole torque may be the dominant torque as was indicated in Figure 62. For that reason, to minimise FACA mass, engineers should strive to bring down the residual dipole as much as possible, too.

At altitudes that are not examined in this work, < 200 km and > 457 km, this graph remains inconclusive. However, given the trends presented, for < 200 km, one should instead account for larger mass budgets than smaller ones, primarily when the satellite orients itself in configurations with a larger projected area, as explained in Figure 46. For > 457 km, it seems that 1 to 2% will suffice.

Hence, while first-order approximations of the disturbances are unknown, it is advisable to initially budget conservatively using the upper trend line (solid), optimistically using the lower trend line (short-dashed), and otherwise use a power trend line as depicted by the long-dashed line. This will serve as a helpful starting point until more refined disturbance estimates are computed.

6.3 Actuator torque and control

To counter the effects that external disturbances cause on the orientation of the satellite, a (set of) flywheel(s) is used to stabilise the satellite in its desired orientation. To achieve this, the ADCS must determine the attitude and angular rate (see 6.3.1). Then, the controller—in this study, a PID controller

(see 6.3.2) combined with feed-forward control (see 6.3.3)—calculates the required control torque to correct deviations. The PID gains are tuned automatically using an optimisation algorithm (see 6.3.4). Additionally, various constraints ensure that the operational limits of the FACAs are respected (see 6.3.5).

6.3.1 Sensed attitude

In reality, the ADCS relies on various sensors to determine the satellite's orientation, as discussed in 2.1.1. For this study, the 'sensed' or 'measured' attitude of the satellite is obtained by computing the rotation from the BFRF to the LVLH frame, since it will be pointing in NADIR direction. Assuming perfect sensing, this process involves the following steps.

The rotation from the body frame 3.1.5 to the LVLH frame 3.1.4 is obtained by multiplying the transpose of the LVLH-to-inertial rotation matrix F_L (Equation 35 presented in 3.2.5) with the body-to-inertial DCM F_B (given by Equation 36 in 3.2.6), which gives the relative rotation matrix T_{LB} shown in Equation 130.

$$T_{LB} = T_{IL}^T T_{IB} = T_{LI} T_{IB} = F_L^T F_B \tag{130}$$

The rotation matrix T_{LB} is then converted into Euler angles using the built-in MATLAB `rotm2eul` function [55], which returns the orientation in terms of roll ϕ, pitch θ, and yaw ψ relative to the LVLH frame, in Equation 131.

$$\begin{bmatrix} \phi \\ \theta \\ \psi \end{bmatrix} = \text{rotm2eul}(T_{LB}, \text{'XYZ'}) \tag{131}$$

These Euler angles represent the attitude error. Under perfect sensing assumptions, these measurements are free of noise. However, in real-world conditions, sensor measurements are affected by errors and uncertainties. To incorporate this aspect into simulations, the measurement errors can be modelled as additive Gaussian (normally distributed) noise. The process involves defining the standard deviation for each Euler angle component based on sensor specifications, then adding randomly generated noise to the ideal measurements:

$$\begin{bmatrix} \phi \\ \theta \\ \psi \end{bmatrix}_{\text{noisy}} = \begin{bmatrix} \phi \\ \theta \\ \psi \end{bmatrix}_{\text{perfect}} + \sigma_N \begin{bmatrix} \mathcal{N}(0,1) \\ \mathcal{N}(0,1) \\ \mathcal{N}(0,1) \end{bmatrix} \tag{132}$$

Here, $\mathcal{N}(0,1)$ denotes a standard normal random variable generated with `randn` in MATLAB. When employing attitude sensors using an adaptive hybrid method discussed in [115] in 2021, the best-case filtered maximum error was in the range of $5 \cdot 10^{-5} - 9 \cdot 10^{-4}$ radians or about $0.003 - 0.05$ degrees. Although sensing and filtering techniques might have advanced to greater accuracy, these quantities provide a good indication of realistic performance. Especially considering that this thesis examines various satellite sizes and orbits.

Hence, the constant sensor noise is therefore set to approximately 0.003 degrees of white noise, corresponding to 10.8 milliarcseconds or $5 \cdot 10^{-5}$ radians, with peak values twice that. A short sample of this noise is presented in Figure 69. Filtering techniques are outside the scope of this study and are therefore left unexamined. Thus, rather than relying on the noise generation and filtering techniques discussed in [115], the noise generation process in this work is simpler and is explained below.

To ensure that all simulations achieve the same attitude-determination performance, a constant time-dependent noise vector is pre-allocated using Gaussian noise with a standard deviation of 0.001 rad. Next, a moving average, Equation 133, is applied with a pull rate of $F_{\text{read-out}} = [2, 10, 50, 100, 200]Hz$, see Figure 68 until most noise lies within the $5 \cdot 10^{-5}$ radian target.

$$y[t] = \frac{1}{F_{\text{read-out}}} \sum_{k=0}^{F_{\text{read-out}}-1} x[t-k] \tag{133}$$

Herein, $x[t]$ is the input signal at time t, $y[t]$ is the filtered output signal, and $F_{\text{read-out}}$ is the window length (number of samples averaged). For each time step t, the filter:

1. Takes the last $F_{\text{read-out}}$ input samples:

$$x[t],\, x[t-1],\, x[t-2],\, \ldots,\, x[t-(F_{\text{read-out}}-1)]$$

2. Sums them:

$$\sum_{k=0}^{F_{\text{read-out}}-1} x[t-k]$$

3. Divides by $F_{\text{read-out}}$ to get their average.

Thus, $y[t]$ is the average of the most recent $F_{\text{read-out}}$ samples of $x[t]$. Moreover, by introducing correlation between neighbouring output samples, the signal is smoothed, reducing rapid fluctuations (high-frequency components). It now acts as a low-pass filter that attenuates high-frequency components; therefore, low-frequency components are more common (higher frequencies are less common) when compared to using the `randn` function directly at $2 \cdot 5 \cdot 10^{-5}$ rad in MATLAB.

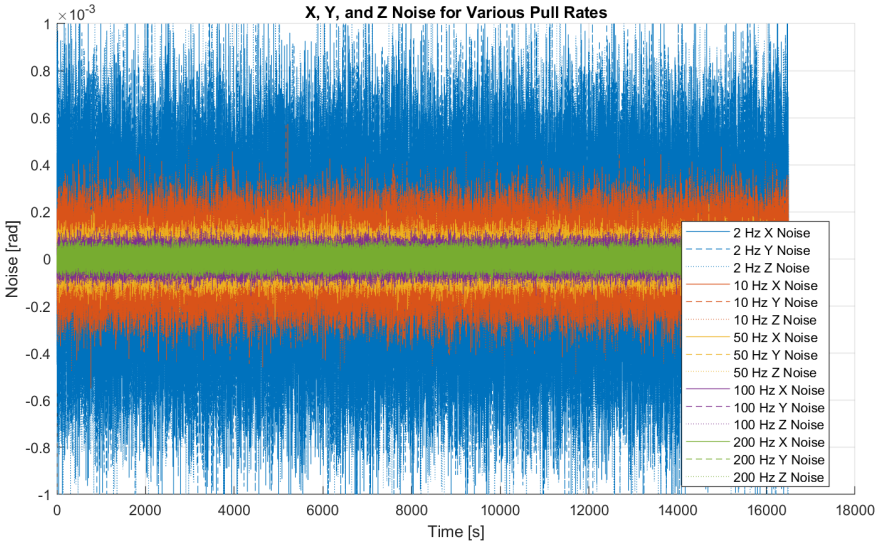

Figure 68: Attitude measurement noise for various pull rates

When comparing this moving-average approach with the best-case performance, the 200 Hz moving average is considered, as this performance (constant $0.5 \cdot 10^{-4}$ *rad*; peak $1 \cdot 10^{-4}$ *rad*) corresponds to the filtering techniques discussed in [115]. As an indication of the noise profile, the first 200 seconds of the time-dependent noise are presented in Figure 69.

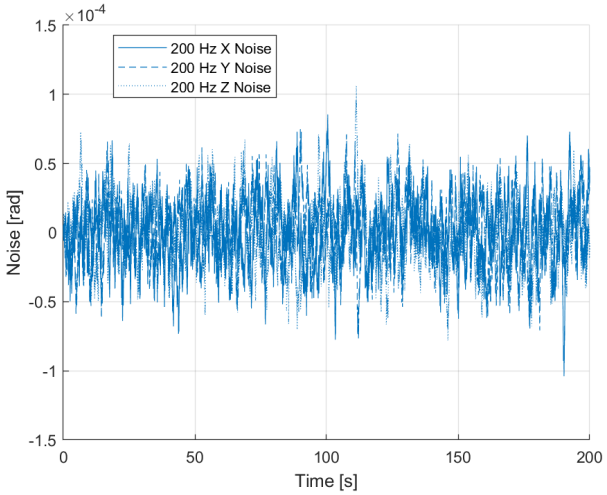

Figure 69: X, Y, and Z Noise for a 200 Hz Pull Rate

6.3.2 P(I)D controller

The main objective is to design a controller that controls the flywheel's output torque to exert a desired control torque T_{control} and stabilise the satellite in its desired orientation. Physically, this means designing a controller that converts a measured attitude into a torque that drives the flywheel, as done in *chapter 6* of '*Efficient and High Precision Momentum Bias Attitude Control for Small Satellite*' [60].

Since the goal is to model the satellite's behaviour, a low-fidelity control law, a proportional-derivative (PD) controller, is often chosen for its simplicity and robustness [107], [38], see Equation 134. When adding an integral error to the PD controller, it is referred to as a proportional-integral-derivative (PID) controller, as presented by the third term on the right-hand side in Equation 135. The performance of both the PD and the PID controllers is dependent on the 'correctness' of the measured attitude error and the tuning of the proportional gains K_p, the derivative gains K_d, and, for the PID controller, also the integral gains K_i. These gains must be tuned to an appropriate value to achieve the desired performance. This tuning is discussed in section 6.3.4.

$$T_{\text{control}_{|PD}} = -K_p \cdot error_{\text{measured}} - K_d \cdot \omega_{B_{\text{measured}}} \tag{134}$$

The integral of the measured error is numerically computed using Euler integration $error_{\text{integral}}(t_i) = error_{\text{integral}}(t_{i-1}) + error_{\text{measured}}(t_i) \cdot dt$, whereby the subscript i denotes the time step.

$$T_{\text{control}_{|PID}} = -K_p \cdot error_{\text{measured}} - K_d \cdot \omega_{B_{\text{measured}}} - K_i \int_{t_0}^{t_i} error_{\text{measured}} dt \tag{135}$$

For this study, a set of Euler angles is chosen as the measure of error, as shown in Equation 136, which provides a more intuitive representation of the satellite's orientation compared to using the vector part of the quaternions; both are valid. The satellite's attitude error is defined with respect to the desired LVLH frame, as discussed in 6.3.1.

$$error_{\text{measured}} = \begin{bmatrix} \phi \\ \theta \\ \psi \end{bmatrix} \tag{136}$$

This attitude measurement can also be used to determine the rotational rate of the satellite by taking the difference between the last state and the current state, such that $\omega_{B_{\text{measured}}} = \frac{error_{\text{measured}}(t_i) - error_{\text{measured}}(t_{i-1})}{dt}$. To reduce computational costs, the rotational rate is assumed to be measured perfectly, and thus, the angular rate is used directly as an input for the measured rotational rate, as shown in Equation 137.

$$\omega_{B_{\text{measured}}}(t_i) = \frac{error_{\text{measured}}(t_i) - error_{\text{measured}}(t_{i-1})}{dt} \approx \omega_B \quad \rightarrow \quad \omega_{B_{\text{measured}}} = \omega_B \tag{137}$$

The attitude control system then uses these error signals to generate appropriate control torques. The errors are scaled via the control gain matrices as shown in Equation 138. Subscript 'D' denotes the diagonal terms (the in-axis gains), and the off-diagonal terms are referred to as 'cross-terms'. They are denoted by the subscript 'c' and account for correcting additional cross-axis coupled errors.

$$K_p = \begin{bmatrix} K_{p,D} & K_{p,c} & K_{p,c} \\ K_{p,c} & K_{p,D} & K_{p,c} \\ K_{p,c} & K_{p,c} & K_{p,D} \end{bmatrix} \quad K_i = \begin{bmatrix} K_{i,D} & K_{i,c} & K_{i,c} \\ K_{i,c} & K_{i,D} & K_{i,c} \\ K_{i,c} & K_{i,c} & K_{i,D} \end{bmatrix} \quad K_d = \begin{bmatrix} K_{d,D} & K_{d,c} & K_{d,c} \\ K_{d,c} & K_{d,D} & K_{d,c} \\ K_{d,c} & K_{d,c} & K_{d,D} \end{bmatrix} \tag{138}$$

6.3.3 Feed-forward control

When a set of flywheels is spun about multiple axes, the net momentum vector changes its direction when an angular acceleration is applied to one or more of the flywheels. Because of the other flywheels being in a spun-up state and the satellite having an angular velocity also, gyroscopic precession will take effect. For that reason, a spun-up or spool-down of a flywheel causes a gyroscopic torque perpendicular to the spin axis. For a set of orthogonal flywheels aligned with the principal axis, this gyroscopic torque must be pre-compensated for. This compensation is done via the second term on the right-hand side of Equation 139. It should be noted, however, that a set of reaction wheels requires this feed-forward

control term, but that a single-axis momentum bias wheel does not, as the cross-product will be zero anyway.

$$T_{\text{control}} = T_{\text{control}} + \omega_B \times h_{fw} \tag{139}$$

Herein, ω_B is the rotational rate of the satellite expressed in the BFRF, and $h_{fw} = I_{fw} \cdot \omega_{fw}$ is the angular momentum of the (set of) flywheel(s) $[kg \cdot m^2/s]$ with their moment of inertia I_{fw} $[kg \cdot m^2]$ at angular velocity ω_{fw} [rad/s].

6.3.4 Tuning the PID controller gains

Manual tuning of PID gains is feasible for a single set of momentum or reaction wheels, but becomes impractical when simulating numerous scenarios. Therefore, automatic tuning is necessary. The built-in optimiser function `fmincon` in MATLAB [50] is employed to solve the constrained non-linear optimisation problem. The optimiser algorithm is selectable within the function. The `active-set` algorithm demonstrates strong performance—good agreement with the objective without causing instabilities—and is therefore selected. Alternative algorithms include `Interior-point` and sequential quadratic programming (`SQP`). However, during testing, the latter two algorithms led to gains whereby instabilities occurred towards the end of the second orbit. All those optimisation processes minimise a cost function that penalises angular rates and attitude errors across half an orbit, thereby aiming to achieve precise and stable pointing while adhering to actuator constraints.

The PID controller incorporates both diagonal and cross-coupling terms to provide control authority along the principal axis. The gains to be optimised include the proportional, integral, and derivative gains for both the diagonal and cross-coupling terms, as shown in Equation 138.

The cost function is defined in Equation 141. The bounds are chosen through trial and error to suit the scope discussed in chapter 2, thereby preventing excessively large values that could negatively impact computational costs. Specifically, the lower and upper bounds, lb and ub, are set in Equation 140, and an initial guess of $g_0 = \frac{ub}{10}$. The upper bounds for the diagonal terms are much larger than for the cross-terms because the feed-forward control (see 6.3.3) already accounts for most of the precession errors generated.

$$\begin{aligned} lb &= [0, 0, 0, 0, 0, 0] \\ ub &= [100, 0.1, 1000, 0.1, 0.001, 1] \end{aligned} \tag{140}$$

The cost function, $C(g)$, Equation 141, quantifies the performance of the PID controller with a given set of gains. It is defined as the weighted sum of the squared angular rates expressed in the BFRF (named PQR, ω_B), and the squared attitude errors, $E = error_{\text{measured}}$ over half an orbit, calculated at each time step t. Half an orbit is chosen as a good compromise between computational cost and performance. In half an orbit, the disturbances modelled (see chapter 5) have seen sufficient alterations to prevent (too much) overfitting of the controller performance. The attitude errors are weighted 100 times more than the angular rates, as pointing precision and accuracy are prioritised; given that the LVLH orientation should align with the NADIR pointing objective, the angular rates should automatically follow. The angular rates are included in the cost function to prevent artificial fast oscillations about the desired attitude (which is now penalised).

$$C(g) = \sum_{t=1}^{N} \left(|P(t)|^2 + |Q(t)|^2 + |R(t)|^2 + 100 \cdot |E_x(t)|^2 + 100 \cdot |E_y(t)|^2 + 100 \cdot |E_z(t)|^2 \right) \tag{141}$$

`fmincon` accepts tolerances as stopping criteria for the optimisation algorithm, balancing the desire for an accurate solution with the computational cost of the optimisation process. For this study, 'StepTolerance', 'OptimalityTolerance', and 'ConstraintTolerance' are set to 10^{-3} to achieve a balance.

Finally, the optimised PID gains, $g_{\text{optimised}}$, are then used to construct the full PID gain matrices (see Equation 138) for implementation in the satellite's ADCS.

6.3.5 Actuator constraints

Control torque saturation and wheel speed limits are imposed to ensure that reaction wheels operate within their physical constraints. These constraints can arise from mechanical, operational, or motor

specifications limitations. The control torque T_{control} demanded by the ADCS is first saturated to the maximum torque that each MW or RW can generate due to torque production limits. Demanding torque beyond these limits results in saturation, in which the wheel delivers only its maximum torque. This saturation is implemented on a per-axis basis ($i = 1, 2, 3$ for XYZ), as shown in Equation 142.

$$T_{\text{control},i} = \begin{cases} T_{\text{control},i} & \text{if } |T_{\text{control},i}| \leq |T_{\text{max},i}| \\ \text{sign}(T_{\text{control},i}) \cdot |T_{\text{max},i}| & \text{if } |T_{\text{control},i}| > |T_{\text{max},i}| \end{cases} \tag{142}$$

In which $T_{\text{control},i}$ is the control torque demand for the i-th wheel (axis), and $T_{\text{max},i}$ is the maximum torque that the i-th wheel can generate.

After torque saturation is applied, wheel speeds are evaluated relative to their maximum allowable rotational velocity values. When a wheel reaches its speed limit, further acceleration in that direction is no longer possible. If a wheel speed exceeds its limit, it is deemed saturated, as described by Equation 143, and the corresponding wheel acceleration is set to zero, according to Equation 144.

$$\omega_i = \begin{cases} \omega_i & \text{if } |\omega_i| \leq |\omega_{\text{max},i}| \\ \text{sign}(\omega_i) \cdot |\omega_{\text{max},i}| & \text{if } |\omega_i| > |\omega_{\text{max},i}| \end{cases} \tag{143}$$

If saturation occurs:

$$\alpha_{\text{wheel}_i} = 0 \quad \text{if } |\omega_i| > |\omega_{\text{max},i}| \tag{144}$$

Where ω_i is the angular speed of the i-th wheel, $\omega_{\text{max},i}$ is the maximum allowable angular speed for that wheel, and α_i is the angular acceleration of the i-th wheel.

Finally, the applied control torque is determined based on the wheel accelerations and the wheel inertia tensor:

$$T_{\text{control}} = I_{\text{wheel}} \cdot \alpha_{\text{wheel}} \tag{145}$$

Herein, I_{wheel} denotes the inertia tensor of the wheel assembly, and α_{wheel} represents the vector of wheel angular accelerations. This calculation ensures that the applied torques correspond to the achievable accelerations within the reaction wheels' physical constraints.

6.4 Example controlled satellite employing a momentum wheel

To assess the effect of a PID controller on the stabilising performance of a satellite subject to both cumulative and cyclic disturbances, a satellite spinning about its intermediate axis is chosen, as this configuration would otherwise be unstable without control. A complete derivation of the instability problem is given in [75]. A physical example of the intermediate axis theorem is illustrated in a *Veritasium* video [104].

The moment of inertia tensor for this pitch-stabilised (Y_B) satellite example is given in Equation 146. On the left-hand side, the satellite's inertia tensor is given (note that $I_{xx} < I_{yy} < I_{zz}$), and on the right-hand side, the inertia tensor of the momentum wheel assembly is given. In the latter, all elements are set to zero except for I_{yy} as there is only one MW present. Furthermore, the momentum wheel speed ω_{MW} is initialised at 5500 RPM in the direction of the satellite's initial pitch rate.

$$I_{\text{total}} = \begin{bmatrix} 0.94 & 0 & 0 \\ 0 & 2.13 & 0 \\ 0 & 0 & 2.51 \end{bmatrix} \quad [kg \cdot m^2] \qquad I_{\text{wheel}} = \begin{bmatrix} 0 & 0 & 0 \\ 0 & 0.0634 & 0 \\ 0 & 0 & 0 \end{bmatrix} \quad [kg \cdot m^2] \tag{146}$$

The introduction of noise into the measured errors does not significantly affect the performance of an MW-stabilised satellite, because it can only control one axis. In fact, it has hardly any impact on performance. This outcome is anticipated because the MW imparts a substantial bias to the satellite's orientation. The gyroscopic stiffness is sufficiently large to dominate the satellite's motion regardless of measurement accuracy. To demonstrate this form of robustness, the following analysis is conducted exclusively with noise. The noise is accounted for as discussed in section 6.3.1.

6.4.1 Unstable satellite with a PD-controlled MW

For this setup, a PD-controlled MW was chosen. As discussed in section 6.3.4, the controller gains must be tuned for the desired performance, which is done manually for this example. Here, the diagonal proportional gains are $K_{p,D} = 0.1$ and the diagonal derivative gains are $K_{d,D} = 0.05$. All cross-product gains are set to zero ($K_{p,c} = K_{i,c} = K_{d,c} = 0$).

The results of the satellite are shown in Figure 70. Several behaviours are identified: high-frequency oscillations are modulated by a lower-frequency envelope; both attitude and angular velocity errors remain bounded (indicating stability); and the pitch error gradually increases over time due to cumulative torques. The high-frequency oscillations arise from precession (high-frequency oscillations) and nutation (high-frequency oscillations with a relatively small amplitude modulated on the precession). At the same time, the cyclic nature of the disturbances present causes the lower frequency envelope on which both the precession and nutation are modulated, similar to the PID-controlled scenario displayed in Figure 71, whereby the precession and nutation are clearly visible when magnified in Figure 72.

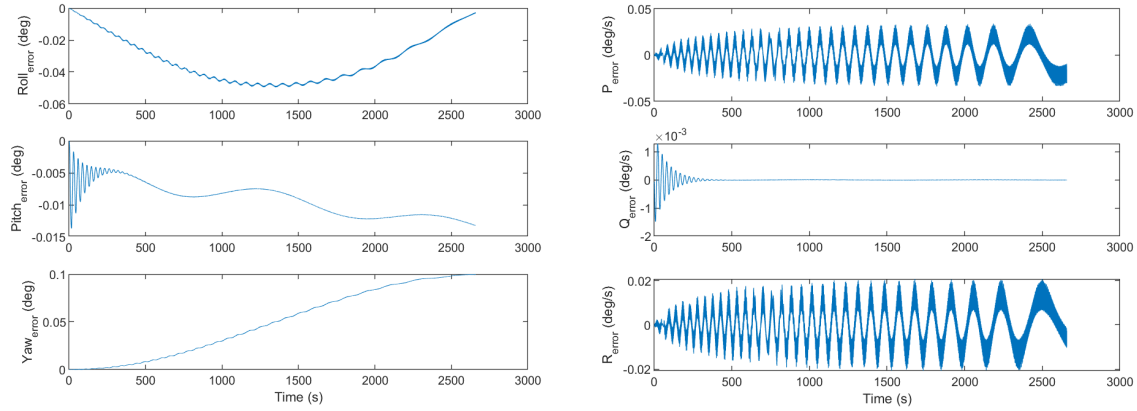

(a) Attitude error

(b) Angular rate error

Figure 70: Disturbed (cyclically and accumulatively) satellite employing a PD-controlled MW in the pitch axis (Y_B)

Another notable phenomenon occurs: the periods of the roll and yaw rate widen as time progresses for the PD-controlled case, because the energy that would otherwise be allocated to the pitching motion is now redirected to the uncontrolled axes (the area below the curves becomes larger). This is most visible towards the region of $t = [2000, 2500]s$ in Figure 70.

6.4.2 Unstable satellite with a PID-controlled MW

Similar to the PD-controlled satellite (see 6.4.1), the PID-controlled satellite is also stable as the diagonal integral gains are set to a sufficiently small value, $K_{i,D} = 0.001$, while not altering the other (PD-)controller gains. Moreover, it improves performance along the pitch axes by attempting to reduce the integral error to zero. This is especially evident in the pitch error of Figure 71a when compared to the results in Figure 70a. The pitch attitude error now oscillates about zero degrees.

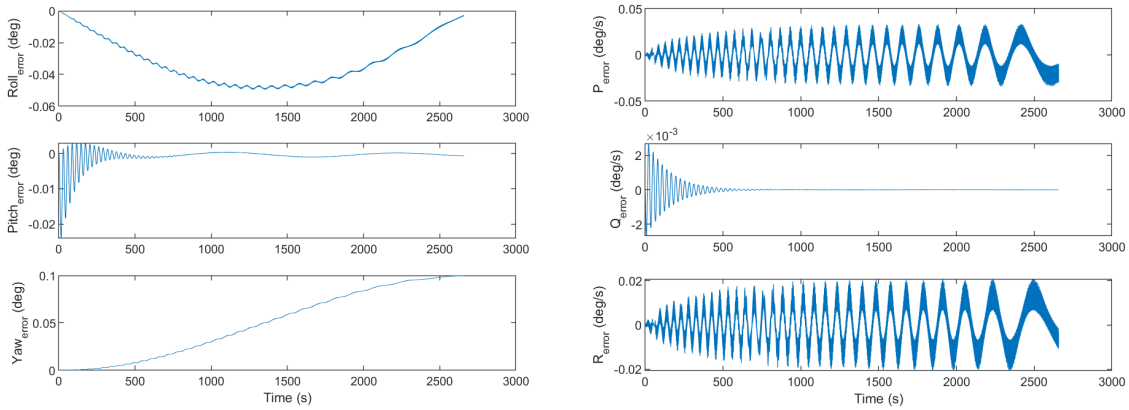

(a) Attitude error (b) Angular rate error

Figure 71: Disturbed (cyclically and accumulatively) Satellite employing a PID-controlled MW in the pitch axis (Y_B)

6.4.3 Precession and Nutation of an unstable satellite with a PID-controlled MW

Inherent to an unsymmetrical satellite, the moment of inertia tensor is not symmetric. That means that precession and nutation (the wobbling motion where the axis of rotation traces out a cone in space) will both be present when torques are experienced about multiple axes [74]. This precession rate depends on the magnitude of the torque and the satellite's moment of inertia. As a consequence, high-frequency oscillations are present in all three principal axes, whereby most of the energy is exchanged between the uncontrolled axes, as is visible in Figure 72b. For each period, the yaw and roll angles are out of phase, and the yaw rate lags the roll rate by approximately 90 degrees. It should be noted that the precession is a relatively slow-frequency high-amplitude oscillation compared to the faster low-amplitude nutation. These effects are less visible in the attitude errors presented in Figure 72a because the disturbance torques primarily govern the attitude errors.

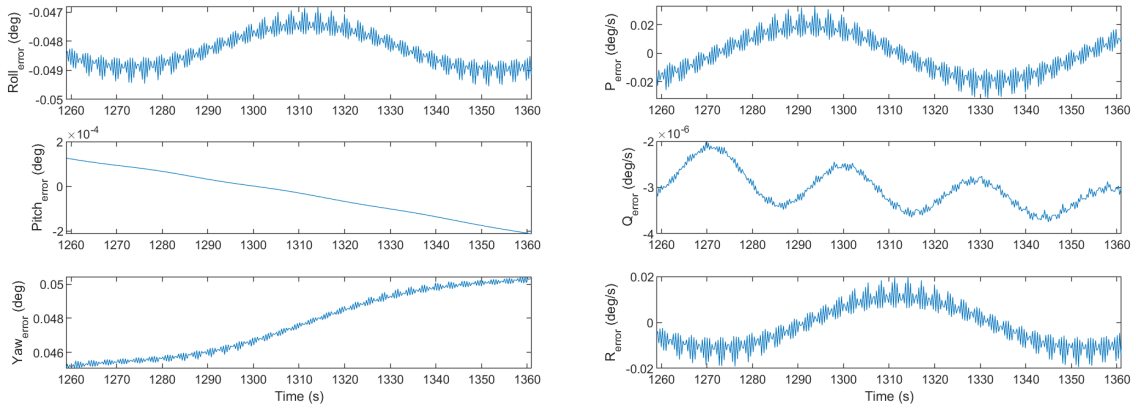

(a) Attitude error (b) Angular rate error

Figure 72: Zoomed in version of Figure 71 about $t = [1259, 1361]s$ to indicate precession and nutation.

6.5 Example P(I)D controlled satellite employing a set of reaction wheels

Similar to section 6.4 wherein the attitude behaviour of a momentum wheel controlled satellite is discussed, here the same satellite is considered with a set of three orthogonally oriented reaction wheels that are aligned with the principal axis. To be able to compare the performances, the inertia tensor I_{total} is taken from Equation 146. Likewise, the wheel tensor is determined following the rationals discussed in section 6.2, and is given in Equation 147. The reaction wheels are initialised with a wheel speed ω_{RW} of 100 RPM rotating about the body axis.

$$I_{\text{wheel}} = \begin{bmatrix} 0.0031 & 0 & 0 \\ 0 & 0.0031 & 0 \\ 0 & 0 & 0.0031 \end{bmatrix} \quad [kg \cdot m^2] \tag{147}$$

Contrary to an MW-stabilised satellite, a RW-stabilised satellite is significantly affected by the introduction of noise. To display the significance, first an example scenario is showcased without noise in section 6.5.1, after which noise is added in section 6.5.2.

6.5.1 RW example P(I)D excluding noise

When considering a proportional-derivative control law, the reaction wheels generate a torque that is proportional to the attitude error and is damped by the satellite's rotational rate. Considering that the set of reaction wheels can act on each axis, and the control law can pre-compensate (feed-up) for the coupling due to precession, the performance is expected to be at least as good as the MW-controlled satellite. This expectation is confirmed when examining Figure 73 and comparing it to the MW results shown in Figure 71. Not only is the performance about the pitch axis approximately equal, but the attitude and rate errors about the roll and yaw axes have improved significantly. A precise numerical comparison is not necessary at this point, as the controller gains are taken from the manual MW tune.

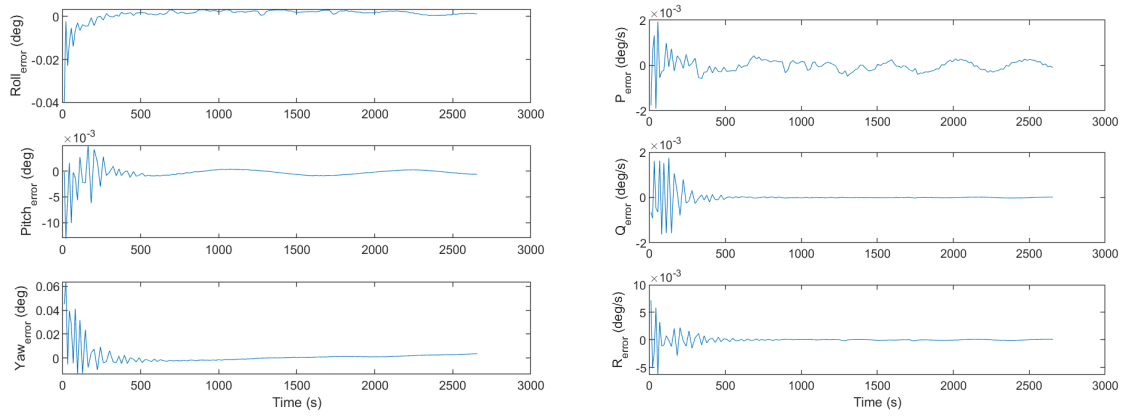

(a) Attitude error

(b) Angular rate error

Figure 73: Disturbed (cyclically and accumulatively) Satellite employing an orthogonal set of PD-controlled RWs

To expand the PD-controlled scenario into a PID-controlled satellite, the integral gains from the MW tune have been adopted again. In the unoptimized scenario, the performance differences between the PD-controlled and PID-controlled satellites are minimal. In fact, as in this case, where $K_{i,D} = 10^{-3}$ and the PD-controlled errors oscillate about zero, the integral error does not grow much, resulting in a negligible change in outcome. For completeness, the attitude and rate error plots are presented in Figure 74. Note that it is visually identical to Figure 73.

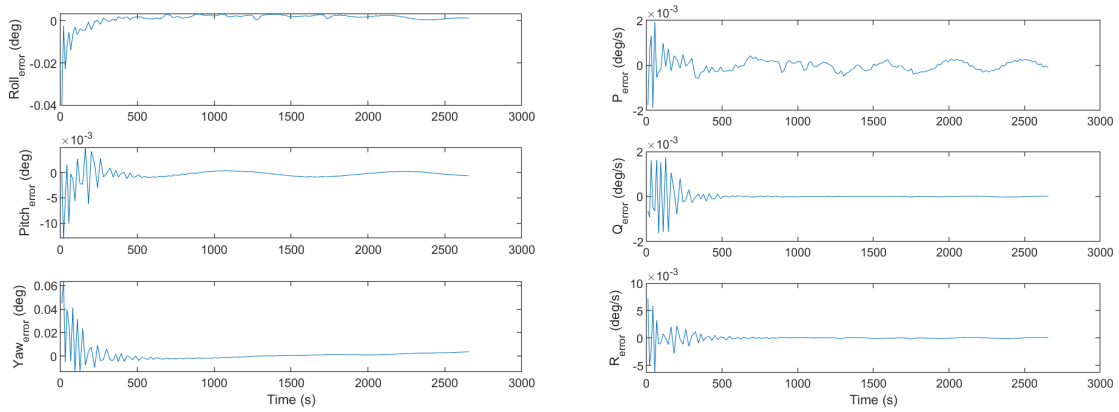

(a) Attitude error (b) Angular rate error

Figure 74: Disturbed (cyclically and accumulatively) Satellite employing an orthogonal set of PID-controlled RWs

Based on these observations, it is expected that a tuned PD controller will perform approximately as well as a PID-controlled satellite.

6.5.2 RW example P(I)D including noise

The introduction of noise, as discussed in section 6.3.1, degrades sensed performance and increases measured error. Consequently, with equal gains, noise is expected to reduce the satellite's stabilising performance. This is indeed observed when comparing the scenario with noise, for both the PD-controlled and the PID-controlled cases, to the scenario that excludes noise. Note that the controlled gains remained unaltered.

PD-controlled with noise
Figure 75 displays the results obtained for the PD-controlled scenario with noise. The results resemble a PD-controlled momentum wheel shown in Figure 70 more than the PD-controlled reaction wheel scenario presented in Figure 73. These findings suggest that, when noise is taken into account, disturbances primarily determine pointing accuracy.

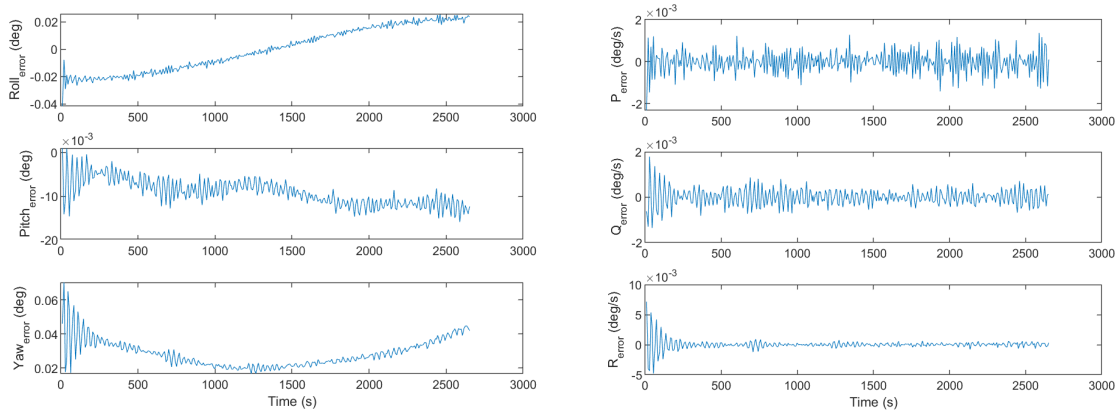

(a) Attitude error (b) Angular rate error

Figure 75: Disturbed (cyclically and accumulatively) satellite employing an orthogonal set of PD-controlled RWs whereby sensed noise is active

PID-controlled with noise
Contrary to the findings for the PD-controlled scenario with noise, adding an integral gain will reduce the satellite's sensitivity to the noise. The integral gain will align the satellite over time because it

compensates for the accumulation of attitude errors. This compensation is clearly visible in Figure 76a, because the attitude errors will approach zero and remain bounded by the noise levels present.

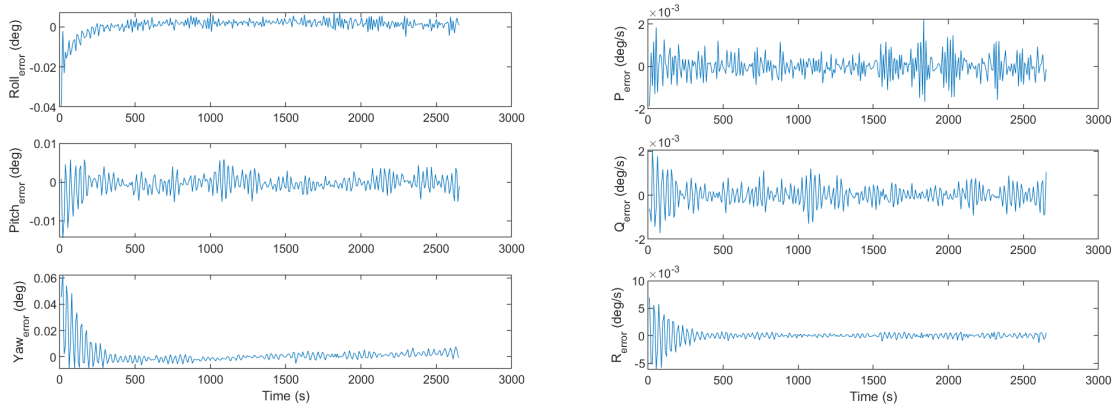

(a) Attitude error

(b) Angular rate error

Figure 76: Disturbed (cyclically and accumulatively) satellite employing an orthogonal set of PID-controlled RWs whereby sensed noise is active

7 Tradespace exploration Setup

This chapter generates and filters out irrelevant samples that will be used to make a performance trade-off between MWs and RWs. This way, the generation of relevant samples within the trade space is minimised while preserving sufficient variability in the Tradespace exploration. In particular, this chapter answers the following research questions:

(B.2) *How can the trade-space of various orbits and designs be reduced to a manageable set of key driving parameters?*
More precisely, the strategy used to generate (section 7.1) and filter (section 7.2) input samples for a satellite design simulation. This process accounts for various parameters and constraints to produce a set of valid design configurations. In these design configurations, several notable trends are highlighted in section 7.3.

(A.4) *For representative small satellite designs, how do these disturbance torques vary with key orbital parameters (altitude, inclination, RAAN) and satellite geometry and attitude?*
The filtered sample set (within feasible constraints), i.e., the trade space, is further reduced by analysing variations in disturbances across various inclinations and RAANS, thereby reducing computational cost in section 7.4.

7.1 Generating samples

As indicated in Figure 77, the first step in simulating RW-controlled and MW-controlled satellites is to generate feasible samples named 'Create Sample Set'. To develop feasible samples, three consecutive steps are taken. First, in this section, inputs per parameter that fall within the scope of this study are presented and discussed. Secondly, combinations of these parameters are evaluated against physical limitations (satellite configuration requirements and design constraints) in section 7.2. Thirdly, as a verification step, the observed trends and validity in the input sample space are discussed in section 7.3.

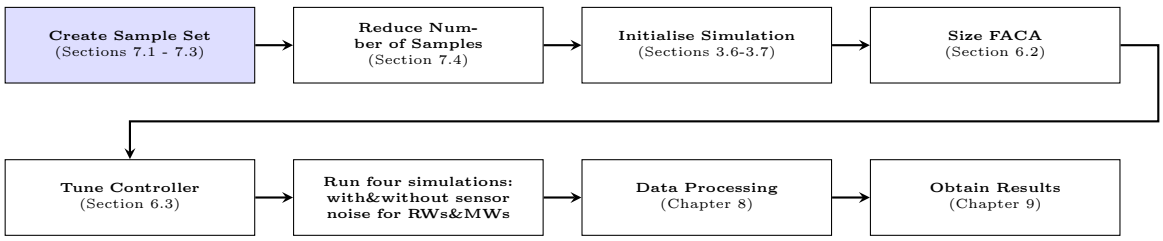

Figure 77: Simulation setup flowchart: Create Sample Set

Chapter 2 detailed the scope of this study, which is used to generate input samples for the simulation. Table 8 summarises the key parameters used as independent inputs for the satellite design simulation, along with their respective units and ranges. The solar array ranges are based on the readily available technologies between 2021 and 2025 ([103], [111]). The upper bound is scaled by approximately 20% to ensure that the results remain relevant as these technologies advance. A uniform distribution within the specified ranges is used to create samples.

Parameter	Description & Rational	Range/Value
Orbital Elements		
h	Altitude: impacts ground resolution	$[200, 650]$ km
i	Inclination: access specific regions on Earth	$[0, 180]$ deg
$RAAN$	Right Ascension of the Ascending Node: access specific regions on Earth	$[0, 360]$ deg
Spacecraft Design (Bus)		
Hb	Circular aperture size: impacts ground resolution	$[0.1, 0.8]$ m
ρ_{bus}	Average bus density: impacts mass moment on inertia	$[800, 1400]$ kg/m^3
Spacecraft Design (Solar Arrays)		
W_kg	Solar Array Power-to-Mass Ratio: affects the overall mass budget	$[70, 200]$ W/kg
W_m2	Solar Array Power Density: influences the required surface area	$[250, 450]$ W/m^2
W_m3	Solar Array Power Volume Density: constrains volume designs	$10^3 \cdot [40, 60]$ W/m^3
Disturbances		
k_cg	Centre of Gravity Offset Scaling Factor: impacts the inertia distribution	$1/100 \cdot [0, 10]$
k_SRP	Solar Radiation Pressure Centre of Pressure Offset Scaling Factor: 4.8.2	$1/100 \cdot [0.5, 5]$
k_AD	Aerodynamic Drag Centre of Pressure Offset Scaling Factor: **??**	$1/100 \cdot [0.5, 5]$
k_RD	Residual Dipole Moment: 4.6.1	$[0, 0.05]$ Am^2
GSD Minimum Theoretical & Instrument Parameters		
SR_{max}	Maximum Spatial Resolution: 2.5.4	1.0 m
λ	Observable Wavelengths: 2.4	$[470 - 830] \cdot 10^{-9}$ m
N	Maximum Number of Mirror Reflections: 2.5.3	7
d	Pixel Size: 2.5.3	$2.5 \cdot 10^{-6}$ m
Q	Quality Factor: 2.5.3	1/1.3

Table 8: Satellite Design Parameters and Ranges

To size the satellite's bus, it is assumed to be cube-shaped or rectangular-shaped in both the NADIR and velocity directions. This ensures that the satellite bus can accommodate the imager, actuators, and other components required for operation. This lengthening also increases the range of possible focal lengths, given the number of reflections permitted. The scaling in both directions can be one to remain cubical (the aperture size), up to three times to assume a rectangular box.

7.2 Sample filtering

Considering all possible combinations of the ranges listed in Table 8 leads to physically impossible scenarios. For that reason, certain requirements and constraints must be imposed. Samples that do not meet these requirements are excluded from simulation.

Satellite configuration requirements:
The simulation sample set must contain satellite configurations that can fulfil the specified nadir-pointing objectives. The samples are therefore tested against the two requirements enumerated below. These two requirements are posed to select feasible sizes for both the satellite bus and deployable solar arrays. The first requirement ensures that the imager fits within the satellite bus and that the satellite bus is large enough to meet the spatial-resolution requirement. The second requirement limits the size of the deployable solar array to avoid unnecessarily large arrays. Together, they form the basis of the satellite configuration as described in section 2.3.

R1 Satellite configurations that do not meet the target spatial resolution should be disregarded from the simulation set. Thus: *the spatial resolution SR shall be smaller than one meter*,

$$SR = h \tan\left(1.22 \frac{\lambda_{max}}{H_b}\right) < SR_{\max} = 1[m]$$

R2 To avoid deploying large solar arrays, a maximum power-generation capability is specified as peak power. Thus: *the peak power delivered from deployed solar arrays shall be smaller than 2 kW*,

$$\text{Peak Power} = 2 \cdot W_{m2} \cdot A_{sp} < 2000[W]$$

Satellite design constraints:
To ensure a feasible and manufacturable design, some design constraints have been posed. These constraints enable the dimensioning and sizing of satellite configurations deemed representative of a preliminary design. Any satellite configuration that does not meet these constraints is excluded from the simulation sample set.

C1 To prevent unrealistically light or heavy satellites, a total mass range is given: *The total mass, m_t, shall be between* 20 *and* 300 *kg*,

$$20 \leq m_t = Hb \cdot Lb \cdot Db \cdot \rho_{\text{bus}} < 300[kg]$$

C2 The satellite bus mass, m_b, budget is considered 85% of the total satellite mass. Together with constraint C3, this constraint ensures that no more than 100% of the mass is occupied. Thus: *The satellite bus mass shall be smaller than* 85% *of the satellite total mass*

$$m_b < 0.85 m_t[kg]$$

C3 The solar panel mass mass, m_{sp}, budget is considered 15% of the total satellite mass. Together with constraint C2, this constraint ensures that no more than 100% of the mass is occupied. Thus: *The satellite solar panel mass shall be smaller than* 15% *of the satellite total mass*

$$0.01 \leq m_{sp} = A_{sp} \cdot \left(\frac{W_{m2}}{W_{kg}} + 0.01 \cdot L \cdot \rho_{\text{bus}} \right) < 0.15 \cdot m_t[kg]$$

C4 The deployable solar arrays should have a minimum thickness to ensure sufficient stiffness (the stiffness calculations are deemed outside of the scope of this work), and a maximum thickness to avoid unrealistic sizing. Furthermore, the longer the solar array, the greater the required thickness. Thus: *The solar panel thickness, SP_t, shall be between* 3 *and* 40 *millimetres.*

$$3 \leq SP_t = \frac{W_{m2}}{W_{m3}} + 0.01L < 40[mm]$$

7.3 Discussion validity samples

The generation of valid input samples scales approximately linearly with the number of unprocessed samples because the sample sets are uniformly distributed. To test this linearity, the following number of unprocessed samples were generated: $[1, 10, 10^2, 10^3, 10^4, 10^5]$. Because of the requirements and constraints posed in 7.2, this generation leads to roughly 7% of valid outputs after processing (or the corresponding number of physically feasible samples becomes $[1, 2, 3, 67, 674, 7037]$).

To discuss the observed trends, the number of unprocessed samples is set to $\#\text{samples}_{\text{unprocessed}} = 10,000$. The data are presented in the figures below; the sample size is 674. This quantity is deemed sufficiently large to analyse trends in the design space and sufficiently small to limit redundancies and to eventually limit the computational time (as only limited computational resources and time are available during this work). Each point represents a single simulation run.

Figure 78 explores the relationships between altitude, inclination, and Right Ascension of the Ascending Node. As expected, the relation between RAAN and inclination remains uniformly distributed, as they do not relate to the physical constraints. When considering the altitude, however, the distributions are affected:

- Inclination vs altitude: a concentration at lower altitudes indicates a focus on missions requiring high spatial resolution, which are typically easier to achieve in LEO. The uniform spread of inclination means that various orbital planes are covered, resulting in a good representation of the disturbances encountered in LEO.
- RAAN vs altitude: Similar to the altitude vs inclination case, a higher density of points at lower altitudes is observed. These findings are consistent with the constraints posed.

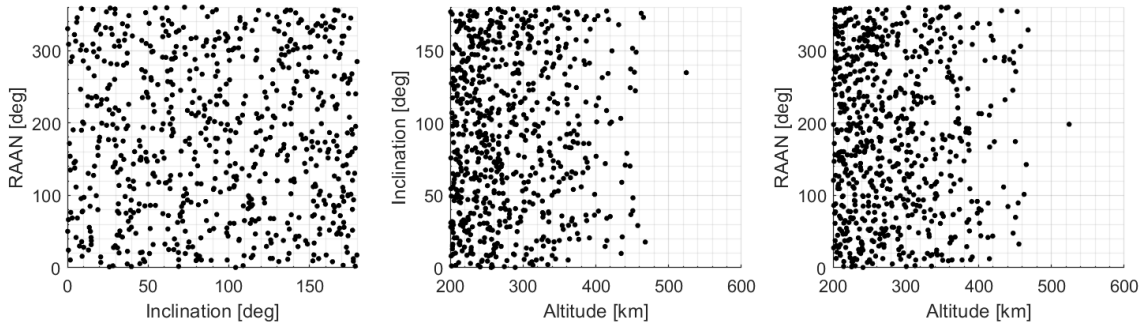

Figure 78: Scatter plots illustrating the distribution of sampled orbital parameters for the satellite mission simulation. RAAN vs inclination (left), inclination vs altitude (centre), and RAAN vs altitude (right).

Figure 79 presents the relationships between the spacecraft design parameters: bus mass, solar panel mass, bus volume, imager aperture, and total spacecraft mass. Herein, some observations are made too:

- Solar panels mass vs bus mass: As the bus mass increases, the allowable solar panel mass also tends to increase. The concentration of smaller solar panels with lower masses is much higher than that of the heavier ones. This suggests that the 10 W minimum peak power, intended to cap solar panel size for smaller satellites, remains inadvertently active on larger spacecraft. This is **not** the case; it is intentional: the satellite bus can, in theory, also be covered by solar arrays, resulting in sufficient power to operate larger satellites as well. This would not affect the mass distribution in any meaningful way; thus, it does not pose validity issues.
- Total mass vs bus volume: the total spacecraft mass and the volume of the bus almost follow a linear relation. This is the case because the solar arrays are assumed to be constructed from lighter materials than the satellite bus. Thus, as the volume grows, the solar arrays increase in size, taking a relatively larger share of the volume. Again, smaller satellites are more densely populated than larger satellites.
- Total mass vs aperture: the total mass of the satellite increases together with an increase in the aperture. However, considerable variation remains in the design solutions. This is expected due to altitude variations. At lower altitudes, a smaller aperture suffices to achieve a GSD of 1 m. At higher altitudes, the aperture must grow too. Nevertheless, for smaller GSDs, the larger satellites can also fly at lower altitudes.

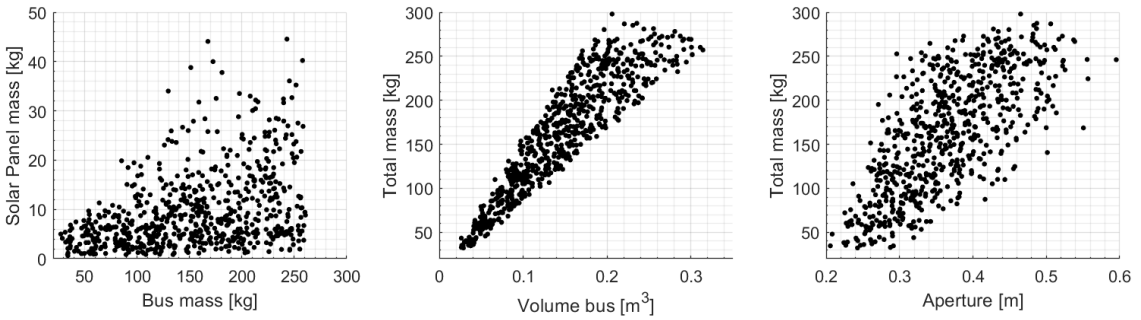

Figure 79: The plots present the simulation distribution between solar panel mass vs bus mass (left), total mass vs bus volume (centre), and total mass vs instrument aperture (right).

Figure 80 presents plots exploring the Ground Sample Distance with three parameters: altitude, total mass, and aperture. Those plots reveal the trend consistent with the expectation that the smallest GSD is capped by altitude and aperture size. Because both are linked to the spacecraft's total mass, this trend also emerges there. Some points are worth taking into consideration for realising a design:

- GSD vs total mass: Higher-mass spacecraft could accommodate larger instruments, more sophisticated stabilisation systems, or more powerful onboard processing, all of which could improve GSD.

- GSD vs aperture: a negative correlation between aperture size and GSD is observed. The trend seems to stop at about Aperture $= 0.5[m]$, and it does. It concerns the focal length (i.e., the number of internal reflections) permitted for the imager. As the number of reflections increases, the trend continues, and the achievable GSD for a satellite with mass 300 kg settles at approximately 0.4 m, within the operational altitude range.

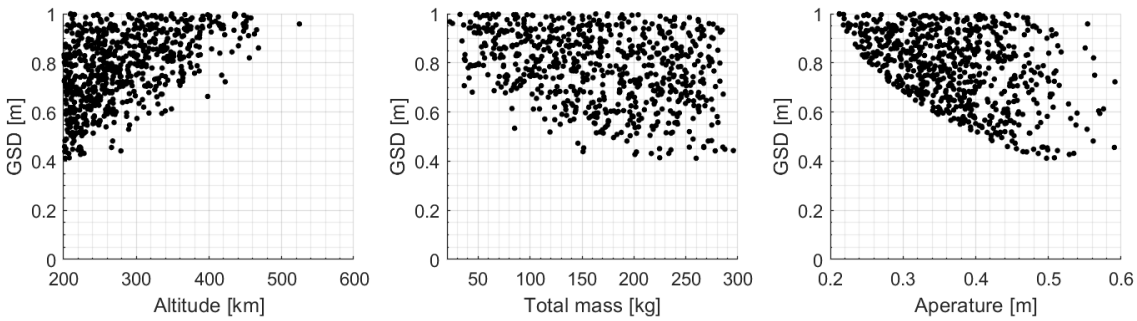

Figure 80: Scatter plots illustrating the distribution of imager performance for the satellite mission simulation. Ground sample distance vs altitude (left), Ground sample distance vs total mass (Middle), and Ground sample distance vs aperture (right).

7.4 Reduce number of samples

The computational cost of a 4-DOF simulation is prohibitive for simulating O(1000) configurations. The objective of this section is to reduce the number of samples to O(100) by sifting the relevant samples from the redundant ones. Thus, this step takes the feasible sample set and reduces it as indicated by 'Reduce Number of Samples' in Figure 81.

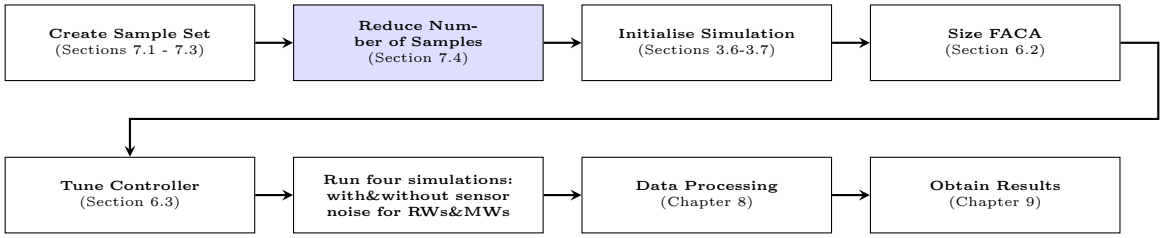

Figure 81: Simulation setup flowchart: Reduce Number of Samples

This section discusses the scenario in which the satellite is spawned at the desired orbit and orientation and remains perfectly pointed at NADIR throughout one orbit. To do that, the orbital inclination and right ascension of the ascending node are examined. For both, the undisturbed overview plots are presented; for inclination in 7.4.1, and for RAAN in 7.4.2. After analysing both, the number of simulations for the disturbed satellite can be reduced from 674 to 128. This conclusion is reached in 7.4.3.

7.4.1 Influence of inclination

In Figure 82, the total disturbance torque versus orbital inclination is investigated. Some key observations are presented below. The inclinations that together form a holistic view of the Tradespace explorations are $i = [[0, 10], [40, 70], [80, 90]]$ degrees.

Below, a brief analysis of the maximum total disturbance torque (corresponding to Figure 82a) is given. For more detail, the components forming the total torque are presented in section **??**.

- For the given sample set of satellites, the maximum disturbance torque seems to be capped at about 10^{-6} till $5 \cdot 10^{-4}$ Nm.
- For most satellites, the most pronounced maximum torque takes place about the Y_B axis (pitch θ), which happens to be the axis of highest angular momentum due to the NADIR pointing condition.

This is advantageous because both an MW and an RW can produce a counter torque about this axis.

- Next, the second most dominant torque direction is about the Z_B axis (yaw ψ). This torque is problematic because it tends to rotate the angular momentum vector into a different orientation and can disrupt alignment with the orbital plane.
- The least dominant disturbance torque appears to be about the X_B axis (roll ϕ). Like the torque about the Z_B axis, this torque will also push the angular momentum vector to be misaligned with the orbital plane.

The analysis average disturbance torque (corresponding to Figure 82b) is shown below. The influence per disturbance is presented in section **??**.

- For the given sample set of satellites, the average disturbance torque seems to be capped at about 10^{-8} to 10^{-4} Nm. This shows that the average torque is between a factor of 5 to 20 times smaller than the maximum torque experienced.
- For most satellites, the most pronounced average torque takes place about the X_B axis (roll ϕ). This is problematic when only a momentum wheel is employed, as this torque cannot be compensated.
- Next, the second most dominant torque direction is about the Z_B axis (yaw ψ). This is problematic when only a momentum wheel is employed, as this torque cannot be compensated.
- The least dominant disturbance torque appears to be about the Y_B axis (pitch θ), which can be countered by both an MW and an RW at the cost of accumulation.

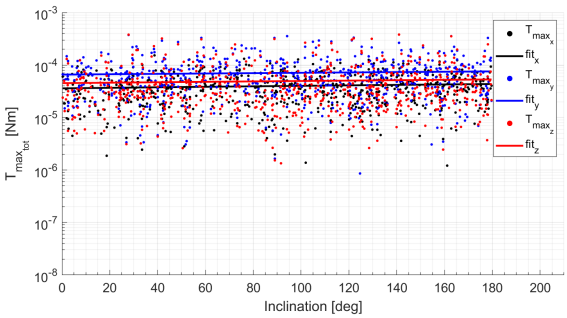

(a) Maximum total disturbance torque (tot) experienced.

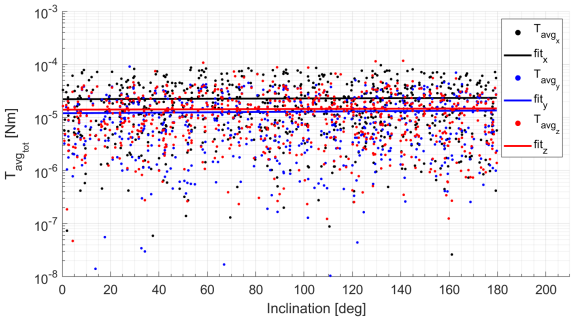

(b) Average total disturbance torque (tot) experienced.

Figure 82: Overview of the undisturbed simulation results: total torque vs inclination for various satellite geometries. This figure presents a comparative analysis of the magnitude of the maximum disturbance torque about each body axis for one orbit as a function of orbital inclination. Subfigure (a) illustrates the distribution of maximum torques experienced, and subfigure (b) illustrates the distribution of average torques experienced; a linear curve fit is used to enhance readability.

Maximum disturbance torque versus orbital inclination per disturbance

The simulations for the maximum torque experienced during an orbit in Figure 83 show that the orbital inclination is not a substantial parameter to investigate for deeper analysis.

- As expected from orbital symmetry, the orbital inclination from 90 to 180 degrees is a mirrored view of 90 to 0 degrees because in one revolution, the satellite is positioned on both sides of the Earth.
- Whereas the aerodynamic (Figure 83a) and gravity gradient torque (Figure 83b) do not show a dependency on orbital inclination, the residual dipole torque (Figure 83c) and solar radiation torque (Figure 83d) do show a dependency.

To reduce the number of simulations, it is worth selecting orbits in the following orbital inclination ranges:

- $i = [0, 10]$ degrees: set a baseline simulation.

- $i = [40, 50]$ degrees: the aerodynamic torque seems to have outliers at regions around 45 and 135 degrees, and so does the gravity gradient torque.
- $i = [60, 70]$ degrees: the solar radiation torque goes to a minimum in this region.
- $i = [80, 90]$ degrees: the residual dipole torque can become the dominant disturbance torque when not designed to minimise it. A minimum in the Z axis does occur at this range.

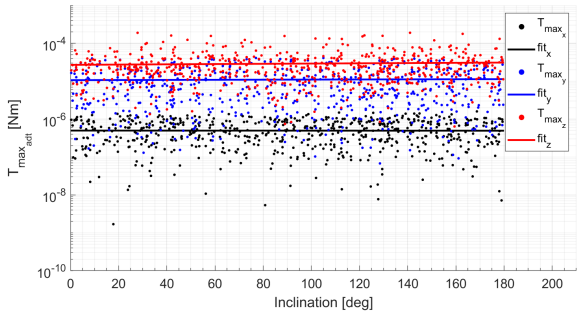

(a) Maximum aerodynamic torque (adt) experienced. From the scattered data, it is seen that the maximum aerodynamic torque is consistent with the locations where the atmospheric density is highest (around $30 - 60$ degrees, see Figure 32).

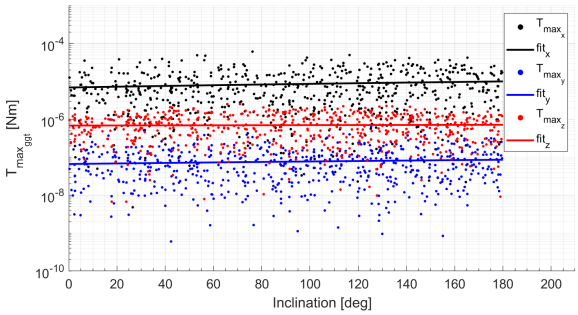

(b) Maximum gravity gradient torque (ggt) experienced. The gravity gradient torque shows a sinusoidal relation with inclination for all three body axes. For the satellite with the solar arrays positioned along the X-axis, the torque about the X-axis is highest, followed by the Z-axis and Y-axis.

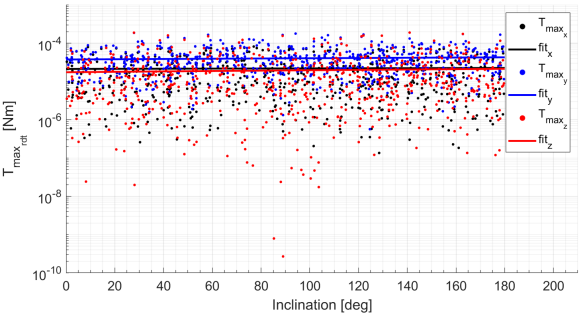

(c) Maximum residual dipole torque (rdt) experienced. In the altitude range for this sample set, the maximum rdt is as significant as the aerodynamic torque.

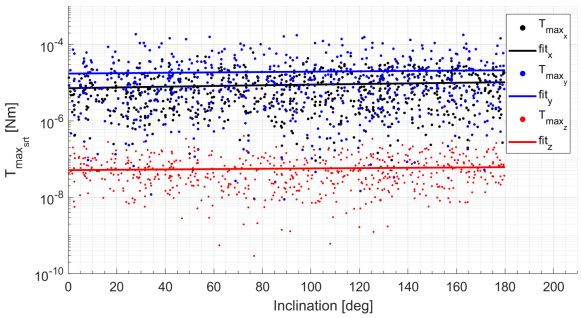

(d) Maximum solar radiation torque (srt) experienced. The Sun is positioned at an angle of about 23.5 degrees; that translates to the srt being minimised at 66.5 and 113.5 degrees for the Z and Y axis.

Figure 83: Overview of the undisturbed simulation results. This figure presents a comparative analysis of the magnitude of the maximum disturbance torque experienced about each body axis in one orbit versus the orbital inclination across various scenarios. Subfigures (a)-(d) illustrate the distribution of maximum torque experienced for various satellite geometries and a linear curve fit to enhance readability.

Average disturbance torque versus orbital inclination per disturbance

Contrary to the observation for the maximum torque, filtering for the average torque experienced during an orbit (see Figure 84) demonstrates that the orbital inclination is a parameter that affects the average torque substantially. Below, some observations are presented:

- As expected from orbital symmetry, the orbital inclination from 90 to 180 degrees is a mirrored view of 90 to 0 degrees because in one revolution, the satellite is positioned on both sides of the Earth.
- The aerodynamic (Figure 86a), the gravity gradient torque (Figure 86b), and the solar radiation torque (Figure 86d) show a dependency on orbital inclination.
- The residual dipole torque (Figure 86c) does not show a dependency.

To reduce the number of simulations, it is worth checking if the selected inclination range required to capture the extremes during the maximum torque analysis also covers the observations for the average torques. Below, the average torques are examined for their range of interest, and whether the selected ranges must be expanded.

- Aerodynamic torque: $i = [0, 10]$ and $i = [80, 90]$. The first range is suitable because it captures the peaks; the latter range is selected because it captures the lower range of average torques. The selected range is therefore accepted.
- Gravity gradient torque: $i = [40, 60]$ and $i = [80, 90]$. The first range is suitable because it captures the peaks in the X_B axis; the latter range is selected because it captures the lower range of average torques. The selected range must therefore be expanded to include $i = [40, 50]$.
- Residual dipole torque: a particular range does not have to be selected. The selected range covers the rdt of interest.
- Solar radiation pressure: for the average solar radiation pressure, there appears to be a maximum around $i = 45$ degrees and a minimum at $i = 90$ degrees. Both fall well within the already defined range of interest.

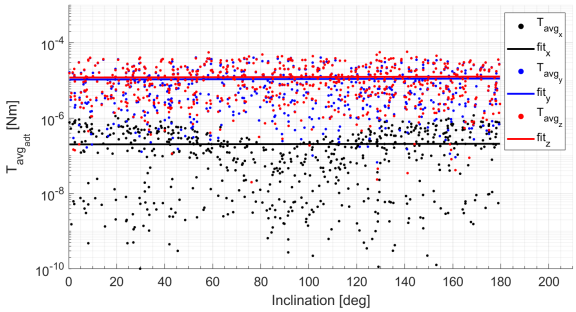

(a) Average aerodynamic torque (adt) experienced.

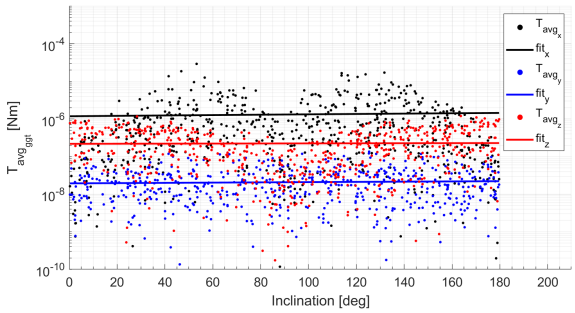

(b) Average gravity gradient torque (ggt) experienced.

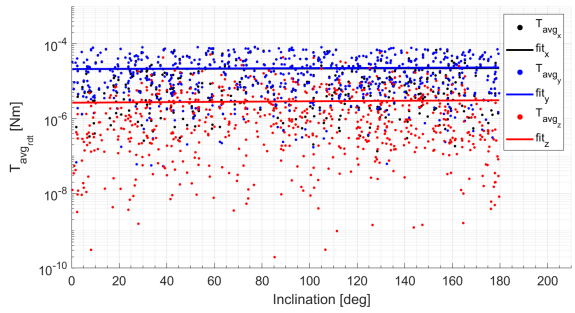

(c) Average residual dipole torque (rdt) experienced.

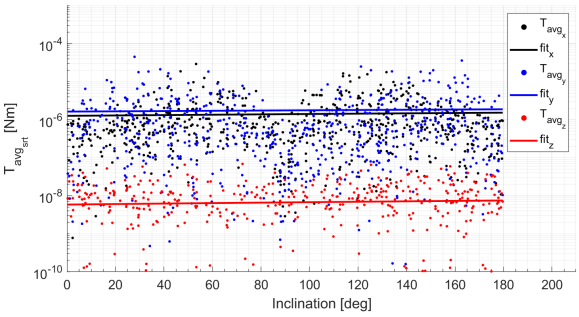

(d) Average solar radiation torque (srt) experienced.

Figure 84: Overview of the undisturbed simulation results. This figure presents a comparative analysis of the average disturbance torque about each body axis during one orbit, as a function of orbital inclination, across various scenarios. Subfigures (a)-(d) illustrate the distribution of average torque experienced for various satellite geometries; a linear curve fit is added to enhance readability.

7.4.2 Influence of RAAN

Similar to the rationals discussed in section 7.4.1, in this section, it is the goal to filter out samples by only including the right ascension of the ascending node ranges of interest.

Maximum disturbance torque versus orbital RAAN per disturbance
The simulations for the maximum torque experienced during an orbit in Figure 85 show that the orbital RAAN is not a parameter to investigate further.

- The aerodynamic torque is independent of RAAN as seen in Figure 85a. Any sample set will suffice.
- The gravity gradient torque (Figure 85b), the residual dipole torque (Figure 85c) and solar radiation torque (Figure 85d) do show a dependency.
- Maybe most importantly, . This means that the

To reduce the number of simulations, it is worth selecting orbits in the following orbital inclination range: RAAN $\Omega = [0, 180]$. This range covers all the needs because the effects are mirrored about the RAAN $\Omega = 180$ degree line. That means that the $\Omega = [180^{+}, 360]$ is redundant.

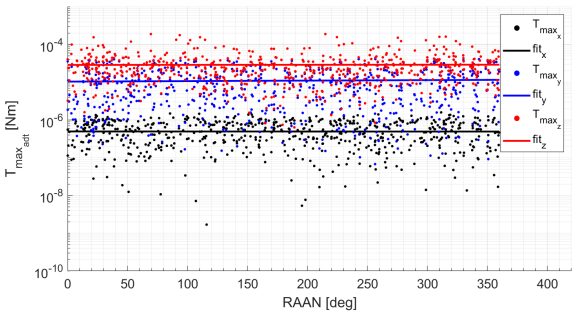

(a) Maximum aerodynamic torque (adt) experienced.

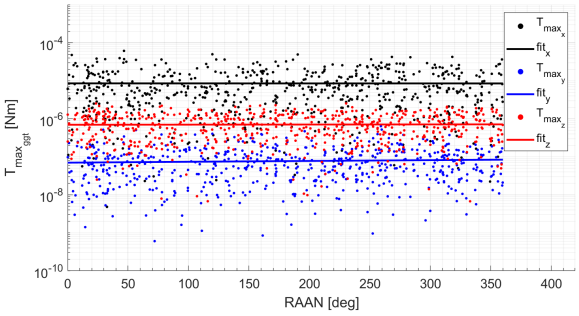

(b) Maximum gravity gradient torque (ggt) experienced.

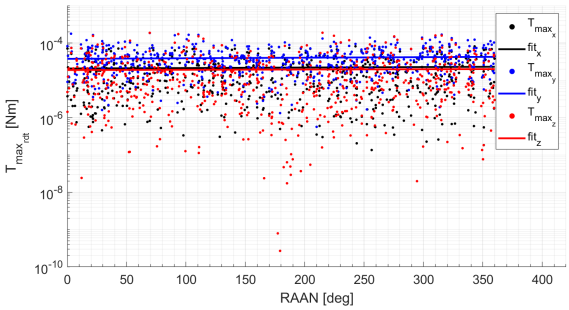

(c) Maximum residual dipole torque (rdt) experienced.

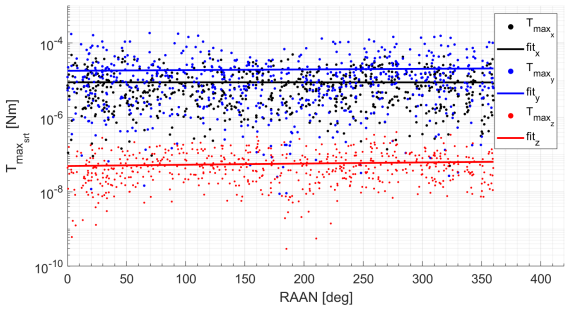

(d) Maximum solar radiation torque (srt) experienced.

Figure 85: Overview of the undisturbed simulation results. This figure presents a comparative analysis of the maximum disturbance torque experienced about each body axis during one orbit, versus the orbital RAAN, across various scenarios. Subfigures (a)-(d) illustrate the distribution of maximum torque experienced for various satellite geometries and a linear curve fit to enhance readability.

Average disturbance torque versus orbital RAAN per disturbance

The observation for the RAAN range only has to cover $\Omega = [0, 180]$ remains valid when considering the average torque experienced during an orbit (see Figure 86). The same 'mirrorred about $\Omega = 180$ degrees' argument is used.

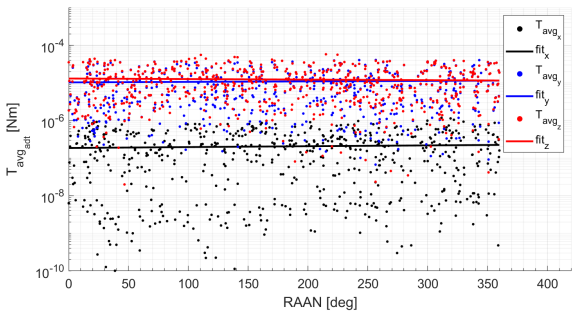

(a) Average aerodynamic torque (adt) experienced.

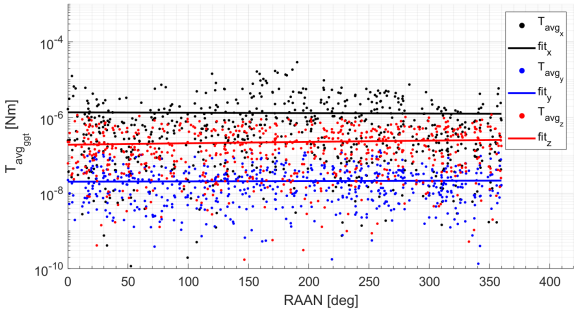

(b) Average gravity gradient torque (ggt) experienced.

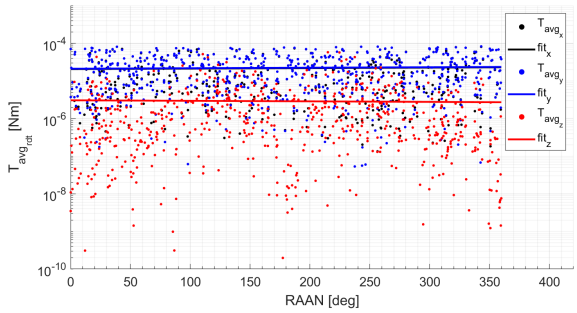

(c) Average residual dipole torque (rdt) experienced.

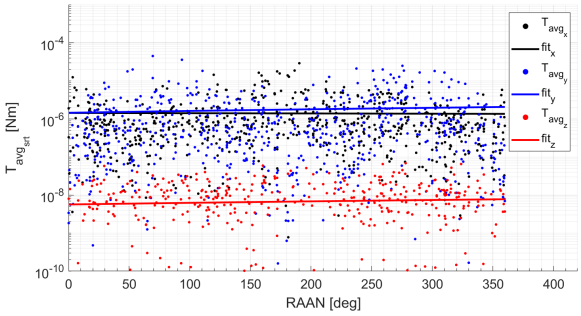

(d) Average solar radiation torque (srt) experienced.

Figure 86: Overview of the undisturbed simulation results. This figure presents a comparative analysis of the average disturbance torque experienced about each body axis in one orbit versus the orbital inclination across various scenarios. Subfigures (a)-(d) illustrate the distribution of average torque experienced for various satellite geometries; a linear curve fit is added to enhance readability.

7.4.3 Reduction in number of simulations necessary

The sample size can be reduced considerably, based on the disturbance torque observations made in sections *Influence of inclination* 7.4.1 and *Influence of RAAN* 7.4.2. The samples of interest are contained in the following ranges:

1. Inclination $i = [[0, 10], [40, 70], [80, 90]]$ (originally $i = [0, 180]$)
2. Right ascension of the ascending node $\Omega = [0, 180]$ (originally $i = [0, 360]$)

This would reduce the number of samples to about 14% ($\frac{5}{18} \cdot \frac{1}{2} = \frac{5}{36}$) of the originally processed samples. This means that, of the 674 samples, 94 are identified as significant for further examination. If only this filtering is applied, this emerges to be exactly the case (remember, the samples were made with a uniform distribution).

There is one caveat, however: the samples must include the extreme values of the spacecraft's total mass. Thus, additional filtering conditions must be applied: the lowest and highest 10% must be retained.

1. If the total mass m_t is smaller than 48 kg, the sample must be kept;
2. If the total mass m_t is larger than 272 kg, the sample must be kept also.

After applying those filters, 128 of 674 samples remain. Their numerical values are documented in Appendix A.1. To verify that there remains a sufficiently large span in design variety, the processed and filtered samples are presented in Figure 87.

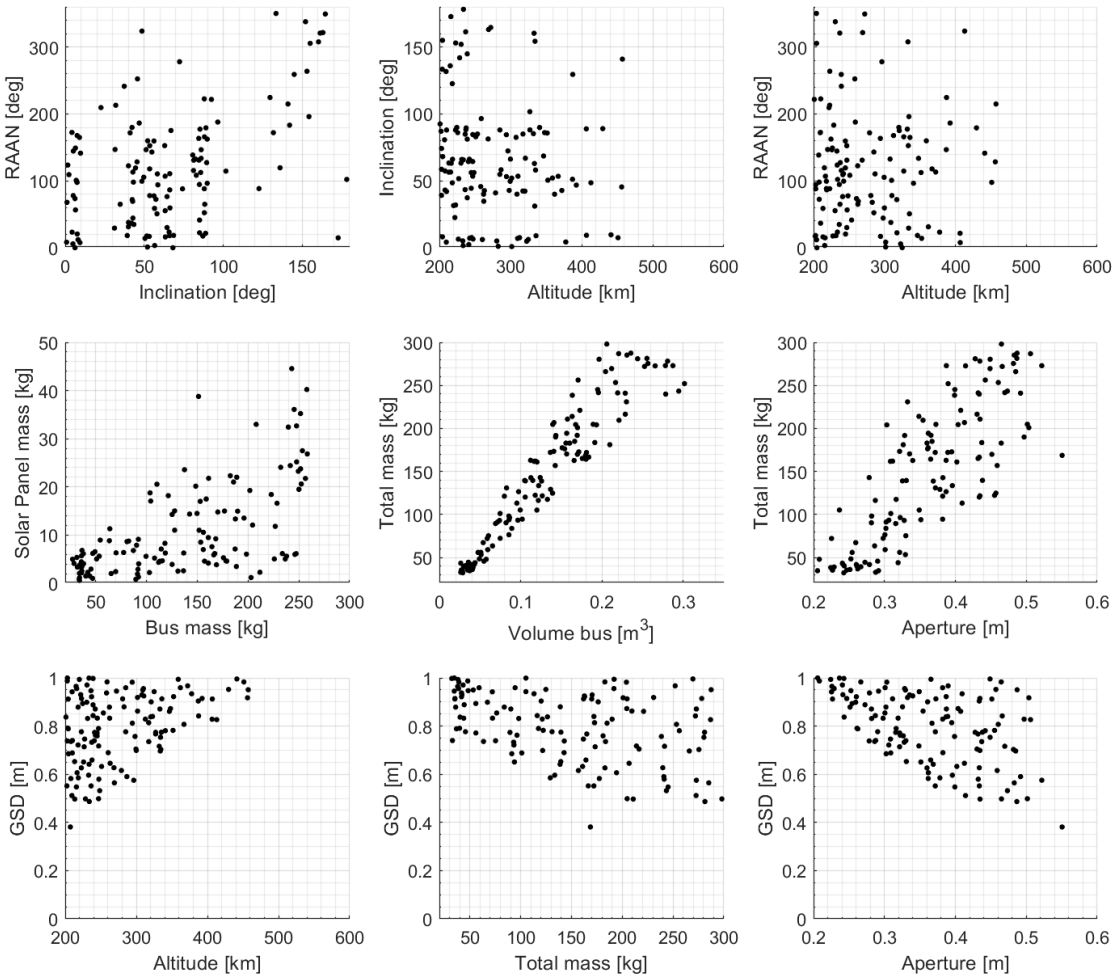

Figure 87: Scatter plots illustrating the distribution of the filtered samples for the satellite mission simulation. The scatter plots are described from left to right, top: RAAN vs inclination, inclination vs altitude, and RAAN vs altitude; middle: solar panel mass vs bus mass, total mass vs bus volume, and total mass vs aperture; bottom: GSD vs altitude, GSD vs total mass, and GSD vs aperture.

What can be concluded from Figure 87 is that the sample set is sufficiently spread to investigate the performance of the satellite, given that the GSD values vary between $0.4 - 1.0$ m, with a total mass ranging from 30 to 300 kg at altitudes between 200 and 460 km. This is tighter than the original scope defined in chapter 2. From Figure 78, it became evident that, for the satellite sizes and masses of interest, flying at altitudes above 480 km does not render a viable design possibility to achieve a GSD smaller than one meter. Thus, the original scope of up to 600 km was optimistic. The filtered range excluded satellites between 460 and 480 km, but the exclusion was considered not significant. Furthermore, from Figure 79, it was observed that satellites with mass less than 30 kg were also not feasible. The original scope of 20 kg was also too optimistic.

8 Data Processing Methodology

This chapter outlines the preprocessing applied to the simulation data, with a particular focus on the development of attitude and angular rate over time. Thus, this step transforms the comprehensive simulation data into performance metrics to enable the subsequent computation of results, as indicated by 'Data Processing' in Figure 88.

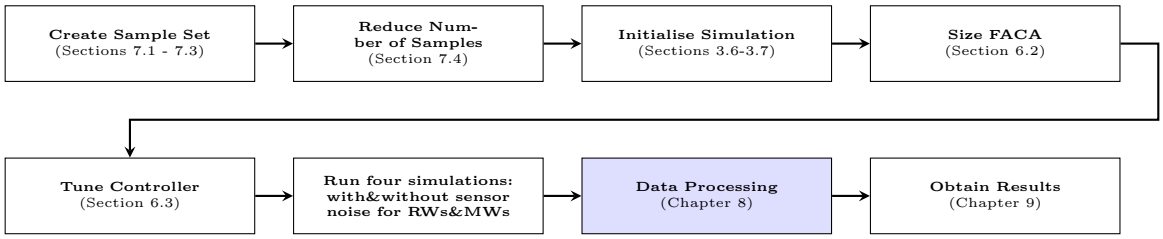

Figure 88: Simulation setup flowchart: Data Processing

This aids in answering the following research question by creating quantifiable metrics:

(B.3) *How does the performance of each actuator type compare when evaluated in a closed-loop simulation against pointing accuracy and precision for a disturbance-rejection scenario?*
To evaluate pointing accuracy and precision, the raw simulation data must be processed into a metric amenable to evaluation, as discussed in section 8.1. The method employed to extract meaningful performance metrics first isolates steady-state behaviour (section 8.2) and, finally, separates frequency components associated with drift and satellite oscillations (section 8.3). Finally, the performance metrics are extracted and stored (section 8.4).

Also, the FACA's flywheel(s) speeds are stored for later analysis.

8.1 Data Preparation

The raw angular rate data, denoted as `PQR_history` or $\omega_{\text{error}}(t)$, is first converted into an error signal relative to its initial state (/desired state), $\omega(t_0)$, according to Equation 148, of which an example is shown in Figure 89. In this example, the initial roll and yaw rates are zero, and the pitch rate equals the rotational rate required to keep the satellite pointing at NADIR (approximately $-0.06774\ deg/s$). Any deviation from those initial rotational rates is considered an error, see Figure 89b.

$$\omega_{\text{error}}(t) = \omega(t) - \omega(t_0) \quad (\texttt{PQR\_error} = \texttt{PQR\_history} - \texttt{PQR\_init}) \tag{148}$$

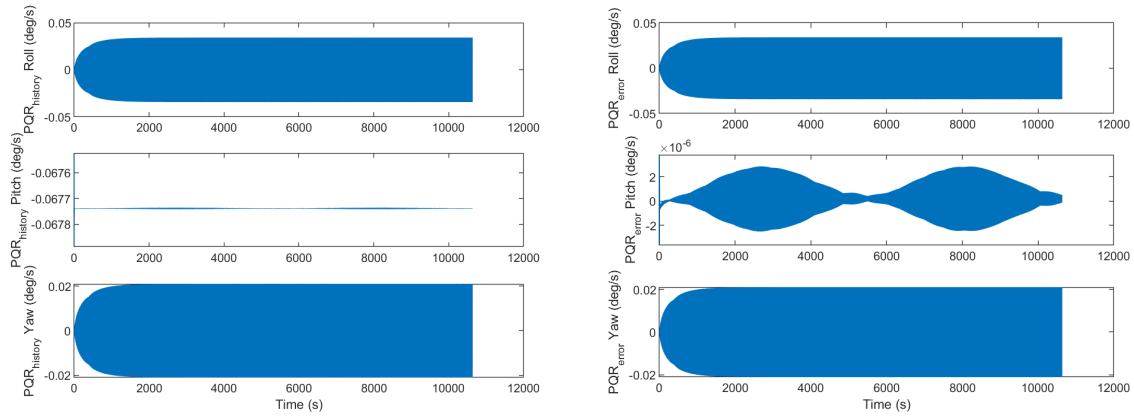

(a) ω signal (`PQR_history`)

(b) ω_{error} signal (`PQR_error`)

Figure 89: Example of the angular rate (PQR) error of an MW stabilized satellite

The raw attitude data, `attitude_history` or $[\phi, \theta, \psi]^T(t)$, is also converted to an error signal, $[\phi, \theta, \psi]^T_{\text{error}}(t)$, by subtracting the NADIR attitude data from the time series. This allows the analysis of deviations from

the desired condition that keep pointing at NADIR, as given in Equation 149. An example of this conversion is illustrated in Figure 90.

$$\begin{bmatrix}\phi\\ \theta\\ \psi\end{bmatrix}_{\text{error}}(t) = \begin{bmatrix}\phi\\ \theta\\ \psi\end{bmatrix}(t) - \begin{bmatrix}\phi\\ \theta\\ \psi\end{bmatrix}_{\text{NADIR}}(t) \quad (\texttt{error\_history} = \texttt{attitude\_history} - \texttt{NADIR\_history}) \tag{149}$$

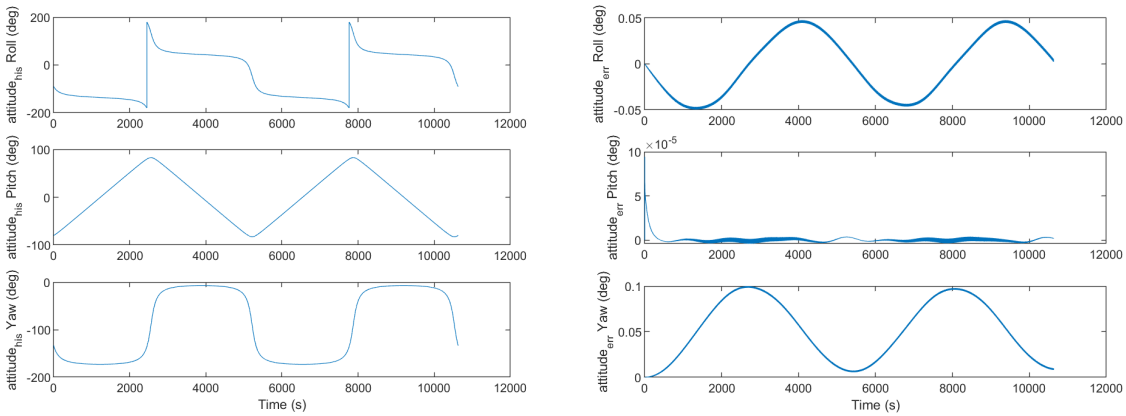

(a) Attitude signal (`attitude_history`)

(b) Attitude error signal (`error_history`)

Figure 90: Example of the attitude error of a MW stabilized satellite. The attitude signal on the left and the attitude error on the right.

Those time-series data, `PQR_error` and `error_history`, among with `wheel_speed_history`, are not uniformly sampled due to the use of the variable time step in the `ODE45` solver. Thus, next, these signals are interpolated onto an equidistant time grid to enable accurate frequency-domain analysis using the Fast Fourier Transform (FFT) [49]. A uniform time vector `t_uniform` is created using `linspace`, spanning the original measurement duration and number of samples. Subsequently, the `interp1` function with a piecewise cubic Hermite interpolating polynomial (`pchip`) method is employed to resample the angular rates (`PQR_history`), attitude error (`error_history`), and wheel speed (`wheel_speed_history`) onto this uniform grid. The use of `pchip` ensures smooth, monotonic interpolation, preserving the local shape of the data [53]. The uniformly distributed data strings received the appended subscript '`_uniform`' for further analysis (in section 8.2).

8.2 Transient Effect Removal

To focus the analysis on the system's steady-state performance, transient effects at the beginning of the experiment are disregarded. The examples for the momentum wheel and reaction wheel satellites, shown in figures 71a and 76a, indicate that transient effects occur within the first 500 seconds. Therefore, the first 500 seconds of the uniformly sampled data are excluded to provide sufficient time for the system to settle following an initial command or disturbance. This filtering is implemented by identifying the index corresponding to the 500-second mark in `t_uniform` and slicing all relevant history arrays accordingly:

```
idx_start = find(t_uniform >= 500, 1, 'first');
t_filtered = t_uniform(idx_start:end);
PQR_error_filtered = PQR_error_uniform(idx_start:end,:);
error_history_filtered = error_history_uniform(idx_start:end,:);
wheel_speed_history_filtered = wheel_speed_history_uniform(idx_start:end,:);
```

The resulting '`_filtered`' variables represent the steady-state segment of the data. An example of an MW-stabilised satellite is shown in Figure 91. Note that for the filtering, the attitude pitch data is used as the 'steady-state' marker - that is, the settling time is approximated visually from Figure 90b - to remove the transient effect at initiation. The exact starting point does not significantly affect the outcome as long as the signals immediately after initiation are disregarded; thus, visually identifying the 500-second mark is deemed adequate.

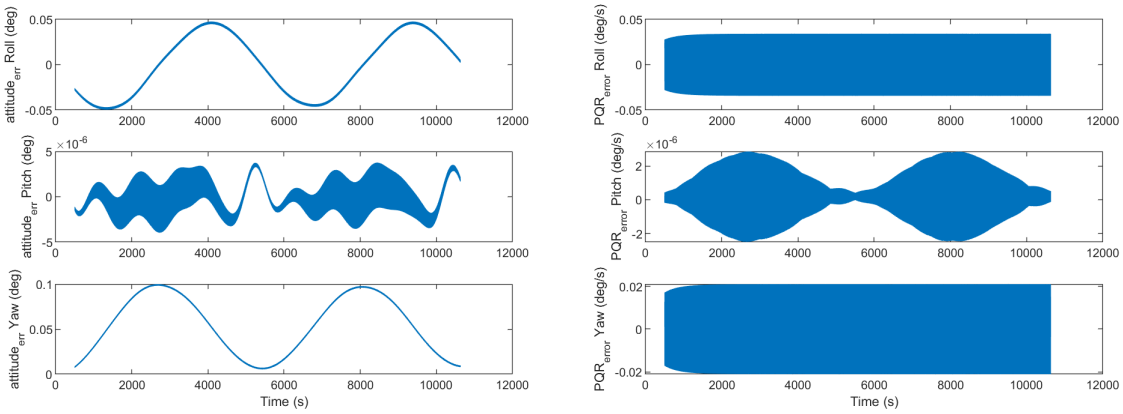

(a) Attitude error

(b) Angular rate error

Figure 91: Example of filtered signals for the the attitude error (left) and the PQR error (right) of an MW stabilised satellite

8.3 Frequency Domain Analysis and Filtering

The filtered time-series data is transformed into the frequency domain using the Fast Fourier Transform (FFT). This allows separation of different frequency components, specifically the higher-frequency oscillations from the low-frequency drift ($< 0.01\ Hz$).

8.3.1 Fast Fourier Transform Computation

The first step in spectral analysis is to determine the effective sampling frequency of the filtered data. The sampling frequency, `Fs_fft`, is calculated as the inverse of the mean time difference between consecutive samples in `t_filtered`, $\Delta t_{\text{filtered}}$, according to Equation 150.

$$F_{s,\text{fft}} = \frac{1}{\text{mean}(\Delta t_{\text{filtered}})} \tag{150}$$

The total number of samples, N, is determined by the length of the filtered time vector, `t_filtered`. The FFT is then applied to the filtered angular rate and attitude error histories using the `fft` function:

```
N = length(t_filtered);
fft_PQR_history = fft(PQR_history_filtered);
fft_error_history = fft(error_history_filtered);
```

A corresponding frequency vector, `f`, is generated to map the FFT output bins to specific frequencies, see Equation 151.

$$f_k = \frac{(k-1) \cdot F_{s,\text{fft}}}{N}, \quad \text{for } k = 1, \ldots, N \tag{151}$$

To isolate drift (low-frequency components) from oscillations (higher-frequency components), frequency-domain masks are created. For this work, signals with periods greater than 100 seconds (1/0.01 Hz) are considered drift. Therefore, a cutoff frequency is defined at 0.01 Hz, `cutoff_freq` = 0.01. Two masks are generated. The construction of these masks handles both even and odd lengths of N to ensure correct symmetry across the Nyquist frequency.

1. `low_mask`: This mask is designed to pass frequencies lower than or equal to `cutoff_freq`. Due to the symmetric nature of the FFT for real-valued signals, the mask must also account for the mirrored positive and negative frequency components.

```
low_mask = (f <= cutoff_freq) | (f >= Fs_fft - cutoff_freq);
if mod(N, 2) == 0
    low_mask = [low_mask(1:N/2), fliplr(low_mask(1:N/2))];
else
    low_mask = [low_mask(1:ceil(N/2)), fliplr(low_mask(1:floor(N/2)))];
end
```

2. `high_mask`: This mask is designed to pass frequencies greater than `cutoff_freq`, effectively filtering out the drift component.

```
% Create high-pass mask
high_mask = (f >= cutoff_freq) & (f <= Fs_fft - cutoff_freq);
if mod(N, 2) == 0
    high_mask = [high_mask(1:N/2), fliplr(high_mask(1:N/2))];
else
    high_mask = [high_mask(1:ceil(N/2)), fliplr(high_mask(1:floor(N/2)))];
end
```

These masks are then applied element-wise to the computed FFTs. This operation effectively zeros out the frequency components outside the desired passband for each filter type:

```
FFT_PQR_history_low = fft_PQR_history .* low_mask';
FFT_PQR_history_high = fft_PQR_history .* high_mask';
FFT_error_history_low = fft_error_history .* low_mask';
FFT_error_history_high = fft_error_history .* high_mask';
```

A visual illustration of these pass bands is depicted in Figure 92. The peaks in oscillations occur at about 3.7 Hz for this example. The drift signal peaks between 10^{-3} and 10^{-4} Hz which corresponds to a period of $1,000$ to $10,000$ seconds stipulating how disturbances accumulate slowly.

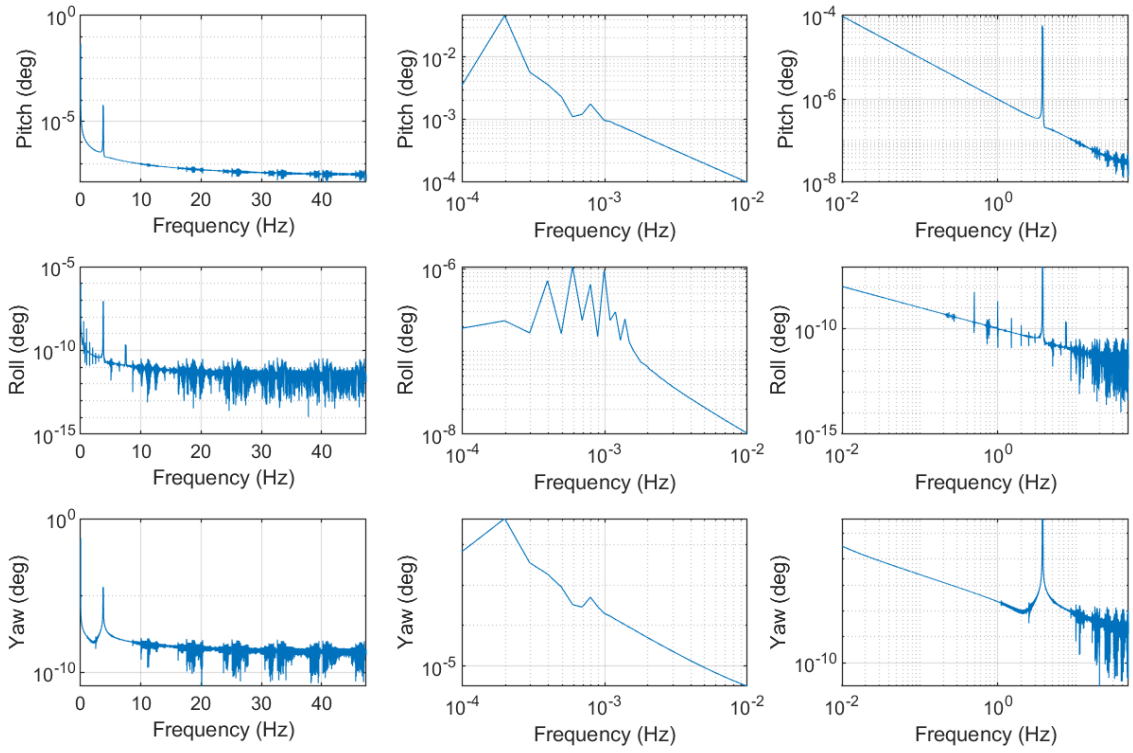

Figure 92: Attitude frequency components of an MW stabilised satellite: FFT of the attitude signals (left), drift component (middle), oscillations (right).

8.3.2 Inverse Fast Fourier Transform and Reconstruction

The filtered frequency-domain signals are converted back into the time domain using the Inverse Fast Fourier Transform (IFFT) with the `ifft` function [51]. The `'symmetric'` flag is used to ensure that the output of the IFFT is real:

```
fft_PQR_history_low = ifft(FFT_PQR_history_low, 'symmetric');
```

```
fft_PQR_history_high = ifft(FFT_PQR_history_high, 'symmetric');
fft_error_history_low = ifft(FFT_error_history_low, 'symmetric');
fft_error_history_high = ifft(FFT_error_history_high, 'symmetric');
```

When performing FFT-based filtering and then employing the inverse FFT, distortions appear (edge effects) at the beginning and end of the reconstructed time-domain signals. To mitigate these distortions, the first and last 10% of the reconstructed signals are discarded. This is achieved by calculating the time duration corresponding to 10% of the total filtered signal length, identifying the start and end indices for the middle 80% segment, and then slicing the data accordingly:

```
t_10 = floor((t_filtered(end)-t_filtered(1))/10);
t_90 = floor(t_filtered(end)-t_10);
idx_strt = find(t_filtered >= t_10, 1, 'first');
idx_end = find(t_filtered >= t_90, 1, 'first');

PQR_history_low = fft_PQR_history_low(idx_strt:idx_end,:);
PQR_history_high = fft_PQR_history_high(idx_strt:idx_end,:);
error_history_low = fft_error_history_low(idx_strt:idx_end,:);
error_history_high = fft_error_history_high(idx_strt:idx_end,:);
```

The resulting data strings, such as `error_history_low` and `error_history_high`, represent the attitude components attributed to drift and oscillations, respectively, with their edge effects removed, providing a clearer view of the system's steady-state frequency performance. An example of such a signal is given in Figure 93.

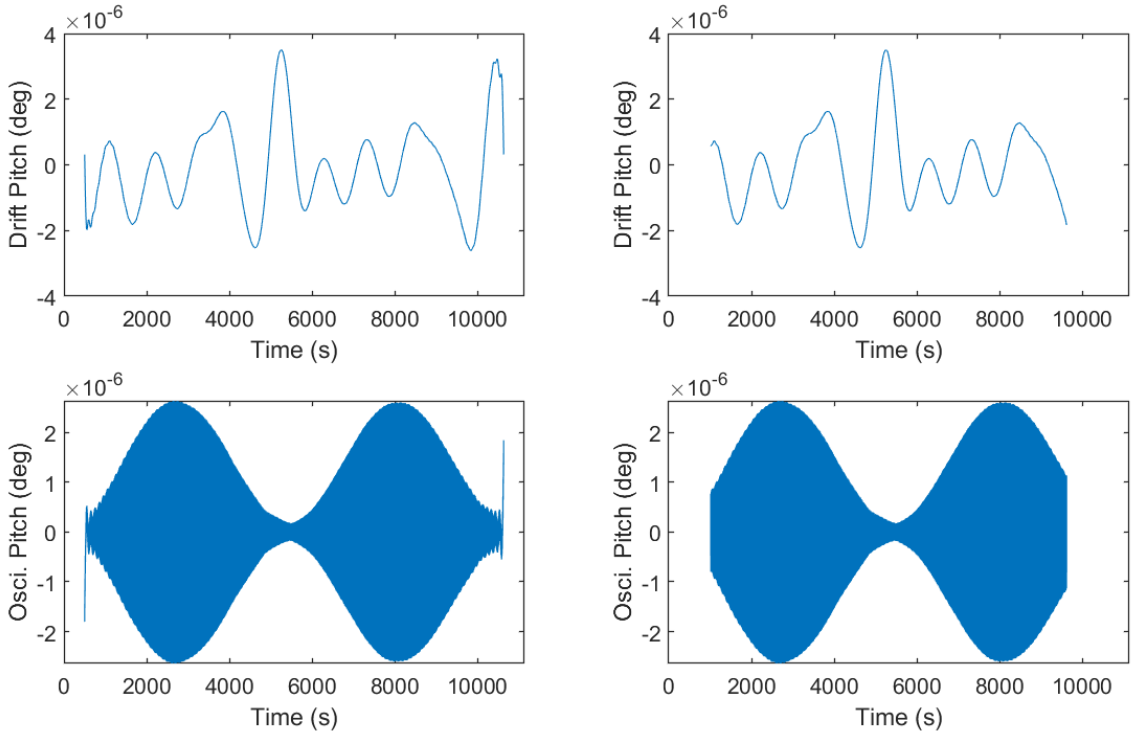

Figure 93: iFFT of the pitch signals: drift component with edge effect (left-top), without edge-effect (right-top), and oscillations with edge effect (left-bottom), without edge-effect (right-bottom).

These signals will be used to compute the performance metrics.

8.4 Performance Metric Extraction

Following the signal processing and frequency-domain separation detailed in section 8.3, the next step is to quantify satellite pointing performance using statistical metrics. This analysis targets the separated drift and oscillation components of the attitude and angular rate errors, as well as the behaviour of the flywheel speeds. The extracted metrics are systematically stored in a results matrix,

`MW_satellite_performance_results`.

The statistical measures employed for evaluating performance are the Root Mean Square (RMS) value, standard deviation (`std`), and maximum recorded value (`max`) for both the attitude and the angular rate errors, and mean, minimum, and maximum values of flywheel speeds. The RMS for a time series $x(t)$ is calculated via Equation 152.

$$X_{\text{RMS}} = \sqrt{\frac{1}{N}\sum_{i=1}^{N} x_i^2} \tag{152}$$

where N is the number of data points and x_i is the i-th sample. Next, the Standard Deviation (std) quantifies the amount of variation of the signal around the mean, and is given by Equation 153.

$$\sigma_X = \sqrt{\frac{1}{N-1}\sum_{i=1}^{N}(x_i - \bar{x})^2} \tag{153}$$

where $\bar{x}$ is the mean of the samples determined via Equation 154.

$$\bar{x} = \frac{1}{N}\sum_{i=1}^{N} x_i \tag{154}$$

The maximum value that the error signal attains is also stored, which provides additional information about the deviation from the intended NADIR direction. To store the intermediate results, the following steps are executed for both the MWs (‘`MW_`’) and the Rws (‘`RW_`’), for both the drift components (‘`_low`’) and the oscillation (‘`_high`’) components. All signals are converted following the same procedure as indicated for the drift components below:

1. The performance metrics for the drift components are extracted from the `error_history_low` (attitude) and `PQR_history_low` (angular rate) signals.
2. For the pitch, roll, and yaw components of the attitude error, the RMS, standard deviation, and maximum values are computed and stored.

```
MW_satellite_performance_results(i,15:17) = sqrt(mean(error_history_low.^2));
MW_satellite_performance_results(i,18:20) = std(error_history_low);
MW_satellite_performance_results(i,21:23) = max(error_history_low);
```

3. Similarly, for the angular rate error components, the RMS, mean, and maximum values are calculated. Note the use of ‘mean’ for rate error, which indicates residual rotational motion in the period that is evaluated.

```
MW_satellite_performance_results(i,24:26) = sqrt(mean(PQR_history_low.^2));
MW_satellite_performance_results(i,27:29) = mean(PQR_history_low);
MW_satellite_performance_results(i,30:32) = max(PQR_history_low);
```

In addition to the attitude and angular rate performance, the behaviour of the flywheel speeds provides insights into the control system’s effort and operational limits. The filtered wheel speed data, `wheel_speed_history_filtered`, is analysed to determine its overall characteristics during steady-state operation. The mean, minimum, and maximum wheel speeds are recorded. These values can be used to assess wheel saturation, power consumption, and micro-vibration emittance.

```
MW_satellite_performance_results(i,51:53)= mean(wheel_speed_history_filtered);
MW_satellite_performance_results(i,54:56)= min(wheel_speed_history_filtered);
MW_satellite_performance_results(i,57:59)= max(wheel_speed_history_filtered);
```

Ultimately, these results provide a basis for comparing the satellites’ pointing accuracy and precision when employing MW or RW, as discussed in chapter 9.

9 Results and Discussion

This chapter presents the results of a Tradespace exploration that quantitatively compares the closed-loop performance of the MW- and Rw-controlled satellites under realistic mission conditions. The methodology is briefly outlined in section 9.1. To quantify the results of the MW- and RW-controlled satellite performance, two metrics are used, and are visualised in Figure 95:

1. Pointing precision or '**oscillations**' refers to a satellite's ability to maintain consistent alignment with a designated target. It is quantified by the deviation of the pointing direction from the desired direction, expressed as the root-mean-square (RMS) error.
2. Pointing accuracy or '**drift**' refers to a satellite's ability to align with a specific, absolute location on Earth. It is defined as the difference between the actual pointing directions, where bias is a primary factor influencing accuracy.

The result analysis directly addresses the research questions concerning comparative performance (B.3) and the synthesis of a selection methodology (B.4).

(B.3) *How does the performance of each actuator type compare when evaluated in a closed-loop simulation against pointing accuracy and precision for a disturbance-rejection scenario?*
Sections 9.2 till 9.5 discuss the comparative performance of MW- and RW-controlled satellites for various scenarios.

(B.4) *How can the quantitative results from the simulations be synthesised into a robust, generalizable selection methodology to recommend the optimal actuator for the stated mission?*
To assess the performance per category, MWs and RWs, within the simulated scenarios, a workflow is set up. Figure 94 illustrates the workflow adopted for the Tradespace exploration conducted in this thesis. This process ensures that the simulation results are statistically relevant, computationally efficient, and directly traceable to specific methodologies detailed throughout this document.

The numerical values for the inputs of the simulations are provided in appendix A. Finally, the conclusions drawn from the Tradespace exploration are presented in section 9.6.

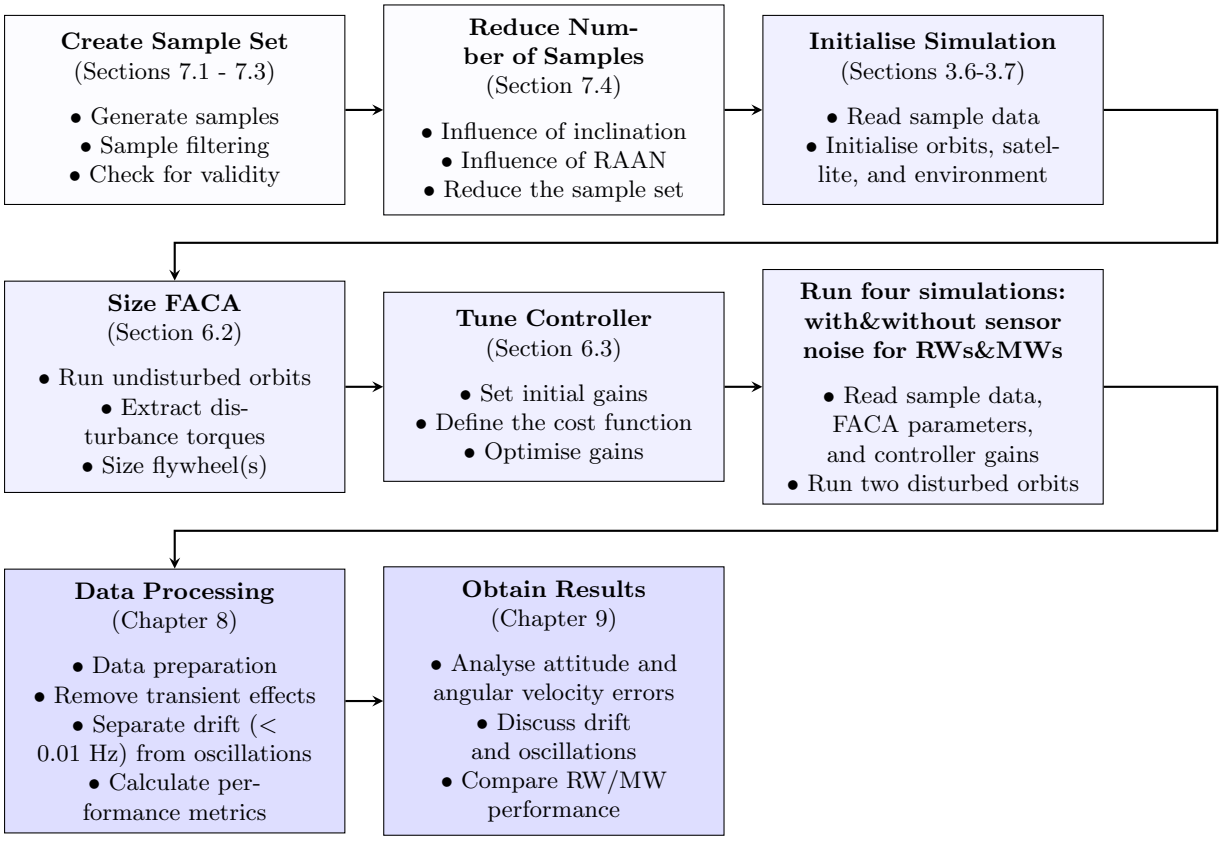

Figure 94: Tradespace exploration setup flowchart.

9.1 Closed-Loop Attitude Control Simulation Methodology

In the mission simulation model (see 3.7), the spacecraft is spawned at a specific position (longitude, latitude, height) with given linear and angular velocities, and at a specified attitude. Euler's equation for rigid bodies determines the satellite's angular acceleration throughout the orbit (see Equation 38), and is solved using the `ode45` solver in Matlab. Euler's equation accounts for the inertia distribution, angular momentum, and the disturbance torque determined by the environmental model (see Chapter 5).

As a consequence of unwanted angular accelerations, the orientation vector, which is attached to the spacecraft, will break alignment with the NADIR pointing vector. The misalignment shall be corrected with fine attitude control actuators. These FACAs are sized based on the methodology presented in 6.2. Using that sizing, the actuator torque is commanded by a tuned PID controller (section 6.3).

Despite efforts to keep pointing NADIR, a time-varying misalignment persists. To comprehend and compare the MW- and RW-controlled satellite pointing performance across many scenarios (as explained in chapter 7), the time signals are condensed into performance metrics (discussed in chapter 8). When the resulting metrics are out of bounds according to two threshold criteria, they are disregarded because they require deeper analysis. The acceptance thresholds are discussed in 9.2.

For '*Perfect sensing of a PID controlled satellite*', section 9.3, this misalignment is sensed perfectly. In contrast, in real-world operation, this sensing is part of attitude determination within the ADCS system, as described in section 6.3.1, and is subject to sensing errors. Therefore, some noise was added to the error vectors to simulate this effect. That scenario is discussed in '*Imperfect sensing of a PID controlled satellite*' 9.4.

A consequence of adding noise is that the performance of an RW-controlled satellite is degraded. In contrast, those of an MW-controlled satellite are not much affected, as presented in section 9.5. Still, in absolute terms, most RW-controlled satellites outperform the MW-controlled. Hence, the RW-controlled satellites are deemed superior as concluded in section **??**.

9.2 Acceptance thresholds

The satellites must perform within an acceptance threshold for their mission to succeed. Thus, two metrics are used to filter for acceptance: maximum oscillations and maximum drift amplitudes.

1. Threshold 1: For this thesis, a continuous push-broom swath width of about 1/3 of the field-of-view is desired. For a swath width of about 3 km, as discussed in section 2.6, this means that the maximum amplitude of the oscillations cannot be larger than 1 km, as indicated by the three horizontal lines in the middle of Figure 95.
2. Threshold 2: The satellite is allowed a slow-moving drift of 10 km for the simulation analysis period of 1.5 orbits ($2{\cdot}T_{\text{orbit}} \approx 11000$ [s] $\rightarrow T_{\text{analysed}} = 0.8{\cdot}(11.000-500) = 8400$ [s] $\rightarrow N_{\text{orbit}} = \frac{8400}{5500} \approx 1.5$). This corresponds to approximately 6.5 km of drift per orbit (twice the field-of-view width).

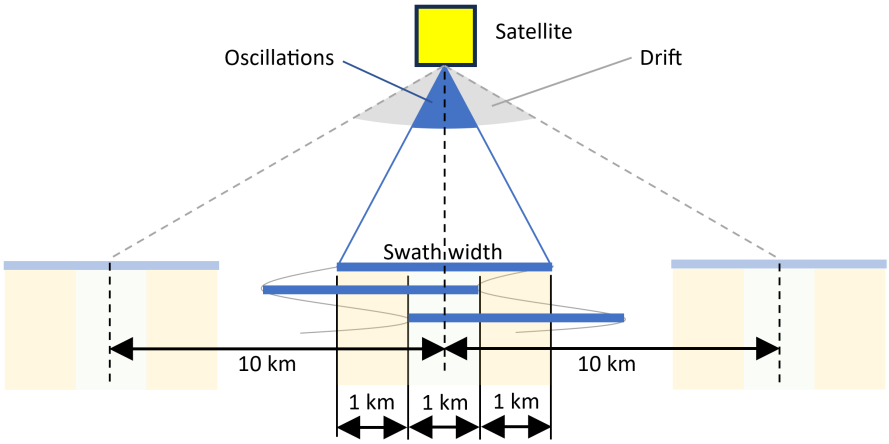

Figure 95: Graphical interpretation of acceptance thresholds: oscillations with a maximum amplitude of 1 km (threshold 1) and drift with a maximum amplitude of 10 km (threshold 2).

The pointing errors relative to the NADIR reference can now be computed. Given the small swath width, the imaged section of Earth is treated as a flat ground plane, and the attitude error angles are used as a direct input (rather than using a single-axis rotation vector known as an axis-angle vector). Equation 155 calculates the ground-plane displacements across- and along-track relative to the NADIR point, and uses this to determine the overall pointing error. These displacements are derived using basic trigonometry, considering the satellite's altitude, h, and its roll and pitch angles.

$$x = h \cdot \tan(\text{roll}) \quad ; \quad y = h \cdot \tan(\text{pitch}) \quad ; \quad R = \sqrt{x^2 + y^2} \tag{155}$$

The angle error stems directly from the yaw error, although it is less relevant, as the engineer can choose any detector format. A visualisation of this pointing error is presented in Figure 96.

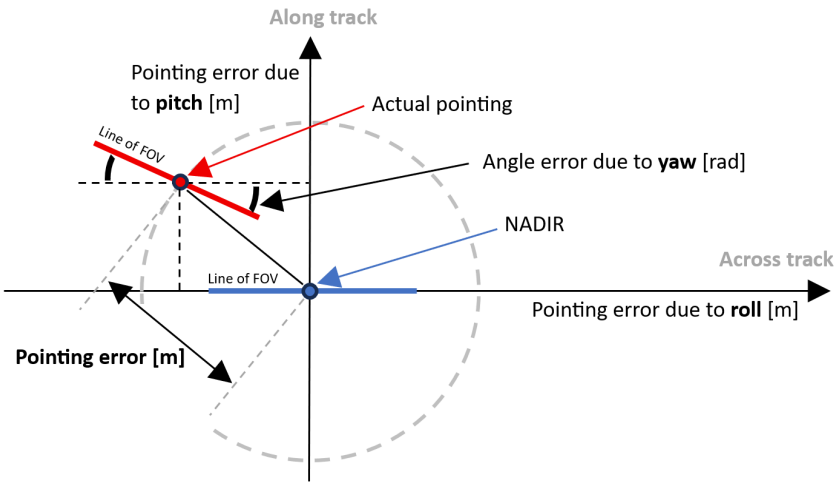

Figure 96: Illustration of satellite pointing errors in along-track and across-track directions. It details the contribution of pitch to along-track pointing error, roll to across-track pointing error, and yaw to angular error, all relative to the NADIR reference. The overall pointing error is depicted as the deviation from the ideal pointing direction.

To filter the results, the acceptance area for the FACA performance is depicted in Figure 97a. When the results are filtered for the 'accepted' area, a comparison between the MWs and RWs can take place.

Next, the RMS RW results are subtracted from the RMS MW results ($MW_{\text{RMS}} - RW_{\text{RMS}}$), which leaves a quantification of how much better the RWs perform with respect to the MWs or vice versa.
Four quadrants exist and are illustrated in Figure 97b. The labels indicate the winning solution; in counter-clockwise order,

- Quadrant 1,'RW', positive values for both oscillations (Y-axis) and drift (X-axis): this indicates that the MW performs (x, y) worse than the RW onboard such a satellite.
- Quadrant 2, 'MW drift', positive values for oscillations (Y-axis) and negative values for drift (X-axis): this indicates that the MW performs y worse in oscillations and $|x|$ in drift better than the RW onboard such a satellite.
- Quadrant 3, 'MW', negative values for both oscillations (Y-axis) and drift (X-axis): this indicates that the MW performs $(|x|, |y|)$ better than the RW onboard such a satellite.
- Quadrant 4, 'MW oscillations', negative values for oscillations (Y-axis) and positive values for drift (X-axis): this indicates that the MW performs $|y|$ better and x worse than the RW onboard such a satellite.

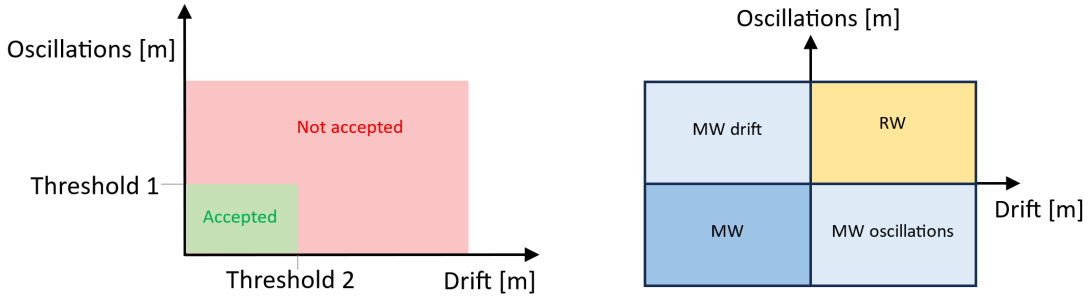

(a) Acceptance regions performance

(b) MW versus RW performance indication

Figure 97: Performance diagrams illustrating (a) acceptance regions based on oscillation and drift thresholds, and (b) a classification of superior performance (MW, MW drift, MW oscillations, RW).

9.3 Perfect sensing of a PID controlled satellite

Figure 98 presents a scatter plot illustrating the Root Mean Square (RMS) drift versus RMS oscillations for attitude control systems utilising RWs and MWs under **perfect sensing** conditions. Both axes are presented on a logarithmic scale, indicating that the performance metrics span several orders of magnitude, referring to the ground pointing error relative to the perfect NADIR reference.

The plot shows two clear groups of data points: blue circles for the *RW - perfect* scenarios and orange circles for the *MW - perfect* scenarios. For both FACAs, there is a general positive correlation. As RMS drift goes up, RMS oscillations also tend to rise, though the data is quite scattered.

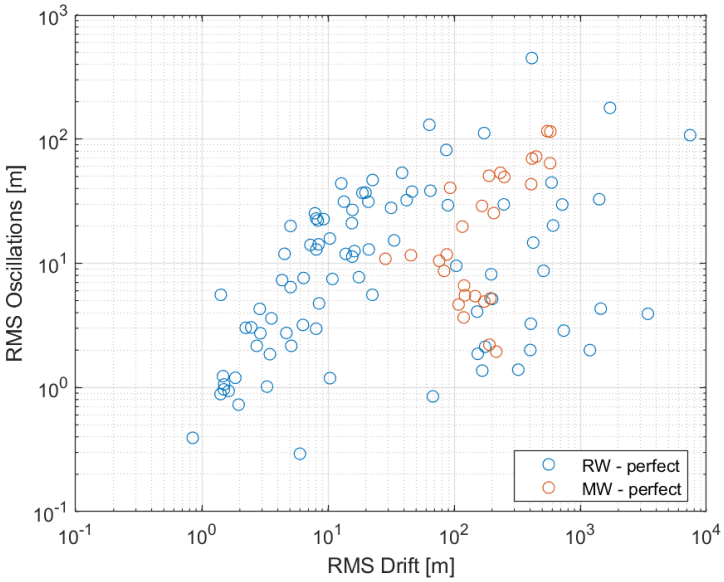

Figure 98: MW versus RW performance indication of accepted satellites: 27 out of 128 (21%) MW and 86 out of 128 (67%) RW satellites are accepted.

Table 9 provides a direct comparison of the key performance characteristics observed in Figure 98.

Table 9: Comparative performance summary of RW and MW controlled satellites under perfect sensing conditions.

Characteristic	**RW-controlled (Perfect Sensing)**	**MW-controlled (Perfect Sensing)**
Drift Range	RMS drift values ranging from approximately 0.5 m to over 8000 m.	Primarily shows RMS drift values between approximately 80 m and 600 m. Does not reach the very low drift values achieved by RWs.
Oscillation Range	RMS oscillations ranging from roughly 0.3 m to over 400 m.	Largely concentrated between 2 m and approximately 100 m.
Best Performance	Lowest RMS drift and oscillation values are exclusively achieved by RW systems (sub-meter level for both). Capable of very high precision (< 1 m).	Does not demonstrate the same level of fine precision as the best-performing RW configurations. Absence of red points in the bottom-left corner of the plot.
Worst Performance	Scenarios extend to the highest error values observed, indicating a wide operational envelope that can encompass less precise control if conditions are unfavourable.	Overall higher drift and oscillation ranges.
Clustering	Shows a broad distribution across the plot, reflecting wide operational versatility.	Points appear more clustered in a specific region of higher drift and moderate oscillations, suggesting a characteristic performance regime.

From the simulated satellites with the parameters described in previous chapters, only 27 out of 128 (21%) MW-controlled and 86 out of 128 (67%) RW-controlled satellites are accepted according to the *maximum* acceptance criteria, see Figure 98. Effectively, three groups exist:

1. Solely an MW provides a viable solution: 5
   Simulation numbers: [9 15 68 77 109]

2. Solely RWs provide a viable solution: 64
   Simulation numbers: [2 10 11 12 13 14 18 20 22 23 27 28 31 32 33 34 35 37 38 39 40 42 45 47 50 51 52 53 55 57 58 61 63 64 67 69 70 72 74 75 76 79 81 82 85 89 90 91 92 93 94 95 96 97 98 104 106 107 111 112 116 117 126 128]

3. Either an MW or RWs provide viable solutions: 22
   Simulation numbers: [5 6 7 8 21 25 26 30 36 41 48 54 56 59 83 103 110 118 119 122 124 127]

For groups (1) and (2), the choice is readily made, given the design constraints. For group (3), however, a classification for superior performance is required and is showcased in Figure 99b.

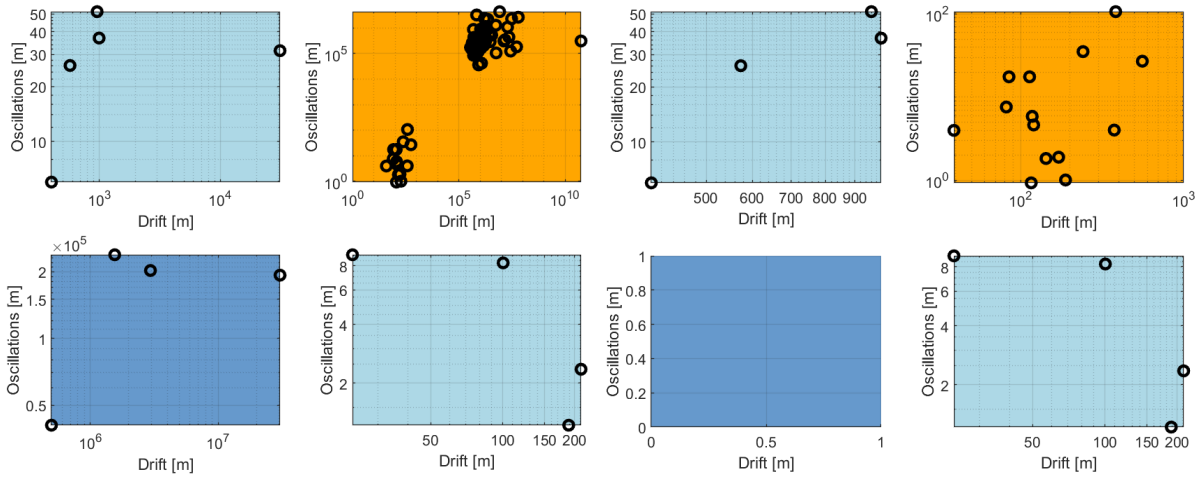

(a) Count (91): Q1, 'RW', 78; Q2, 'MW drift', 5; Q3, 'MW', 4; Q4, 'MW oscillations', 4.

(b) Count (22): Q1, 'RW', 14; Q2, 'MW drift', 4; Q3, 'MW', 0; Q4, 'MW oscillations', 4.

Figure 99: Perfect sensing, MW versus RW performance indication per quadrant (a) whether either solution is accepted and (b) whereby both solutions fall in the acceptance region. Absolute values are used because of the logarithmic axes.

Interestingly, in the group where both MWs and RWs are an option, not a single MW appears in the third quadrant. Both quadrant two and four show that MW-solutions are a good alternative to employed RWs, but at the cost of either oscillations or drift. The remainder (the majority) of RWs are superior in performance by tens to hundreds of meters in drift and by meters to a hundred meters in oscillations.

Summarising, the following outcomes are found:

1. In 5 scenarios (3.9%), MWs are the superior choice
2. In 8 scenarios (6.3%), both MWs and RWs are a compromised choice.
3. In 78 scenarios (60.9%), RWs are the superior choice.
4. In 37 scenarios (28.9%), no feasible solution exist.

Finally, the data on perfect sensing strongly suggest that RW-controlled satellites offer the potential for higher precision and lower error magnitudes (both drift and oscillations) than MW-controlled satellites, especially when aiming for stringent pointing requirements.

9.4 Imperfect sensing of a PID controlled satellite

Figure 100 presents a scatter plot illustrating the Root Mean Square (RMS) drift versus RMS oscillations for RW- and MW-controlled satellites under **imperfect sensing** conditions. As in perfect-sensing scenarios, both axes are on a logarithmic scale, and the units are in meters, referring to a pointing error relative to the perfect NADIR reference.

Compared to the perfect-sensing scenarios, there is a general upward and rightward shift in both data clusters, indicating an expected degradation in performance (higher drift and/or oscillations) when sensing is not ideal. The positive correlation between RMS drift and RMS oscillations persists across both actuator types, although for the RWs it the scatter spreads out further.

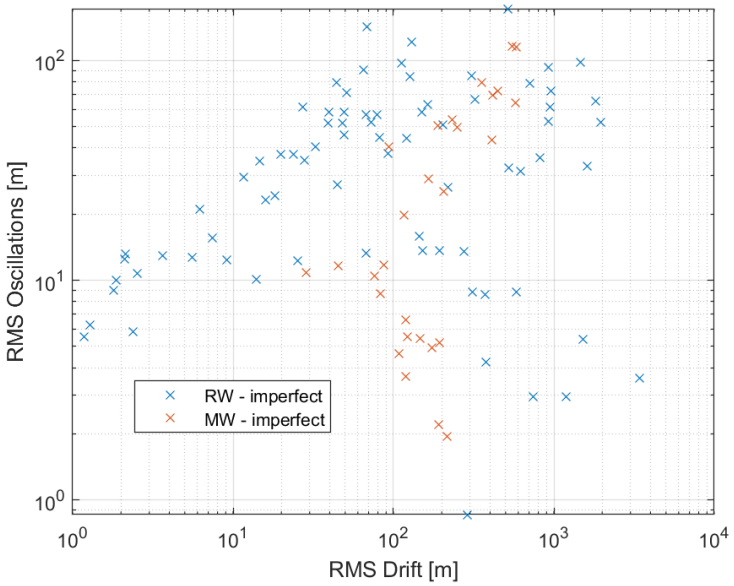

Figure 100: Imperfect sensing, MW versus RW performance indication of accepted satellites: 28 out of 128 (22%) MW and 76 out of 128 (59%) RW satellites are accepted.

Table 10 provides a direct comparison of the key performance characteristics observed in Figure 100.

Table 10: Comparative performance summary of RW and MW controlled satellites under imperfect (noisy) sensing conditions.

Characteristic	**RW-controlled (Imperfect Sensing)**	**MW-controlled (Imperfect Sensing)**
Drift Range	RMS drift values ranging from approximately 1 m to over 3000 m.	Primarily shows RMS drift values between approximately 50 m and 700 m. Similar to the perfect case but slightly wider.
Oscillation Range	RMS oscillations ranging from roughly 1 m to about 200 m.	Largely concentrated between 2 m and approximately 120 m.
Best Performance	The minimum drift is now around $1-2$ m and minimum oscillations is close to 1 m, but most oscillations start at approximately 3 m.	The drift values appear to be at best about 30 m. For few, the lowest oscillation values appear slightly higher than in the perfect MW case (worsened around $2-3$ m).
Worst Performance	Scenarios extend to the highest observed error values, similar to the perfect case, maintaining a broad operational envelope.	Overall higher drift and oscillation ranges. Consistent with the perfect sensing scenarios.
Clustering	Shows a broad distribution across the plot. Performance has shifted towards higher error values compared to the perfect sensing scenarios.	Points remain clustered in a specific region of higher drift and moderate oscillations, indicating a characteristic performance regime, similar to the perfect sensing scenario.

Only 28 out of 128 (22%) MW-controlled ($+1$) and 76 out of 128 (59%) RW-controlled (-10) satellites are accepted according to the *maximum* acceptance criteria, see Figure 98. Effectively, three groups exist:

1. Solely an MW provides a viable solution: 7
   Simulation numbers: [9 15 36 41 68 77 109]

2. Solely RWs provide a viable solution: 55
   Simulation numbers: [10 11 12 13 18 20 22 27 28 31 32 34 35 37 38 39 42 45 47 50 52 53 55 57 61 63 64 67 69 70 72 74 75 76 79 81 82 85 91 92 93 94 95 96 97 98 104 106 107 111 112 116 117 126 128]

3. Either an MW or RWs provide viable solutions: 21
   Simulation numbers: [5 6 7 8 21 25 26 30 48 54 56 59 83 90 103 110 118 119 122 124 127]

For groups (1) and (2), the choice is readily made, given the design constraints. For group (3), however, a classification for superior performance is required and is showcased in Figure 101b.

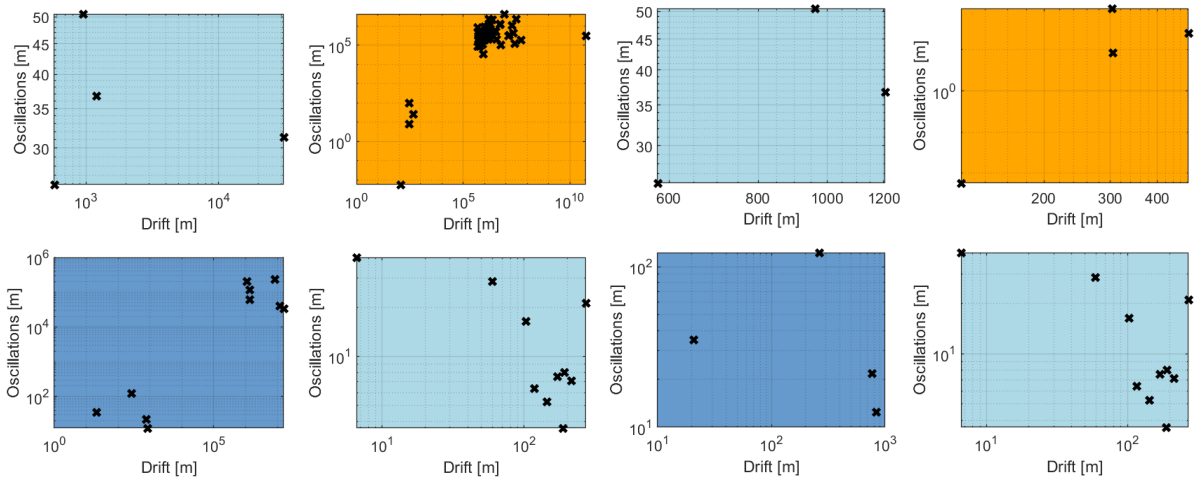

(a) Count (83): Q1, 'RW', 59; Q2, 'MW drift', 4; Q3, 'MW', 10; Q4, 'MW oscillations', 10.

(b) Count (21): Q1, 'RW', 4; Q2, 'MW drift', 3; Q3, 'MW', 4; Q4, 'MW oscillations', 10.

Figure 101: Imperfect sensing, MW versus RW performance indication per quadrant (a) whether either solution is accepted and (b) whereby both solutions fall in the acceptance region. Absolute values are used because of the logarithmic axes.

Notably, the number of viable design solutions has reduced. Moreover, MWs appear to become a more competitive alternative as seen in the third quadrant. Both quadrant two and four show that MW-solutions are an alternative to RWs, but at the cost of either oscillations or drift. The remainder (the majority) of RWs are superior in performance by tens to hundreds of meters in drift and by meters to a hundred meters in oscillations.

Summarising, the following outcomes are found:

1. In 11 (+6) scenarios (8.6%), MWs are the superior choice
2. In 13 (+5) scenarios (10.2%), both MWs and RWs are a compromised choice.
3. In 59 (−19) scenarios (46.1%), RWs are the superior choice.
4. In 45 (+8) scenarios (35.2%), no feasible solution exist.

Thus, despite the performance degradation caused by imperfect sensing, RW-controlled satellites still demonstrate superior precision, achieving lower overall RMS drift and oscillation magnitudes than MW-controlled systems. The inherent operational characteristics of MWs continue to limit their ability to reach the same level of fine pointing accuracy as RWs, even under these non-ideal sensing conditions.

9.5 Perfect versus imperfect sensing

Figure 102 presents a consolidated scatter plot of Figures 98 and 100. Three key observations can be made. First, the introduction of imperfect sensing shifts the entire performance landscape for RWs towards higher RMS drift and RMS oscillation values. The very high-precision region (bottom-left corner) is less populated, indicating that sensor noise and inaccuracies directly affect the ability to achieve sub-meter-level control. Secondly, the MW-controlled satellites are hardly affected by the introduction of sensing noise. Lastly, regarding relative performance, even with imperfect sensing, RW systems generally maintain their advantage in achieving lower minimum drift and oscillation values than MW systems. The range of performance for RWs remains broader, suggesting greater adaptability but also a larger potential for degraded performance under certain conditions.

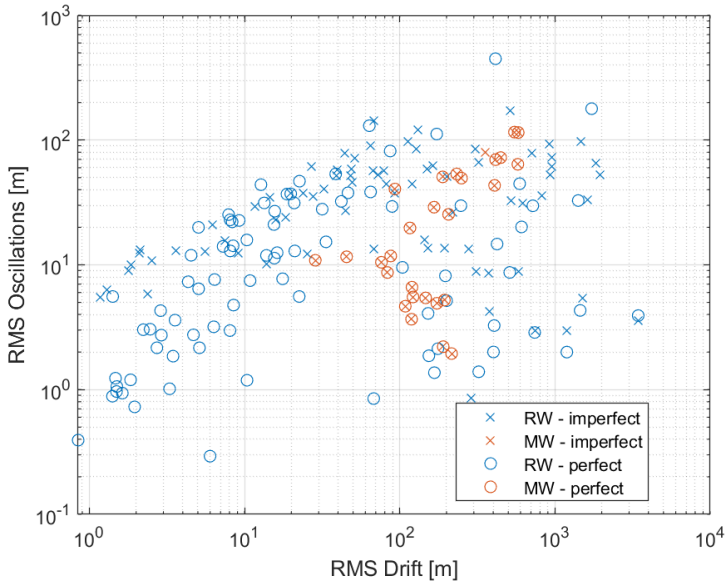

Figure 102: Perfect and Imperfect sensing, MW versus RW performance indication of accepted satellites.

One question arises when examining the RW/MW perfect versus imperfect data, '*By how much is the performance per scenario degraded?*'. To answer this question, the `RW_perfect` data is subtracted from the `RW_imperfect` data, and similarly for the MW data. This comparison is plotted in Figure 103. It illustrates the absolute performance degradation, defined as the magnitude of change in RMS Drift and RMS Oscillations when transitioning from perfect to imperfect sensing conditions.

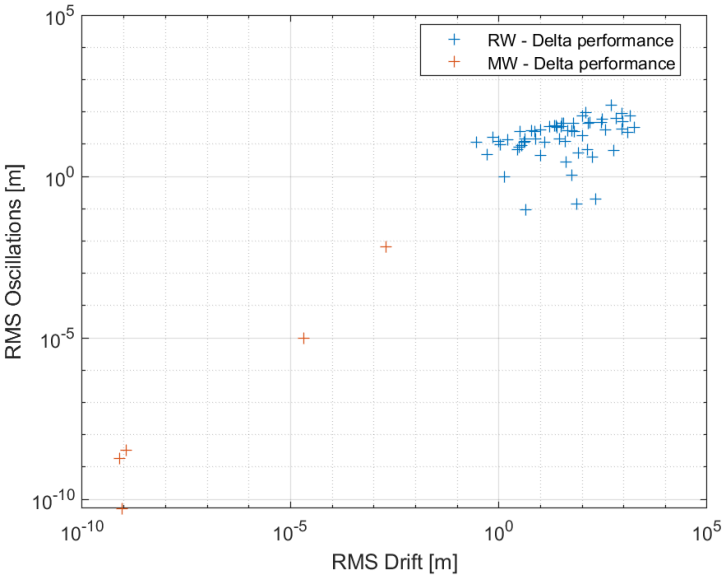

Figure 103: RW performance degradation: imperfect versus perfect sensing.

The RW-controlled satellites (blue data points) are predominantly clustered in the region of relatively higher degradation. The RMS Drift degradation for RWs typically ranges from approximately $10^{-0.5}$ m (around 0.3 m) to over 10^{2} m (hundreds of meters). Similarly, the RMS Oscillations degradation spans from about 10^{-1} m to over 10^{2} m. The clustering around values of 10^{0} m to 10^{2} m for both degradation metrics indicates that RW performance is generally significantly impacted by imperfect sensing. For many scenarios, the absolute increase in error is in the order of meters to tens or hundreds of meters.

The degradation in RMS Drift for MWs ranges from approximately 10^{-10} m to around 10^{0} m (1 meter). While some MW scenarios show negligible drift degradation, others can experience up to a meter increase in drift. However, even the highest drift degradation for MWs is still significantly lower than

the upper range observed for RWs. The very low RMS oscillation degradation and generally lower RMS Drift degradation in MW systems suggest that they are comparatively more robust or less sensitive to imperfect sensing. The inherent gyroscopic stiffness provided by a large momentum bias effectively filters or dampens the impact of sensor noise on the satellite's angular rates, thereby limiting increases in oscillatory behaviour.

9.6 Tradespace exploration conclusions

In summary, although imperfect sensing reduces the absolute performance of both RW and MW-controlled satellites by increasing the RMS drift and oscillation magnitudes, the relative advantage of RW satellites for high-precision applications remains evident. Nonetheless, there are scenarios thinkable in which MW-controlled satellites will outperform RW-controlled ones. For example, when using (very) noisy attitude measurements. This means that MWs can not be ruled out immediately.

Despite imperfect sensing, some RW-controlled satellites continue to exhibit the lowest RMS drift and oscillation values in the data (approximately $1 - 2$ m for both metrics, compared to less than 1 m with perfect sensing). Consequently, for missions requiring the highest precision, RW-controlled satellites generally remain the preferred option, even when accounting for real-world sensing limitations.

In contrast, MW-controlled satellites consistently exhibit a narrower performance range, characterised by inherently higher minimum RMS drift values. Although their performance also declines with imperfect sensing, by much less, their intrinsic operating characteristics (explained in section 6.4.3) establish a baseline for achievable precision that remains inferior to the optimal performance of RW-controlled satellites.

Therefore, this analysis concludes that for missions with stringent pointing requirements, RWs remain the preferred actuator choice even under imperfect sensing conditions. However, the performance degradation resulting from sensing limitations should be systematically incorporated into the overall error budget and mission design. Also, the controller must be designed such that the satellite will not become unstable due to cumulative torques and noisy (sensing) errors.

10 Conclusions and Recommendations

This chapter presents the conclusions derived from the research conducted in this thesis. It synthesises the findings to provide definitive answers to the posed research questions in section 10.1, reflects on the scientific contribution in 10.2, reflects on the limitations in 10.3, and provides practical recommendations for the industry and future academic research in 10.4 and 10.5, respectively.

10.1 Main Conclusions

This thesis established a model-based framework for selecting and sizing Fine Attitude Control Actuators (FACAs) for nadir-pointing small satellites in Low Earth Orbit. The satellites' sizes, masses, and shapes were derived from the minimum dimensions required to achieve sub-meter panchromatic spatial resolution for Earth observation. A high-fidelity, modular simulation environment was developed in MATLAB to model orbital dynamics, dominant disturbance torques, and closed-loop actuator performance. This tool enabled a quantitative trade-off analysis between RW-controlled and MW-controlled satellites based on pointing accuracy and precision, whereby the FACA assemblies we allocated identical mass and volume constraints.

Per satellite, several parameters are output to provide a first approximation for FACA sizing, along with the flywheel rotational rates required for an approximately 3 km field of view with oscillations of maximum amplitude of 1 km (about 1/3 the field of view) and a drift (< 0.01 Hz) with a maximum amplitude of 10 km (about 3 times the field of view).

The main conclusions, structured around the main research questions, are as follows:

A. *What are the key performance trade-offs for selecting a fine attitude control actuator for a nadir-pointing small satellite in Low Earth Orbit?*
The primary trade-off concerns the mission objective, namely ***reorient-ability***. If the satellite must be capable of agile manoeuvres along multiple axes, the MW would be ruled out due to its inherent gyroscopic stiffness when being in the spun-up state. Thus, if the satellite were to reorient itself when employing an MW, the momentum would first have to be offloaded before initiating an off-spin-axis manoeuvre. Hence, if the satellite must manoeuvre quickly, it would require either reaction wheels or Control Moment Gyros (CMGs). Qualitatively, an RW assembly has greater angular momentum per unit volume and mass, whereas a CMG has a superior torque-to-power ratio. A quantitative comparison between the performance of RWs and CMGs is not conducted in this thesis, though. If the mission objective is to provide stable along-track pointing, both MW- and RW-controlled satellites are an option, and are modelled in this work. The CMG is ruled out due to its unnecessary complexity.

   The second and third performance trade-offs concern ***pointing accuracy and precision***. These metrics are essential for assessing stable nadir-pointing, as they indicate how well the satellite maintains alignment and the magnitude of mispointing in the along- and across-track directions. Both metrics can be improved by employing larger-in-mass or larger-in-size flywheels, along with more sophisticated sensing and control algorithms.

   Thus, the fourth trade-off arguments for FACA selection and sizing were quantified as the ***required torque authority***, driven predominantly by orbital altitude and satellite cross-sectional area, ***versus the total actuator mass***. An equal '*pointing accuracy and precision*' performance can be achieved for either FACA, but at the cost of the inequivalent total actuator mass.

B. *B. For a sub-meter spatial-resolution nadir-pointing Earth observation mission, which fine attitude control actuator is the most suitable candidate when evaluated against pointing error?*
For the defined mission scope of a sub-meter resolution, nadir-pointing Earth observation satellite, with a pointing precision and accuracy requirement of 1 km and 6.5 km per orbit, respectively, the ***reaction wheel assembly*** was determined to be the most suitable FACA. It consistently outperformed the MW-controlled satellite when attitude determination or sensing noise was set to zero. It predominantly outperformed it under realistic sensing noise levels typical of current-state-of-the-art sensors. The RW-controlled satellites met the stringent pointing-precision requirement across a wide

range of simulated orbital conditions. The best-performing models achieved an order-of-magnitude lower RMS error in both pointing accuracy and precision than the momentum-bias alternative.

To quantify, under equal FACA assembly masses and design-volume constraints, the lowest RMS drift and oscillation values are achieved exclusively by RW-controlled satellites. They achieve very high precision and accuracy (< 1 m) for perfect sensing and high precision and accuracy (< 3 m) for imperfect sensing. The MW-controlled alternatives appeared less susceptible to noise due to their inherent momentum bias. Their best-case scenarios for both perfect and imperfect sensing show that high precision is also possible at approximately 2 m, at the expense of a roughly 200 m pointing accuracy. However, the overall trend for the MW-controlled satellites that met the acceptance threshold requirements indicated a precision of approximately 5 to 100 meters, with a pointing accuracy of roughly 200 m.

10.2 Scientific Contribution

The primary scientific contribution of this work is a generalised, validated simulation framework that enables quantitative prediction of closed-loop attitude performance from high-level mission parameters. The developed mass and sizing estimation for RW flywheels showed good agreement with commercial actuator systems, providing a practical tool for rapid sizing during early-phase mission design studies. From a systems engineering perspective, it is clear that many solutions exist for selecting a sub-meter spatial-resolution satellite operating in low Earth orbit. Creating a trade-space simulation can be an effective tool for eliminating undesirable candidates before a preliminary design is considered.

10.3 Reflection on Research Scope and Limitations

While the research questions were answered comprehensively within the defined scope, the study was limited to rigid-body dynamics with 4-DOF and idealised sensor models. The initial assumption of a purely Keplerian orbit does not reflect a proper 6-DOF condition, whereby, for example, the $J2$ effects cause a deviation from the satellite's trajectory, nor does it account for orbital decay. Additionally, because only two orbits are simulated, temporal environmental changes have been ignored. Further, only one symmetrical satellite configuration (solar panel-satellite bus-solar panel) was examined, although the framework permits examination of multiple configurations. The findings are therefore most directly applicable to small, rigid satellites without flexible appendages.

Furthermore, not all RW-controlled satellites performed as expected. The cause for this underperforming behaviour is not examined, and leaves room for discussion. It is unclear at this point what the exact cause is. The undesired performing satellites should be reviewed on a case-by-case basis to identify causal relationships. Options include, but are not limited to: a) undersizing of the actuator's flywheel due to slight deviations in attitude causing significant deviations in experienced external torques (remember: the undisturbed torques were taken to size the actuator), b) closed-loop sensitivities in the control loop, c) intermediate axis chosen as stabilising axis, adding to attitude sensitivities, or d) numerical integration errors as the simulation settings were fixed to be able to evaluate many scenarios.

10.4 Recommendations for industry applications

Based on the conclusions of this thesis, the following recommendations are made for satellite mission designers and systems engineers:

1. **Prioritise reaction wheel actuators**:
   For stable pointing missions in which high pointing precision, such as for high-resolution imaging, is the primary requirement, a reaction wheel assembly should be the default choice unless a specific rationale exists for examining alternative actuators.
2. **Utilise the developed RW mass and sizing estimation parametric model**:
   As described in section 6.2, during a preliminary design phase, first-order estimates for attitude control subsystem mass budgets can be made quite easily.
3. **Conduct a high-fidelity disturbance torque analysis early in the design process**:
   The maximum required torque is the primary driver of actuator sizing and selection, but the disturbance torque also varies significantly with orbital position, altitude, and space weather phenomena.

4. **Allocate sufficient FACA mass budget**:
   The mass budget required to stabilise the satellite within specifications varies strongly with orbital altitude as depicted in Figure 67.

5. **Run a Monte-Carlo Simulation**:
   When a Trade-Space Simulation identifies viable design configurations, it is advisable to examine one or more cases in greater detail. In such a scenario, it is advisable to run a Monte Carlo simulation to mitigate uncertainties in preliminary sizing, torque offloading, and sensitivities to temporal disturbances (i.e., worst-case space weather) and off-nadir pointing modes.

10.5 Recommendations for Future Research

To build upon the findings of this work, the following recommendations for future research are proposed:

1. **Investigate the pointing performance for various satellite configurations**:
   Using the proposed 4-DOF modular simulation framework, various satellite configurations can be modelled, including asymmetric solar panels, mass distributions, and appendages such as antennas.

2. **Incorporate a micro-vibration model**:
   Sensing noise severely degraded the pointing performance of an RW-controlled satellite. It is therefore expected that noise from internal rotating mechanical devices, such as FACAs, which cause micro-vibrations [3], [28], [45], [61], [89], also pose ADCS challenges. When this noise is emitted at frequencies within the sensing and actuation bandwidths, it impacts pointing performance. When image quality is being evaluated, micro-vibrations cannot be ignored.

3. **Investigate noise filtering techniques**:
   Mitigate most sensing noise from entering the control feedback, as it significantly degrades pointing precision and accuracy.

4. **Expand Actuator Model Library:**
   Integrate models of control-moment gyroscopes, magnetorquers, and micro-thrusters to enable more comprehensive trade-space and mission analysis.

5. **Experimental Validation:**
   Validate the simulation framework against a hybrid simulation using hardware-in-the-loop test bench data or on-orbit telemetry from a mission with a well-documented configuration.

6. **Investigate Advanced Control Strategies:**
   Explore the integration and performance of modern control techniques, such as robust control [68] or machine-learning-based adaptive controllers [67], within the developed framework.

References

[1] Yusuf Acar and Nadjim M Horri. "Optimal momentum unloading of reaction wheels in the presence of attitude control errors". In: *AIAA Guidance, Navigation, and Control (GNC) Conference*. 2013, p. 4962.

[2] Advanced Navigation. *NED Coordinate System*. https://docs.advancednavigation.com/gnss-compass/NedCoordSystem.htm. Accessed: 2024-05-30.

[3] Hassan Alkomy and Jinjun Shan. "Modeling and validation of reaction wheel micro-vibrations considering imbalances and bearing disturbances". In: *Journal of Sound and Vibration* 492 (2021), p. 115766. ISSN: 0022-460X. DOI: https://doi.org/10.1016/j.jsv.2020.115766. URL: https://www.sciencedirect.com/science/article/pii/S0022460X20305952.

[4] Steven S Andrews. "Thermal radiation". In: *Light and Waves: A Conceptual Exploration of Physics*. Springer, 2023, pp. 307–328.

[5] ASTROFEIN. *Reaction Wheels*. https://www.astrofein.com/en/reaction-wheels/. Accessed: August 18, 2025. 2025.

[6] Kashyapa Naren Athreyas, Anusha Banninthaya, and Wee Seng Lim. "System Design for Small Satellites in Very Low Earth Orbit". In: (2024).

[7] *AVNIR-2 - Earth Online - ESA*. 2023. URL: https://earth.esa.int/eogateway/instruments/avnir-2.

[8] Yochoong Bang and Hyung Don Choi. "Attitude control of a bias momentum satellite using moment of inertia". In: *IEEE Transactions on Aerospace and Electronic Systems* 38.1 (2002), pp. 243–250. DOI: 10.1109/7.993243.

[9] Ferdinand P. Beer et al. *Vector Mechanics for Engineers: Statics and Dynamics*. 11th. McGraw-Hill Education, 2017.

[10] Divya Bhatia. "Attitude Determination and Control System Design of Sub-Arcsecond Pointing Spacecraft". In: *Journal of Guidance, Control, and Dynamics* 44.2 (2021), pp. 295–314. DOI: 10.2514/1.G005116. eprint: https://doi.org/10.2514/1.G005116. URL: https://doi.org/10.2514/1.G005116.

[11] Guzmán Borque Gallego, Emmanuel Onillon, and Leopoldo Rossini. "10 - Attitude determination and control system relying on magnetic bearing reaction wheels". In: *Next Generation CubeSats and SmallSats*. Ed. by Francesco Branz et al. Elsevier, 2023, pp. 223–238. ISBN: 978-0-12-824541-5. DOI: https://doi.org/10.1016/B978-0-12-824541-5.00004-2. URL: https://www.sciencedirect.com/science/article/pii/B9780128245415000042.

[12] Meryem Bouras and Hassan Berbia. "Review of Attitude Control Approaches for ADCS Optimization and Faults Tolerance". In: *2019 8th International Conference on Modeling Simulation and Applied Optimization (ICMSAO)*. 2019, pp. 1–4. DOI: 10.1109/ICMSAO.2019.8880358.

[13] Benjamin Brenny et al. "Development of spectrometers for the TANGO greenhouse gas monitoring missions". In: *International Conference on Space Optics — ICSO 2022*. Ed. by Kyriaki Minoglou, Nikos Karafolas, and Bruno Cugny. Vol. 12777. International Society for Optics and Photonics. SPIE, 2023, 127771S. DOI: 10.1117/12.2689936. URL: https://doi.org/10.1117/12.2689936.

[14] British Geological Survey (BGS). *The Earth's Magnetic Field: An Overview*. Accessed 21 July 2025. URL: http://www.geomag.bgs.ac.uk/education/earthmag.html.

[15] Roger W. Brockett. *Finite dimensional linear systems*. Wiley, 1970.

[16] James A Cavender. "Gravity-gradient torque with the lowest zonal harmonic". In: *Aerospace science and technology* 5.1 (2001), pp. 69–71.

[17] NOAA National Geophysical Data Center. *International Geomagnetic Reference Field (IGRF) Model*. Accessed: 2025-08-01. 2022. URL: http://www.ngdc.noaa.gov/IAGA/vmod/igrf.html.

[18] Chuckage. *Earth-centered, Earth-fixed coordinate system*. https://en.wikipedia.org/wiki/Earth-centered,_Earth-fixed_coordinate_system. [Online; accessed 30-May-2024]. 2024.

[19] N.H. Crisp et al. "The benefits of very low earth orbit for earth observation missions". In: *Progress in Aerospace Sciences* 117 (2020), p. 100619. ISSN: 0376-0421. DOI: https://doi.org/10.1016/j.paerosci.2020.100619. URL: https://www.sciencedirect.com/science/article/pii/S0376042120300312.

[20] *CubeSat Reaction Wheels Control System SatBus 4RW0*. 2019. URL: https://nanoavionics.com/cubesat-components/cubesat-reaction-wheels-control-system-satbus-4rw/.

[21] Wei Du, Bong Wie, and Mark Whorton. "Dynamic Modeling and Flight Control Simulation of a Large Flexible Launch Vehicle". In: Aug. 2008. ISBN: 978-1-60086-999-0. DOI: 10.2514/6.2008-6620.

[22] NOAA National Centers for Environmental Information. *Geomagnetic kp and ap Indices @ONLINE*. July 2021. URL: https://www.ngdc.noaa.gov/stp/GEOMAG/kp_ap.html#:~:text=The%20Ap*%20index%20is%20defined,associated%20with%20the%20storm%20event.

[23] European Space Agency. *Low Earth orbit*. https://www.esa.int/ESA_Multimedia/Images/2020/03/Low_Earth_orbit. [Accessed 07 November 2025]. 2020.

[24] *File: Atmospheric electromagnetic transmittance or opacity.png - Wikimedia Commons*. 2007. URL: https://commons.wikimedia.org/wiki/File:Atmospheric_electromagnetic_transmittance_or_opacity.jpg.

[25] William M. Folkner et al. *The Planetary and Lunar Ephemerides DE430 and DE431*. Tech. rep. IPN Progress Report 42-196. February 15, 2014. Jet Propulsion Laboratory, California Institute of Technology, 2014.

[26] With Qiang Fu. "4 - Radiative Transfer". In: *Atmospheric Science (Second Edition)*. Ed. by John M. Wallace and Peter V. Hobbs. Second Edition. San Diego: Academic Press, 2006, pp. 113–152. ISBN: 978-0-12-732951-2. DOI: https://doi.org/10.1016/B978-0-12-732951-2.50009-0. URL: https://www.sciencedirect.com/science/article/pii/B9780127329512500090.

[27] Dan Gao et al. "Design and simulation of ultra-thin and high-efficiency silicon-based trichromatic PIN photodiode arrays for visible light communication". In: *Optics Communications* 475 (2020), p. 126296. DOI: 10.1016/j.optcom.2020.126296. URL: https://www.sciencedirect.com/science/article/pii/S0030401820307136.

[28] Mohan Hao et al. "Torque Ripple Minimization of Reaction Flywheel Based on Linear Extended State Observer". In: *2023 26th International Conference on Electrical Machines and Systems (ICEMS)*. 2023, pp. 3844–3848. DOI: 10.1109/ICEMS59686.2023.10345186.

[29] H. B. Hassrizal and J. A. Rossiter. "A survey of control strategies for spacecraft attitude and orientation". In: *2016 UKACC 11th International Conference on Control (CONTROL)*. 2016, pp. 1–6. DOI: 10.1109/CONTROL.2016.7737543.

[30] Liang He et al. "Developments of attitude determination and control system of microsats: A survey". In: *Proceedings of the Institution of Mechanical Engineers, Part I: Journal of Systems and Control Engineering* 235.10 (2021), pp. 1733–1750. DOI: 10.1177/0959651819895173. eprint: https://doi.org/10.1177/0959651819895173. URL: https://doi.org/10.1177/0959651819895173.

[31] Zuliana Ismail and Renuganth Varatharajoo. "A study of reaction wheel configurations for a 3-axis satellite attitude control". In: *Advances in Space Research* 45.6 (2010), pp. 750–759. ISSN: 0273-1177. DOI: https://doi.org/10.1016/j.asr.2009.11.004. URL: https://www.sciencedirect.com/science/article/pii/S0273117709007078.

[32] Yifan Jiang et al. "Aerodynamic drag analysis and reduction strategy for satellites in Very Low Earth Orbit". In: *Aerospace Science and Technology* 132 (2023), p. 108077. ISSN: 1270-9638. DOI: https://doi.org/10.1016/j.ast.2022.108077. URL: https://www.sciencedirect.com/science/article/pii/S1270963822007519.

[33] Karim Kamalaldin et al. "Design and Testing of Attitude Determination and Control Subsystem for Alainsat-I: 3U Cubesat". In: July 2023, pp. 257–260. DOI: 10.1109/IGARSS52108.2023.10282690.

[34] A. Kamp. *TU/D Reader: Space Instrumentation Engineering AE4880 – Astrodynamics and Satellite Systems*. Faculty of Aerospace Engineering, Delft University of Technology, November 2007. 2007.

[35] Kinga Karwowska and Damian Wierzbicki. "Using Super-Resolution Algorithms for Small Satellite Imagery: A Systematic Review". In: *IEEE Journal of Selected Topics in Applied Earth Observations and Remote Sensing* 15 (2022), pp. 3292–3312. DOI: 10.1109/JSTARS.2022.3167646.

[36] *Kepler Space Telescope Reaction Wheel Remains a Concern*. 2013. URL: https://spacenews.com/34692kepler-space-telescope-reaction-wheel-remains-a-concern/.

[37] Ragab Khalil. "DIGITAL COMPASS, IS IT ERROR FREE?" In: (). URL: https://www.researchgate.net/publication/268412487_DIGITAL_COMPASS_IS_IT_ERROR_FREE.

[38] B. Khouane et al. "PD Controller Design for Three-Axis Attitude Stabilization of a Microsatellite Using Reaction Wheels". In: *IC-AIRES 2024, Lecture Notes in Networks and Systems*. Ed. by M. Hatti. Vol. 1238. Springer Nature Switzerland AG, 2025, pp. 161–169. DOI: 10.1007/978-3-031-80301-7_18. URL: https://doi.org/10.1007/978-3-031-80301-7_18.

[39] Stanley Q. Kidder and Thomas H. Vonder Haar. "2 - Orbits and Navigation". In: *Satellite Meteorology*. Ed. by Stanley Q. Kidder and Thomas H. Vonder Haar. San Diego: Academic Press, 1995, pp. 15–46. ISBN: 978-0-12-406430-0. DOI: https://doi.org/10.1016/B978-0-08-057200-0.50006-7. URL: https://www.sciencedirect.com/science/article/pii/B9780080572000500067.

[40] Dongwoo Kim and Taejin Chung. "Design of an Elliptical Orbit for High-Resolution Optical Observation at a Very Low Altitude over the Korean Peninsula". In: *Journal of Astron. Space Sci.* 40.1 (2023). pISSN: 2093-5587, eISSN: 2093-1409, pp. 35–44. DOI: 10.5140/JASS.2023.40.1.35. URL: https://doi.org/10.5140/JASS.2023.40.1.35.

[41] Joseph R. Kopacz, Roman Herschitz, and Jason Roney. "Small satellites an overview and assessment". In: *Acta Astronautica* 170 (2020), pp. 93–105. ISSN: 0094-5765. DOI: https://doi.org/10.1016/j.actaastro.2020.01.034. URL: https://www.sciencedirect.com/science/article/pii/S0094576520300540.

[42] N Sai Krishna et al. "Design and implementation of a reaction wheel system for CubeSats". In: *2018 IEEE Aerospace Conference*. 2018, pp. 1–7. DOI: 10.1109/AERO.2018.8396584.

[43] Abdelmadjid Lassakeur, R Roubache, and N Bekhadda. "A survey of the Magnetic Dipole Moment Determination Methods Applied on CubeSats and Nanosatellites". In: Sept. 2022.

[44] Hamilton Law et al. "Breaking the Smallsat Barriers to Sub-50cm Imaging". In: *37th Annual Small Satellite Conference* (2023). URL: https://digitalcommons.usu.edu/smallsat/2023/all2023/174/.

[45] M.P. Le. "Micro-disturbances in reaction wheels". English. Proefontwerp. Phd Thesis 1 (Research TU/e / Graduation TU/e). Applied Physics and Science Education, Mar. 2017. ISBN: 978-90-386-4221-5.

[46] Pierre Magnan. "The essential contribution of CMOS imaging technologies to Earth Observation applications". In: *ESSDERC 2021 - IEEE 51st European Solid-State Device Research Conference (ESSDERC)*. 2021, pp. 35–42. DOI: 10.1109/ESSDERC53440.2021.9631779.

[47] F. Landis Markley and John L. Crassidis. *Fundamentals of Spacecraft Attitude Determination and Control*. Springer, 2014.

[48] MathWorks. *decYear - Decimal Year Calculator*. https://nbodyphysics.com/blog/gravity-engine-doc-1-3-2-2-2/orbit-parameters/. Matlab function documentation for decyear, used for converting date/time to decimal year. 2025.

[49] MathWorks. *fft*. Accessed: July 2025. 2025. URL: https://nl.mathworks.com/help/matlab/ref/fft.html.

[50] MathWorks. *fmincon*. https://nl.mathworks.com/help/optim/ug/fmincon.html. Accessed: July 2025. 1994-2025.

[51] MathWorks. *ifft*. Accessed: July 2025. 2025. URL: https://nl.mathworks.com/help/matlab/ref/ifft.html.

[52] MathWorks. *NRLMSISE-00 Atmosphere Model*. MATLAB Help Center. Accessed 21 July 2025. 1994-2025. URL: https://nl.mathworks.com/help/aeroblks/nrlmsise00atmospheremodel.html.

[53] MathWorks. *pchip*. Accessed: July 2025. 2025. URL: https://nl.mathworks.com/help/matlab/ref/pchip.html.

[54] MathWorks. *quatmultiply - Calculate product of two quaternions*. Accessed: 16-05-2025. 2025. URL: https://nl.mathworks.com/help/aerotbx/ug/quatmultiply.html.

[55] MathWorks. *rotm2eul: Convert Rotation Matrix to Euler Angles*. MATLAB function from the Robotics System Toolbox. 2014–2022. URL: https://www.mathworks.com/help/robotics/ref/rotm2eul.html.

[56] James K Miller and Connie J Weeks. "Outgassing accelerations of a spacecraft". In: *AAS/AIAA Astrodynamics Specialists Conference, January, Tampa, Florida*. 2006.

[57] *Model 750 - Educational Control Products - ecp*. 2023. URL: http://www.ecpsystems.com/docs/ECP_Gyroscope_Model_750.pdf.

[58] Kenneth Moe and Mildred M. Moe. "Gas–surface interactions and satellite drag coefficients". In: *Planetary and Space Science* 53.8 (2005), pp. 793–801. ISSN: 0032-0633. DOI: https://doi.org/10.1016/j.pss.2005.03.005. URL: https://www.sciencedirect.com/science/article/pii/S0032063305000486.

[59] David Mostaza Prieto, Benjamin P. Graziano, and Peter C.E. Roberts. "Spacecraft drag modelling". In: *Progress in Aerospace Sciences* 64 (2014), pp. 56–65. ISSN: 0376-0421. DOI: https://doi.org/10.1016/j.paerosci.2013.09.001. URL: https://www.sciencedirect.com/science/article/pii/S0376042113000754.

[60] Mohammad Mukhayadi. "Efficient and high precision momentum bias attitude control for small satellite". PhD thesis. Dissertation, Berlin, Technische Universität Berlin, 2020, 2021.

[61] P Muthuganapathy et al. "Friction torque prediction of precision ball bearing unit for reaction wheel actuators for spacecraft applications". In: *International Journal of System Assurance Engineering and Management* (2025), pp. 1–14.

[62] National Geospatial-Intelligence Agency (NGA). *World Geodetic System 1984 (WGS 84)*. https://earth-info.nga.mil/index.php?dir=wgs84&action=wgs84. Accessed: 16-05-2025. National Geospatial-Intelligence Agency.

[63] National Oceanic and Atmospheric Administration (NOAA). *World Magnetic Model*. https://ngdc.noaa.gov/geomag/WMM/. Accessed: 2024-30-05.

[64] Rod Nave. *Moment of Inertia: Hollow Cylinder*. 2025. URL: %7Bhttp://hyperphysics.phy-astr.gsu.edu/hbase/icyl.html#icyl3%7D.

[65] nbodyphysics. *N-body Physics and Orbital Parameters*. https://nbodyphysics.com/blog/gravity-engine-doc-1-3-2-2-2/orbit-parameters/. Comprehensive overview of orbital elements, gravity engines, and simulation tutorials, sourced from a detailed web document on N-body physics and orbital mechanics. 2025.

[66] *Newcomers Earth Observation Guide — ESA Space Solutions*. 2020. URL: https://business.esa.int/newcomers-earth-observation-guide#:~:text=The%20electromagnetic%20transparency%20of%20the,from%201%20cm%20to%2011m)..

[67] Snyoll Oghim et al. "Deep reinforcement learning-based attitude control for spacecraft using control moment gyros". In: *Advances in Space Research* 75.1 (2025), pp. 1129–1144. ISSN: 0273-1177. DOI: https://doi.org/10.1016/j.asr.2024.07.078. URL: https://www.sciencedirect.com/science/article/pii/S027311772400797X.

[68] K. Olfe et al. "Design and experimental verification of a robust control to avoid individual calibration of multiple reaction wheels in satellites". In: *Advances in Space Research* 75.1 (2025), pp. 767–778. ISSN: 0273-1177. DOI: https://doi.org/10.1016/j.asr.2024.09.053. URL: https://www.sciencedirect.com/science/article/pii/S0273117724009864.

[69] Michael Paluszek. *ADCS - Spacecraft Attitude Determination and Control*. Plainsboro, NJ, United States: Elsevier, 2023. ISBN: 978-0-323-99915-1. DOI: 10.1016/C2021-0-00544-7.

[70] Massimiliano Pastena et al. "Overview of ESA's Earth Observation upcoming small satellites missions". In: *34th Annual AIAA/USU Conference on Small Satellites* (2020). URL: https://digitalcommons.usu.edu/smallsat/2020/all2020/127/.

[71] R. Pastore et al. "Outgassing effect in polymeric composites exposed to space environment thermal-vacuum conditions". In: *Acta Astronautica* 170 (2020), pp. 466–471. ISSN: 0094-5765. DOI: https://doi.org/10.1016/j.actaastro.2020.02.019. URL: https://www.sciencedirect.com/science/article/pii/S0094576520300813.

[72] Nikolay V. Pavlyukevich and Yury V. Polezhaev. *Accommodation Coefficient*. A-TO-Z Guide to Thermodynamics, Heat & Mass Transfer, and Fluids Engineering. Article added: 1 February 2011, Article last modified: 3 February 2011. Feb. 2011. DOI: 10.1615/AtoZ.a.accommodation_coefficient. URL: https://www.begellhouse.com/references/a-to-z-guide-to-thermodynamics-heat-mass-transfer-and-fluids-engineering/accommodation-coefficient.html.

[73] F.L. Pedrotti and L.S. Pedrotti. *Introduction to Optics*. Prentice Hall, 1993. ISBN: 9780135015452. URL: https://books.google.nl/books?id=YrLvAAAAMAAJ.

[74] J. Peraire and S. Widnall. *16.07 Dynamics, Fall 2009 Version 2.0, Lecture L29 - 3D Rigid Body Dynamics*. Lecture Notes, MIT. Fall 2009. URL: https://ocw.mit.edu/courses/16-07-dynamics-fall-2009/f5b25c0af8ec4f76776221c148ea15b3_MIT16_07F09_Lec29.pdf.

[75] J. Peraire and S. Widnall. *16.07 Dynamics, Fall 2009 Version 3.0, Lecture L28 - 3D Rigid Body Dynamics: Equations of Motion; Euler's Equations*. Lecture Notes, MIT. Fall 2009. URL: https://ocw.mit.edu/courses/16-07-dynamics-fall-2009/5e1d8699338146e5127080b880b906d6_MIT16_07F09_Lec28.pdf.

[76] J. M. Picone et al. "NRLMSISE-00 empirical model of the atmosphere: Statistical comparisons and scientific issues". In: *Journal of Geophysical Research: Space Physics* 107.A12 (2002), SIA 15-1-SIA 15–16. DOI: https://doi.org/10.1029/2002JA009430. eprint: https://agupubs.onlinelibrary.wiley.com/doi/pdf/10.1029/2002JA009430. URL: https://agupubs.onlinelibrary.wiley.com/doi/abs/10.1029/2002JA009430.

[77] JM Picone et al. "NRLMSISE-00 empirical model of the atmosphere: Statistical comparisons and scientific issues". In: *Journal of Geophysical Research: Space Physics* 107.A12 (2002), SIA–15.

[78] Rudrapatna V. Ramnath. *Computation and asymptotics*. Includes bibliographical references. 2012. URL: http://dx.doi.org/10.1007/978-3-642-25749-0.

[79] Benny Rievers et al. "Numerical Prediction of Satellite Surface Forces with Application to Rosetta". In: *Advances in the Astronautical Sciences* 143 (Jan. 2012), pp. 1123–1142.

[80] Carlos M Roithmayr. "Contribution of zonal harmonics to gravitational moment". In: *Journal of Guidance, Control, and Dynamics* 14.1 (1991), pp. 210–214.

[81] Hirobumi Saito et al. "300 Mbps Downlink Communications from 50kg Class Small Satellites". In: (2013).

[82] K. Sathyan et al. "Long-term lubrication of momentum wheels used in spacecrafts—An overview". In: *Tribology International* 43.1 (2010), pp. 259–267. ISSN: 0301-679X. DOI: https://doi.org/10.1016/j.triboint.2009.05.033. URL: https://www.sciencedirect.com/science/article/pii/S0301679X09001716.

[83] Michael Scharfe et al. "Design and development of a compact magnetic bearing momentum wheel for micro and small satellites". In: (Sept. 2023).

[84] S. Schwinde et al. "Development of advanced silver coatings for telescope mirrors". In: *Advances in Optical and Mechanical Technologies for Telescopes and Instrumentation V*. Ed. by Ramón Navarro and Roland Geyl. Vol. 12188. International Society for Optics and Photonics. SPIE, 2022, p. 121881X. DOI: 10.1117/12.2627710. URL: https://doi.org/10.1117/12.2627710.

[85] scivision and Daniel Kastinen. *space-physics/msise00: Python bugfix for Python 3.9*. Version v1.11.1. Dec. 2024. DOI: 10.5281/zenodo.14532758. URL: https://doi.org/10.5281/zenodo.14532758.

[86] Florian Seitz and Harald Schuh. "Earth Rotation". In: *Sciences of Geodesy - I: Advances and Future Directions*. Ed. by Guochang Xu. Berlin, Heidelberg: Springer Berlin Heidelberg, 2010, pp. 185–227. ISBN: 978-3-642-11741-1. DOI: 10.1007/978-3-642-11741-1_6. URL: https://doi.org/10.1007/978-3-642-11741-1_6.

[87] Abolfazl Shirazi and Mehran Mirshams. "Design and performance simulation of a satellite momentum exchange actuator". In: *Australian Journal of Mechanical Engineering* 14.1 (2016), pp. 1–9. DOI: 10.1080/14484846.2015.1093223. eprint: https://doi.org/10.1080/14484846.2015.1093223. URL: https://doi.org/10.1080/14484846.2015.1093223.

[88] *Small Satellite Reaction Wheel*. 2019. URL: https://engineering.usu.edu/mae/students/senior-projects/fall2019-spring2020/small-satellite-reaction-wheel.

[89] G. Smet and S. Patti. "A Mechanisms Perspective on Microvibration – Good Practices and Lessons Learned". In: 2018.

[90] Lucas Snyder. *orbit1.svg*. 2007. URL: https://en.m.wikipedia.org/wiki/File:Orbit1.svg.

[91] Spaceacademy. *A MODEL FROM 180 to 500 KM @ONLINE*. July 2021. URL: https://www.spaceacademy.net.au/watch/debris/atmosmod.htm.

[92] Graeme L. Stephens et al. "The albedo of Earth". In: *Reviews of Geophysics* 53.1 (2015), pp. 141–163. DOI: https://doi.org/10.1002/2014RG000449. eprint: https://agupubs.onlinelibrary.wiley.com/doi/pdf/10.1002/2014RG000449. URL: https://agupubs.onlinelibrary.wiley.com/doi/abs/10.1002/2014RG000449.

[93] Mikihiro Sugita. "Torque distribution algorithm for effective use of reaction wheel torques and angular momentums". In: *Acta Astronautica* 139 (2017), pp. 18–23. ISSN: 0094-5765. DOI: https://doi.org/10.1016/j.actaastro.2017.06.014. URL: https://www.sciencedirect.com/science/article/pii/S0094576516313698.

[94] Yee-Chee Tao and R Ramnath. "Satellite attitude prediction by multiple time scales method". In: *NASA STI/Recon Technical Report N* 76 (1975), p. 21252.

[95] Lorenzo Tarabini Castellani et al. "PROBA-3 mission". In: *International Journal of Space Science and Engineering 5* 1.4 (2013), pp. 349–366.

[96] NCEI Geomagnetic Modeling Team and British Geological Survey. *World Magnetic Model 2020*. https://doi.org/10.25921/11v3-da71. Accessed: 2024-05-30. 2019.

[97] UP42 Team. *How Pansharpening Improves Satellite Imagery*. Apr. 2021. URL: https://up42.com/blog/how-pansharpening-improves-satellite-imagery.

[98] Telescope-Optics.net. *Diffraction Image and Point Spread Function (PSF)*. https://www.telescope-optics.net/diffraction_image.htm. Accessed: 2025-08-06.

[99] The MathWorks, Inc. *atan2 - Four quadrant inverse tangent*. Built-in function in MATLAB. 1984-2015. URL: https://nl.mathworks.com/help/matlab/ref/double.atan2.html.

[100] Alvaro Valenzuela, Karin Reinke, and Simon Jones. "A new metric for the assessment of spatial resolution in satellite imagers". In: *International Journal of Applied Earth Observation and Geoinformation* 114 (2022), p. 103051. ISSN: 1569-8432. DOI: https://doi.org/10.1016/j.jag.2022.103051. URL: https://www.sciencedirect.com/science/article/pii/S1569843222002394.

[101] Jozef C Van Der Ha and Vaios J Lappas. "Long-term attitude drift of spinning spacecraft under solar radiation torques". In: *Journal of Guidance, Control, and Dynamics* 30.5 (2007), pp. 1470–1479.

[102] J.P. Veefkind et al. "TROPOMI on the ESA Sentinel-5 Precursor: A GMES mission for global observations of the atmospheric composition for climate, air quality and ozone layer applications". In: *Remote Sensing of Environment* 120 (2012). The Sentinel Missions - New Opportunities for Science, pp. 70–83. ISSN: 0034-4257. DOI: https://doi.org/10.1016/j.rse.2011.09.027. URL: https://www.sciencedirect.com/science/article/pii/S0034425712000661.

[103] Rosaria Verduci et al. "Solar Energy in Space Applications: Review and Technology Perspectives". In: *Advanced Energy Materials* 12.29 (2022), p. 2200125. DOI: https://doi.org/10.1002/aenm.202200125. eprint: https://onlinelibrary.wiley.com/doi/pdf/10.1002/aenm.202200125. URL: https://onlinelibrary.wiley.com/doi/abs/10.1002/aenm.202200125.

[104] Veritasium. *The Bizarre Behavior of Rotating Bodies*. Accessed: July 2025. Sept. 2019. URL: https://youtu.be/1VPfZ_XzisU?si=n__uL3ZQpl1d0QZ7.

[105] Tim Visser et al. "Torque model verification for the GOCE satellite". In: *Advances in Space Research* 62.5 (2018), pp. 1114–1136.

[106] Ronny Votel and Doug Sinclair. "Comparison of control moment gyros and reaction wheels for small earth-observing satellites". In: (2012).

[107] Hao Wang et al. "Adaptive Momentum Distribution Jitter Control for Microsatellite". In: *Journal of Guidance, Control, and Dynamics* 42.3 (2019). DOI: 10.2514/1.G003909. URL: https://doi.org/10.2514/1.G003909.

[108] Hao Wang et al. "Adaptive momentum distribution jitter control for microsatellite". In: *Journal of Guidance, Control, and Dynamics* 42.3 (2019), pp. 632–641.

[109] Avishai Weiss, Uroš V Kalabić, and Stefano Di Cairano. "Station keeping and momentum management of low-thrust satellites using MPC". In: *Aerospace Science and Technology* 76 (2018), pp. 229–241.

[110] James R. Wertz and Wiley J. Larson. *Space Mission Analysis and Design*. 3rd. Kluwer Academic/-Plenum Publishers, 2011.

[111] Sasha V Weston et al. *State-of-the-Art Small Spacecraft Technology*. Technical Publication (TP) 20250000142. Acquired: January 7, 2025; Funded by NASA's Space Technology Mission Directorate (STMD); Publicly available as of September 30, 2024. Ames Research Center, Jan. 2025. URL: https://ntrs.nasa.gov/api/citations/20250000142/downloads/SOA%202025_Final.pdf.

[112] Wikipedia contributors. *Parallel axis theorem — Wikipedia, The Free Encyclopedia*. [Online; accessed 10-July-2025]. 2025. URL: https://en.wikipedia.org/w/index.php?title=Parallel_axis_theorem&oldid=1229936192.

[113] Sebastián Xambó Descamps. "Euler and the dynamics of rigid bodies". In: *Quaderns d'història de l'enginyeria* 9 (2008), pp. 279–303.

[114] Daiqin Yang et al. "Remote sensing image super-resolution: Challenges and approaches". In: July 2015, pp. 196–200. DOI: 10.1109/ICDSP.2015.7251858.

[115] Zhengguo Yuan et al. "Fault Detection, Isolation, and Reconstruction for Satellite Attitude Sensors Using an Adaptive Hybrid Method". In: *IEEE Transactions on Instrumentation and Measurement* 70 (2021), pp. 1–12. DOI: 10.1109/TIM.2021.3097404.

A Simulation data

This appendix provides the complete set of numerical data and design parameters that serve as the foundational inputs for the simulation and trade-off analysis presented in the main body of this thesis. The figures contained herein are direct outputs from the simulation framework described in chapters 6 till 9.6. The data is organised into three categories:

A.1 **Satellite Orbital and Geometric Properties** (Figure 104): Details the initial conditions and physical dimensions defining the satellite across all simulated scenarios.

A.2 **Force and Torque Application Points** (Figure 105): Specifies the locations of external disturbance forces relative to the satellite's centre of mass, which are critical for calculating disturbance torques.

A.3 **Actuator Design Specifications:** Presents the sizing and PID control gains for the two actuator assemblies analysed:

- Momentum Wheel Parameters (Figure 106)
- Reaction Wheel Assembly Parameters (Figure 107)

These datasets enable a quantitative comparison of the satellite's response to environmental disturbances and the performance of the corresponding attitude control actuators. The values listed are in SI units.

A.1 Satellite orbital and Geometric Properties

Sample #	Flyheight [	Inclination	RAAN [deg]	GSD [m]	Hb [m]	Lb [m]	Db [m]	V_bus [m3]	Wp1 = Wp2	Lp1 = Lp2 [	t1 = t2 [m]	V_p1 = V_p	mass_bus	mass_sp1	mass_tot [kg]
1	201024	92.5	221.7	0.84	0.243	0.412	0.317	0.032	0.779	0.243	0.018	0.003	35.928	2.227	40.382
2	202379	87.1	17.5	0.55	0.372	0.496	0.981	0.181	0.924	0.372	0.017	0.006	164.455	3.796	172.046
3	202963	39.2	18.2	0.99	0.208	0.597	0.464	0.058	0.354	0.208	0.01	0.001	46.907	0.511	47.929
4	203024	58.6	94.1	0.74	0.279	0.592	0.753	0.124	0.933	0.279	0.014	0.004	136.659	3.142	142.944
5	203054	74.2	88.1	1	0.206	0.426	0.323	0.028	0.271	0.206	0.009	0	34.003	0.308	34.619
6	204027	133.4	350.2	0.79	0.261	0.459	0.306	0.037	0.741	0.261	0.013	0.003	36.441	1.732	39.904
7	204304	8.2	12	0.91	0.227	0.352	0.337	0.027	0.306	0.227	0.009	0.001	34.132	0.573	35.278
8	204335	155	305.5	0.79	0.262	0.4	0.346	0.036	0.95	0.262	0.014	0.004	31.461	2.683	36.826
9	204658	68.1	0.1	0.69	0.302	0.723	0.327	0.072	0.933	0.302	0.017	0.005	82.52	4.376	91.272
10	207294	80.7	138.6	0.38	0.551	0.576	0.567	0.18	1.408	0.551	0.02	0.015	148.497	10.077	168.651
11	207969	43.2	98.2	0.74	0.286	0.416	0.549	0.065	1.073	0.286	0.022	0.007	54.511	4.483	63.476
12	208003	57.4	72.4	0.58	0.362	0.572	0.73	0.151	0.976	0.362	0.015	0.005	168.214	4.618	177.449
13	209377	131.7	172	0.51	0.414	0.606	1.058	0.265	1.573	0.414	0.024	0.015	249.442	11.63	272.702
14	209721	4.3	172.4	0.94	0.225	0.397	0.658	0.059	0.593	0.225	0.014	0.002	69.689	1.212	72.113
15	209994	42	36.8	0.69	0.309	0.691	0.35	0.075	0.938	0.309	0.016	0.005	91.983	4.565	101.113
16	210151	88	222.5	0.74	0.288	0.318	0.288	0.026	0.747	0.288	0.013	0.003	28.717	2.061	32.84
17	213268	56.5	58.8	0.65	0.331	0.541	0.586	0.105	1.25	0.331	0.02	0.008	125.193	7.146	139.485
18	213372	63.4	16.2	0.5	0.435	0.754	0.481	0.158	1.368	0.435	0.018	0.011	188.806	11.008	210.822
19	215263	136	119.5	0.96	0.226	0.262	0.582	0.034	0.72	0.226	0.015	0.002	34.221	1.888	37.996
20	215758	56.6	3.4	0.55	0.399	0.407	1.197	0.195	1.26	0.399	0.02	0.01	228.513	8.311	245.134
21	216185	172.7	14.8	0.96	0.229	0.239	0.545	0.03	0.591	0.229	0.012	0.002	36.371	1.278	38.926
22	216705	63.2	107	0.61	0.362	0.447	0.969	0.157	0.763	0.362	0.018	0.005	187.258	3.557	194.372
23	218109	48.5	99.5	0.72	0.306	0.416	0.758	0.097	0.375	0.306	0.01	0.001	92.083	0.65	93.383
24	218150	122.6	88.4	0.88	0.251	0.376	0.429	0.041	0.623	0.251	0.012	0.002	33.997	1.041	36.08
25	218505	66.1	86.6	0.59	0.378	0.885	0.409	0.137	0.542	0.378	0.015	0.003	125.262	1.96	129.183
26	219946	31.5	146.9	0.99	0.224	0.382	0.483	0.041	0.601	0.224	0.014	0.002	36.118	1.083	38.284
27	221783	22.6	209.5	0.93	0.241	0.316	0.564	0.043	0.826	0.241	0.014	0.003	38.094	2.041	42.175
28	222732	88	88.3	0.63	0.36	0.448	0.965	0.156	0.63	0.36	0.016	0.004	178.342	2.315	182.973
29	222735	32	213	0.76	0.29	0.326	0.578	0.055	0.466	0.29	0.01	0.001	44.203	0.755	45.713
30	222908	153	263.8	0.91	0.247	0.376	0.376	0.035	0.742	0.247	0.016	0.003	31.95	1.679	35.308
31	224549	89.9	162.4	0.89	0.254	0.583	0.32	0.048	1.009	0.254	0.017	0.004	49.341	3.275	55.891
32	225824	86	146.5	0.65	0.351	0.648	0.377	0.086	0.872	0.351	0.015	0.005	87.101	3.404	93.91
33	226616	6.5	149	0.71	0.321	0.46	0.953	0.141	0.764	0.321	0.014	0.004	167.181	3.087	173.355
34	227243	51.6	17.6	0.75	0.308	0.743	0.509	0.117	0.624	0.308	0.015	0.003	157.149	2.295	161.739
35	228495	142	183.2	0.5	0.465	0.593	0.748	0.206	1.718	0.465	0.027	0.021	257.806	20.112	298.029
36	230341	63.3	55.4	0.9	0.259	0.312	0.666	0.054	0.473	0.259	0.01	0.001	65.218	1.011	67.24
37	230656	152.1	337.8	0.97	0.241	0.342	0.319	0.026	0.932	0.241	0.017	0.004	36.51	3.415	43.34
38	231544	66	18.1	0.83	0.282	0.755	0.401	0.086	0.95	0.282	0.019	0.005	90.218	3.951	98.119
39	232969	5.2	144.5	0.6	0.396	0.768	0.402	0.122	0.465	0.396	0.013	0.002	131.002	1.263	133.529
40	233386	1.7	123.6	1	0.237	0.63	0.667	0.099	0.591	0.237	0.012	0.002	102.931	1.116	105.163
41	233622	65.7	23.5	0.64	0.369	0.516	0.661	0.126	1.101	0.369	0.018	0.007	127.769	5.512	138.794
42	233889	178.2	102.2	0.49	0.487	0.831	0.631	0.255	1.865	0.487	0.026	0.024	245.337	18.039	281.414
43	236237	43.4	34.9	0.95	0.253	0.477	0.408	0.049	0.641	0.253	0.015	0.002	45.402	1.477	48.355
44	236323	84.9	94.7	0.55	0.434	0.827	0.513	0.184	1.068	0.434	0.017	0.008	156.026	5.289	166.605
45	237036	161.3	320.9	0.92	0.26	0.442	0.361	0.042	0.934	0.26	0.017	0.004	36.088	2.853	41.795
46	237317	88.3	65	0.73	0.328	0.354	0.638	0.074	0.394	0.328	0.013	0.002	91.17	0.956	93.082
47	237661	89.5	127.3	0.66	0.365	0.676	0.731	0.18	1.281	0.365	0.022	0.01	149.743	7.257	164.258
48	239106	144.9	259.1	0.89	0.273	0.432	0.303	0.036	0.516	0.273	0.012	0.002	42.172	1.136	44.444
49	239141	37.3	241.4	1	0.243	0.28	0.423	0.029	0.945	0.243	0.016	0.004	27.22	2.498	32.217
50	239167	81.2	115.5	0.84	0.287	0.541	0.783	0.122	0.796	0.287	0.012	0.003	111.951	2.177	116.306
51	240963	64.4	76.5	0.74	0.33	0.45	0.407	0.06	1.162	0.33	0.02	0.008	63.951	5.661	75.272
52	241353	2.4	109.3	0.77	0.316	0.317	0.691	0.069	0.989	0.316	0.015	0.005	80.823	4.328	89.48
53	242191	66.2	110.7	0.87	0.282	0.355	0.82	0.082	0.293	0.282	0.008	0.001	89.513	0.417	90.348
54	242538	7.2	99.6	0.76	0.322	0.34	0.788	0.086	0.668	0.322	0.013	0.003	92.355	2.022	96.399
55	244818	44.5	119.4	0.76	0.326	0.866	0.742	0.21	0.763	0.326	0.018	0.004	175.778	2.647	181.071
56	244843	56.2	159.6	0.77	0.321	0.48	0.331	0.051	0.8	0.321	0.014	0.004	50.912	2.528	55.969
57	245155	7.6	20.6	0.83	0.298	0.613	0.41	0.075	1.126	0.298	0.019	0.006	63.453	4.417	72.287
58	246884	53.5	152.5	0.79	0.316	0.667	0.63	0.133	0.74	0.316	0.014	0.003	112.955	2.28	117.515
59	246899	64.4	30.2	0.5	0.502	0.624	0.605	0.189	1.409	0.502	0.023	0.016	182.486	11.159	204.805
60	247003	84.6	130.9	0.72	0.349	0.651	0.72	0.163	0.354	0.349	0.012	0.001	211.69	1.144	213.978
61	247350	6.5	56.5	0.58	0.432	1.126	0.451	0.219	1.224	0.432	0.021	0.011	222.818	9.216	241.25
62	248596	56.2	77.6	0.53	0.473	1.142	0.545	0.295	0.774	0.473	0.014	0.005	237.818	2.813	243.443
63	251157	82.9	108.3	0.63	0.402	0.504	0.592	0.12	1.48	0.402	0.021	0.013	137.396	11.791	160.978
64	253654	85	41.4	0.85	0.301	0.518	0.549	0.086	1.027	0.301	0.016	0.005	70.091	3.166	76.422
65	258145	45.7	252.3	0.94	0.279	0.386	0.369	0.04	0.424	0.279	0.013	0.001	40.309	0.754	41.817
66	258922	96.5	187.8	0.98	0.267	0.346	0.341	0.032	0.634	0.267	0.013	0.002	35.85	1.662	39.174
67	260450	6.2	73.5	0.69	0.382	0.688	0.427	0.113	1.236	0.382	0.021	0.01	127.686	7.511	142.707
68	262191	40	122.5	0.88	0.302	0.339	0.872	0.089	0.982	0.302	0.016	0.005	77.472	3.198	83.869
69	262530	34.8	65.1	0.83	0.319	0.398	0.345	0.044	0.901	0.319	0.018	0.005	37.814	3.072	43.958
70	263173	42.7	69.4	0.65	0.413	0.498	0.685	0.141	1.281	0.413	0.019	0.01	185.744	10.512	206.768
71	268540	81.3	130.9	0.63	0.434	0.879	0.73	0.278	0.681	0.434	0.015	0.004	233.7	3.081	239.862
72	269201	163.1	321.6	0.56	0.483	0.875	0.546	0.231	1.365	0.483	0.022	0.015	258.321	13.425	285.171
73	272199	164.6	349.3	0.95	0.292	0.36	0.357	0.037	0.31	0.292	0.011	0.001	33.742	0.44	34.623
74	279008	41	171.8	0.62	0.459	0.493	0.631	0.143	1.147	0.459	0.019	0.01	142.464	7.187	156.838
75	280750	5.1	78	0.91	0.311	0.777	0.488	0.118	0.897	0.311	0.016	0.004	153.406	4.269	161.943
76	282785	1.1	67.9	0.88	0.325	0.682	0.477	0.106	0.466	0.325	0.012	0.002	136.408	1.297	139.002
77	285068	54.9	143.1	0.78	0.372	0.387	0.574	0.083	1.347	0.372	0.019	0.01	110.318	10.285	130.887
78	285098	88.1	52.3	0.96	0.301	0.436	0.454	0.059	0.875	0.301	0.015	0.004	53.477	2.818	59.112
79	286713	58.3	110.4	0.59	0.492	0.68	0.684	0.229	1.806	0.492	0.023	0.02	207.964	16.496	240.955
80	294223	84.5	163.5	0.98	0.303	0.766	0.832	0.193	0.304	0.303	0.01	0.001	202.944	0.598	204.141
81	294383	53.2	17	0.81	0.367	0.86	0.527	0.167	1.307	0.367	0.022	0.011	170.218	7.396	185.009
82	296409	72.4	278	0.58	0.522	0.546	1.008	0.287	1.557	0.522	0.022	0.018	247.755	12.595	272.945
83	298137	42.8	44.4	0.76	0.399	0.617	0.665	0.164	0.957	0.399	0.018	0.007	226.714	5.91	238.533
84	299560	49.7	105.4	0.7	0.43	0.851	0.624	0.229	1.074	0.43	0.017	0.008	204.424	6.043	216.509
85	299941	66.3	59.5	0.7	0.435	0.474	0.614	0.127	0.87	0.435	0.015	0.006	114.531	3.557	121.645
86	301726	52.1	1.2	0.92	0.333	0.954	0.725	0.23	0.795	0.333	0.013	0.003	225.818	2.526	230.87
87	301759	0.9	8.4	0.86	0.354	0.718	0.868	0.221	1.318	0.354	0.021	0.01	195.99	6.766	209.523
88	307921	82.5	132.5	0.93	0.335	0.685	0.681	0.157	1.047	0.335	0.018	0.006	160.863	4.744	170.352
89	309067	40.1	37.9	0.95	0.33	0.369	0.423	0.051	0.857	0.33	0.014	0.004	47.139	3.101	53.342
90	310025	7	100.8	0.96	0.328	0.486	0.897	0.143	1.254	0.328	0.019	0.008	176.797	7.495	191.788
91	310521	53.5	78	0.93	0.34	0.721	0.677	0.166	1.221	0.34	0.017	0.007	151.756	5.509	162.774
92	312761	7.6	167.8	0.83	0.382	0.503	0.416	0.08	1.222	0.382	0.022	0.01	104.192	8.537	121.266
93	317418	42.4	72	0.81	0.395	0.77	0.564	0.172	0.625	0.395	0.013	0.003	168.917	1.928	172.774
94	317542	85	22.4	0.74	0.437	0.493	0.887	0.191	0.596	0.437	0.014	0.004	178.989	2.303	183.596
95	320330	42.3	179.9	0.84	0.387	0.644	0.391	0.097	0.869	0.387	0.015	0.005	118.183	4.147	126.477
96	320883	66.9	175.2	0.9	0.361	0.529	0.808	0.154	1.407	0.361	0.023	0.012	158.777	8.749	176.275
97	322814	4.9	5.8	0.84	0.389	0.767	0.457	0.137	0.669	0.389	0.014	0.004	166.203	2.95	172.103
98	324988	6.2	0.1	0.94	0.349	0.812	0.423	0.12	0.764	0.349	0.017	0.004	99.545	2.802	105.149
99	327202	101.7	114.6	0.77	0.428	0.54	1.056	0.244	1.675	0.428	0.022	0.015	253.498	13.759	281.017
100	327260	88.1	165.8	0.77	0.432	0.657	0.62	0.176	0.611	0.432	0.013	0.003	160.92	2.094	165.109
101	332216	85.3	177.3	0.72	0.47	0.625	0.667	0.196	0.53	0.47	0.011	0.003	236.564	2.521	241.605
102	333144	160.3	307.7	0.87	0.387	0.698	1.028	0.278	1.534	0.387	0.024	0.014	252.375	10.306	272.987
103	333657	63	152.6	0.7	0.485	0.582	0.725	0.204	1.277	0.485	0.022	0.013	241.559	12.214	265.988
104	334124	31.2	29.4	0.75	0.449	0.817	0.536	0.197	1.558	0.449	0.023	0.016	247.698	16.336	280.37
105	334516	154.3	196	0.7	0.482	0.911	0.584	0.257	1.429	0.482	0.019	0.013	251.688	11.882	275.451
106	335240	58.1	50.8	0.77	0.438	0.573	0.458	0.115	1.287	0.438	0.023	0.013	121.427	9.093	139.614
107	335935	9	164.9	0.91	0.373	0.478	0.783	0.139	1.125	0.373	0.018	0.007	189.742	7.484	204.711
108	340903	89.9	96.4	0.78	0.442	0.516	0.749	0.171	1.233	0.442	0.023	0.013	232.143	12.035	256.212
109	346522	68.6	18.4	0.86	0.407	0.613	0.692	0.173	1.363	0.407	0.02	0.011	201.754	9.628	221.011
110	347992	86	133.7	0.87	0.404	0.789	0.526	0.168	0.627	0.404	0.016	0.004	198.421	3.024	204.469
111	351618	85.7	112.5	0.78	0.455	0.512	0.506	0.118	1.429	0.455	0.022	0.014	103.49	9.387	122.264
112	352430	50.5	14.1	0.92	0.387	0.68	0.426	0.112	0.649	0.387	0.013	0.003	155.945	3.506	162.957
113	358949	52.1	159.8	0.99	0.366	0.915	0.507	0.17	0.524	0.366	0.013	0.002	188.493	1.744	191.982
114	361952	40	31.4	0.96	0.382	0.504	0.529	0.102	0.473	0.382	0.012	0.002	91.639	1.456	94.551
115	367068	53.5	117.9	0.81	0.46	0.754	0.624	0.217	0.627	0.46	0.012	0.003	247.228	3.074	253.377
116	372205	42.8	113.2	0.97	0.39	0.831	0.931	0.302	0.748	0.39	0.014	0.004	246.076	2.998	252.071
117	377765	4.3	23.4	0.93	0.41	0.446	0.522	0.095	0.65	0.41	0.015	0.004	107.956	2.614	113.184
118	387178	51.2	146.6	0.9	0.434	0.473	0.514	0.106	0.578	0.434	0.013	0.003	115.54	2.335	120.211
119	387547	129.6	224.6	0.84	0.466	0.62	0.873	0.252	1.753	0.466	0.025	0.021	239.653	16.208	272.07
120	392565	46.8	186.4	0.91	0.435	1.097	0.589	0.281	1.562	0.435	0.023	0.016	256.467	10.877	278.222
121	406607	88.9	21.6	0.83	0.497	0.566	0.508	0.143	1.785	0.497	0.028	0.025	151.265	19.393	190.051
122	406811	9.4	7.8	0.91	0.451	0.515	0.73	0.17	1.177	0.451	0.021	0.011	152.927	8.506	169.938
123	413069	48.6	323.7	0.83	0.506	0.787	0.554	0.221	1.665	0.506	0.025	0.021	251.643	17.615	286.874
124	429757	89	179.2	0.95	0.457	0.595	0.512	0.139	0.8	0.457	0.014	0.005	118.53	3.138	124.806
125	441339	9.7	141.3	1	0.449	0.938	0.503	0.212	1.208	0.449	0.019	0.01	250.034	9.749	269.531
126	451200	7.5	97.8	0.98	0.465	0.494	0.699	0.16	1.428	0.465	0.019	0.013	161.137	10.892	182.921
127	456291	45.5	128.4	0.92	0.504	0.608	0.555	0.17	1.026	0.504	0.016	0.008	187.508	6.679	200.866
128	457344	141	214.9	0.95	0.487	0.773	0.625	0.236	1.908	0.487	0.027	0.025	242.956	22.28	287.516

Figure 104: Satellite orbital and geometric Properties per simulation [m, deg, deg, m, m, m, m^3, m, m, m, m^3, kg, kg, kg].

A.2 Satellite force vector locations

Sample #	r_cg_offset	r_cg_offset	r_cg_offset	norm_CG_	r_SPRcp_o	r_SPRcp_o	r_SPRcp_o	norm_SRP_	r_ADcp_off	r_ADcp_off	r_ADcp_off	norm_AD_i	RD_vector_	RD_vector_	RD_vector_	norm_RD_ [Am2]
1	-0.019	0.032	0	0.037	0	0.014	0	0.014	0	-0.015	0.012	0.019	0	-0.022	0.022	0.031
2	-0.035	0	0.093	0.1	0.002	0	-0.006	0.007	0	-0.006	0	0.006	-0.008	-0.008	0.008	0.014
3	0	0.048	0	0.048	0	0	0	0	0	0	0.017	0.017	0	-0.032	0.032	0.045
4	0	-0.04	0.051	0.065	-0.003	0	0.008	0.008	-0.005	0	0.015	0.016	-0.008	-0.008	0.008	0.014
5	-0.012	0.024	0.018	0.033	0	-0.007	-0.005	0.008	-0.005	0.011	0	0.012	0.025	0.025	-0.025	0.043
6	0	0	0	0	0.011	0.019	0.013	0.026	0	-0.008	-0.005	0.01	-0.005	0.005	0	0.007
7	0	0	0.007	0.007	-0.007	-0.01	-0.01	0.016	0	0	0	0	0	-0.028	0.028	0.039
8	0.011	-0.017	0.015	0.025	0.005	0.008	0	0.009	0.002	-0.003	0	0.004	0	-0.022	-0.022	0.031
9	-0.019	0	0.021	0.029	0	0	0	0	0	-0.008	0	0.008	0	-0.02	0.02	0.028
10	0.044	-0.046	0	0.064	-0.012	0.013	0	0.018	0	0.021	0	0.021	0	0.032	-0.032	0.045
11	0	-0.006	0.007	0.009	0.004	0	0	0.004	0.002	-0.003	0.004	0.005	-0.001	0	0.001	0.002
12	-0.016	-0.025	0	0.03	0.005	0	-0.009	0.01	0	0.011	-0.014	0.017	-0.008	-0.008	0.008	0.014
13	0.018	-0.026	0	0.032	-0.015	-0.021	0	0.026	0.012	0	-0.03	0.032	0	-0.033	0.033	0.047
14	0	0.001	0	0.001	0	-0.018	0.029	0.034	-0.007	-0.012	-0.02	0.025	0.016	0.016	0.016	0.027
15	0.004	0	0	0.004	0.003	0	0	0.003	0.003	0.008	-0.004	0.009	0	0.048	0	0.048
16	-0.024	-0.027	0.024	0.044	0	-0.003	0.003	0.004	0	0.011	0.01	0.015	-0.01	0.01	0.01	0.017
17	0	0	0.006	0.006	0	0	0	0	0.013	0	-0.023	0.027	0	0.033	-0.033	0.047
18	0	-0.041	-0.026	0.048	0	0	0.004	0.004	-0.003	0	-0.003	0.005	0.004	0.004	0	0.006
19	0.014	0.017	0	0.022	0.006	-0.007	0	0.009	0.002	-0.003	0.006	0.007	-0.011	0.011	0	0.015
20	-0.027	-0.027	-0.08	0.089	0	0	0.01	0.01	0	-0.002	-0.007	0.007	0	0	0.005	0.005
21	0.009	0.01	0.022	0.026	0	-0.011	0.024	0.026	0.008	-0.009	0	0.012	0.023	0	-0.023	0.032
22	0.006	-0.007	0	0.009	0	0	0	0	0	0.015	0.032	0.035	-0.041	0	0	0.041
23	0	-0.026	-0.047	0.053	-0.004	0.005	0.009	0.011	0.004	0.005	0.009	0.011	0	0.045	0	0.045
24	-0.02	-0.03	0.034	0.049	0.011	-0.017	0	0.02	0.005	0.007	-0.008	0.012	-0.007	0.007	-0.007	0.012
25	-0.011	0	-0.011	0.015	0.002	-0.005	-0.002	0.005	-0.014	0.034	-0.016	0.04	0.013	-0.013	0.013	0.022
26	0	0	0	0	-0.004	-0.006	0	0.007	0.002	-0.003	-0.004	0.005	-0.008	0.008	0.008	0.014
27	0.006	-0.008	-0.014	0.017	-0.009	-0.011	0	0.014	-0.012	-0.016	0	0.02	-0.024	0.024	-0.024	0.041
28	0.002	0	0	0.002	0	0	0.029	0.029	0	0	0.042	0.042	0.012	0	-0.012	0.017
29	0	0.002	0	0.002	0.009	-0.01	0.018	0.023	0.01	-0.011	-0.02	0.025	0	-0.017	0.017	0.025
30	0.016	0	-0.025	0.03	0.006	0.009	0	0.011	0	0	0.013	0.013	0.021	0	0.021	0.029
31	-0.023	0	-0.03	0.038	0.012	-0.027	0.015	0.033	0.002	-0.005	0.003	0.006	0.025	0.025	0	0.035
32	0	0.031	0.018	0.036	-0.015	-0.027	0.016	0.035	0.01	0	-0.01	0.014	0.004	-0.004	0	0.006
33	0.002	0.003	0	0.004	0.008	0.011	0.024	0.027	0	-0.022	0	0.022	-0.005	-0.005	0	0.007
34	-0.02	0	0.033	0.039	0	0	0.008	0.008	0	-0.009	0	0.009	0.027	0.027	0.027	0.047
35	0	0.05	-0.063	0.08	-0.017	0	0	0.017	0	0	-0.027	0.027	0	0	-0.038	0.038
36	0.018	-0.022	0.046	0.054	-0.007	-0.008	0	0.011	0.012	0	0	0.012	0.012	0	0	0.012
37	0	0.023	-0.022	0.032	-0.004	0	0.006	0.007	0.012	0.017	0	0.021	0	0.033	-0.033	0.047
38	-0.025	0	0.036	0.043	0	-0.024	-0.013	0.028	0.011	-0.029	0	0.031	0.01	-0.01	0.01	0.017
39	0.024	-0.046	0.024	0.057	-0.018	-0.035	0	0.04	0	0.013	-0.007	0.015	0.022	0	0.022	0.03
40	0.008	0.022	0	0.024	0.005	0	0.014	0.015	-0.007	-0.019	0.02	0.028	-0.025	-0.025	0.025	0.044
41	0.008	-0.012	-0.015	0.021	0.01	0	0	0.01	0	0	0.006	0.006	0	-0.047	0	0.047
42	0.023	-0.039	-0.029	0.054	0	-0.006	-0.005	0.008	0	0	0	0	-0.019	0.019	0.019	0.032
43	-0.009	0	0	0.009	0	-0.007	-0.006	0.01	0	0.011	0	0.011	0	0.033	0	0.033
44	0	-0.043	-0.027	0.05	0.011	0	0.013	0.016	0.014	0.027	0	0.031	0.005	-0.005	0.005	0.008
45	-0.009	-0.014	0	0.017	-0.002	0.004	0	0.005	0	-0.018	0.014	0.023	0.021	0	0.021	0.029
46	0.02	0	0	0.02	0	0.012	0	0.012	0	0	-0.013	0.013	0.019	0.019	0	0.027
47	-0.016	0.03	-0.032	0.046	0	-0.004	-0.005	0.006	0.005	0	-0.011	0.012	0	0.013	-0.013	0.019
48	0.005	-0.008	0.005	0.01	0	0.015	-0.01	0.018	-0.003	0	0.003	0.005	0.028	0.028	0.028	0.049
49	0	-0.028	0.042	0.051	-0.011	0.013	-0.02	0.026	-0.008	-0.009	0.014	0.019	-0.014	0.014	0.014	0.024
50	-0.012	-0.023	0.034	0.043	-0.002	0	0	0.002	-0.011	0.02	-0.029	0.037	0.026	0	0	0.026
51	-0.005	0.007	0	0.009	0.01	0	0	0.01	0	-0.019	-0.018	0.026	0.012	-0.012	0	0.017
52	0.031	-0.031	-0.068	0.081	-0.01	-0.01	-0.021	0.025	0.009	0	0	0.009	-0.029	0	0.029	0.041
53	0.013	-0.016	0.037	0.043	0.004	0.004	0.01	0.012	0	-0.013	-0.029	0.032	-0.018	0.018	0.018	0.032
54	0	0.029	0	0.029	0.012	0.013	0	0.017	0	0	-0.004	0.004	0	-0.033	-0.033	0.047
55	0.009	0	0.02	0.022	-0.009	0	0.021	0.023	0	-0.011	0.01	0.015	0	-0.03	0.03	0.043
56	0.001	-0.002	0.001	0.003	-0.013	0.019	0.013	0.027	0.004	0	-0.004	0.005	-0.011	0	0	0.011
57	-0.014	-0.029	-0.019	0.037	0.005	0.011	0	0.012	-0.014	0	0	0.014	-0.02	0	-0.02	0.029
58	0.016	0.033	-0.032	0.049	0.01	0	0	0.01	0.004	-0.009	0.009	0.013	0.019	0	0.019	0.027
59	0.004	-0.005	-0.005	0.009	0	0.027	0	0.027	-0.008	-0.01	0	0.013	0	-0.021	0.021	0.029
60	0.019	-0.036	-0.04	0.057	-0.003	-0.007	0.007	0.01	-0.009	0.016	-0.018	0.026	0.024	0.024	0.024	0.041
61	0	0	0	0	-0.02	-0.051	0.021	0.059	-0.007	0	0	0.007	-0.016	0.016	0.016	0.028
62	0	0	0	0	0	0.041	0	0.041	0	-0.019	0.009	0.021	0	0	0	0
63	0	-0.007	-0.008	0.011	-0.003	0.003	0.004	0.006	0	0.01	0	0.01	0	0.03	0.03	0.043
64	-0.004	0.006	0	0.007	-0.005	0	0	0.005	-0.003	0.006	0	0.007	0	-0.013	0	0.013
65	-0.016	0	-0.021	0.026	0.006	-0.009	-0.009	0.014	0	-0.009	0	0.009	0.024	0.024	0.024	0.041
66	0	-0.004	-0.004	0.005	0.007	0	-0.009	0.012	0.009	0.012	-0.012	0.02	-0.033	-0.033	0	0.047
67	-0.009	0.016	0.01	0.021	0.012	0	-0.014	0.019	0	-0.015	0	0.015	0.005	-0.005	-0.005	0.009
68	0	-0.019	0.049	0.053	0.007	0.008	0.021	0.023	0	-0.011	0.029	0.031	0	0	0.025	0.025
69	0.023	-0.028	0	0.036	-0.011	0	0	0.011	0	0.008	-0.007	0.011	-0.006	0.006	0	0.009
70	0	-0.049	0.067	0.083	0.017	0	0	0.017	0	0.019	0	0.019	0	0.028	0	0.028
71	-0.022	0.045	0.037	0.062	-0.018	0.036	0.03	0.05	0	-0.016	0.013	0.021	0.034	0	0.034	0.048
72	-0.007	-0.012	0.008	0.016	-0.008	0.014	-0.009	0.018	0.008	-0.015	0	0.017	-0.001	0.001	-0.001	0.002
73	0	0.01	0	0.01	0.005	0	0	0.005	-0.014	0	-0.017	0.022	0	-0.01	0	0.01
74	0	-0.019	0.024	0.03	0	0.009	-0.012	0.015	-0.012	-0.012	0	0.017	0.015	-0.015	0.015	0.026
75	0	-0.033	0	0.033	-0.009	0	0.014	0.017	-0.004	-0.01	0	0.011	0.005	0	-0.005	0.006
76	-0.008	0.017	0.012	0.023	0	0	0.021	0.021	-0.011	0.023	-0.016	0.03	0	0.012	0.012	0.018
77	-0.003	0	0	0.003	0	-0.004	0.006	0.007	-0.009	-0.009	0.014	0.019	-0.016	0	-0.016	0.022
78	0	0	0.018	0.018	0.003	0	0.005	0.006	0.005	0.008	-0.008	0.012	0.004	0.004	0.004	0.007
79	0	-0.012	-0.012	0.017	0	0.007	0	0.007	0	0	-0.023	0.023	0.014	0	0	0.014
80	-0.027	-0.068	-0.074	0.104	0	0	-0.007	0.007	0	0.033	0.035	0.048	0	-0.004	0.004	0.005
81	0.007	0	0.009	0.011	0.004	0.009	0	0.01	0	0.01	-0.006	0.011	0.018	-0.018	0.018	0.032
82	-0.011	0	0	0.011	-0.025	0	0.047	0.053	0.02	0	-0.038	0.043	-0.012	-0.012	-0.012	0.02
83	0.024	0.038	0.041	0.061	0.009	0.014	-0.015	0.022	0	0	0.02	0.02	0.039	0	0	0.039
84	-0.004	0.008	0.006	0.011	0.02	0.04	0.029	0.054	-0.02	-0.039	-0.028	0.052	0	0.017	0.017	0.024
85	0	0	-0.04	0.04	0	-0.016	0.021	0.027	-0.011	0.012	-0.016	0.023	0	0.02	0	0.02
86	0	-0.014	0	0.014	-0.016	0.045	0.034	0.059	0.016	0	0	0.016	0.012	-0.012	-0.012	0.02
87	0.016	0	-0.04	0.043	-0.016	-0.032	0	0.036	-0.017	-0.034	0	0.038	-0.019	0.019	0	0.027
88	-0.012	0	0	0.012	0	0.027	0	0.027	0.016	0	0	0.016	0	-0.022	-0.022	0.031
89	-0.03	-0.033	-0.038	0.059	0.003	0.003	0.004	0.006	0.011	0.012	-0.014	0.022	0.026	-0.026	0.026	0.044
90	0.017	-0.025	0.046	0.055	0	-0.018	-0.033	0.037	0	-0.024	0	0.024	0.009	0	0	0.009
91	-0.018	-0.039	-0.036	0.056	0.016	0	-0.033	0.037	0.005	-0.011	-0.01	0.016	0.005	-0.005	0	0.007
92	0.022	-0.029	0	0.036	0.011	-0.014	0	0.018	0.018	0	0	0.018	-0.026	-0.026	-0.026	0.044
93	0.006	-0.011	0.008	0.015	0	0	0.018	0.018	0	0.029	-0.021	0.036	0	0	0.043	0.043
94	-0.029	0	-0.059	0.066	-0.015	0.017	-0.031	0.038	0	-0.01	0	0.01	0.028	-0.028	0.028	0.048
95	-0.001	-0.002	0	0.002	-0.017	0.027	0.017	0.036	0	0	-0.011	0.011	0.013	0	0	0.013
96	-0.013	0.019	0.029	0.037	0.017	0.025	-0.038	0.049	0	0	-0.014	0.014	-0.021	0.021	-0.021	0.036
97	-0.014	0.028	0.017	0.035	0	0	0.004	0.004	0	0.005	0.003	0.005	0	-0.032	-0.032	0.046
98	-0.032	0.075	0	0.082	-0.007	-0.017	-0.009	0.02	0.009	0	-0.011	0.014	0	0.021	0	0.021
99	-0.014	-0.018	0	0.022	-0.011	-0.013	0	0.017	0.009	0	-0.023	0.024	0	-0.027	-0.027	0.038
100	0.011	0.016	0.016	0.025	-0.015	0.022	0.021	0.034	-0.004	0	-0.006	0.007	0	-0.009	0	0.009
101	-0.006	0	-0.008	0.01	-0.016	-0.021	0.023	0.035	0.002	-0.003	0	0.004	-0.024	-0.024	0.024	0.041
102	0	-0.033	0.049	0.059	0.009	0	0	0.009	-0.007	-0.013	0.019	0.024	0	0	-0.026	0.026
103	-0.031	0	-0.046	0.055	-0.023	0	0.035	0.042	0.017	-0.021	0	0.027	-0.01	0	0.01	0.014
104	-0.024	0.044	0.029	0.058	0.022	-0.04	0	0.046	0.02	0.037	0.024	0.049	0	0.016	0.016	0.023
105	0	0.072	-0.046	0.086	-0.019	-0.035	-0.023	0.046	0	0	0	0	0.002	0.002	0.002	0.004
106	0.004	0	0	0.004	0.014	0.019	0	0.024	0	0	0	0	-0.003	-0.003	-0.003	0.005
107	0	0.008	0.013	0.015	-0.005	-0.006	0	0.008	0.008	-0.01	0.016	0.021	-0.019	0.019	0	0.028
108	0	0	0.05	0.05	-0.013	0.015	-0.022	0.03	0	0	0	0	0	0.015	-0.015	0.022
109	0	-0.015	0	0.015	0	-0.025	0.028	0.037	0	-0.027	-0.03	0.041	0	0	-0.011	0.011
110	-0.014	-0.027	-0.018	0.035	-0.007	0	0.009	0.012	0.014	0.027	-0.018	0.035	0	0.025	-0.025	0.035
111	0	0.037	-0.036	0.052	-0.018	0	-0.02	0.028	0	0.004	0.004	0.006	-0.01	0.01	0	0.014
112	-0.016	-0.028	0.017	0.036	0	-0.019	-0.012	0.023	0.013	-0.023	0	0.027	-0.013	0.013	-0.013	0.023
113	0	-0.078	0.043	0.089	-0.017	0.041	-0.023	0.05	0	0.012	0	0.012	0.01	0	-0.01	0.014
114	0.005	0	0.006	0.008	0.009	0	-0.012	0.015	-0.018	0	0.024	0.03	0.021	0.021	0.021	0.037
115	-0.005	0	-0.007	0.009	-0.012	0	-0.016	0.02	-0.013	0	0	0.013	0	-0.025	0	0.025
116	0.027	-0.057	0	0.063	-0.011	-0.023	-0.026	0.036	0.005	0	0.013	0.014	-0.022	-0.022	0	0.031
117	0	0.022	0.026	0.034	0.02	0.022	-0.026	0.039	0.011	-0.012	0.015	0.022	0.034	-0.034	0	0.048
118	0	0.037	0	0.037	-0.018	-0.02	0	0.027	0.005	-0.006	0.006	0.01	0	0	0.035	0.035
119	0.026	-0.035	-0.049	0.065	0.006	-0.008	0.012	0.016	-0.019	0	-0.035	0.04	0.019	-0.019	0.019	0.033
120	0	0.051	-0.027	0.058	0	0	0.003	0.003	-0.021	0	-0.029	0.036	0.022	-0.022	-0.022	0.039
121	-0.008	0	0	0.008	0.023	-0.026	0.023	0.042	0.003	0.004	0.003	0.006	0.026	-0.026	0.026	0.045
122	0	-0.049	0	0.049	0	-0.019	-0.026	0.032	0	0	-0.027	0.027	-0.016	0	0.016	0.022
123	-0.036	0	-0.04	0.054	0.022	0	0.024	0.033	-0.01	-0.016	0	0.019	0.029	0.029	0.029	0.05
124	0	-0.032	-0.028	0.043	0	0	0.025	0.025	0.01	-0.013	-0.011	0.02	0.016	-0.016	0.016	0.027
125	-0.037	-0.077	0.041	0.095	0	-0.033	0.018	0.037	0	0.008	0	0.008	0.022	0.022	-0.022	0.039
126	-0.031	0.033	0.047	0.065	-0.017	0.018	-0.025	0.035	0	0	0	0	-0.025	-0.025	0	0.035
127	0	-0.059	-0.054	0.08	-0.006	0	0	0.006	-0.005	0.006	0	0.008	0	0	-0.032	0.032
128	0	-0.03	0.025	0.039	0.012	0	0	0.012	-0.023	0	-0.029	0.037	0	0.024	0.024	0.035

Figure 105: Satellite force vector locations with respect to a neutral centre of mass per simulation. The units are expressed in meters unless stated otherwise.

A.3 FACA Design parameters

Sample #	Outer radius [m]	Inner radius [m]	thickness [m]	mass [kg]	Ixx [m4]	Iyy [m4]	Izz [m4]	max torque [Nm]	pd [-]	id [-]	dd [-]	pc [-]	ic [-]	dc [-]
1	0.1032	0.1158	0.0617	4.64	0.00	5.58E-02	0.00	1.06E-04	50.00076	0.371355	2.551273	0	0	0
2	0.17	0.1769	0.0745	4.85	0.00	1.46E-01	0.00	1.12E-04	50	0.5	2.5	0	0	0
3	0.0885	0.0991	0.0896	4.84	0.00	4.28E-02	0.00	9.88E-05	50.00309	1	2.333517	0	0	0
4	0.1252	0.1326	0.0888	4.57	0.00	7.60E-02	0.00	1.01E-04	50	0.5	2.5	0	0	0
5	0.0825	0.0979	0.0638	4.83	0.00	3.96E-02	0.00	9.71E-05	49.97915	0.484381	2.578026	0	0	0
6	0.1145	0.1244	0.0688	4.44	0.00	6.34E-02	0.00	9.74E-05	50.00386	0.537488	2.415526	0	0	0
7	0.093	0.108	0.0528	4.34	0.00	4.41E-02	0.00	9.25E-05	49.99925	1	2.410641	0	0	0
8	0.1135	0.1249	0.0601	4.44	0.00	6.32E-02	0.00	1.03E-04	50	0.5	2.5	0	0	0
9	0.1386	0.144	0.1085	4.48	0.00	8.95E-02	0.00	1.07E-04	78.88263	0	0.75405	0	0	0
10	0.2572	0.2622	0.0695	4.93	0.00	3.33E-01	0.00	1.65E-04	50	0.5	2.5	0	0	0
11	0.1265	0.1362	0.0624	4.31	0.00	7.44E-02	0.00	1.07E-04	50	0.5	2.5	0	0	0
12	0.1666	0.1722	0.0858	4.39	0.00	1.26E-01	0.00	1.02E-04	50	0.5	2.5	0	0	0
13	0.1923	0.1973	0.0849	4.52	0.00	1.71E-01	0.00	1.33E-04	0	1	5	0	0	0
14	0.0952	0.1073	0.0595	3.96	0.00	4.07E-02	0.00	8.01E-05	100	0.73166	2.470093	0	0	0
15	0.142	0.1471	0.1036	4.13	0.00	8.63E-02	0.00	9.51E-05	14.84355	0.151493	2.40995	0	0	0
16	0.125	0.1369	0.0477	4.05	0.00	6.96E-02	0.00	8.13E-05	50	0.5	2.5	0	0	0
17	0.1518	0.1576	0.0812	3.97	0.00	9.50E-02	0.00	1.24E-04	50	0.5	2.5	0	0	0
18	0.202	0.207	0.074	4.13	0.00	1.73E-01	0.00	1.67E-04	50	0.5	2.5	0	0	0
19	0.0905	0.1076	0.0393	3.63	0.00	3.58E-02	0.00	7.12E-05	50	0.5	2.5	0	0	0
20	0.1836	0.1901	0.0611	4.03	0.00	1.41E-01	0.00	1.54E-04	50	0.5	2.5	0	0	0
21	0.0908	0.1091	0.0359	3.58	0.00	3.61E-02	0.00	6.76E-05	23.38969	0.620835	3.856895	0	0	0
22	0.1661	0.1723	0.067	3.81	0.00	1.09E-01	0.00	8.59E-05	50	0.5	2.5	0	0	0
23	0.1384	0.1458	0.0624	3.57	0.00	7.22E-02	0.00	6.72E-05	50	0.5	2.5	0	0	0
24	0.1098	0.1197	0.0564	3.50	0.00	4.62E-02	0.00	6.39E-05	51.40472	0.607558	4.043246	0	0	0
25	0.1751	0.1801	0.0769	3.73	0.00	1.18E-01	0.00	7.05E-05	49.9997	0.518122	2.502286	0	0	0
26	0.0961	0.1067	0.0574	3.36	0.00	3.46E-02	0.00	6.02E-05	100	0	5	0	0	0
27	0.1033	0.1149	0.0474	3.27	0.00	3.91E-02	0.00	5.93E-05	50	0.5	2.5	0	0	0
28	0.1657	0.1714	0.0673	3.49	0.00	9.90E-02	0.00	7.16E-05	46.07521	0.539486	2.319408	0	0	0
29	0.129	0.1383	0.049	3.32	0.00	5.93E-02	0.00	5.49E-05	5.43E-06	1.87E-06	0.145532	0	0	0
30	0.1081	0.1175	0.0563	3.25	0.00	4.14E-02	0.00	5.81E-05	11.9207	0.278926	1.901356	0	0	0
31	0.1156	0.1212	0.0875	3.16	0.00	4.44E-02	0.00	5.34E-05	50	0.5	2.5	0	0	0
32	0.1623	0.1673	0.0731	3.29	0.00	8.94E-02	0.00	5.61E-05	50	0.5	2.5	0	0	0
33	0.1474	0.153	0.069	3.17	0.00	7.16E-02	0.00	6.27E-05	50	0.5	2.5	0	0	0
34	0.1419	0.1469	0.0794	3.13	0.00	6.53E-02	0.00	5.33E-05	50	0.5	2.5	0	0	0
35	0.2164	0.2214	0.0552	3.30	0.00	1.58E-01	0.00	1.50E-04	50	0.5	2.5	0	0	0
36	0.114	0.1236	0.0468	2.91	0.00	4.12E-02	0.00	4.68E-05	100	0.24563	4.994494	0	0	0
37	0.1052	0.1146	0.0513	2.87	0.00	3.48E-02	0.00	5.63E-05	74.99847	0.249976	1.249771	0	0	0
38	0.1293	0.1343	0.0804	2.89	0.00	5.03E-02	0.00	5.64E-05	50	0.5	2.5	0	0	0
39	0.1834	0.1884	0.0602	3.06	0.00	1.06E-01	0.00	4.61E-05	50	0.5	2.5	0	0	0
40	0.1076	0.1126	0.0916	2.75	0.00	3.34E-02	0.00	4.54E-05	50.00161	0.500719	2.589455	0	0	0
41	0.1706	0.1756	0.0627	2.96	0.00	8.89E-02	0.00	7.49E-05	41.86608	0	0	0	0	0
42	0.2268	0.2318	0.049	3.07	0.00	1.61E-01	0.00	2.45E-04	99.9998	0.999998	0.000611	0	0	0
43	0.1145	0.1203	0.0716	2.66	0.00	3.67E-02	0.00	4.03E-05	100	0	0	0	0	0
44	0.2016	0.2066	0.053	2.95	0.00	1.23E-01	0.00	6.08E-05	50	0.5	2.5	0	0	0
45	0.1179	0.124	0.0663	2.66	0.00	3.90E-02	0.00	4.75E-05	50	0.5	2.5	0	0	0
46	0.1499	0.1561	0.0531	2.73	0.00	6.40E-02	0.00	4.08E-05	75	0.25	1.25	0	0	0
47	0.1689	0.1739	0.0629	2.94	0.00	8.65E-02	0.00	8.37E-05	50	0.5	2.5	0	0	0
48	0.124	0.1298	0.0648	2.61	0.00	4.20E-02	0.00	3.72E-05	37.34063	0.574068	5	0	0	0
49	0.1058	0.1156	0.042	2.49	0.00	3.06E-02	0.00	3.99E-05	50	0.5	2.5	0	0	0
50	0.1317	0.1367	0.0713	2.61	0.00	4.71E-02	0.00	3.94E-05	50	0.5	2.5	0	0	0
51	0.1522	0.1572	0.0626	2.65	0.00	6.33E-02	0.00	6.88E-05	50	0.5	2.5	0	0	0
52	0.1436	0.1504	0.0475	2.59	0.00	5.60E-02	0.00	5.26E-05	50	0.5	2.5	0	0	0
53	0.1275	0.1341	0.0533	2.51	0.00	4.30E-02	0.00	4.23E-05	25	0.75	1.25	0	0	0
54	0.1473	0.1534	0.051	2.53	0.00	5.73E-02	0.00	3.70E-05	47.11277	0.440102	2.821149	0	0	0
55	0.1504	0.1554	0.0574	2.40	0.00	5.60E-02	0.00	3.51E-05	50	0.5	2.5	0	0	0
56	0.1481	0.1531	0.0593	2.44	0.00	5.54E-02	0.00	3.42E-05	64.536	0	0.004898	0	0	0
57	0.137	0.142	0.0645	2.46	0.00	4.78E-02	0.00	5.14E-05	50	0.5	2.5	0	0	0
58	0.1457	0.1507	0.0585	2.37	0.00	5.20E-02	0.00	2.94E-05	50	0.5	2.5	0	0	0
59	0.2338	0.2388	0.0426	2.75	0.00	1.54E-01	0.00	1.49E-04	100	5.55E-17	0	0	0	0
60	0.161	0.166	0.0543	2.42	0.00	6.48E-02	0.00	4.00E-05	50	0.5	2.5	0	0	0
61	0.2008	0.2058	0.0476	2.64	0.00	1.09E-01	0.00	8.71E-05	50	0.5	2.5	0	0	0
62	0.2204	0.2254	0.0425	2.58	0.00	1.28E-01	0.00	7.18E-05	50	0.5	2.5	0	0	0
63	0.1865	0.1915	0.0556	2.87	0.00	1.03E-01	0.00	1.44E-04	49.98458	0.625	2.429199	0	0	0
64	0.1382	0.1432	0.0563	2.16	0.00	4.28E-02	0.00	3.84E-05	50	0.5	2.5	0	0	0
65	0.1278	0.1328	0.0556	1.98	0.00	3.36E-02	0.00	2.29E-05	50	0.5	2.5	0	0	0
66	0.1214	0.127	0.0519	1.94	0.00	3.00E-02	0.00	2.37E-05	56.4475	1	5	0	0	0
67	0.1771	0.1821	0.0447	2.19	0.00	7.07E-02	0.00	6.58E-05	97.91688	0.535644	0.253609	0	0	0
68	0.1386	0.1439	0.0508	2.06	0.00	4.11E-02	0.00	3.74E-05	99.21898	1	5	0	0	0
69	0.147	0.152	0.0486	1.98	0.00	4.43E-02	0.00	3.23E-05	50	0.5	2.5	0	0	0
70	0.1916	0.1966	0.0482	2.56	0.00	9.63E-02	0.00	1.14E-04	50	0.5	2.5	0	0	0
71	0.2015	0.2065	0.0339	1.89	0.00	7.86E-02	0.00	2.25E-05	50	0.5	2.5	0	0	0
72	0.225	0.23	0.0374	2.33	0.00	1.20E-01	0.00	1.31E-04	50	0.5	2.5	0	0	0
73	0.1339	0.1389	0.0447	1.66	0.00	3.10E-02	0.00	1.57E-05	60.74223	0.801607	4.516243	0	0	0
74	0.2135	0.2185	0.03	1.77	0.00	8.26E-02	0.00	3.82E-05	50	0.5	2.5	0	0	0
75	0.1433	0.1483	0.0387	1.54	0.00	3.27E-02	0.00	2.41E-05	49.80469	0.501953	2.509766	0	0	0
76	0.15	0.155	0.0357	1.49	0.00	3.46E-02	0.00	1.60E-05	50	0.5	2.5	0	0	0
77	0.172	0.177	0.0485	2.31	0.00	7.04E-02	0.00	8.59E-05	13.88707	0	0	0	0	0
78	0.1383	0.1433	0.0371	1.43	0.00	2.83E-02	0.00	2.06E-05	50	0.5	2.5	0	0	0
79	0.2292	0.2342	0.0665	4.21	0.00	2.26E-01	0.00	2.63E-04	39.22677	0.556036	0.909431	0	0	0
80	0.1394	0.1444	0.0333	1.29	0.00	2.59E-02	0.00	1.38E-05	50	0.5	2.5	0	0	0
81	0.1698	0.1748	0.0284	1.33	0.00	3.96E-02	0.00	5.93E-05	50	0.5	2.5	0	0	0
82	0.2435	0.2485	0.025	1.68	0.00	1.02E-01	0.00	1.87E-04	50	0.5	2.5	0	0	0
83	0.1849	0.1899	0.0265	1.35	0.00	4.76E-02	0.00	3.51E-05	98.11309	0.831668	1.204141	0	0	0
84	0.2	0.205	0.0301	1.66	0.00	6.81E-02	0.00	3.90E-05	50	0.5	2.5	0	0	0
85	0.202	0.207	0.0234	1.31	0.00	5.46E-02	0.00	2.64E-05	50	0.5	2.5	0	0	0
86	0.1534	0.1584	0.029	1.23	0.00	2.99E-02	0.00	3.53E-05	50	0.5	2.5	0	0	0
87	0.1638	0.1688	0.0271	1.23	0.00	3.40E-02	0.00	4.44E-05	50	0.5	2.5	0	0	0
88	0.1548	0.1598	0.0287	1.23	0.00	3.05E-02	0.00	2.26E-05	50	0.5	2.5	0	0	0
89	0.1519	0.1569	0.0265	1.12	0.00	2.67E-02	0.00	1.99E-05	50	0.5	2.5	0	0	0
90	0.1514	0.1564	0.0311	1.31	0.00	3.10E-02	0.00	6.06E-05	100	0.250563	2.349934	0	0	0
91	0.1568	0.1618	0.0307	1.33	0.00	3.39E-02	0.00	3.96E-05	50	0.5	2.5	0	0	0
92	0.1769	0.1819	0.024	1.17	0.00	3.78E-02	0.00	4.95E-05	50	0.5	2.5	0	0	0
93	0.183	0.188	0.0207	1.05	0.00	3.61E-02	0.00	1.46E-05	50	0.5	2.5	0	0	0
94	0.2032	0.2082	0.0206	1.16	0.00	4.89E-02	0.00	2.52E-05	50	0.5	2.5	0	0	0
95	0.1792	0.1842	0.0209	1.04	0.00	3.43E-02	0.00	1.17E-05	50	0.5	2.5	0	0	0
96	0.1668	0.1718	0.0264	1.22	0.00	3.50E-02	0.00	1.88E-05	50	0.5	2.5	0	0	0
97	0.1803	0.1853	0.0198	0.99	0.00	3.30E-02	0.00	1.54E-05	50	0.5	2.5	0	0	0
98	0.1612	0.1662	0.0208	0.93	0.00	2.49E-02	0.00	1.32E-05	50	0.5	2.5	0	0	0
99	0.1988	0.2038	0.0639	3.51	0.00	1.42E-01	0.00	2.03E-04	50	0.5	2.5	0	0	0
100	0.2007	0.2057	0.0174	0.96	0.00	3.97E-02	0.00	4.94E-06	50	0.5	2.5	0	0	0
101	0.2187	0.2237	0.0156	0.94	0.00	4.59E-02	0.00	6.18E-06	50	0.5	2.5	0	0	0
102	0.1794	0.1844	0.0342	1.70	0.00	5.62E-02	0.00	1.13E-04	50	0.5	2.5	0	0	0
103	0.226	0.231	0.0346	2.16	0.00	1.13E-01	0.00	6.73E-05	55.38473	0	4.272634	0	0	0
104	0.2088	0.2138	0.0296	1.71	0.00	7.62E-02	0.00	1.72E-04	50	0.5	2.5	0	0	0
105	0.2245	0.2295	0.0229	1.42	0.00	7.29E-02	0.00	7.39E-05	50	0.5	2.5	0	0	0
106	0.2037	0.2087	0.0163	0.92	0.00	3.89E-02	0.00	7.70E-05	50	0.5	2.5	0	0	0
107	0.1724	0.1774	0.0201	0.96	0.00	2.93E-02	0.00	4.36E-05	50	0.5	2.5	0	0	0
108	0.2055	0.2105	0.0238	1.35	0.00	5.83E-02	0.00	9.37E-05	50	0.5	2.5	0	0	0
109	0.189	0.194	0.0309	1.61	0.00	5.92E-02	0.00	9.12E-05	11.52488	0.147309	2.093058	0	0	0
110	0.1873	0.1923	0.0147	0.76	0.00	2.75E-02	0.00	1.33E-05	100	0	5	0	0	0
111	0.2118	0.2168	0.0354	2.07	0.00	9.51E-02	0.00	8.89E-05	50	0.5	2.5	0	0	0
112	0.1793	0.1843	0.0148	0.73	0.00	2.42E-02	0.00	1.29E-05	50	0.5	2.5	0	0	0
113	0.1691	0.1741	0.0324	1.52	0.00	4.47E-02	0.00	2.41E-05	50	0.5	2.5	0	0	0
114	0.1769	0.1819	0.0131	0.64	0.00	2.06E-02	0.00	4.24E-06	50	0.5	2.5	0	0	0
115	0.2143	0.2193	0.0142	0.84	0.00	3.94E-02	0.00	1.10E-05	50	0.5	2.5	0	0	0
116	0.1806	0.1856	0.018	0.90	0.00	3.02E-02	0.00	1.84E-05	50	0.5	2.5	0	0	0
117	0.19	0.195	0.0104	0.55	0.00	2.03E-02	0.00	8.58E-06	50	0.5	2.5	0	0	0
118	0.2015	0.2065	0.0122	0.68	0.00	2.81E-02	0.00	7.01E-06	59.3278	0	0	0	0	0
119	0.2169	0.2219	0.069	4.14	0.00	1.99E-01	0.00	2.20E-04	50.00057	0.75	2.492082	0	0	0
120	0.2019	0.2069	0.0403	2.25	0.00	9.38E-02	0.00	5.06E-05	50	0.5	2.5	0	0	0
121	0.2316	0.2366	0.0579	3.70	0.00	2.03E-01	0.00	2.61E-04	50	0.5	2.5	0	0	0
122	0.21	0.215	0.0105	0.60	0.00	2.73E-02	0.00	6.26E-05	100	3.86E-06	1.24999	0	0	0
123	0.2359	0.2409	0.018	1.17	0.00	6.65E-02	0.00	2.12E-04	100	1	5	0	0	0
124	0.1957	0.2007	0.005	0.27	0.00	1.06E-02	0.00	2.01E-06	43.76486	0.030954	5	0	0	0
125	0.2087	0.2137	0.0166	0.95	0.00	4.25E-02	0.00	5.11E-05	50	0.5	2.5	0	0	0
126	0.2163	0.2213	0.025	1.49	0.00	7.15E-02	0.00	1.00E-04	67.38282	0.698753	2.74874	0	0	0
127	0.2348	0.2398	0.0258	1.67	0.00	9.41E-02	0.00	3.94E-05	100	0.153045	3.503919	0	0	0
128	0.2269	0.2319	0.0695	4.35	0.00	2.29E-01	0.00	2.66E-04	50	0.5	2.5	0	0	0

Figure 106: Momentum Wheel Design parameters.

Sample #	Outer radius [m]	Inner radius [m]	thickness [m]	mass [kg]	Ixx [m4]	Iyy [m4]	Izz [m4]	max torque [Nm]	pd [-]	id [-]	dd [-]	pc [-]	ic [-]	dc [-]
1	0.0563	0.0625	0.0352	1.255	3.38E-03	3.38E-03	3.38E-03	1.06E-04	0.075107	0.000765	0.037282	0.000804	7.46E-06	3.92E-05
2	0.0527	0.0585	0.0488	1.310	3.30E-03	3.30E-03	3.30E-03	1.12E-04	0.07545	0	0	0	0	0.000282
3	0.0513	0.057	0.0533	1.309	3.18E-03	3.18E-03	3.18E-03	9.88E-05	0.162815	0.005674	0.100233	0.005674	3.19E-05	0.000156
4	0.0545	0.0605	0.0392	1.235	3.19E-03	3.19E-03	3.19E-03	1.01E-04	0.048713	0.000363	0.018164	0.003095	3.63E-06	1.82E-05
5	0.0513	0.057	0.0531	1.306	3.17E-03	3.17E-03	3.17E-03	9.71E-05	0.09311	0.001552	0.077956	0.001575	1.60E-05	4.66E-05
6	0.0546	0.0607	0.0368	1.199	3.09E-03	3.09E-03	3.09E-03	9.74E-05	0.13513	0.001656	0.067066	0.002095	3.82E-05	0.000187
7	0.0556	0.0618	0.0328	1.173	3.06E-03	3.06E-03	3.06E-03	9.25E-05	0.067847	0.003582	0.066328	0.003894	3.89E-05	0.000193
8	0.0546	0.0607	0.0368	1.199	3.09E-03	3.09E-03	3.09E-03	1.03E-04	0.256646	0.004844	0.249299	0.01	5.16E-05	0.000242
9	0.0532	0.0591	0.0416	1.212	3.03E-03	3.03E-03	3.03E-03	1.07E-04	0.096875	0.000969	0.04862	0.000969	1.28E-05	4.84E-05
10	0.0477	0.053	0.0688	1.333	2.93E-03	2.93E-03	2.93E-03	1.65E-04	0.546111	0.001103	0.276414	0.00504	5.47E-05	0.000362
11	0.0528	0.0587	0.04	1.164	2.86E-03	2.86E-03	2.86E-03	1.07E-04	0.002467	6.56E-06	0.046921	6.29E-07	3.16E-07	4.81E-07
12	0.0507	0.0563	0.048	1.185	2.77E-03	2.77E-03	2.77E-03	1.02E-04	0.048805	1.42E-05	0.023233	0.006701	4.24E-06	5.20E-07
13	0.0497	0.0552	0.0536	1.221	2.80E-03	2.80E-03	2.80E-03	1.33E-04	1	0.000363	0	0.01	0	0
14	0.0536	0.0595	0.0328	1.069	2.60E-03	2.60E-03	2.60E-03	8.01E-05	0.104462	0.00164	0.122459	0.00207	2.27E-05	0.000106
15	0.0511	0.0568	0.0424	1.116	2.60E-03	2.60E-03	2.60E-03	9.51E-05	0.054926	0.000117	0.000422	3.91E-05	1.17E-06	5.84E-06
16	0.0515	0.0572	0.04	1.094	2.56E-03	2.56E-03	2.56E-03	8.13E-05	0.082585	0.001601	0.071697	0.001089	7.78E-06	8.03E-05
17	0.0495	0.055	0.0448	1.072	2.38E-03	2.38E-03	2.38E-03	1.24E-04	7.24E-10	0.01	0.0217	0.01	0	0.0005
18	0.0472	0.0524	0.056	1.117	2.34E-03	2.34E-03	2.34E-03	1.67E-04	0.045762	3.63E-05	0.022019	8.46E-11	0	3.13E-10
19	0.0517	0.0574	0.0328	0.980	2.23E-03	2.23E-03	2.23E-03	7.12E-05	0.08569	0.000855	0.056573	0.000857	8.57E-06	4.28E-05
20	0.0477	0.053	0.052	1.088	2.30E-03	2.30E-03	2.30E-03	1.54E-04	0.987958	0.000232	0.182146	0.009999	0.0001	0.0005
21	0.0511	0.0568	0.0336	0.969	2.17E-03	2.17E-03	2.17E-03	6.76E-05	0.100439	0.001	0.049976	0.001	1.00E-05	5.02E-05
22	0.0477	0.053	0.048	1.030	2.15E-03	2.15E-03	2.15E-03	8.59E-05	0.560217	0.001338	0.258768	0.006116	1.20E-05	0.00026
23	0.0483	0.0537	0.0416	0.966	2.03E-03	2.03E-03	2.03E-03	6.72E-05	0.460611	7.81E-05	0.000663	7.81E-05	7.81E-07	0.000496
24	0.0498	0.0553	0.036	0.946	2.05E-03	2.05E-03	2.05E-03	6.39E-05	0.04826	0.000502	0.026913	0.001108	4.83E-06	5.61E-05
25	0.0468	0.052	0.0496	1.008	2.05E-03	2.05E-03	2.05E-03	7.05E-05	0.548671	0.00043	0.023782	0.005976	5.00E-06	0.000236
26	0.05	0.0556	0.0328	0.907	1.95E-03	1.95E-03	1.95E-03	6.02E-05	0.128125	0.001281	0.048438	0.001281	1.28E-05	6.41E-05
27	0.049	0.0544	0.0344	0.885	1.84E-03	1.84E-03	1.84E-03	5.93E-05	0.114733	0.000534	0.04938	0.000537	4.61E-06	0.000292
28	0.0459	0.051	0.048	0.942	1.84E-03	1.84E-03	1.84E-03	7.16E-05	0.225211	7.48E-22	0.120032	0.01	2.66E-05	1.17E-10
29	0.0473	0.0526	0.04	0.897	1.80E-03	1.80E-03	1.80E-03	5.49E-05	0.110628	0.001073	0.060059	0.001063	1.06E-05	8.28E-05
30	0.0485	0.0539	0.0352	0.878	1.80E-03	1.80E-03	1.80E-03	5.81E-05	0.074483	0.000856	0.04878	0.001387	7.45E-06	8.87E-05
31	0.0477	0.053	0.036	0.855	1.71E-03	1.71E-03	1.71E-03	5.34E-05	0.550062	0.000136	0.024942	0.000465	7.68E-05	0.00014
32	0.045	0.05	0.0472	0.890	1.67E-03	1.67E-03	1.67E-03	5.61E-05	1	0	0.020718	0.01	-3.39E-21	0
33	0.0455	0.0505	0.0432	0.857	1.61E-03	1.61E-03	1.61E-03	6.27E-05	0.98467	0.001385	0.380719	0.007943	4.31E-06	4.58E-05
34	0.0455	0.0505	0.0424	0.847	1.59E-03	1.59E-03	1.59E-03	5.33E-05	0.096885	9.90E-05	0.039822	0	3.33E-05	0.0005
35	0.0419	0.0466	0.0592	0.892	1.51E-03	1.51E-03	1.51E-03	1.50E-04	0.09266	4.91E-06	0.050169	0.009776	0	0.000238
36	0.0458	0.0509	0.0368	0.787	1.47E-03	1.47E-03	1.47E-03	4.68E-05	0.098594	0.001149	0.048746	0.001244	1.23E-05	6.13E-05
37	0.0464	0.0515	0.0344	0.776	1.46E-03	1.46E-03	1.46E-03	5.63E-05	0.549355	0.005509	0.275439	0.000499	5.50E-05	2.49E-05
38	0.0449	0.0499	0.0392	0.782	1.42E-03	1.42E-03	1.42E-03	5.64E-05	0.628433	0.000974	0.127782	0.01	0	0.000469
39	0.0423	0.047	0.052	0.826	1.40E-03	1.40E-03	1.40E-03	4.61E-05	0.205272	0.000756	0.05011	0.000203	8.77E-05	0.000333
40	0.0455	0.0506	0.0344	0.744	1.36E-03	1.36E-03	1.36E-03	4.54E-05	0.826228	0.000702	0.048659	0.007868	6.80E-05	0.000465
41	0.0426	0.0473	0.0488	0.801	1.36E-03	1.36E-03	1.36E-03	7.49E-05	0.794754	0.003799	0.222791	0.004112	2.53E-05	6.05E-06
42	0.04	0.0445	0.0616	0.829	1.29E-03	1.29E-03	1.29E-03	2.45E-04	1	0	0.499999	0	0.0001	0
43	0.0444	0.0493	0.036	0.720	1.26E-03	1.26E-03	1.26E-03	4.03E-05	0.107296	0.001351	0.052998	0.001041	1.35E-05	5.20E-05
44	0.0407	0.0452	0.056	0.799	1.27E-03	1.27E-03	1.27E-03	6.08E-05	0.087895	0.001464	0.044325	0.000879	1.50E-05	7.52E-05
45	0.0441	0.049	0.0368	0.719	1.25E-03	1.25E-03	1.25E-03	4.75E-05	0.705743	0.001192	0.129934	0.005494	1.66E-05	7.88E-05
46	0.0424	0.0471	0.044	0.738	1.23E-03	1.23E-03	1.23E-03	4.08E-05	0.775	0.00775	0.0125	0.007061	7.75E-05	0.000138
47	0.0427	0.0474	0.048	0.796	1.35E-03	1.35E-03	1.35E-03	8.37E-05	0.189821	0.000355	0.063851	0.003501	1.24E-05	5.80E-05
48	0.0432	0.048	0.0384	0.704	1.19E-03	1.19E-03	1.19E-03	3.72E-05	0.082532	0.00058	0.024764	0.000579	4.95E-06	2.49E-05
49	0.0434	0.0482	0.0352	0.673	1.13E-03	1.13E-03	1.13E-03	3.99E-05	0.502641	0.002785	0.275089	0.007514	4.61E-05	4.70E-05
50	0.0428	0.0475	0.04	0.706	1.17E-03	1.17E-03	1.17E-03	3.94E-05	0.419791	6.12E-07	0.016445	0.01	1.95E-07	1.48E-05
51	0.0416	0.0462	0.0448	0.715	1.15E-03	1.15E-03	1.15E-03	6.88E-05	0.655149	0.003581	0.144352	0.002004	1.24E-05	0.000337
52	0.0417	0.0463	0.0432	0.701	1.12E-03	1.12E-03	1.12E-03	5.26E-05	0.015144	0	0	0	0	-1.36E-20
53	0.0423	0.047	0.0392	0.680	1.10E-03	1.10E-03	1.10E-03	4.23E-05	0.087277	0	0.044697	0	0	0
54	0.041	0.0456	0.044	0.685	1.07E-03	1.07E-03	1.07E-03	3.70E-05	0.155907	0.000152	0.02421	0.006419	2.72E-06	0.000185
55	0.0401	0.0445	0.044	0.648	9.67E-04	9.67E-04	9.67E-04	3.51E-05	0.525698	0	0.302723	0	0	0
56	0.0406	0.0451	0.0432	0.659	1.01E-03	1.01E-03	1.01E-03	3.42E-05	0.560351	0.002409	0.142304	0.002244	2.05E-05	0.000149
57	0.0414	0.046	0.0408	0.664	1.04E-03	1.04E-03	1.04E-03	5.14E-05	1	0	0	0.000497	0	0
58	0.0401	0.0445	0.0432	0.639	9.53E-04	9.53E-04	9.53E-04	2.94E-05	0.974577	0.0004	0.092746	0.009936	7.21E-07	0.000469
59	0.0378	0.042	0.0632	0.743	1.04E-03	1.04E-03	1.04E-03	1.49E-04	0.016782	1.60E-07	0	0	0	0.0005
60	0.0396	0.044	0.0464	0.655	9.65E-04	9.65E-04	9.65E-04	4.00E-05	0.104921	0.001053	0.051658	0.000994	1.03E-05	4.97E-05
61	0.0387	0.043	0.056	0.714	1.03E-03	1.03E-03	1.03E-03	8.71E-05	0.015617	0	0	0	1.56E-06	0
62	0.0374	0.0416	0.06	0.699	9.56E-04	9.56E-04	9.56E-04	7.18E-05	0.104598	0.000381	0.03855	0.0027	7.81E-07	0.000488
63	0.041	0.0455	0.0528	0.776	1.24E-03	1.24E-03	1.24E-03	1.44E-04	0.687677	0.001809	0.23229	0.002689	3.78E-05	0.000246
64	0.039	0.0433	0.0416	0.585	8.24E-04	8.24E-04	8.24E-04	3.84E-05	0.548423	0.000543	0.276028	0.007786	2.45E-06	1.23E-05
65	0.0382	0.0424	0.0392	0.535	7.18E-04	7.18E-04	7.18E-04	2.29E-05	0.03076	0.00024	0.016035	0.00024	2.37E-06	0.000134
66	0.0383	0.0426	0.0376	0.526	7.08E-04	7.08E-04	7.08E-04	2.37E-05	0.32456	0.003296	0.16306	0.00323	3.24E-05	0.000162
67	0.0369	0.041	0.0504	0.593	7.73E-04	7.73E-04	7.73E-04	6.58E-05	0.748942	0	0.5	0	0.0001	0
68	0.0382	0.0424	0.0416	0.557	7.55E-04	7.55E-04	7.55E-04	3.74E-05	0.474121	0.008875	0.290719	0.000125	3.88E-05	0.000194
69	0.0371	0.0412	0.0432	0.536	6.91E-04	6.91E-04	6.91E-04	3.23E-05	0.647857	0	0	0	0	0
70	0.0387	0.043	0.0536	0.691	9.93E-04	9.93E-04	9.93E-04	1.14E-04	0.546881	0.000469	0.033304	0.000781	7.81E-06	3.91E-05
71	0.0333	0.037	0.056	0.510	5.55E-04	5.55E-04	5.55E-04	2.25E-05	0.096875	0.001281	0.064062	0.001281	9.69E-06	6.41E-05
72	0.0354	0.0393	0.0616	0.628	7.75E-04	7.75E-04	7.75E-04	1.31E-04	1	0	0.5	0	0	6.78E-21
73	0.0352	0.0391	0.04	0.450	5.21E-04	5.21E-04	5.21E-04	1.57E-05	0.097784	0.00171	0.066535	0.000782	1.71E-05	4.59E-05
74	0.0319	0.0354	0.0584	0.478	4.81E-04	4.81E-04	4.81E-04	3.82E-05	0.121105	0.00022	0.105901	0.00557	1.78E-05	1.41E-05
75	0.0334	0.0371	0.0424	0.416	4.41E-04	4.41E-04	4.41E-04	2.41E-05	0.067612	3.91E-05	2.34E-05	0	3.84E-07	0.000492
76	0.0325	0.0361	0.044	0.402	4.06E-04	4.06E-04	4.06E-04	1.60E-05	0.60382	0.00017	0.045781	0.006717	2.19E-05	0.000351
77	0.0382	0.0424	0.0488	0.624	8.64E-04	8.64E-04	8.64E-04	8.59E-05	0.005267	-1.08E-19	0.5	0	8.47E-22	-6.78E-21
78	0.0325	0.0361	0.0416	0.386	3.87E-04	3.87E-04	3.87E-04	2.06E-05	0.517745	0.007597	0.143402	0.000235	2.87E-05	0.000143
79	0.0459	0.051	0.0624	1.137	2.29E-03	2.29E-03	2.29E-03	2.63E-04	0.447482	1.93E-05	1.86E-06	2.52E-05	9.63E-07	0.0005
80	0.0311	0.0345	0.0416	0.348	3.21E-04	3.21E-04	3.21E-04	1.38E-05	0.30968	0.003918	0.050045	0.003529	3.32E-05	0.000196
81	0.0299	0.0332	0.0488	0.360	3.15E-04	3.15E-04	3.15E-04	5.93E-05	0.047711	3.25E-19	0.485368	0	-6.78E-21	0
82	0.0298	0.0331	0.0656	0.454	4.06E-04	4.06E-04	4.06E-04	1.87E-04	0.066788	-2.17E-18	0	0	1.36E-20	-1.36E-20
83	0.0294	0.0327	0.052	0.366	3.13E-04	3.13E-04	3.13E-04	3.51E-05	0.238968	0	0	0	0.0001	0.0005
84	0.0316	0.0351	0.0552	0.449	4.42E-04	4.42E-04	4.42E-04	3.90E-05	0.1	0.001	0.05	0.001	1.00E-05	5.00E-05
85	0.0282	0.0313	0.056	0.353	2.80E-04	2.80E-04	2.80E-04	2.64E-05	0.172962	-3.25E-19	0	6.51E-19	0	2.03E-20
86	0.0297	0.033	0.0448	0.333	2.85E-04	2.85E-04	2.85E-04	3.53E-05	0.275	0.00775	0.305767	0.00275	7.75E-05	0.000387
87	0.0292	0.0324	0.0472	0.333	2.76E-04	2.76E-04	2.76E-04	4.44E-05	0.099909	0.001009	0.050423	0.001009	9.99E-06	4.99E-05
88	0.0297	0.033	0.0448	0.333	2.85E-04	2.85E-04	2.85E-04	2.26E-05	0.989333	0.005625	0.018741	0	0	0.000438
89	0.0284	0.0316	0.0448	0.302	2.38E-04	2.38E-04	2.38E-04	1.99E-05	0.759727	0.003573	0.089529	0.005288	3.03E-05	9.34E-05
90	0.0307	0.0341	0.044	0.353	3.21E-04	3.21E-04	3.21E-04	6.06E-05	0.515034	3.36E-09	0	0	5.00E-05	0.00025
91	0.0306	0.034	0.0456	0.361	3.27E-04	3.27E-04	3.27E-04	3.96E-05	0.517054	0.000255	0.012492	0.007747	7.75E-05	0.000387
92	0.0279	0.031	0.0504	0.317	2.44E-04	2.44E-04	2.44E-04	4.95E-05	0.163525	0.000389	0.484488	0.009989	9.47E-05	3.91E-06
93	0.0262	0.0291	0.052	0.283	1.94E-04	1.94E-04	1.94E-04	1.48E-05	0.109535	0	0	0	0	0
94	0.0266	0.0296	0.056	0.312	2.22E-04	2.22E-04	2.22E-04	2.52E-05	0.195491	0.000193	0.041053	0.000162	3.02E-06	3.29E-05
95	0.0264	0.0293	0.0504	0.280	1.94E-04	1.94E-04	1.94E-04	1.17E-05	0.049011	2.48E-06	1.38E-08	0	5.39E-10	1.91E-09
96	0.0289	0.0321	0.048	0.330	2.70E-04	2.70E-04	2.70E-04	1.88E-05	0.070654	3.43E-06	0.000159	0.000321	7.53E-07	3.92E-06
97	0.0256	0.0285	0.0512	0.267	1.76E-04	1.76E-04	1.76E-04	1.54E-05	0.32073	0	0	4.34E-19	3.39E-21	-6.78E-21
98	0.0258	0.0287	0.0464	0.251	1.65E-04	1.65E-04	1.65E-04	1.32E-05	0.236099	2.75E-06	2.03E-09	2.71E-07	2.75E-08	0
99	0.0441	0.049	0.0552	0.949	1.75E-03	1.75E-03	1.75E-03	2.03E-04	0.1	0.001	0.05	0.001	1.00E-05	5.00E-05
100	0.0245	0.0272	0.056	0.260	1.57E-04	1.57E-04	1.57E-04	4.94E-06	0.591156	6.10E-19	0.5	0	1.00E-04	0
101	0.0236	0.0262	0.06	0.254	1.44E-04	1.44E-04	1.44E-04	6.18E-06	0.050221	8.78E-05	0.003902	8.10E-05	7.80E-07	0.000496
102	0.0329	0.0366	0.0504	0.459	4.84E-04	4.84E-04	4.84E-04	1.13E-04	0.094304	0.000171	0.048781	0	0	4.24E-09
103	0.0342	0.038	0.0616	0.583	6.75E-04	6.75E-04	6.75E-04	6.73E-05	0.023988	0	0.068416	0	0	0.0005
104	0.0315	0.035	0.0576	0.461	4.53E-04	4.53E-04	4.53E-04	1.72E-04	0.621323	0.000417	0.082766	0.007197	5.02E-05	0.000435
105	0.0283	0.0315	0.0608	0.382	3.09E-04	3.09E-04	3.09E-04	7.39E-05	0.09375	0.001563	0.078125	0.001563	1.56E-05	4.69E-05
106	0.0239	0.0266	0.056	0.247	1.44E-04	1.44E-04	1.44E-04	7.70E-05	0.742529	9.23E-06	0	0	0	0
107	0.0257	0.0286	0.0488	0.259	1.71E-04	1.71E-04	1.71E-04	4.36E-05	0.179369	7.40E-05	0.004854	0.00046	0	2.39E-05
108	0.0284	0.0316	0.0568	0.364	2.94E-04	2.94E-04	2.94E-04	9.37E-05	0.488788	0.00067	0.01385	0.009857	9.97E-05	0
109	0.0317	0.0352	0.0528	0.436	4.29E-04	4.29E-04	4.29E-04	9.12E-05	0.200408	0.01	0.5	0.01	0.0001	0.0005
110	0.0225	0.025	0.0528	0.206	1.06E-04	1.06E-04	1.06E-04	1.33E-05	0.780118	0	5.55E-17	0	0	0.0005
111	0.0342	0.038	0.0584	0.559	6.43E-04	6.43E-04	6.43E-04	8.89E-05	0.309362	0	0.04375	6.84E-14	0.0001	0
112	0.0225	0.025	0.0504	0.198	1.01E-04	1.01E-04	1.01E-04	1.29E-05	1	0	0.264149	0	0	0.0005
113	0.0317	0.0352	0.0488	0.411	4.01E-04	4.01E-04	4.01E-04	2.41E-05	0.099219	0.00107	0.049609	0.000992	9.92E-06	4.96E-05
114	0.0211	0.0235	0.0504	0.173	7.87E-05	7.87E-05	7.87E-05	4.24E-06	1	0.000918	0.074609	0.002206	0.0001	0
115	0.0225	0.025	0.0592	0.227	1.17E-04	1.17E-04	1.17E-04	1.10E-05	0.075	0.00075	0.0375	0.00075	3.25E-05	3.75E-05
116	0.0246	0.0273	0.0512	0.243	1.47E-04	1.47E-04	1.47E-04	1.84E-05	0.013072	-5.42E-19	0	-5.42E-19	0	0.0005
117	0.0192	0.0213	0.0536	0.148	5.58E-05	5.58E-05	5.58E-05	8.58E-06	0.547493	0.000492	0.278516	0.005414	4.92E-06	0.000271
118	0.0208	0.0231	0.056	0.182	8.08E-05	8.08E-05	8.08E-05	7.01E-06	0.052381	4.03E-05	0	0.000556	0	8.19E-06
119	0.0464	0.0515	0.0592	1.118	2.28E-03	2.28E-03	2.28E-03	2.20E-04	0.989433	0.000545	0.077364	0.00113	7.80E-06	4.35E-05
120	0.036	0.04	0.056	0.607	7.66E-04	7.66E-04	7.66E-04	5.06E-05	0.0375	0.001625	0.081255	0.001625	3.74E-06	1.88E-05
121	0.0432	0.048	0.0632	1.001	1.81E-03	1.81E-03	1.81E-03	2.61E-04	0.205863	0.002371	0.118554	0.00116	2.06E-05	4.24E-05
122	0.0195	0.0217	0.0576	0.163	6.43E-05	6.43E-05	6.43E-05	6.26E-05	0.679977	0.000239	0.001884	0.007656	0	4.31E-05
123	0.0255	0.0283	0.064	0.316	2.09E-04	2.09E-04	2.09E-04	2.12E-04	0.56069	0.000784	0.024319	0.005708	4.80E-06	4.27E-05
124	0.018	0.02	0.0267	0.073	2.29E-05	2.29E-05	2.29E-05	2.01E-06	0.091504	0	0.039049	1.17E-06	4.91E-08	0.000499
125	0.0241	0.0268	0.0576	0.257	1.52E-04	1.52E-04	1.52E-04	5.11E-05	0.05	0.0055	0.275	0.0005	5.50E-05	0.000275
126	0.0293	0.0326	0.0592	0.403	3.47E-04	3.47E-04	3.47E-04	1.00E-04	0.766189	0.000688	0.236374	0.001983	3.36E-05	6.57E-05
127	0.0301	0.0335	0.0632	0.452	4.12E-04	4.12E-04	4.12E-04	3.94E-05	1	0	0	0	0.0001	0.0005
128	0.0468	0.052	0.0616	1.176	2.46E-03	2.46E-03	2.46E-03	2.66E-04	0.548504	0.000502	0.277117	0.006027	4.39E-06	0.000239

Figure 107: Reaction Wheel Assembly Design parameters.